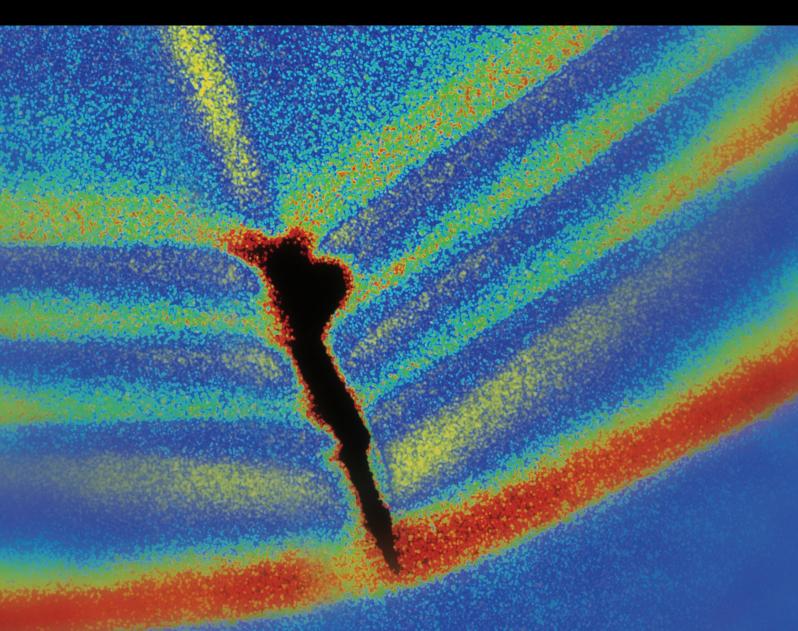
Risk, Reliability, and Uncertainty Quantification of Structural Systems Subjected to Shock and Vibration

Lead Guest Editor: Aly M. Aly

Guest Editors: Mohammad A. Hariri-Ardebili, Elena Dragomirescu,

and Jiming Xie



Risk, Reliability, and Uncertainty Quantification of Structural Systems Subjected to Shock and Vibration

Risk, Reliability, and Uncertainty Quantification of Structural Systems Subjected to Shock and Vibration

Lead Guest Editor: Aly M. Aly

Guest Editors: Mohammad A. Hariri-Ardebili,

Elena Dragomirescu, and Jiming Xie



Editorial Board

Brij N. Agrawal, USA Felix Albu, Romania Marco Alfano, Italy Sumeet S. Aphale, UK Hassan Askari, Canada Lutz Auersch, Germany Matteo Aureli, USA Mahmoud Bayat, USA Marco Belloli, Italy Giosuè Boscato, Italy Francesco Braghin, Italy Rafał Burdzik, Poland Salvatore Caddemi, Italy Ivo Caliò, Italy Antonio Carcaterra, Italy Dumitru I. Caruntu, USA Cristina Castejón, Spain Nicola Caterino, Italy Gabriele Cazzulani, Italy Noel Challamel, France Athanasios Chasalevris, UK Xavier Chiementin, France Nawawi Chouw, New Zealand Simone Cinquemani, Italy Pedro A. Costa, Portugal Alvaro Cunha, Portugal Giorgio Dalpiaz, Italy Farhang Daneshmand, Canada Silvio L.T. de Souza, Brazil Dario Di Maio, UK Luigi Di Sarno, Italy Longjun Dong, China Lorenzo Dozio, Italy Mohamed El Badaoui, France Mohammad Elahinia, USA Fiorenzo A. Fazzolari, UK Matteo Filippi, Italy Piotr Folega, Poland Paola Forte, Italy Francesco Franco, Italy Juan C. G. Prada, Spain Pedro Galvín, Spain Gianluca Gatti, Italy Marco Gherlone, Italy

Anindya Ghoshal, USA Gilbert R. Gillich, Romania Nere Gil-Negrete, Spain Adam Glowacz, Poland Itzhak Green, USA Hassan Haddadpour, Iran M. Amin Hariri-Ardebili, USA M.I. Herreros, Spain Hamid Hosano, Japan Reza Jazar, Australia Sakdirat Kaewunruen, UK Yuri S. Karinski, Israel Jeong-Hoi Koo, USA Georges Kouroussis, Belgium Mickaël Lallart, France Luca Landi, Italy Marco Lepidi, Italy Zhixiong Li, China Manuel Lopez Aenlle, Spain Nuno M. Maia, Portugal Stefano Manzoni, Italy Giuseppe Carlo Marano, Italy Stefano Marchesiello, Italy Francesco S. Marulo, Italy Jean-Mathieu Mencik, France Laurent Mevel, France Fabio Minghini, Italy Mahdi Mohammadpour, UK Rui Moreira, Portugal Emiliano Mucchi, Italy Peter Múčka, Slovakia Sara Muggiasca, Italy Tony Murmu, UK Pedro Museros, Spain Roberto Nascimbene, Italy Sundararajan Natarajan, India Toshiaki Natsuki, Japan Miguel Neves, Portugal Nicola Nisticò, Italy Roberto Palma, Spain A. Papageorgiou, Greece Francesco Pellicano, Italy Paolo Pennacchi, Italy

Giuseppe Petrone, Italy

Evgeny Petrov, UK Giuseppe Piccardo, Italy Antonina Pirrotta, Italy Franck Poisson, France Luca Pugi, Italy Mohammad Rafiee, Canada Carlo Rainieri, Italy José J. Rangel-Magdaleno, Mexico Didier Rémond, France Francesco Ripamonti, Italy Riccardo Rubini, Italy Salvatore Russo, Italy Giuseppe Ruta, Italy Edoardo Sabbioni, Italy Filippo Santucci de Magistris, Italy Onome E. Scott-Emuakpor, USA Roger Serra, France Chengzhi Shi, USA Vadim V. Silberschmidt, UK Kumar V. Singh, USA Jean-Jacques Sinou, France Isabelle Sochet, France Alba Sofi, Italy Jussi Sopanen, Finland Stefano Sorace, Italy Andrea Spaggiari, Italy Shuaishuai Sun, Australia Chao Tao, China Marco Tarabini, Italy Gloria Terenzi, Italy Mario Terzo, Italy Tai Thai, Australia Marc Thomas, Canada Hamid Toopchi-Nezhad, Iran Carlo Trigona, Italy Federica Tubino, Italy Nerio Tullini, Italy Angelo Marcelo Tusset, Brazil Jens Twiefel, Germany Filippo Ubertini, Italy Marcello Vanali, Italy F. Viadero, Spain M. Ahmer Wadee, UK

Jörg Wallaschek, Germany

Matthew J. Whelan, USA Agnieszka Wylomanska, Poland Davood Younesian, Iran Enrico Zappino, Italy Radoslaw Zimroz, Poland

Contents

Risk, Reliability, and Uncertainty Quantification of Structural Systems Subjected to Shock and Vibration

Aly Mousaad Aly , M. Amin Hariri-Ardebili , Elena Dragomirescu , and Jiming Xie Editorial (3 pages), Article ID 3269734, Volume 2018 (2018)

Cylindrical Shell with Junctions: Uncertainty Quantification of Free Vibration and Frequency Response Analysis

Harri Hakula (D), Vesa Kaarnioja (D), and Mikael Laaksonen (D) Research Article (16 pages), Article ID 5817940, Volume 2018 (2018)

The Influence of the Track Parameters on Vibration Characteristics of Subway Tunnel

Wenbo Shi , Linchang Miao , Junhui Luo , and Honglei Zhang Research Article (12 pages), Article ID 2506909, Volume 2018 (2018)

Wind-Induced Response of Inclined and Yawed Ice-Accreted Stay Cable Models

Songyu Cao, Himan Hojat Jalali , and Elena Dragomirescu Research Article (12 pages), Article ID 6853047, Volume 2018 (2018)

Reliability and Random Lifetime Models of Planetary Gear Systems

Peng Gao D, Liyang Xie D, and Wei Hu Research Article (12 pages), Article ID 9106404, Volume 2018 (2018)

A New Erosion Model for Wind-Induced Structural Vibrations

Keqin Yan , Yi Zhang , and Tao Cheng Research Article (8 pages), Article ID 6839062, Volume 2018 (2018)

Experimental Study of the Debris Flow Slurry Impact and Distribution

Haixin Zhao, Lingkan Yao D, Yong You D, Baoliang Wang D, and Cong Zhang Research Article (15 pages), Article ID 5460362, Volume 2018 (2018)

Theoretical Study of Synchronous Behavior in a Dual-Pendulum-Rotor System

Fang Pan (D), Hou Yongjun (D), Dai Liming (D), and Du Mingjun (D) Research Article (13 pages), Article ID 9824631, Volume 2018 (2018)

A Copula-Based and Monte Carlo Sampling Approach for Structural Dynamics Model Updating with Interval Uncertainty

Xueqian Chen D, Zhanpeng Shen, and Xinen Liu Research Article (11 pages), Article ID 3958016, Volume 2018 (2018)

Remaining Useful Life Prediction Method of Rolling Bearings Based on Pchip-EEMD-GM(1, 1) Model

Fengtao Wang D, Xiaofei Liu D, Chenxi Liu D, Hongkun Li D, and Qingkai Han D Research Article (10 pages), Article ID 3013684, Volume 2018 (2018)

Response Surface Method for Material Uncertainty Quantification of Infrastructures

Mohammad Amin Hariri-Ardebili , S. Mahdi Seyed-Kolbadi, and Mohammad Noori Review Article (14 pages), Article ID 1784203, Volume 2018 (2018)

Blast Parameter Optimization Study Based on a Blast Crater Experiment

Xi-liang Zhang, Hai-bao Yi D, Hong-hao Ma, and Zhao-wu Shen Research Article (12 pages), Article ID 8031735, Volume 2018 (2018)

Quasi-Static Cyclic Test on a Concrete-Encased Frame-Reinforced Concrete Tube Building Model

Lei Zeng D, Yunfeng Xiao, Juan Chen, and Yiguang Chen

Research Article (14 pages), Article ID 5643872, Volume 2018 (2018)

Research on the Fatigue Properties of High Strength Concrete after Exposure to High Temperature under Low Cyclic Compressive Loading

Linhao Wang, Haijing Gao , Haibiao Gao, and Zhili Luo Research Article (11 pages), Article ID 3762685, Volume 2018 (2018)

Study on the Nonlinear Characteristics of a Rotating Flexible Blade with Dovetail Interface Feature

Chaofeng Li , Zengchuang Shen, Bingfu Zhong, and Bangchun Wen Research Article (13 pages), Article ID 4923898, Volume 2018 (2018)

Seismic Performance of Base-Isolated Precast Concrete Shear Wall Structure with AHW Connections

Wei Wang D, Aiqun Li, and Xingxing Wang Research Article (22 pages), Article ID 9632523, Volume 2018 (2018)

Hybrid Structural Reliability Analysis under Multisource Uncertainties Based on Universal Grey Numbers

Xingfa Yang, Jie Liu, Xiaoyue Chen, Qixiang Qing, and Guilin Wen (D) Research Article (7 pages), Article ID 3529479, Volume 2018 (2018)

Hindawi Shock and Vibration Volume 2018, Article ID 3269734, 3 pages https://doi.org/10.1155/2018/3269734

Editorial

Risk, Reliability, and Uncertainty Quantification of Structural Systems Subjected to Shock and Vibration

Aly Mousaad Aly , M. Amin Hariri-Ardebili, Lean Dragomirescu, Amin Hariri-Ardebili

Correspondence should be addressed to Aly Mousaad Aly; aly@lsu.edu

Received 28 October 2018; Accepted 29 October 2018; Published 18 December 2018

Copyright © 2018 Aly Mousaad Aly et al. This is an open access article distributed under the Creative Commons Attribution License, which permits unrestricted use, distribution, and reproduction in any medium, provided the original work is properly cited.

Deterministic analysis methods, even when they are based on detailed modeling, may not precisely reflect the reliability of engineering structures. The alternative is to perform risk analysis under the probabilistic assumption and propagate the uncertainty in different design variables. This is an important and crucial task, especially for structures subjected to shock and vibration. The design and analysis of ordinary structures subjected to single and multiple hazard dynamic loads are real-world related engineering applications such as critical dams and nuclear power plants under hydrodynamic shock and earthquake impact; synoptic and nonsynoptic wind-induced structural vibrations; vehicle-induced vibrations in bridges; wind, wave, and seismic impact on offshore structures and wind turbines; and earthquake-induced vibrations in structures.

The articles presented in this special issue are focused on the state-of-the-art techniques, methods, and applications in risk, reliability, and uncertainty quantification of structural and infrastructure systems under shock and vibration loadings. Overall, 29 submissions were received by the editorial team, and 16 manuscripts have been accepted for publication. Figure 1 shows "word cloud" data mined from all accepted papers, indicating repetition of relevant keywords.

Nonlinear dynamic analysis and design of concrete dams are affected by two main uncertainty sources, i.e., epistemic and aleatory. In the paper by M. A. Hariri-Ardebili et al. "Response Surface Method for Material Uncertainty Quantification of Infrastructures," the authors proposed a

response surface metamodel in order to quantify the material uncertainty in arch dams subjected to seismic excitation. The proposed technique revealed a good agreement with Latin hypercube sampling while reducing the computational efforts considerably. A concrete damage index was shown in terms of the fragility curves.

Quantitative analysis of the dynamic behaviors of soft soils during the metro train operation is a very important task for risk analysis. In the paper by W. Shi et al. "The Influence of the Track Parameters on Vibration Characteristics of Subway Tunnel," the authors performed a series of parametric nonlinear finite element coupled simulations to compute the time-variant vertical acceleration of the rail, the sleepers, and the surface of the tunnel. The results are applicable to metro design and provide guidance during tunnel construction.

Rolling bearings are critical components that determine the remaining lifetime of machinery in which their failure may lead to catastrophic accidents. In the paper by F. Wang et al. "Remaining Useful Life Prediction Method of Rolling Bearings Based on Pchip-EEMD-GM(1, 1) Model," the authors proposed a trend prediction method for the remaining useful life of a rolling bearing. The model is based on the feature's dimension reduction via kernel principal components, as well as the calculation of the temporal hazard rate. Full life testing of rolling bearings is provided, showing that the proposed model has higher accuracy compared to existing methods, revealing its feasibility and effectiveness for predicting the remaining life.

¹Louisiana State University, Baton Rouge, LA 70803, USA

²University of Colorado at Boulder, Boulder, CO 80309, USA

³University of Ottawa, Ottawa, Canada

⁴Zhejiang University, Hangzhou, China



FIGURE 1: Word cloud from all accepted papers.

Although the uncertainty quantification with probabilistic methods is a useful technique in reliability analysis, the model parameters may not be precisely represented due to several reasons in engineering practices. In the paper by X. Yang et al. "Hybrid Structural Reliability Analysis under Multisource Uncertainties Based on Universal Grey Numbers," the authors proposed an efficient approach to analyze structural reliability with random-interval-fuzzy hybrid parameters. Also, they employed the universal grey mathematics to solve this nonprobabilistic problem.

The applications of high-strength concrete are widely observed in complex structures of modern architectures which may undergo fatigue after exposure to high temperatures. In the paper by L. Wang et al. "Research on the Fatigue Properties of High Strength Concrete after Exposure to High Temperature under Low Cyclic Compressive Loading," the authors performed low cyclic compressive loading on high strength concrete exposed to high temperatures, using an electrohydraulic servo fatigue testing machine. Several analytical models were proposed based on regression analysis.

The accuracy of finite element modeling can be increased by updating the uncertain parameters during reliability analysis. In the paper by X. Chen et al. "A Copula-Based and Monte Carlo Sampling Approach for Structural Dynamics Model Updating with Interval Uncertainty," the authors proposed a model updating approach in structural dynamics with interval uncertain parameters. They computed the confidence intervals of updating parameters using the nonparametric kernel density estimation approach.

The nonlinear dry friction force produced by the dovetail interface plays an important role in vibration attenuation. The effect of dry friction vibration reduction is significant when the rotating speed is slow or the friction coefficient is small. In the paper by C. Li et al. "Study on the Nonlinear Characteristics of a Rotating Flexible Blade with Dovetail Interface Feature," the authors proposed a dynamical model to simulate the nonlinear characteristics of a flexible blade. The model is based on macro-stick-slip mechanical modeling of dry friction to simulate the constraint condition of the flexible blade.

The force of debris flow on the dam distributes unevenly, and the impact force is large in the middle and decreases gradually to both sides. In the paper by H. Zhao et al. "Experimental Study of the Debris Flow Slurry Impact and Distribution," the authors present a new method to calculate debris flow slurry impact. A series of experimental tests were conducted on a dam with various densities, channel slopes, and dam front angles.

In a concrete-encased steel frame-reinforced concrete core tube building, the core tube bears major loading and exhibits overturning failure; afterwards, the frame transfers the surplus load and exhibits column tensile failure and joint panel shear failure. In the paper by L. Zeng et al. "Quasi-Static Cyclic Test on a Concrete-Encased Frame-Reinforced Concrete Tube Building Model," the authors performed a 1: 5 reduced-scale quasi-static testing with multipoint loading and quantified parameters such as hysteretic characteristics, strain distribution, and energy dissipation.

In numerical simulation of thin solids, the sources of uncertainty are related to material parameters and geometry representing manufacturing imperfections. In the paper by H. Hakula et al. "Cylindrical Shell with Junctions: Uncertainty Quantification of Free Vibration and Frequency Response Analysis," the authors solved the multiparametric free vibration of the complex shell under uncertainty using stochastic collocation with the p-version of the finite element method.

The wind-induced erosion coefficient is a function of air density, sow particle density, snow particle radius, and snow particle strength bond. In the paper by K. Yan et al. "A New Erosion Model for Wind-Induced Structural Vibrations," the authors proposed an advanced erosion coefficient model including the probability distribution and value range. Detailed randomness of the structural vibrations is studied as well.

Vertical and torsional vibrations of ice-accreted stay cables are increased with the increase of vertical and yaw angles. Also, larger ice thickness increases vertical and torsional vibration amplitudes. In the paper by S. Cao et al. "Wind-Induced Response of Inclined and Yawed Ice-Accreted Stay Cable Models," the authors performed several wind tunnel tests and CFD simulations. The ice-accretion profiles dimensions and yaw and vertical inclination angles were studied parametrically.

The rational resistant line or explosive charge depth in mines should be 0.86 times the optimal resistant line. In the paper by X.-l. Zhang et al. "Blast Parameter Optimization Study Based on a Blast Crater Experiment," the authors conducted a small charge-forward blast crater experiment to study the relationship among the rock volume blasted, the explosive unit consumption, the bulk yield, and the depth ratio. The proposed regression-based equations are shown to be optimized, efficient, and economical.

Planetary gear systems are widely used in technological systems which have the advantages of compact structures, high transmission efficiency, and large transmission ratio. In the paper by P. Gao et al. "Reliability and Random Lifetime Models of Planetary Gear Systems," the authors developed dynamic reliability models in which load, geometric, and

material parameters are considered inputs for random lifetime models. Monte Carlo simulations are adopted for validation.

Improved assembly of horizontal wall connections in base-isolated precast concrete shear wall structures is useful and effective, and it fulfils the requirements to withstand seismic excitations. In the paper by W. Wang et al. "Seismic Performance of Base-Isolated Precast Concrete Shear Wall Structure with AHW Connections," the authors conduced two 1:4 small-scaled shake table tests: a lead-rubber bearing base-isolated structure model and a base-fixed structure model.

The spring stiffness, the installation angular of the motor, and rotation direction of the rotors have a large influence on the stability of the synchronization state in the coupling system, and the mass ratios of the system are irrelevant. In the paper by F. Pan et al. "Theoretical Study of Synchronous Behavior in a Dual-Pendulum-Rotor System," the authors proposed a simplified mechanical model of the dual-pendulum-rotor systems.

We hope that this special issue would shed light on recent advances and developments in the area of uncertainty quantification in structural systems and attract attention of the scientific community to pursue further research and studies, leading to rapid implementation of advanced reliable and risk-based models in various aspects of Civil, Mechanical, and Materials Engineering.

Conflicts of Interest

The editors declare that they have no conflicts of interest.

Acknowledgments

We would like to express our appreciation to all authors for their informative contributions and the reviewers for their support and constructive critiques that made this special journal issue possible.

> Aly Mousaad Aly M. Amin Hariri-Ardebili Elena Dragomirescu Jiming Xie

Hindawi Shock and Vibration Volume 2018, Article ID 5817940, 16 pages https://doi.org/10.1155/2018/5817940

Research Article

Cylindrical Shell with Junctions: Uncertainty Quantification of Free Vibration and Frequency Response Analysis

Harri Hakula 🕟, Vesa Kaarnioja 🕞, and Mikael Laaksonen 🕞

Aalto University, School of Science, Department of Mathematics and Systems Analysis, P.O. Box 11100, FI-00076 Aalto, Finland

Correspondence should be addressed to Harri Hakula; harri.hakula@aalto.fi

Received 27 April 2018; Revised 29 September 2018; Accepted 16 October 2018; Published 2 December 2018

Guest Editor: Aly Mousaad Aly

Copyright © 2018 Harri Hakula et al. This is an open access article distributed under the Creative Commons Attribution License, which permits unrestricted use, distribution, and reproduction in any medium, provided the original work is properly cited.

Numerical simulation of thin solids remains one of the challenges in computational mechanics. The 3D elasticity problems of shells of revolution are dimensionally reduced in different ways depending on the symmetries of the configurations resulting in corresponding 2D models. In this paper, we solve the multiparametric free vibration of complex shell configurations under uncertainty using stochastic collocation with the *p*-version of finite element method and apply the collocation approach to frequency response analysis. In numerical examples, the sources of uncertainty are related to material parameters and geometry representing manufacturing imperfections. All stochastic collocation results have been verified with Monte Carlo methods.

1. Introduction

Numerical simulation of thin solids remains one of the challenges in computational mechanics. The advent of stochastic finite element methods has led to new possibilities in simulations, where it is possible to replace isotropy assumptions with statistical models of material parameters or incorporate manufacturing imperfections with parametrized computational domains and derive statistical quantities of interest such as expectation and variance of the solution. Here, we discuss two special classes of such uncertainty quantification problems: free vibration of shells of revolution and directly related frequency response analysis. What makes the specific shell configurations interesting from the application point of view is that they include junctions and shell-solid couplings. Free vibrations of cylinder-cone configurations have been studied by many authors before [1-4]. There also exists an exhaustive literature review on shells with junctions [5].

In vibration problems, the sources of uncertainty relate to materials and geometry. In this paper, the stochastic vibration problems are solved using a *nonintrusive* approach, the stochastic collocation [6]. Collocation methods are particularly appealing in problems with parameterized (random) domains. The standard approach is to solve the problem at specified quadrature points and interpolate over the points. If

the number of random variables is high, this leads to the *curse* of dimensionality which can be alleviated up to a point with special high-dimensional quadratures, the so-called sparse grids [7–10]. If the uncertainty is only in the material parameters, one can apply the *intrusive* approach such as stochastic Galerkin methods, see [11] and references therein.

Sparse grids are designed to satisfy given requirements for quadrature rules. It is, however, possible to construct similar interpolation operators even if the point set is limited to some subset of the parameter space (partial sparse grids), or, crucially, points are added to the sparse grid. In both cases, the construction is the same [12]. Every point in a sparse grid corresponds to some realization of the random field. If some real measurements become available and the data can be identified as points in the parameter space, they can be incorporated into the interpolation operator.

The two model problems studied here are a wind turbine tower resonance problem and the free vibration of a classical long cylinder-cone junction combined with T-junction via kinematic constraints. The wind turbine tower problem is inspired by an earlier study [13], where the tower is modeled as a solid due to solver limitations. The long cylinder case is in turn inspired by a photograph of a collapsed pipe ([14], p. 82).

We have studied related stochastic shell eigenproblems in the previous work [15], but only for cylinders with

constant thickness. In this study, in all cases one, of the random parameters is geometric which changes the character of the computational problems considerably. However, the underlying theoretical properties remain the same. One of the characteristic features of multiparametric eigenvalue problems is that the order of eigenpairs in the spectrum may vary over the parameter space, a phenomenon referred to as *crossing* of the modes.

In this paper, we show how the existing methods can be applied to shell problems that have characteristics that differ from those covered in the literature until now. We do observe crossing of the modes in the wind turbine tower problem which is satisfying since it highlights the fact that this feature is not an artificial mathematical concept but something that is present in standard engineering problems. The stochastic framework for eigenproblems is applied to frequency response analysis in a straightforward manner, yet the resulting method is new. We also demonstrate in connection with frequency response analysis that interpolation operators based on partial sparse grids can provide useful information.

All simulations have been computed using *p*-version of the finite element method [16]. The results derived using collocation on sparse grids have been verified using the Monte Carlo method.

The rest of this paper is organized as follows. In Section 2, the two shell models used in this paper are introduced; in Section 3, the stochastic variant is given with the solution algorithms; Section 3.5 covers the multivariate interpolation construction; the frequency response analysis is briefly outlined in Section 4; the numerical experiments are covered in detail in Section 5; finally, conclusions are drawn in Section 6.

2. Shell Eigenproblem

Assuming a time harmonic displacement field, the free vibration problem for a general shell leads to the following abstract *eigenvalue* problem: find $\mathbf{u} \in \mathbb{R}^3$ and $\omega^2 \in \mathbb{R}$ such that

$$\begin{cases}
\mathbf{S}\mathbf{u} = \omega^2 \mathbf{M}\mathbf{u}, \\
+ \text{boundary conditions,}
\end{cases}$$
(1)

where $\mathbf{u} = \{u, v, w\}$ represents the shell displacement field, while ω^2 represents the square of the eigenfrequency. In the abstract setting, **S** and **M** are differential operators representing deformation energy and inertia, respectively. In the discrete setting, they refer to corresponding stiffness and mass matrices.

Simulation of thin solids using standard finite elements is difficult, since one (small thickness) dimension dominates the discretization. In the following, we shall derive two variants of problem (1) by employing different dimension reductions for shells of revolution. Instead of working in 3D, the elasticity equations are dimensionally reduced either in thickness or in the case of axisymmetric domains, using a suitable ansatz.

2.1. Shell Geometry. In the following, we let a profile function y = f(x) revolve about the x-axis. Naturally, the profile function defines the local radius of the shell. Shells of

revolution can formally be characterized as domains in \mathbb{R}^3 of type

$$\Omega = \{ \mathbf{x} + \eta(\mathbf{x})\mathbf{n}(\mathbf{x}) | \mathbf{x} \in D, -d_0(\mathbf{x}) < \eta(\mathbf{x}) < d_1(\mathbf{x}) \},$$
 (2)

where D is a (mid)surface of revolution, $\mathbf{n}(\mathbf{x})$ is the unit normal to D, and $d(\mathbf{x}) = d_1(\mathbf{x}) + d_0(\mathbf{x})$ is the thickness of the shell measured in the direction of the normal. An illustration of such a configuration is given in Figure 1.

2.1.1. Constant (Dimensionless) Thickness. Let us have $d(\mathbf{x}) = d$ (constant) and define principal curvature coordinates, where only four parameters, the radii of principal curvature R_1 , R_2 , and the so-called Lamé parameters, A_1 , A_2 , which relate coordinates changes to arc lengths, are needed to specify the curvature and the metric on D. The displacement vector field of the midsurface $\mathbf{u} = \{u, v, w\}$ can be interpreted as projections to directions

$$\mathbf{e}_{1} = \frac{1}{A_{1}} \frac{\partial \Psi}{\partial x_{1}},$$

$$\mathbf{e}_{2} = \frac{1}{A_{2}} \frac{\partial \Psi}{\partial x_{2}},$$

$$\mathbf{e}_{3} = \mathbf{e}_{1} \times \mathbf{e}_{2},$$
(3)

where $\Psi(x_1, x_2)$ is a suitable parametrization of the surface of revolution, $\mathbf{e}_1, \mathbf{e}_2$ are the unit tangent vectors along the principal curvature lines, and \mathbf{e}_3 is the unit normal. In other words,

$$\mathbf{u} = u\mathbf{e}_1 + v\mathbf{e}_2 + w\mathbf{e}_3. \tag{4}$$

Assuming that the shell profile is given by $f(x_1)$, the geometry parameters are

$$A_{1}(x_{1}) = \sqrt{1 + [f'(x_{1})]^{2}},$$

$$A_{2}(x_{1}) = f(x_{1}),$$

$$R_{1}(x_{1}) = -\frac{A_{1}(x_{1})^{3}}{f''(x_{1})},$$

$$R_{2}(x_{1}) = A_{1}(x_{1})A_{2}(x_{1}).$$
(5)

Both cylinders and cones are examples of parabolic shells according to the theory of surfaces by Gauss. This follows from the fact that, in both cases, $f''(x_1) = 0$. In particular the reciprocal function

$$\frac{1}{R_1(x_1)} = 0. (6)$$

For a cylinder with a constant radius, $f(x_1) = 1$, say, we get

$$A_1(x_1) = A_2(x_1) = R_2(x_1) = 1,$$

$$\frac{1}{R_1(x_1)} = 0.$$
(7)

In the following, we shall keep the general form of the parameters in the equations.

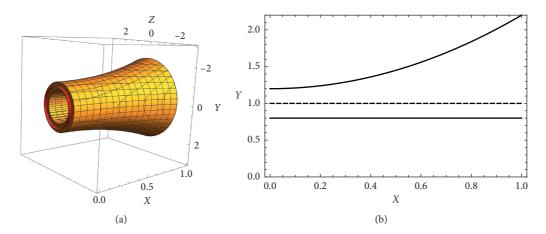


FIGURE 1: Shell of revolution with variable axial thickness; midsurface indicated with (a) red colour and (b) dashed line. (a) Shell of revolution. (b) Cross section; midsurface f(x) = 1 (dashed), lower surface $f(x) = d_0(x)$ and upper surface $f(x) + d_1(x)$ (solid).

We can now define the *dimensionless* thickness t as t = d/R, where $R \sim R_2$ is the unit length. In the following, we assume that $R \sim 1$, and thus, use the two thickness concepts denoted by d and t interchangeably.

2.2. Reduction in Thickness. The free vibration problem for a general shell (1) in the case of shell of revolution with constant thickness t leads to the following eigenvalue problem: find $\mathbf{u}(t)$ and $\omega^2(t) \in \mathbb{R}$ such that

$$\begin{cases} tA_{\mathbf{m}}\mathbf{u}(t) + tA_{\mathbf{s}}\mathbf{u}(t) + t^{3}A_{\mathbf{b}}\mathbf{u}(t) = \omega^{2}(t)M(t)\mathbf{u}(t), \\ + \text{boundary conditions.} \end{cases}$$
(8)

where $\mathbf{u}(t)$ represents the shell displacement field, while $\omega^2(t)$ represents the square of the eigenfrequency. The differential operators $A_{\rm m}$, $A_{\rm s}$, and $A_{\rm b}$ account for membrane, shear, and bending potential energies, respectively, and are *independent of t*. Finally, M(t) is the inertia operator, which in this case can be split into the sum $M(t) = tM^l + t^3M^r$, with M^l (displacements) and M^r (rotations) *independent of t*. Many well-known shell models fall into this framework.

Let us next consider the variational formulation of problem (8). Accordingly, we introduce the space V of admissible displacements and consider the problem: find $(\mathbf{u}(t), \omega^2(t)) \in V \times \mathbb{R}$ such that

$$ta_{\mathbf{m}}(\mathbf{u}(t), \mathbf{v}) + ta_{\mathbf{s}}(\mathbf{u}(t), \mathbf{v}) + t^{3}a_{\mathbf{b}}(\mathbf{u}(t), \mathbf{v})$$
$$= \omega^{2}(t)m(t; \mathbf{u}(t), \mathbf{v}) \quad \forall \mathbf{v} \in V,$$
 (9)

where $a_{\rm m}(\cdot,\cdot)$, $a_{\rm s}(\cdot,\cdot)$, $a_{\rm b}(\cdot,\cdot)$, and $m(t;\cdot,\cdot)$ are the bilinear forms associated with the operators $A_{\rm m}$, $A_{\rm s}$, $A_{\rm b}$, and M(t), respectively. Obviously, the space V and the three bilinear forms depend on the chosen shell model [17].

2.2.1. Two-Dimensional Model. Our two-dimensional shell model is the so-called Reissner-Naghdi model [17], where the transverse deflections are approximated with low-order polynomials. The resulting vector field has

five components $\mathbf{u}=(u,v,w,\theta,\psi)$, where the first three are the standard displacements and the latter two are the rotations in the axial and angular directions, respectively. Here, we adopt the convention that the computational domain $\widehat{\Omega}_t \subset \mathbb{R}^2$ is given by the surface parametrization, and the axial/angular coordinates are denoted by x and y:

$$\widehat{\Omega}_t = \{ (x, y) \mid a \le x \le b, 0 \le y < 2\pi \}. \tag{10}$$

Deformation energy $\mathcal{A}(\mathbf{u}, \mathbf{u})$ is divided into bending, membrane, and shear energies, denoted by subscripts B, M, and S, respectively.

$$\mathscr{A}(\mathbf{u}, \mathbf{u}) = t^2 \mathscr{A}_{\mathrm{B}}(\mathbf{u}, \mathbf{u}) + \mathscr{A}_{\mathrm{M}}(\mathbf{u}, \mathbf{u}) + \mathscr{A}_{\mathrm{S}}(\mathbf{u}, \mathbf{u}). \tag{11}$$

Notice that we can safely cancel out one power of *t*. Bending, membrane, and shear energies are given as follows [18]:

$$t^{2} \mathcal{A}_{B}(\mathbf{u}, \mathbf{u}) = t^{2} \int_{\widehat{\Omega}_{t}} E(x, y) \left[\nu \left(\kappa_{11}(\mathbf{u}) + \kappa_{22}(\mathbf{u}) \right)^{2} + (1 - \nu) \sum_{i,j=1}^{2} \kappa_{ij}(\mathbf{u})^{2} \right] A_{1}(x, y) A_{2}(x, y) dx dy,$$

$$\mathcal{A}_{M}(\mathbf{u}, \mathbf{u}) = 12 \int_{\widehat{\Omega}_{t}} E(x, y) \left[\nu \left(\beta_{11}(\mathbf{u}) + \beta_{22}(\mathbf{u}) \right)^{2} + (1 - \nu) \sum_{i,j=1}^{2} \beta_{ij}(\mathbf{u})^{2} \right] A_{1}(x, y) A_{2}(x, y) dx dy,$$

$$\mathcal{A}_{S}(\mathbf{u}, \mathbf{u}) = 6(1 - \nu) \int_{\widehat{\Omega}_{t}} E(x, y) \left[\left(\rho_{1}(\mathbf{u})^{2} + \rho_{2}(\mathbf{u}) \right)^{2} \right] \times A_{1}(x, y) A_{2}(x, y) dx dy,$$

$$(12)$$

where v is the Poisson ratio (constant) and E(x, y) is Young's modulus with scaling $1/(12(1-v^2))$.

The symmetric 2D strains, bending (κ) , membrane (β) , and shear (ρ) , are defined as

$$\kappa_{11} = \frac{1}{A_1} \frac{\partial \theta}{\partial x} + \frac{\psi}{A_1 A_2} \frac{\partial A_2}{\partial y},$$

$$\kappa_{22} = \frac{1}{A_2} \frac{\partial \psi}{\partial y} + \frac{\theta}{A_1 A_2} \frac{\partial A_2}{\partial x},$$

$$\kappa_{12} = \frac{1}{2} \left[\frac{1}{A_1} \frac{\partial \psi}{\partial x} + \frac{1}{A_2} \frac{\partial \theta}{\partial y} - \frac{\theta}{A_1 A_2} \frac{\partial A_2}{\partial y} - \frac{\psi}{A_1 A_2} \frac{\partial A_2}{\partial x} \right]$$

$$- \frac{1}{R_1} \left(\frac{1}{A_2} \frac{\partial u}{\partial y} - \frac{v}{A_1 A_2} \frac{\partial A_2}{\partial x} \right) - \frac{1}{R_2} \left(\frac{1}{A_1} \frac{\partial v}{\partial x} - \frac{u}{A_1 A_2} \frac{\partial A_1}{\partial y} \right),$$

$$\beta_{11} = \frac{1}{A_1} \frac{\partial u}{\partial x} + \frac{v}{A_1 A_2} \frac{\partial A_1}{\partial y} + \frac{w}{R_1},$$

$$\beta_{22} = \frac{1}{A_2} \frac{\partial v}{\partial y} + \frac{u}{A_1 A_2} \frac{\partial A_2}{\partial x} + \frac{w}{R_2},$$

$$\beta_{12} = \frac{1}{2} \left(\frac{1}{A_1} \frac{\partial v}{\partial x} + \frac{1}{A_2} \frac{\partial u}{\partial y} - \frac{u}{A_1 A_2} \frac{\partial A_1}{\partial y} - \frac{v}{A_1 A_2} \frac{\partial A_2}{\partial x} \right),$$

$$\rho_1 = \frac{1}{A_1} \frac{\partial w}{\partial x} - \frac{u}{R_1} - \theta,$$

$$\rho_2 = \frac{1}{A_2} \frac{\partial w}{\partial y} - \frac{v}{R_2} - \psi.$$
(13)

In our experiments, the shell profiles are functions of *x* only, but not necessarily constant; hence, the strains are presented in a general form.

The stiffness matrix **S** is obtained after integration and assembly. Here, the mass matrix **M** is the standard 2D one with density σ except for the scaling of the rotation components and surface differential $A_1(x, y)A_2(x, y)$.

2.3. Reduction through Ansatz. The 3D elasticity equations for shells of revolution can be reduced to two-dimensional ones using a suitable ansatz [19]. For shells of revolution, the eigenmodes $\mathbf{u}(x, y, z)$ or $\mathbf{u}(x, r, \alpha)$ in cylindrical coordinates have either one of the forms:

$$\mathbf{u}_{1}(x, y, z) = \mathbf{u}_{1}(x, r, \alpha) = \begin{pmatrix} u(x, r)\cos(K\alpha) \\ v(x, r)\sin(K\alpha) \\ w(x, r)\cos(K\alpha) \end{pmatrix}, \quad (14)$$

$$\mathbf{u}_{2}(x, y, z) = \mathbf{u}_{2}(x, r, \alpha) = \begin{pmatrix} u(x, r)\sin(K\alpha) \\ v(x, r)\cos(K\alpha) \\ w(x, r)\sin(K\alpha) \end{pmatrix}, \quad (15)$$

where *K* is the harmonic wavenumber. Thus, given a profile function r = y = f(x), with $x \in [a, b]$, the computational domain $\widehat{\Omega}$ is 2D only:

$$\widehat{\Omega} = \{ (x, r + \eta(x)) \mid a \le x \le b, -d_0(x) < \eta(x) < d_1(x) \},$$
(16)

where the auxiliary functions $d_i(x)$ again simply indicate that the thickness $d(x) = d_1(x) + d_0(x)$ need not be constant.

Deformation energy $\mathcal{A}(\mathbf{u}, \mathbf{u})$ is defined as

$$\mathcal{A}(\mathbf{u}, \mathbf{u}) = r^3 \int_{\widehat{\Omega}} E(x, y)$$

$$\cdot \left[\frac{\nu}{(1+\nu)(1-2\nu)} (\operatorname{tr} \epsilon)^2 + \frac{1}{1+\nu} \sum_{i,j=1}^3 \epsilon_{ij}^2 \right] dx \, d\eta,$$
(17)

where the symmetric 3D strains ϵ_{ij} are

$$\epsilon_{11} = \frac{\partial u}{\partial x},$$

$$\epsilon_{12} = \frac{1}{2} \left(-\frac{K}{r+\eta} u + \frac{\partial v}{\partial x} \right),$$

$$\epsilon_{13} = \frac{1}{2} \left(\frac{\partial u}{\partial \eta} + \frac{\partial w}{\partial x} \right),$$

$$\epsilon_{22} = \frac{1}{r+\eta} (Kv + w),$$

$$\epsilon_{23} = \frac{1}{2} \left(\frac{\partial v}{\partial \eta} - \frac{1}{r+\eta} (v + Kw) \right),$$

$$\epsilon_{33} = \frac{\partial w}{\partial \eta}.$$
(18)

The stiffness matrix $\bf S$ is obtained after integration and assembly. Here, the mass matrix $\bf M$ is the standard 3D one with density σ .

2.4. Special Features of Shell Problems

2.4.1. Boundary Layers. The solutions of shell problems, static or dynamic, often include boundary layers and even internal layers, each of which has its own characteristic length scale [20]. Internal layers are generated by geometric features, such as cuts and holes, or changes in curvature, for instance, at shell junctions. The layers either decay exponentially toward the boundary or oscillate with exponentially decaying amplitude. For parabolic shells, it is known that the axial boundary layers decay exponentially with a characteristic length scale $\sim \sqrt{t}$. If there are generators for internal layers, then the layers oscillate in the angular direction with characteristic length scale $\sim \sqrt[4]{t}$. There also exists an axial internal layer of a very long range $\sim 1/\sqrt{t}$.

Identification of the boundary layer structure or *layer resolution* is a useful tool for assessing the quality of the discretized solution and providing guidance for setting up the discretization, for instance, in mesh generation. If the solution is not dominated by the layers, we simply observe the underlying smooth part of the solution.

2.4.2. Numerical Locking. One of the numerical difficulties associated with thin structures is the so-called *numerical locking*, which means unavoidable loss of optimal

convergence rate due to parameter-dependent error amplification [21]. We use the *p*-version of the finite element method [16] in order to alleviate the (possible) locking and ensure convergence.

3. Stochastic Shell Eigenproblem

The stochastic extension of the free vibration problem arises from introducing uncertainties in the material parameters and the geometry of the shell. In the context of this paper, we assume that these uncertainties may be parametrized using a finite number of uniformly distributed random variables. The approximate solution statistics are then computed employing a sparse grid stochastic collocation operator.

3.1. The Stochastic Eigenproblem. We let the material and geometric uncertainties be represented by a vector of mutually independent random variables $\xi = (\xi_1, \xi_2, \dots, \xi_M)$ taking values in a suitable domain $\Gamma \subset \mathbb{R}^M$ for some $M \in \mathbb{N}$. For uniformly distributed random variables, we may, without loss of generality, assume a scaling such that $\Gamma \coloneqq [-1, 1]^M$.

First, we assume a set of geometric parameters $(\xi_1, \xi_2, \ldots, \xi_{m'})$ and let the computational domain be given by a function $D(\xi) = D(\xi_1, \xi_2, \ldots, \xi_{m'})$. Second, we assume a set of material parameters $(\xi_{m'+1}, \xi_{m'+2}, \ldots, \xi_{M})$, and let Young's modulus be a random field expressed in the form

$$E(\mathbf{x}, \xi) = E_0(\mathbf{x}) + \sum_{m=m'+1}^{M} E_m(\mathbf{x}) \xi_m, \quad \mathbf{x} \in D(\xi).$$
 (19)

The parametrization (19) may, for instance, result from a Karhunen–Loéve expansion of the underlying random field E. We assume that the random field is strictly uniformly positive and uniformly bounded, i.e., there exists $E_{\min}, E_{\max} > 0$ such that

$$E_{\min} \le \underset{x \in D(\xi)}{\operatorname{ess inf}} E(\mathbf{x}, \xi) \le \underset{x \in D(\xi)}{\operatorname{ess sup}} E(\mathbf{x}, \xi) \le E_{\max}, \tag{20}$$

for all $\xi \in \Gamma$.

Let $L^2_{\mu}(\Gamma)$ denote a weighted L^2 -space, where μ is the uniform product probability measure associated with the probability distribution of $\xi \in \Gamma$. For functions in $L^2_{\mu}(\Gamma)$, we define the expected value

$$\mathbb{E}[\nu] = \int_{\Gamma} \nu(\xi) d\mu(\xi), \tag{21}$$

and variance $Var[v] = \mathbb{E}[(v - \mathbb{E}[v])^2]$.

Assuming stochastic models for the computational domain and Young's modulus, the eigenpairs of the free vibration problem now depend on $\xi \in \Gamma$. The stochastic eigenvalue problem is obtained simply by replacing the differential operators in (8) with their stochastic counterparts and assuming that the resulting equation holds for every realization of $\xi \in \Gamma$. In the variational form, the problem reads find functions $\mathbf{u}(t):\Gamma \longrightarrow V$ and $\omega^2(t):\Gamma \longrightarrow \mathbb{R}$ such that for all $\xi \in \Gamma$, we have

$$ta_{\mathbf{m}}(\xi; \mathbf{u}(t, \xi), \mathbf{v}) + ta_{\mathbf{s}}(\xi; \mathbf{u}(t, \xi), \mathbf{v}) + t^{3}a_{\mathbf{b}}(\xi; \mathbf{u}(t, \xi), \mathbf{v})$$

$$= \omega^{2}(t, \xi)m(t, \xi; \mathbf{u}(t, \xi), \mathbf{v}), \quad \forall \mathbf{v} \in V,$$
(22)

where $a_{\rm m}(\xi;\cdot,\cdot)$, $a_{\rm s}(\xi;\cdot,\cdot)$, $a_{\rm b}(\xi;\cdot,\cdot)$, and $m(t,\xi;\cdot,\cdot)$ are stochastic equivalents of the deterministic bilinear forms in (9). We assume that the eigenvector $\mathbf{u}(t,\xi)$ is normalized with respect to the inner product $m(t,\xi;\cdot,\cdot)$ for all $\xi \in \Gamma$.

3.2. Eigenvalue Crossings. In the context of stochastic eigenvalue problems, special care must be taken in order to make sure that different realizations of the solution are in fact comparable. This is true for shell eigenvalue problems in particular, since the eigenvalues of thin cylindrical shells are typically tightly clustered. Double eigenvalues may appear due to symmetries and physical properties of the shell might be such that eigenvalues corresponding to different harmonic wavenumbers appear very close to each other. When the problems are brought to stochastic setting, we may face the issue of eigenvalue crossings. The ordering of the eigenvalues associated with each mode may be different for different realizations of the problem. This issue has previously been illustrated in [11] and considered in the case of shell eigenvalue problems in [15].

In our examples, the eigenvalue crossings do not pose computational difficulties. When the problem is reduced through ansatz (14) or (15), the eigenmodes are separated by wavenumber K, and as a result for any fixed K, the eigenvalues of the reduced problem appear well-separated. However, one should bear in mind that the eigenvalues of the original 3D problem may still cross: In Section 5, we present numerical examples which illustrate that a kth smallest eigenvalue may be associated with eigenmodes with different wavenumbers for different values of the stochastic variables. Moreover, as revealed by the ansatz, each eigenvalue of the dimensionally reduced problem is actually associated with an eigenspace of dimension two.

3.3. The Spatially Discretized Eigenvalue Problem. We employ standard high-order finite elements with polynomial order $p \in \mathbb{N}$. For any fixed t > 0, the spatially discretized problem may be written as a parametric matrix eigenvalue problem: find $\lambda_p : \Gamma \longrightarrow \mathbb{R}$ and $\mathbf{y}_p : \Gamma \longrightarrow \mathbb{R}^n$ such that

$$\mathbf{S}(\xi)\mathbf{y}_{p}(\xi) = \lambda_{p}(\xi)\mathbf{M}(\xi)\mathbf{y}_{p}(\xi), \quad \forall \xi \in \Gamma,$$
 (23)

where n is the dimension of the discretization space. Here, \mathbf{M} and \mathbf{S} are the mass matrix and the stiffness matrix, which obviously depend on $\xi \in \Gamma$. For any fixed $\xi \in \Gamma$, problem (23) reduces to a positive-definite generalized matrix eigenvalue problem.

We let $\langle \cdot, \cdot \rangle_{\mathbf{M}(\xi)}$ and $\| \cdot \|_{\mathbf{M}(\xi)}$ denote the inner product and norm induced by the mass matrix. We assume the eigenvector to be normalized according to $\|\mathbf{y}_p(\xi)\|_{\mathbf{M}(\xi)} = 1$ for all $\xi \in \Gamma$. Moreover, we fix its sign so that the inner product $\langle \mathbf{y}_p(0), \mathbf{y}_p(\xi) \rangle_{\mathbf{M}(\xi)}$, where $\mathbf{y}_p(0)$ is a suitable reference solution, is positive for every $\xi \in \Gamma$. In practice, we may disregard the possibility that the inner product is zero,

and therefore, as long as the discrete eigenvalues are simple, the solution is well defined for all $\xi \in \Gamma$.

3.4. Stochastic Collocation on Sparse Grids. We introduce an anisotropic Smolyak-type sparse grid collocation operator ([6, 22, 23]) for resolving the effects of the random variables $\xi \in \Gamma$.

Assume a finite multiindex set $\mathscr{A} \subset \mathbb{N}_0^M$. For $\alpha, \beta \in \mathscr{A}$ we write $\alpha \leq \beta$ if $\alpha_m \leq \beta_m$ for all $m \geq 1$. For simplicity, we make the assumption that \mathscr{A} is monotone in the following sense: whenever $\beta \in \mathbb{N}_0^M$ is such that $\beta \leq \alpha$ for some $\alpha \in \mathscr{A}$, then $\beta \in \mathscr{A}$. Let L_p be the univariate Legendre polynomial of degree p. Denote by $\left\{\chi_k^{(p)}\right\}_{k=0}^p$ the zeros of L_{p+1} . We define the one-dimensional Lagrange interpolation operators $\mathscr{F}_p^{(m)}$ via

$$\left(\mathcal{F}_{p}^{(m)}v\right)\left(\xi_{m}\right) = \sum_{k=0}^{p} v\left(\chi_{k}^{(p)}\right)\ell_{k}^{(p)}\left(\xi_{m}\right),\tag{24}$$

where $\left\{\ell_k^{(p)}\right\}_{k=0}^p$ are the related Lagrange basis polynomials of degree p. Finally, we define the sparse collocation operator as

$$\mathcal{J}_{\mathcal{A}} := \sum_{\alpha \in \mathcal{A}} \bigotimes_{m=1}^{M} \left(\mathcal{J}_{\alpha_m}^{(m)} - \mathcal{J}_{\alpha_{m-1}}^{(m)} \right). \tag{25}$$

The operator (25) may be rewritten in a computationally more convenient form

$$\mathcal{F}_{\mathcal{A}} = \sum_{\alpha \in \mathcal{A}} \sum_{\beta \in \mathcal{G}_{+}} (-1)^{\|\alpha - \beta\| 1} \bigotimes_{m=1}^{M} \mathcal{F}_{\beta_{m}}^{(m)}, \tag{26}$$

where $\mathcal{G}_{\alpha} := \{ \beta \in \mathbb{N}_0^M | \alpha - 1 \le \beta \le \alpha \}$. We see that the complete grid of collocation points is now given by

$$X_{\mathscr{A}} := \bigcup_{\alpha \in \mathscr{A}} \bigcup_{\beta \in \mathscr{G}_{\alpha}} \prod_{m=1}^{M} \left\{ \chi_{k}^{(\beta_{m})} \right\}_{k=0}^{\beta_{m}}$$

$$= \bigcup_{\alpha \in \mathscr{A}} \prod_{m=1}^{M} \left\{ \chi_{k}^{(\alpha_{m})} \right\}_{k=0}^{\alpha_{m}}.$$
(27)

Statistics, such as the expected value and variance, of the solution may now be computed by applying the one-dimensional Gauss–Legendre quadrature rules on the components of (26). The accuracy of the collocated approximation is ultimately determined by the smoothness of the solution as well as the choice of the multiindex set $\mathcal{A} \subset \mathbb{N}_0^M$, see [6] for a detailed analysis. Similar results in the context of source problems have been presented in [22–25].

3.5. Stochastic Collocation on Partial Sparse Grids. In the framework of this paper, each collocation point in the stochastic space Γ corresponds to a single measurement configuration. In contrast to idealized mathematical models, the range of practical measurement settings may be limited to a small subset of Γ . In this section, we discuss one method to carry out the analysis of the response statistics of a random field in a subset of Γ .

We approach this problem from the viewpoint of polynomial interpolation. In the following, we assume for simplicity that $\Gamma = [-1, 1]^M$. Let $X = \{\chi_1, \dots, \chi_N\} \subset \Gamma$

denote a set of collocation points, and let $\mathcal{B} = \{\mathcal{L}_1, \dots, \mathcal{L}_J\}$, $J \ge N$, be a set of orthogonal polynomial basis functions with respect to the measure $d\mu$ satisfying

$$\int_{\Gamma} \mathcal{L}_{i}(\xi) \mathcal{L}_{j}(\xi) d\mu(\xi) = 0 \quad \text{whenever } i \neq j.$$
 (28)

In addition, we denote

$$\gamma_k = \left(\int_{\Gamma} \mathcal{L}_k(\xi)^2 d\mu(\xi)\right)^{1/2} \quad \text{for } k \in \{1, \dots, J\}.$$
 (29)

We assume that the basis functions in \mathcal{B} are ordered in degree lexicographic order. In particular, \mathcal{L}_1 is constant.

Let $\beta=(\beta_1,\ldots,\beta_N)$ denote a subsequence of $\{1,2,\ldots,J\}$ so that each element of β corresponds to one and only one element of this set. Then for any such subsequence, we can construct the Vandermonde-like matrix $V_\beta=(\mathcal{L}_i(\chi_j))_{i\in\beta,1\leq j\leq N}$. If V_β is invertible, then for any input $f:\Gamma\longrightarrow\mathbb{R}$ we can set

$$(c_1 \cdots c_N) = (f(\chi_1) \cdots f(\chi_N))V_{\mathcal{J}}^{-1}, \tag{30}$$

so that the Lagrange interpolating polynomial

$$P(\xi) = \sum_{i=1}^{N} c_i \mathcal{L}_{\beta_i}(\xi), \tag{31}$$

satisfies $P(\chi_i) = f(\chi_i)$ for all $i \in \{1, ..., N\}$. If $\beta_1 = 1$, then the expansion coefficients can be used to estimate the response statistics of f via

$$\mathbb{E}[f] \approx \gamma_1^{-1} c_1,\tag{32}$$

$$Var[f] \approx (\gamma_{\beta_2}^{-1} c_2)^2 + \dots + (\gamma_{\beta_N}^{-1} c_N)^2.$$
 (33)

Following [12], it turns out that the Vandermonde-like matrices related to the Smolyak interpolating polynomials are remarkably well conditioned. One may find a well-conditioned interpolating polynomial for a subset of a sparse grid by proceeding in the following way:

- (i) Let $X = \{\chi_1, \dots, \chi_N\}$ be a subset of a sparse grid $\mathcal{X} = \{\chi_1, \dots, \chi_I\}$
- (ii) Let $\mathcal{B} = \{\mathcal{L}_1, \dots, \mathcal{L}_J\}$ be the Smolyak polynomial basis functions (cf. [26])
- (iii) Let $\beta = (\beta_1, \dots, \beta_N)$ denote a subsequence corresponding to the row indices of the maximum volume submatrix of $W = (\mathcal{L}_i(\chi_i))_{1 \le i \le J, 1 \le j \le N}$
- (iv) Form the Lagrange interpolating polynomial $Pf(\xi) = \sum_{i=1}^{N} c_i \mathcal{L}_{\beta_i}(\xi)$, where the coefficients $c_1, \ldots, c_N \in \mathbb{R}$ are obtained as in (30)

The use of the maximum volume submatrix ensures both that the Lagrange interpolation polynomial is well defined and that system (45) is sufficiently well conditioned.

In practical calculations, finding the analytical maximum volume submatrix is in general an NP-hard problem. However, there exist several algorithms in the literature which can be used to find the approximate maximum volume submatrix in a computationally efficient manner. We use the MaxVol algorithm proposed in [27]. A related algorithm has been discussed in [28].

4. Frequency Response Analysis

In frequency response analysis, the idea is to study the excitation or applied force in the frequency domain. Therefore, the uncertainty in the eigenproblem is directly translated to frequency response. In the deterministic setting, the procedure is as follows [29]: starting from the equation of motion for the system,

$$\mathbf{M}\ddot{\mathbf{x}} + \mathbf{C}\dot{\mathbf{x}} + \mathbf{S}\mathbf{x} = \mathbf{f},\tag{34}$$

where M is the mass matrix, C is the viscous damping matrix, S is the stiffness matrix, f is the force vector, and x is the displacement vector. In our context, M and S are defined as mentioned above, and the viscous damping matrix is taken to be a constant diagonal matrix $C = 2\delta I$, where $\delta = 1/2000$.

In the case of harmonic excitation, a steady-state solution is sought, and the force and the corresponding response can be expressed as harmonic functions as

$$\mathbf{f} = \hat{f}(\omega)e^{i\omega t},$$

$$\mathbf{x} = \hat{x}(\omega)e^{i\omega t}.$$
(35)

Taking the first and second derivatives of equation (34) and substituting using (35) leads to

$$-\omega^{2}\mathbf{M}\widehat{x}(\omega)e^{i\omega t} + i\omega\mathbf{C}\widehat{x}(\omega)e^{i\omega t} + \mathbf{S}\widehat{x}(\omega)e^{i\omega t} = \widehat{f}(\omega)e^{i\omega t},$$
(36)

thus reducing to a linear system of equations:

$$(-\omega^2 \mathbf{M} + i\omega \mathbf{C} + \mathbf{S})\widehat{\mathbf{x}}(\omega) = \widehat{f}(\omega). \tag{37}$$

Any quantity of interest can then be derived from the solution $\widehat{x}(\omega)$. In the following, we consider maximal transverse deflections w_{\max} as the quantity of interest.

4.1. Frequency Response Analysis with Sparse Grids. The collocation methods are invariant with respect to the quantity of interest, and therefore, the application to frequency response is straightforward.

Let us consider four-dimensional second-order Smolyak-Gauss-Legendre quadrature points $\mathcal{X}^{\mathrm{GL}}$ and the second-order Smolyak-Clenshaw-Curtis quadrature points $\mathcal{X}^{\mathrm{CC}}$ with 41 points. Let $(P_k)_{k=0}^{\infty}$ denote the standard orthonormal univariate Legendre polynomials generated by the three-term recursion:

$$P_{0}(x) = 1,$$

$$P_{1}(x) = x,$$

$$(k+1)P_{k+1}(x) = (2k+1)xP_{k}(x) - kP_{k-1}(x), \quad k \ge 1,$$
(38)

and define the sequence m(0) = 0, m(1) = 1, and $m(k) = 2^{k-1} + 1$ for k > 1. The standard Smolyak polynomial basis functions for the dimension 4, second-level Smolyak rule are then given by [26]

$$\mathcal{B} = \bigcup_{\substack{\alpha \in \mathbb{Z}_+^4 \\ 4 \le \|\alpha\| \| 1 \le 4+2}} B_{\alpha},\tag{39}$$

where

$$B_{\alpha} = \left\{ P_{i_1-1}(\xi_1) \cdots P_{i_4-1}(\xi_4); m(\alpha_j - 1) + 1 \le i_j \le m(\alpha_j), \right.$$

$$1 \le j \le 4 \right\}$$

$$(40)$$

for $\alpha \in \mathbb{Z}_+^4$. With this convention, $\#\mathscr{B} = \#\mathscr{X}^{GL} = \#\mathscr{X}^{CC} = 41$ and the interpolation problem is well posed for the full sparse grids.

In order to make the problem well posed for some partial grids $X^{\mathrm{GL}} \subset \mathcal{X}^{\mathrm{GL}}$ and $X^{\mathrm{CC}} \subset \mathcal{X}^{\mathrm{CC}}$, we proceed as in Section 3.5 and construct the rectangular Vandermonde-like matrix $W = (\mathcal{L}(\xi))_{\mathcal{L} \in \mathcal{B}, \xi \in \mathcal{X}}$ and choose its maximum volume submatrix V using the MaxVol algorithm. We compute the expectation $\mathbb{E}[w_{\mathrm{max}}]$ and upper confidence envelope $\mathbb{E}[w_{\mathrm{max}}] + \sqrt{\mathrm{Var}[w_{\mathrm{max}}]}$ using formulae (32) and (33) for each frequency, respectively.

5. Numerical Experiments

In the numerical experiments, at least one of the sources of uncertainty is related to some geometric feature, for instance, diameter of a cylinder or local thickness of a shell. In the finite element context, this means that in order to compute statistics over a set of solutions, it is necessary to introduce some nominal domain onto which every other realization of the discretized domain is mapped. In a general situation, this could be done via conformal mappings, and in specific situations as happens to be here, the meshes can be guaranteed to be topologically equivalent ensuring errors only in the immediate vicinity of the random parts of the domain.

Material constants adopted for all simulations are $E = 2.069 \times 10^{11}$ MPa, $\nu = 1/3$, and $\rho = 7868$ kg/m³, unless otherwise specified. Also, in the following examples, we employ the sparse collocation operator (25) with total degree multiindex sets

$$\mathcal{A} = \mathcal{A}_L := \left\{ \alpha \in \mathbb{N}_0^M \, \middle| \, \sum_{m=1} \alpha_m \le L \right\},\tag{41}$$

where applicable. All computations were performed on an Intel Xeon(R) CPU E3-1230 v5 3.40 GHz (eight cores) desktop with 32 GB of RAM.

5.1. Tower Configuration: Free Vibration. Our first example is an idealized wind turbine tower (Figure 2). We can apply dimension reduction via ansatz as in Section 2.3 and arrive at a highly nontrivial shell-solid configuration. Notice that in this formulation, we model the shell as a solid which is computationally feasible in 2D, and the resulting systems can be solved for different harmonic wavenumbers as outlined above.

The tower is assembled with four parts: a thin shell of thickness t=1/100 and vertical length of 11 units $(x \in [-1,10])$, a top ring of height $C_1=2/5$ and width 3/4, and two base rings, inner and outer ones, of height $D_1=2/5$ and random widths W_1 and W_2 , respectively. An additional source of randomness comes from varying thickness of the

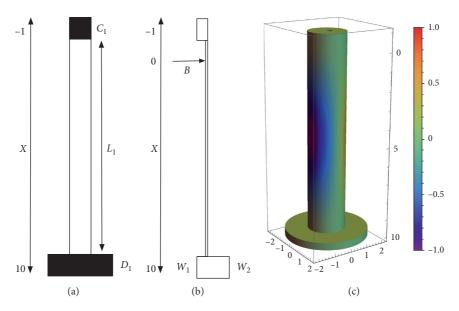


FIGURE 2: Tower configuration: Computational domain; B indicates the location of the assumed manufacturing imperfections at x = 0. (a) Shell-solid model; diameter of the base is random. (b) Computational domain. (c) Lowest mode; normalized transverse detection w; rainbow colour scale.

shell near the top ring, centered at x = 0. Here, the varying thickness can be interpreted as manufacturing imperfection or damage to the structure. The tower configuration is detailed also in Figure 2.

Let us define the computational domain $\widehat{\Omega}$ to be a union of five parameterized domains:

$$\widehat{\Omega} = \bigcup_{i=1}^{5} \widehat{\Omega}_{i},\tag{42}$$

where

$$\begin{split} \widehat{\Omega}_1 &= \big\{ (x,r+\eta) \mid -1 \le x \le -1 - C_1, -3/4 - t/2 \le \eta \le t/2 \big\}, \\ \widehat{\Omega}_2 &= \big\{ (x,r+\eta) \mid -1 - C_1 \le x \le -b, -t/2 \le \eta \le t/2 \big\}, \\ \widehat{\Omega}_3 &= \big\{ (x,r+\eta) \mid -b \le x \le b, -\phi \left(bx,t;a,b \right) \le \eta \le \phi \left(bx,t;a,b \right) \big\}, \\ \widehat{\Omega}_4 &= \big\{ (x,r+\eta) \mid b \le x \le 10 - D_1, -t/2 \le \eta \le t/2 \big\}, \end{split}$$

$$\widehat{\Omega}_5 = \left\{ (x, r + \eta) \mid 10 - D_1 \le x \le 10, -t/2 - W_1 \le \eta \le t/2 + W_2 \right\}. \tag{43}$$

The random variables and their ranges used in different experiments are (Figure 2)

Tower
$$\overline{W_1} \quad [1/4, 3/4]$$

$$W_2 \quad [1/4, 5/4]$$

$$a \quad (0, 1/2]$$

$$b \quad [3/40, 1/8],$$
(44)

where a and b are parameters in the shape modeling the imperfection taken to be symmetric on the inner and outer surfaces:

$$\phi(s,t;a,b) = \frac{t\left((a-1)b^4s^4 - 2(a-1)b^4s^2 + ab^4\right)}{2b^4},$$
 (45)

where *s* is the coordinate scaled to center the shape around x = 0. For a plot of the profiles, see Figure 3.

In each experiment, the dimension of the stochastic space is M=4, and the random vector $\xi\in\Gamma$ is obtained by scaling the geometric parameters to the interval [-1,1]. The base of the tower is clamped, that is, fully kinematically constrained. The p-version of FEM is used with p=4 resulting in a linear system with 14247 d.o.f. The multiindex set is \mathscr{A}_L , with L=3. Per collocation point, the time spent is approximately 40 seconds; 10 seconds for solution and 30 seconds for obtaining statistics.

In Tables 1 and 2, we have listed statistics for eight of the smallest eigenvalues of the tower configuration with the corresponding wavenumber K. Of interest is the pair of fourth and fifth smallest eigenvalues since the values are fairly close to each other; in other words, they form a cluster. Indeed, if we track the modes over the parameter space, we see that crossing occurs, i.e., different eigenmodes are associated with the fourth smallest eigenvalue for different realizations of the problem. Also notice that the actual squares of frequencies vary (at least) within range [4562.30, 4578.79] for K=4, with the expected value = 4572.40. This means that in a multiparametric setting, the number of modes observed within a fixed range of frequencies is not necessarily constant over the whole parameter space.

The statistics presented in Tables 1 and 2 were verified by a Monte Carlo simulation of S = 1000 samples. A comparison of the results obtained by Monte Carlo and collocation algorithms has been presented in Table 3. The central limit theorem guarantees (stochastic) error bounds for statistics computed via Monte Carlo: the error in the expected value of the quantity of interest is given by $\sqrt{\text{Var}[\cdot]/S}$. From Table 3, we see that the errors between the two solutions fall well within the tolerances of the Monte Carlo results.

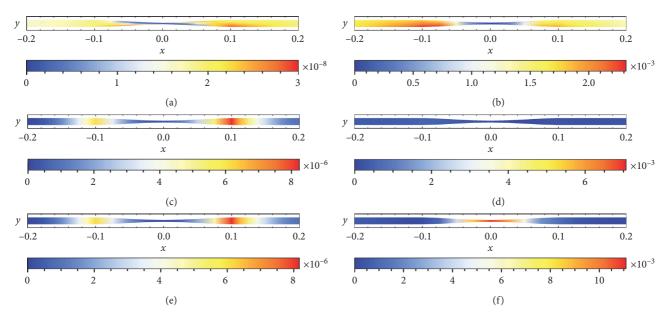


FIGURE 3: Variances of the tower configuration near the manufacturing defect: components of the first (left) and third (right) eigenmodes for K = 1. Solution computed with p = 4 and L = 3 (165 collocation points). (a) Component μ of the first eigenmode. (b) Component μ of the third eigenmode. (c) Component ν of the first eigenmode. (d) Component ν of the third eigenmode. (e) Component ν of the first eigenmode. (f) Component ν of the third eigenmode.

Table 1: Statistics and wavenumbers of the eight smallest (in expected value) eigenvalues of the tower configuration as defined by the wavenumber K.

$\mathbb{E}[\omega^2]$	$Var[\omega^2]$	$\sqrt{\operatorname{Var}[\omega^2]}$	K
79.7358	0.00175638	0.0419092	1
2055.46	218.179	14.7709	3
3449.66	2194.93	46.8501	2
4548.42	989.703	31.4595	0
4572.40	30.0598	5.48268	4
5958.11	2550.51	50.5026	0
6664.07	446.766	21.1368	4
7296.49	3535.53	59.4603	3

Table 2: The eigenmodes evaluated at two different points in Γ (solution computed with p=4 and L=3 (165 collocation points)).

_	_		_
$\xi = (-0.9, 0.9)$	0, 0, 0)	$\xi = (0.9, 0,$	0,0)
ω^2	K	ω^2	K
79.7681	1	79.6528	1
2072.60	3	2028.05	3
3503.49	2	3361.97	2
4578.79	4	4485.45	0
4581.93	0	4562.30	4
6013.69	0	5861.08	0
6688.77	4	6625.28	4
7365.13	3	7185.36	3

The effect of the manufacturing imperfection is illustrated for the eigenmodes associated with K=1 in Figure 3. High-localized variance in the computed displacements means that the uncertainty in derived quantities of interest such as stresses is likely to be highest. In Figure 3, we see that the variance of the transverse deflection of the third eigenmode for K=1 is localized exactly at the thinnest part

Table 3: The errors between eigenvalues computed by collocation $(\omega_{\rm C}^0)$ and Monte Carlo $(\omega_{\rm MC}^0)$ methods. The eight smallest (in expected value) eigenvalues of the tower configuration.

$\varepsilon_{ m mean}$	$arepsilon_{ ext{stdev}}$	$arepsilon_{ m MC}$
0.000453485	0.000637457	0.00130513
0.0120954	0.0580925	0.465259
0.0444178	0.205332	1.47504
0.0921339	0.163266	0.989675
0.00269920	0.0209490	0.172715
0.0590391	0.293009	1.58777
0.00789916	0.0910774	0.665526
0.0626177	0.263587	1.87197

The error measures are as follows: error in expected value $\varepsilon_{\text{mean}} = |\mathbb{E}[\omega_{\text{MC}}^2] - \mathbb{E}[\omega_{\text{C}}^2]|$, error in standard deviation $\varepsilon_{\text{stdev}} = |\sqrt{\text{Var}[\omega_{\text{MC}}^2]} - \sqrt{\text{Var}[\omega_{\text{C}}^2]}|$, and Monte Carlo standard error $\varepsilon_{\text{MC}} = \sqrt{\text{Var}[\omega_{\text{MC}}^2]/S}$.

indicating a highly likely location for failure of the tower. This is of course what we would expect.

5.2. Cylinder with Junctions. Our second example is a cylinder with two junctions: a T-junction with another cylinder and a cone extension at one end of the cylinder. Since we limit ourselves to shells of revolution, we remove the T-junction through clamped boundary conditions. Here, the sources of uncertainty are the random radius (diameter) of the circular T-junction, i.e., a circular hole in our modeling, D_1 , the slope of the cone, ζ , and Young's modulus. The radius of the cylindrical part is constant = 1, and the dimensionless thickness is constant t = 1/100. For the long cylinder, the distance of the center of the hole to ends is $L_1 = 10\pi$ and the distance to the cone is $L_2 = 40\pi/7$, and for the short one, the lengths are simply scaled by 10. For a schematic of the construction, see Figure 4.

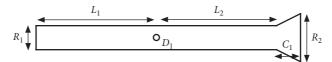


FIGURE 4: Cylinder-cylinder-cone schematic. The cylinder diameter $R_1 = 2$, L_1 , L_2 , and C_1 are deterministic: $L_1 + L_2 + C_1 = 20\pi$; the diameter of the hole D_1 is random, and the cone diameter R_2 is random since it depends on the random slope of the cone.

Now the computational domain is periodic in the angular direction:

$$\widehat{\Omega}_t = \frac{([-10\pi, 10\pi] \times [0, 2\pi])}{\text{Disk}((0, 0), D_1/2)}.$$
(46)

Notice that the change in the slope does not affect the computational domain.

The random variables and their ranges used in different experiments are

where ζ is the slope of the cone. Finally, the parameters ξ_3 and ξ_4 correspond Karhunen–Loéve basis functions, i.e., terms $E_3(\mathbf{x}) = \sin x$ and $E_4(\mathbf{x}) = \sin 2x$ in the expansion (19). Again, in each experiment the dimension of the stochastic space is M=4, and the random vector $\xi \in \Gamma$ is obtained by scaling the geometric parameters to the interval [-1,1]. Both ends of the cylinder are clamped, as well as the T-junction interface, that is, fully kinematically constrained. The p-version of FEM is used with p=3 resulting in a linear system with 41280 d.o.f. The multiindex set is \mathcal{A}_L with L=2. Per collocation point, the time spent is approximately 60 seconds; 10 seconds for solution and 50 seconds for obtaining statistics.

We study both free vibration and frequency response for this configuration.

5.2.1. Free Vibration. Let us first examine the lowest modes of the two structures. Interestingly, when comparing the two subfigures of Figure 5, the colours indicate that indeed in the long cylinder, the long-range internal layer of $1/\sqrt{t}$ emerges in the lowest mode. However, none of the shorter characteristic length scales have strong amplitudes in the transverse deflection in this case.

In Table 4, we have listed statistics for four of the smallest eigenvalues of the short and long cylinder configurations. In this case, the eigenvalues appear well separated. Again, the statistics were verified by a Monte Carlo simulation of S = 1000 samples. A comparison of the results obtained by Monte Carlo and collocation algorithms has been presented in Table 5. As discussed before, we see from the figures in Table 5 that the errors between the two solutions fall well within the tolerances of the Monte Carlo results.

Statistics of the first eigenmode for the long cylinder with junctions have been presented in Figure 6. The long-range layer is clearly visible in the second, third, and fifth components. The effect of the cone junction is distinctly manifested in the statistics of the fourth component. The standard deviations of the two smallest eigenvalues are approximately 62 and 50 percent of the respective expected values. The ratio of the expected values is approximately 0.21, and thus, the eigenvalues at least appear to be well separated.

Statistics of the first eigenmode for the short cylinder with junctions have been presented in Figure 7. In this case, we do not observe a separate long-range layer. The effect of the cone junction is never the less apparent in the statistics of the fourth component. The standard deviations of the two smallest eigenvalues are now approximately 31 and 49 percent of the respective expected values. The ratio of the expected values is approximately 0.24, and thus, the eigenvalues again appear to be well separated.

In Figure 8, the short-range effects of the T-junction have been highlighted. The statistics of the fifth component have been shown in vicinity of the junction for both cylinders. The relative strength of the long-range axial layer in the long cylinder can be observed, whereas in the short cylinder, the angular oscillatory layer is dominant. In both configurations, there is a hint of short-range axial layer emanating from the hole.

5.2.2. Frequency Response Analysis. For the frequency response analysis of the short cylinder, the load is chosen to be $F(x, y) = 1000 \cos(y/2)N$, and the angular frequency range is taken to be $\omega \in 2\pi\{5, 10, ..., 200\}$ Hz. In our analysis, all modes are present; no attempt to choose, for instance, a subspace of lowest modes has been made.

We first carry out the solution of the frequency response statistics subject to the abovementioned second-order Smolyak–Gauss–Legendre quadrature points $\mathcal{X}^{\mathrm{GL}}$ and the second-order Smolyak–Clenshaw–Curtis quadrature points $\mathcal{X}^{\mathrm{CC}}$ and then consider their respective subsets with 25 points defined by setting

$$X^{\text{GL}} = \left\{ (\xi_1, \dots, \xi_4) \in \mathcal{X}^{\text{GL}} \mid \xi_1 = 0 \right\},$$

$$X^{\text{CC}} = \left\{ (\xi_1, \dots, \xi_4) \in \mathcal{X}^{\text{CC}} \mid \xi_1 = 0 \right\},$$
(48)

where the choice $\xi_1 = 0$ is arbitrary. In the context of this numerical experiment, it means that the diameter of the hole is fixed at its expected value.

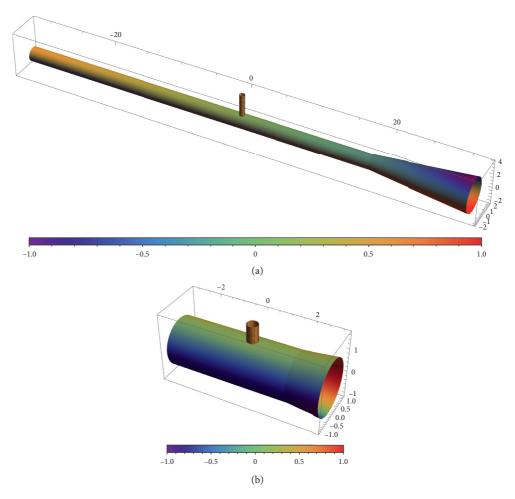


FIGURE 5: Shell configuration: t = 1/100; lowest mode; normalized transverse deflection w; rainbow colour scale. (a) Long cylinder with T-junction and cone junction; frequency = 1 Hz; $x \in [-10\pi, 10\pi]$; cone: $[40\pi/7, 10\pi]$. (b) Short cylinder with T-junction and cone junction; frequency = 10 Hz; $x \in [-\pi, \pi]$; cone: $[4\pi/7, \pi]$.

Table 4: Statistics of the four smallest eigenvalues of the long (a) and short (b) cylinder with junctions (solution computed with p = 3 and L = 2 (45 collocation points)).

	=	
$\mathbb{E}[\omega^2]$	$Var[\omega^2]$	$\sqrt{\operatorname{Var}[\omega^2]}$
(a) Long cylinder		
3.12173	3.70583	1.92505
15.1519	57.9719	7.61393
25.7390	161.805	12.7203
88.1692	239.444	15.4740
(b) Short cylinder		
58.6626	335.750	18.3235
240.370	13908.9	117.936
655.337	4200.64	64.8123
1137.43	10215.8	101.073

Let us first consider sparse grids \mathcal{X}^{GL} and \mathcal{X}^{CC} . In Figure 9, we show two frequency response graphs where the expected values of the quantity of interest, the maximal transverse deflection w_{\max} , are shown along standard deviations. It is clear that the frequency response is sensitive to perturbations to the parameters. The two point sets are not hierarchic, and thus, one cannot expect to get exactly identical responses. Moreover, distributions of the values of

Table 5: The errors between eigenvalues computed by collocation $(\omega_{\rm C}^2)$ and Monte Carlo $(\omega_{\rm MC}^2)$ methods. The four smallest eigenvalues of the long (a) and short (b) cylinders.

$\varepsilon_{ m mean}$	$arepsilon_{ ext{stdev}}$	$arepsilon_{ m MC}$
(a) Long cylinder		
0.0652920	0.0150364	0.0604000
0.287854	0.187262	0.234852
0.430142	0.00845208	0.401983
0.503874	0.199000	0.483037
(b) Short cylinder		
0.0134338	0.473668	0.564461
0.163070	1.13330	3.76530
0.422822	1.92808	1.98858
1.12535	9.27454	3.48951

The error measures are as follows: error in expected value $\varepsilon_{mean} = |\mathbb{E}[\omega_{MC}^2] - \mathbb{E}[\omega_C^2]|$, error in standard deviation $\varepsilon_{stdev} = |\sqrt{Var[\omega_{MC}^2]} - \sqrt{Var[\omega_C^2]}|$, and Monte Carlo standard error $\varepsilon_{MC} = \sqrt{Var[\omega_{MC}^2]/S}$.

the quantity of interest appear to be exponential. This is illustrated in Figure 10. The maximal transverse deflection $w_{\rm max}$ at any given frequency depends on how well the tail of the distribution is approximated.

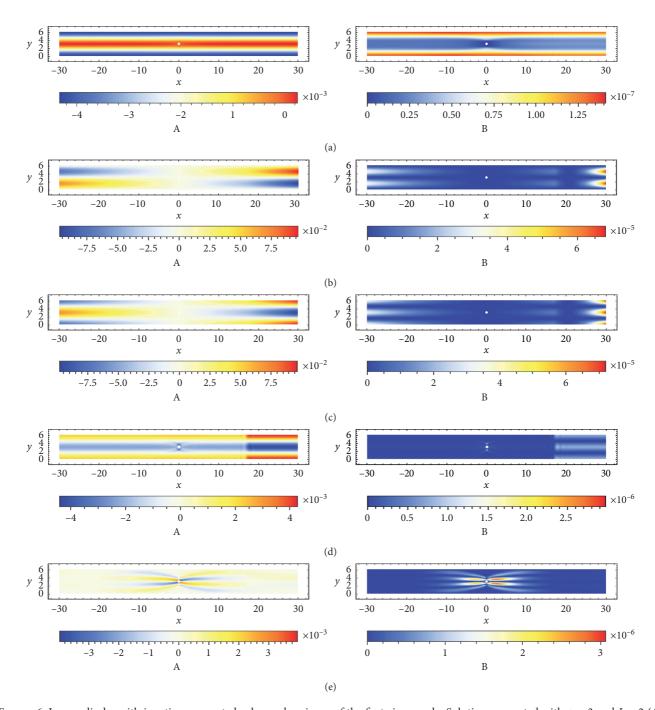


FIGURE 6: Long cylinder with junctions: expected value and variance of the first eigenmode. Solution computed with p=3 and L=2 (45 collocation points). (a) Expected value (A) and variance (B) of the component μ . (b) Expected value (A) and variance (B) of the component ν . (c) Expected value (A) and variance (B) of the component ψ . (d) Expected value (A) and variance (B) of the component ψ .

Let us next move to the partial sparse grids $\mathcal{X} \in \{X^{\text{CC}}, X^{\text{GL}}\}$. The results are displayed in Figure 11. The results should be compared with Figure 9; in particular, sampling the stochastic space with fixed first component already characterizes the locations of the maxima in the frequency response. However, the maximal amplitudes are different, again reflecting the fact that the points sets are not hierarchic.

Remark 1. We emphasise that if it were possible to identify real measurements as points in the grid, with this approach, one could augment simulations with real data and arrive at more realistic interpolation operators.

This example underlines the fact that in multiparametric situations, it is always necessary to think in terms of distributions and relate the observed statistics to them.

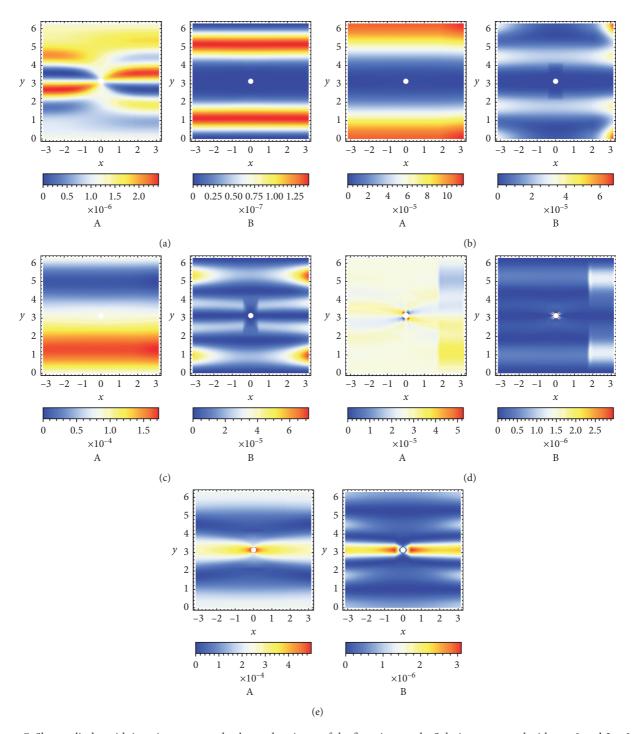


FIGURE 7: Short cylinder with junctions: expected value and variance of the first eigenmode. Solution computed with p=3 and L=2 (45 collocation points). (a) Expected value (A) and variance (B) of the component μ . (b) Expected value (A) and variance (B) of the component ν . (c) Expected value (A) and variance (B) of the component ψ . (d) Expected value (A) and variance (B) of the component ψ . (e) Expected value (A) and variance (B) of the component ψ .

6. Conclusions

Multiparametric vibration problems and especially those involving thin domains are and remain challenging. We have studied two vibration problems rooted in practice, yet artificial in terms of the parametrization of the random model. The efficacy of the stochastic collocation has been

demonstrated, and its extension to frequency response analysis has been demonstrated. More specifically, in the context of thin shells, the boundary layers, including internal ones, are shown to have the predicted characteristic length scales, and their contribution to statistics such as variance is clearly illustrated in the results. In vibration-related problem, the frequency response analysis, the importance of

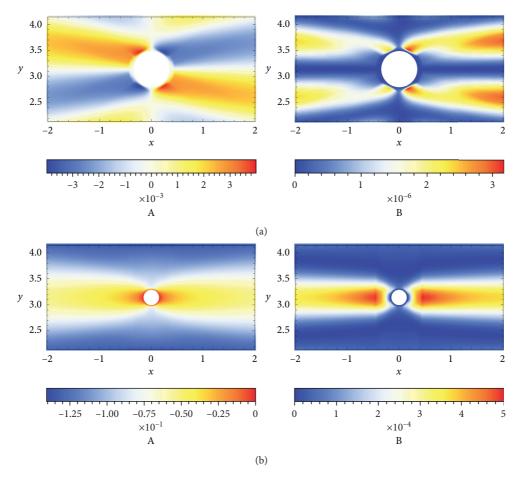


Figure 8: Statistics of the fifth field component ψ near the T-junction. (a) Long cylinder: expected value (A) and variance (B). (b) Short cylinder: expected value (A) and variance (B).

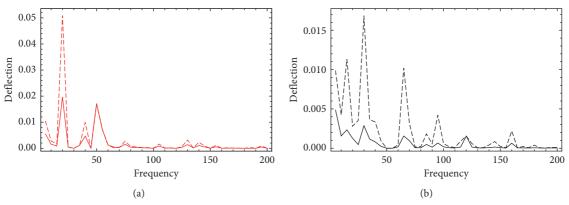


FIGURE 9: Continued.

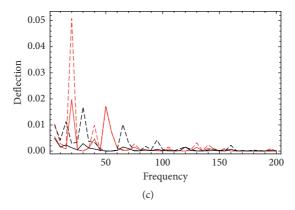


Figure 9: Frequency response: comparison of sparse grids: \mathcal{X}^{GL} vs \mathcal{X}^{CC} ; maximal transverse deflection w_{max} vs frequency; dashed line represents the added standard deviation. (a) Gauss \mathcal{X}^{GL} p=2, 41 points. (b) Clenshaw–Curtis \mathcal{X}^{CC} p=2, 41 points. (c) Combined.

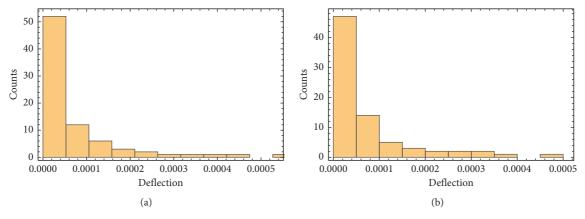


FIGURE 10: Frequency response distribution: Transverse deflections over the combined sparse grids \mathcal{X}^{GL} and \mathcal{X}^{CC} . (a) Frequency = 65 Hz. (b) Frequency = 85 Hz.

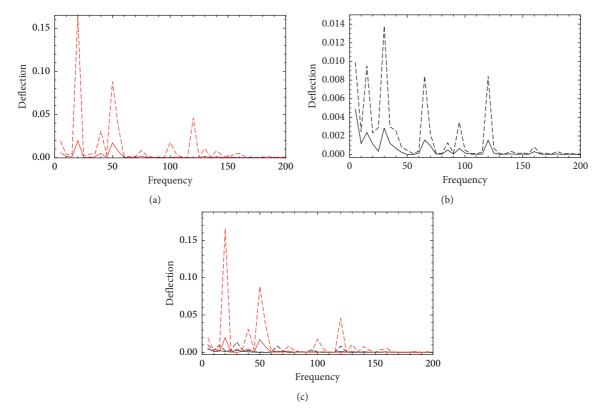


Figure 11: Frequency response: comparison of partial sparse grids: $X^{\rm GL}$ vs $X^{\rm CC}$; maximal transverse deflection $w_{\rm max}$ vs frequency; dashed line represents the added standard deviation. (a) Gauss $\mathcal{X}^{\rm GL}$ p=2, 25 points. (b) Clenshaw–Curtis $\mathcal{X}^{\rm CC}$ p=2, 25 points. (c) Combined.

gaining complete statistical understanding of the results is underlined.

Data Availability

No data were used to support this study.

Conflicts of Interest

The authors declare that there are no conflicts of interest regarding the publication of this paper.

References

- [1] Y. Qu, Y. Chen, X. Long, H. Hua, and G. Meng, "A variational method for free vibration analysis of joined cylindrical-conical shells," *Journal of Vibration and Control*, vol. 19, no. 16, pp. 2319–2334, 2013.
- [2] M. Kouchakzadeh and M. Shakouri, "Free vibration analysis of joined cross-ply laminated conical shells," *International Journal of Mechanical Sciences*, vol. 78, pp. 118–125, 2014.
- [3] X. Ma, G. Jin, Y. Xiong, and Z. Liu, "Free and forced vibration analysis of coupled conical-cylindrical shells with arbitrary boundary conditions," *International Journal of Mechanical Sciences*, vol. 88, pp. 122–137, 2014.
- [4] M. Shakouri and M. Kouchakzadeh, "Free vibration analysis of joined conical shells: analytical and experimental study," *Thin-Walled Structures*, vol. 85, pp. 350–358, 2014.
- [5] W. Pietraszkiewicz and V. Konopińska, "Junctions in shell structures: a review," *Thin Walled Structures*, vol. 95, pp. 310–334, 2015.
- [6] R. Andreev and C. Schwab, "Sparse tensor approximation of parametric eigenvalue problems," in *Lecture Notes in Computational Science and Engineering*, vol. 83, pp. 203–241, Springer, Berlin, Germany, 2012.
- [7] S. Smolyak, "Quadrature and interpolation formulas for tensor products of certain classes of functions," *Soviet Mathematics Doklady*, vol. 4, pp. 240–243, 1963.
- [8] C. Zenger, "Sparse grids," in Parallel Algorithms for Partial Differential Equations, W. Hackbusch, Ed., vol. 31, pp. 241– 251, 1991.
- [9] E. Novak and K. Ritter, "High dimensional integration of smooth functions over cubes," *Numerische Mathematik*, vol. 75, pp. 79–97, 1996.
- [10] H.-J. Bungartz and M. Griebel, "Sparse grids," Acta Numerica, vol. 13, pp. 1–123, 2004.
- [11] H. Hakula and M. Laaksonen, "Asymptotic convergence of spectral inverse iterations for stochastic eigenvalue problems," 2017, https://arxiv.org/abs/1706.03558.
- [12] V. Kaarnioja, "On applying the maximum volume principle to a basis selection problem in multivariate polynomial interpolation," pp. 1–18, 2017, https://arxiv.org/abs/1512.07424.
- [13] A. Sjöström, C. Novak, H. Ule, D. Bard, K. Persson, and G. Sandberg, "Wind turbine tower resonance," in *Proceedings* of *Inter Noise 2014*, The International Institute of Noise Control Engineering, Melbourne, VIC, Australia, November 2014
- [14] S. Salahshour and F. Fallah, "Elastic collapse of thin long cylindrical shells under external pressure," *Thin Walled Structures*, vol. 124, pp. 81–87, 2018.
- [15] H. Hakula and M. Laaksonen, "Multiparametric shell eigenvalue problems," Computer Methods in Applied Mechanics and Engineering, vol. 343, pp. 721–745, 2018.

[16] B. Szabo and I. Babuska, Finite Element Analysis, Wiley, Hoboken, NJ, USA, 1991.

- [17] D. Chapelle and K. J. Bathe, The Finite Element Analysis of Shells, Springer-Verlag, Berlin, Germany, 2003.
- [18] M. Malinen, "On the classical shell model underlying bilinear degenerated shell finite elements: general shell geometry," *International Journal for Numerical Methods in Engineering*, vol. 55, no. 6, pp. 629–652, 2002.
- [19] O. Ovaskainen and J. Pitkäranta, "An h-p-n adaptive finite element scheme for shell problems," *Advances in Engineering Software*, vol. 26, no. 3, pp. 201–207, 1996.
- [20] J. Pitkäranta, A.-M. Matache, and C. Schwab, "Fourier mode analysis of layers in shallow shell deformations," *Computer Methods in Applied Mechanics and Engineering*, vol. 190, no. 22-23, pp. 2943–2975, 2001.
- [21] H. Hakula, Y. Leino, and J. Pitkäranta, "Scale resolution, locking, and high-order finite element modelling of shells," *Computer Methods in Applied Mechanics and Engineering*, vol. 133, no. 3-4, pp. 157–182, 1996.
- [22] F. Nobile, R. Tempone, and C. G. Webster, "An anisotropic sparse grid stochastic collocation method for partial differential equations with random input data," SIAM Journal on Numerical Analysis, vol. 46, no. 5, pp. 2411–2442, 2008.
- [23] M. Bieri, "A sparse composite collocation finite element method for elliptic SPDEs," SIAM Journal on Numerical Analysis, vol. 49, no. 6, pp. 2277–2301, 2011.
- [24] I. Babuska, F. Nobile, and R. Tempone, "A stochastic collocation method for elliptic partial differential equations with random input data," SIAM Journal on Numerical Analysis, vol. 45, no. 3, pp. 1005–1034, 2007.
- [25] A. Chkifa, A. Cohen, and C. Schwab, "High-dimensional adaptive sparse polynomial interpolation and applications to parametric PDEs," *Foundations of Computational Mathematics*, vol. 14, no. 4, pp. 601–633, 2014.
- [26] V. Barthelmann, E. Novak, and K. Ritter, "High dimensional polynomial interpolation on sparse grids," Advances in Computational Mathematics, vol. 12, no. 4, pp. 273–288, 2000.
- [27] S. A. Goreinov, I. V. Oseledets, D. V. Savostyanov, E. E. Tyrtyshnikov, and N. L. Zamarashkin, "How to find a good submatrix," in *Matrix methods: Theory, Algorithms and Applications*, pp. 247–256, World Scientific Publishing, Singapore, 2010.
- [28] A. Civril and M. Magdon-Ismail, "On selecting a maximum volume sub-matrix of a matrix and related problems," *Theoretical Computer Science*, vol. 410, no. 47-49, pp. 4801–4811, 2009.
- [29] D. J. Inman, Engineering Vibration, Pearson, London, UK, 2008.

Hindawi Shock and Vibration Volume 2018, Article ID 2506909, 12 pages https://doi.org/10.1155/2018/2506909

Research Article

The Influence of the Track Parameters on Vibration Characteristics of Subway Tunnel

Wenbo Shi , 1,2 Linchang Miao , Junhui Luo , 4 and Honglei Zhang , 5

Correspondence should be addressed to Wenbo Shi; shwanbe@163.com and Linchang Miao; lc.miao@seu.edu.cn

Received 13 March 2018; Revised 23 May 2018; Accepted 19 June 2018; Published 18 October 2018

Academic Editor: Elena Dragomirescu

Copyright © 2018 Wenbo Shi et al. This is an open access article distributed under the Creative Commons Attribution License, which permits unrestricted use, distribution, and reproduction in any medium, provided the original work is properly cited.

In soft soil areas, such as the Nanjing, it is very important to quantitatively analyze the dynamic behaviors of soft soils during the metro train operation. A nonlinear coupling model of wheel-track and a finite element calculation model of tunnel and soil were established based on the mechanical character of elastic supporting block ballastless track and the actual parameters of Nanjing soft soil. The time-variant vertical acceleration of the rail, the sleepers, and the surface of the tunnel can be calculated by the models, and the frequency dependence acceleration was verified by the fast Fourier transform algorithm. A modified vibration power level for human sensitivity was used to quantify the vibration energy of each part of the system, and the impact of the parameters in the model was evaluated. The results can be applied to the metro design and construction, which also can be the guidance during the tunnel construction.

1. Introduction

With the continuous development of urbanization, the urban traffic is getting increasingly crowded. It is turning into the biggest chronic disease of the cities [1], which consists of traffic congestion, fog and haze weather, vehicle noise, and so on, and the subway is a best way to solve it. The metro that plays an important role in the modern life begins to spring up in many cities of China, and it shows a fast, convenient, and environment-friendly way. China's metro construction is entering a new period when both the construction speed and scale are first in the world, with 94 lines in operation, 120 lines in construction, and over 150 billion gross investment [2]. However, the vibrations induced by the high-speed moving metro trains for the surrounding metro lines will become a significant problem which has to be solved.

The research studies, which include metro vehicle and track coupling system and vibration energy transform in the

soil, usually consist of two independent sections. Studies on vehicle-track dynamics have been performed for a long time in many countries through the establishment of coupling model. Timoshenko [3] presented to use the frequencydomain technique to analyze track dynamics with continuously supported Euler beam. Xu et al. [4] established the vehicle/track interaction model, which can be used to reveal the interaction mechanisms between the moving vehicles and the guiding tracks. Aggestam et al. [5] evaluated the wheel-rail contact forces, bending moments in the concrete panel and load distributions on the supporting foundation by two generic slab track models including one or two layers of concrete slabs. Lopes et al. [6] focused on the experimental validation of a numerical approach previously proposed for the prediction of vibrations inside buildings due to railway traffic in tunnels. Three autonomous models compose the numerical model in order to simulate the generation, propagation, and reception of vibrations. Studies in recent years have been a trend to regard the vehicle and track model

¹School of Traffic and Transportation, Xuchang College, Xuchang 461000, China

²Henan Small and Medium-Sized Cities Public Transport Information Engineering Research Center, Xuchang 461000, China

³Institute of Geotechnical Engineering, Southeast University, Nanjing 210018, China

⁴Guangxi Communications Planning Surveying and Designing Institute Co., Ltd., Nanning 530029, China

⁵Henan Zhibo Architectural Design Group Co., Ltd., Xuchang 461000, China

as an integral system on dynamics of wheel-rail interactions [7–12].

Research that focused on the propagation of vibration caused from the wheel-rail exceeding in the soil has also been developed many years in the world. The models, which used to solve the problem of vibration wave propagation in the soil caused by metro operation, can be classified into two categories: the finite element models (FEMs) and analytical method. Analytical method is confined by many hypotheses, like supposing the soil material as elastic continuum material, supposing the load applied on the tunnel is harmonic in both space and time, and so on. Forrest and Hunt [13] described a three-dimensional model for the dynamics of a deep underground railway tunnel in infinite soil, and the ground vibration due to excitation by running trains in frequency 20 to 100 Hz was analyzed. Bian et al. [14] used a 2.5D FEM formulation with viscous artificial boundaries to model wave propagation from underground moving loads. The periodic 2.5D FEM models for the dynamic simulation of tunnels have been extensively applied to simulate the dynamic interaction between soil and tunnel structures [15, 16]. Many models established in research papers above assumed radius of the model from the center of the tunnel increases towards infinity in every direction; therefore, it can not calculate the remnant vibration energy transform to the surface of the soil. The subway operation problem is clearly a moving load problem, and some elegant solutions in FEM appear in the literature. Amado-Mendes et al. [17] devised the subway finite element model to determine the dynamic stress and analyzed dynamic response under vibration loading. The relationship between the train speed and the vibrations on the track with a FEM model is studied by El Kacimi et al. [18]. Gardien and Stuit [19] established a modular model that consists of static deflection model, track model, and the propagation model, and the effect of change element size, soil stiffness, damping, and boundary conditions is analyzed. Ekevid et al. [20] described in detail the mesh refinement and coarsening in the case of HST applications, with successful validations. Ju [21] investigated the characteristics of building vibrations induced by adjacent moving trucks using finite element analyses. Regarding urban traffic, research is scarcer. Andersen and Jones [22] investigated the quality of the results obtained from a 2D-coupled FE-BE model comparing it with a 3D-coupled FE-BE model. Real et al. [23] developed a 3D numerical FEM model of a railway tunnel to predict railway-induced vibrations. Vogiatzis [24] studied the effect of ground-borne vibrations generated by underground metro and their effects on ancient monuments.

The research of the subway system mostly focused on the vibration damping track, and the vehicle-wheel coupling system was established; the effect on the environment by subway vibration was discussed through field measurement and data fitting during the metro operation. Quantitatively analyzing each parameter's influences, which focused on system vibration energy causing and spreading, is particularly important through establishing a vehicle-rail-sleeper-ballast-lining-soil body model. The subway tunnel buried in a soft soil area will have a big settlement, which is caused by the vibration energy of vehicle long cycle action during the

process of vehicle operation, because the soft clay has the characteristics of high water content, big compressibility, and low intention. The practical engineering shows that the subsidence generated approximately 16 cm of Shanghai metro line 1 during the metro long-term operation, and the largest subsidence near the Helen Road station has reached 30 cm [25], and thus, analyzing the effect of track parameters on the vibration energy generate and transform in soft soil area has important implications.

2. Vehicle-Track Coupling Model

The settlement of the soft soil surrounding along metro lines is caused by the long-term cyclic loading during the metro operation. The magnitude of settlement mainly depends on the force at the vehicle-track contact and the vertical vibration acceleration of the system; thus, how to reduce the effect of the vibration becomes a key, which can decrease the soil settlement. Considering the vehicle leading and trailing bogie symmetrically arranged in general, and the ups and downs of vibration of car body with nodding vibration will not cause coupling, the half car body model is established, which is based on the geometric characteristics of the elastic supporting block ballastless track, as shown in Figure 1.

3. The Vehicle Model of the Metro Train

As shown in Figure 1, $M_{\rm c}$, $M_{\rm t}$, and $M_{\rm w}$ stand for the quality of half train body, the bogie, and the wheel set, respectively; $J_{\rm t}$ is nod inertia of the body's frame; $K_{\rm sz}$ and $K_{\rm pz}$ is the stiffness of the vehicle primary and secondary suspension; $C_{\rm sz}$ and $C_{\rm pz}$ is the damping of the vehicle primary and secondary suspension; and $z_{\rm 1}$ and $z_{\rm 2}$ are, respectively, for the location of the wheel-rail contact irregularity. Vibration equation about the upper part of the vehicle model is established according to the Hamilton principle as follows:

$$[M_{n}]\{\ddot{u}\} + [C_{n}]\{\dot{u}\} + [K_{n}]\{u\} = \{P_{n}\}. \tag{1}$$

4. The Track Model of the Metro

The elastic supporting block ballastless track is supported by rail, fasteners, concrete supporting block, rubber pads under supporting block, rubber boots, concrete track bed, etc., and the track's vertical stiffness and damping is mainly provided by the fasteners and the piece of rubber pad. These components of the model can use the stiffness and damping parameters to describe them, such as, $K_{\rm r}$, $C_{\rm r}$ and $K_{\rm s}$, $C_{\rm s}$, respectively. Thus, acceleration of vibration of the elastic supporting block ballastless track is mainly reflected on the rail and concrete supporting block.

Newton and Clark [26] analyzed the impact on the vehicle-track coupling nonlinear system with assuming track for Euler beam and Timoshenko beam, respectively. The results showed that the Timoshenko beam has a higher accuracy when analyzing the rail shear stress; however, the computational time was higher for the Timoshenko beam. This paper uses the Euler model because the two beams have little difference in accuracy in the analysis of the vertical

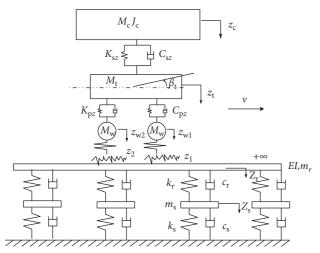


FIGURE 1: The half-vehicle-track coupled nonlinear model.

vibration displacement of the track. The differential equation of rail vibration deformation under the relevant knowledge of mechanics of materials is as follows:

$$EI\frac{\partial^{4}Z_{r}(x,t)}{\partial x^{4}} + m_{r}\frac{\partial^{2}Z_{r}(x,t)}{\partial t^{2}} = -\sum_{i=1}^{N}F_{rsi}(t)\delta(x-x_{i}) + \sum_{j=1}^{2}p_{j}(t)\delta(x-x_{wj}),$$

$$(2)$$

 $F_{rsi}(t) = K_{pi}[Z_r(x_i, t) - Z_{si}(t)] + C_{pi}[\dot{Z}_r(x_i, t)]$ $-\dot{Z}_{si}(t)$], δ is the Dirac function, $Z_{si}(t)$ is the sleeper vibration displacement, F_{rsi} is the reaction supporting force of the *i*th root sleeper, and p_i is the wheel-rail coupling force at the sites of jth wheels.

The vibration equation on sleeper is as follows:

$$K_{p}[Z_{r}(x_{i},t) - Z_{si}(t)] + C_{p}[\dot{Z}_{r}(x_{i},t) - \dot{Z}_{si}(t)] - K_{b}Z_{si}(t) - C_{b}\dot{Z}_{si}(t) = M_{si}\ddot{Z}_{si}(t).$$
(3)

Assumptions on the two ends of the rail are simply supported, the boundary conditions for the moment can be obtained, and the displacement of the rail and bending moment on the cross section is zero at x = 0 [27, 28].

The corresponding characteristic function, namely, the

free vibration modal is as follows:

$$Y_{\rm r}(x) = C_1 \sin \frac{r\pi x}{l} \qquad (r = 1, 2, ...). \tag{4}$$

By orthogonal processing of the characteristic function by $\int_0^L mY_{\rm r}^2(x)dx=1$, it can be obtained that $C_1=\sqrt{2/ml}$,

and then the free vibration modal equation is as follows:

$$Y_{\rm r}(x) = \sqrt{\frac{2}{ml}} \sin \frac{r\pi x}{l} \qquad (r = 1, 2, ...). \tag{5}$$

So

$$Z_{\rm r}(x_i,t) = Y(x)q(t) = \sqrt{\frac{2}{m_{\rm r}l}}\sin\frac{k\pi x}{l}q_k(t). \tag{6}$$

Simplifying the track nonlinearity equations by substituting Equation (6) into Equations (2) and (3), the final vibration equation is as follows:

$$[M_1]\{\ddot{q}\} + [C_1]\{\dot{q}\} + [K_1]\{q\} = \{P_1\}. \tag{7}$$

The enough mode number is the guarantee to be the precision in the process of solving the vibration equation of the track by using the modal analysis method [29]. The results of numerical calculations show that the calculation accuracy can well meet the requirements if the mode number is greater than $0.5 L/L_s$, where L is the rail length and L_s is the distance of the adjacent sleepers.

5. Nonlinear Contact Stress Calculation of the Wheel-Track

The wheel-track contact stress can be calculated based on Hertz nonlinear contact theory, and the wheel-track vertical force is as follows:

$$p(t) = \left[\frac{1}{G}\delta_{Z(t)}\right]^{3/2},\tag{8}$$

where G is the wheel-rail contact constant, a wheel-rail contact constant's empirical formula for a contact constant is $G=4.57R^{-0.149}\times 10^{-8}$, and $\delta_{Z(t)}$ is for elastic compression between the wheel and track.

It can be very well to connect the upper vehicle model and the lower track model, which made them as a complete system with Equation (8).

6. The Newmark Integration Method

Time-stepping integration provides the best way for a numerical solution of the equations of motion of the vehicletrack system including nonlinearities. Writing the vehicle vibration equation and the track vibration equation in a same way is shown in the following equation:

$$[M]\{\ddot{x}\} + [C]\{\dot{x}\} + [K]\{x\} = \{P\}. \tag{9}$$

The useful approach to calculate these equations is the method of the Newmark explicit iterative which is used widely in engineering practice. Assuming that $\{\ddot{x}\}_{t-1}$, $\{\dot{x}\}_t$, and $\{x\}_t$ are known at time t, in $t + \Delta t$ moment, the equation solution can be expressed as follows:

$$\begin{cases} \{x\}_{n+1} = \{x\}_n + \{\dot{x}\}_n \Delta t + \left(\frac{1}{2} + \psi\right) \{\ddot{x}\}_n \Delta t^2 - \psi \{\ddot{x}\}_{n-1} \Delta t^2, \\ \{\dot{x}\}_{n+1} = \{\dot{x}\}_n + (1 + \varphi) \{\ddot{x}\}_n \Delta t - \varphi \{\ddot{x}\}_{n-1} \Delta t, \end{cases}$$
(10)

where Δt is the time step and ψ and φ are free parameters which control the stability and numerical dissipation of the algorithm. The next step vibration expression can be written as shown in Equation (11) by substituting the above solving method with initial condition into the system vibration equation:

$$[M]\{\ddot{x}\}_{n+1} + [C]_{n+1}\{\dot{x}\}_{n+1} + [K]_{n+1}\{x\}_{n+1} = \{P\}_{n+1}. \tag{11}$$

For each time step, calculate the displacements and velocities of the vehicle calculate model (1) and the track calculate model (7) with the Newmark integration method, and

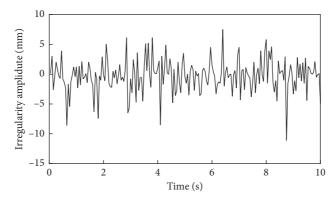


FIGURE 2: Track random irregularity.

TABLE 1: Vehicle parameters in specific value.

Quantity	Half vehicle quality (M_c)	Bogie quality $(M_{\rm t})$	Bogie pitch moment of inertia (J_t)		Primary suspension stiffness (K_{sz})	Primary suspension damping (C_{sz})	The second suspension stiffness (K_{pz})	The second suspension damping (C_{pz})	Half of bogie wheelbase (<i>l</i> _h)
Value	38500 kg	2980 kg	$3605 \mathrm{kg/m^2}$	1350 kg	$2.14 \times 10^6 \text{N/m}$	$4.9 \times 10^4 \mathrm{N} \cdot \mathrm{s/m}$	$2.535 \times 10^6 \text{N/m}$	$1.96 \times 10^5 \mathrm{N \cdot s/m}$	1.2 m

the nonlinear wheel-track contact forces can then be determined based on the calculated Equation (8). With these known results, the accelerations of the vehicle and the track are finally calculated from each equation of motion.

7. Applying of the Stochastic Irregularity

In general, the stochastic irregularity in the vehicle-track modelling is used to represent the vehicle travel state because of the nondeterministic excitation in the wheel-track system. As the rail surface geometry is influenced by many complex factors, these effects caused by the track irregularity have obvious randomness. The spectrum density function of the metro track for line grade six from America Railway Standard is used in this calculation. The simulation using trigonometric series method converts track irregularity power spectrum to the time domain excitation function which applied to the system as a random excitation. The final amplitude curves of vertical track irregularity is shown in Figure 2.

8. The Result Solutions of the Vehicle-Track Coupled Model

The parameters adopted for computing system at Section 1 are listed in Tables 1 and 2.

The speed of the metro vehicle is 40–80 km/h in a general way, and the faster the speed is, the bigger the wheel-track contact force is. In this calculation, the speed of the vehicle is set to 80 km/h. According to the vehicle-track nonlinear coupled calculation model shown at Section 1 and the parameter values shown at Tables 1 and 2, the displacement of the sleeper in the process of metro vehicle driving can be basically in agreement with the Newmark integration method. Priest and Powrie [30] used geophones to measure

the sleeper's displacement during train service and used a modified beam on an elastic foundation method (BOEF) to calculate the displacement of the sleeper. The time domain result is shown in Figure 3.

These show similar behavior of the sleeper displacement during the operation in Figure 3. The calculation of vehicle-track coupled model is closer to the measured one when compared with BOEF method; nevertheless, the decay of the displacement is slower than BOEF method because of the characteristic of the modal analysis.

The accuracy of the vibration prediction depends on the chosen input parameters in the system. The vehicle-track nonlinear coupling system can be used to analyze the influence of the parameters' change on the system vibration, including vehicle speed, the stiffness and damping of the fastener and the rubber pad, random irregularity, and wave depth. Nevertheless, the most easily implemented measure is to adjust the stiffness and damping of the fastener and the rubber pad for the engineering practice. Thus, analysis effect of the stiffness and damping of the fastener and the rubber pad will play a key role in the vibration-controlling technique design of the practical engineering.

According to the nonlinear-coupled system established earlier, the rail and sleeper vibration acceleration in time domain can be obtained in the process of metro vehicles driving shown in Figures 4 and 5 shows the acceleration power spectrum density of the rail and sleeper vibration.

Figures 4 and 5 show that the acceleration amplitude of the rail vibration is bigger than the sleeper, which illustrates the energy of vibration attenuated in the spread of rail, fasteners, sleeper, and the rubber pad. Thus, the quantitative analysis of track parameters is of great significance for vibration energy transmission system.

Single bogie is able to be applied for the qualitative analysis of influence on vibration generation and attenuation during its transform by parameter change.

TABLE 2: Wheel coupling system orbit parameters in specific value.

	F			1 70 1				TT. 111.	11. 1		
\geq	Ine quality of Quantity the rail unit	Rail elastic	Rail section	Fastener vertical	Fastener	Sleeper		Under the steeper Under the steeper C40 concrete Concrete rubber pad elastic Poisson's	Under the sleeper rubber pad	C40 concrete elastic	Concrete Poisson's
	length $(m_{\rm r})$		merua (1)	stiffness (K _r)	uamping (Cr)	ianiping (C_r) quanty (m_s) spacing (a)	spacing (u)	stiffness (K _s)	damping (C _s)	modulus (E_c) ratio (ν)	ratio (ν)
/alue	$60\mathrm{kg/m}$	$2.059 \times 10^{11} \mathrm{Pa}$	$0.059 \times 10^{11} \mathrm{Pa} \ 2.037 \times 10^{-5} \mathrm{m}^4 \ 7.8$	$7.8 \times 10^7 \mathrm{N/m}$	$\times 10^7 \mathrm{N/m}$ $5 \times 10^4 \mathrm{N \cdot s/m}$		$0.545\mathrm{m}$	$7.8 \times 10^7 \mathrm{N/m}$	$5.88 \times 10^4 \mathrm{M \cdot s/m}$ $3 \times 10^{10} \mathrm{Pa}$ 0.2	$3 \times 10^{10} \mathrm{Pa}$	0.2

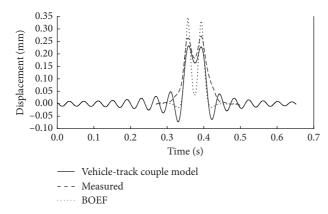


FIGURE 3: Comparison of measured sleeper displacement with that obtained from using the vehicle-track coupled model and BOEF model for a single bogie.

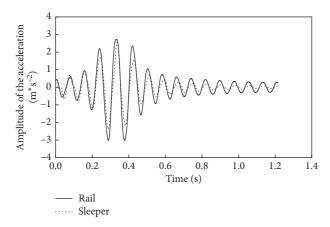


FIGURE 4: Rail and sleeper vibration acceleration time-domain amplitude.

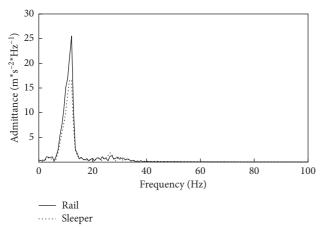


FIGURE 5: Rail and sleeper vibration acceleration amplitude in frequency domain.

The magnitude of the vertical load on tunnel can be calculated according to Equation (12), and the result is shown in Figure 6

$$P = Z_{\rm s}K_{\rm s} + V_{\rm s}C_{\rm s}. (12)$$

9. The Introduction of the Modified Vibration Power Level Index

The modified vibration power level index is used to quantify the sense of the human body for the environmental vibration and to clearly recognize the harm to human body by vibration. According to the recommendations in International Standards Organization (ISO2631), the most sensitive human body to vibration frequency is mainly concentrated in the domain of 1–80 Hz, meanwhile the human body responds to the vibration of different directions shown in Figure 7.

Based on the investigations of International Standards Organization, human body sensitive degree is different to the vibration of different frequency ranges [31]. The modified vibration power level is an index to evaluate the influence of vibration on human by amending the effective amplitude of acceleration based on human reactivity, and the unit of the modified vibration power level is dB, which shows the logarithmic ratio of vibration energy. The definition of vibration energy index formula is as follows:

$$L_e = 20\log\frac{a_e}{a_0},\tag{13}$$

where $a_0 = 1 \times 10^{-6} \,\text{m/s}^2$ and a_e is the correction of acceleration RMS, and the specified solving equation is as follows:

$$a_e = \sqrt{\sum a_n^2 \cdot 10^{C_n/10}},\tag{14}$$

where a_n is the effective acceleration amplitude for n Hz and C_n is the modification value according to the human response to vibration, as shown in Figure 7, and the specific value is given in Table 3.

The rail and sleeper vibration acceleration amplitude in time domain can be calculated according to the vehicle-track coupling nonlinear model presented in this paper; and then its power spectral density amplitude is obtained by the fast Fourier transform. However, the analysis of the data often adopts the method of 1/2 octave bands to the calculation of modified vibration power level. The standard of 1/2 octave bands is the number of center frequency in multiples of 2 of the center frequency, and modified vibration power level of human feeling can be obtained by the sum of vibration energy in each center frequency range. And the vibration virtual value of acceleration in each center frequency bandwidth, namely, a_n , is the vibration acceleration rootmean-square in the frequency domain, and its expression is as follows:

$$a_n = \sqrt{a_1^2 + a_2^2 + a_3^2 + \cdots}. (15)$$

Therefore, the influence of each parameter of the system on the vibration performance can be calculated by the modified vibration power level in the proposed model, and the quantified analysis effect on the system vibration of different parameters has come true by this way.

By using the above method, specific figures of the system vibration power level affected by the change of parameters in

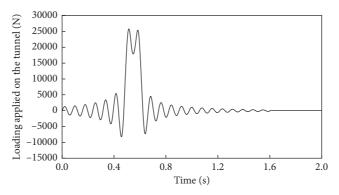


FIGURE 6: Vertical load applied on the tunnel shell.

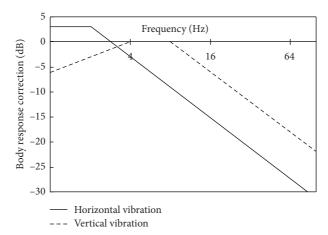


FIGURE 7: Human body response to different direction vibration.

Table 3: Modification value of vertical effective acceleration within the center frequency.

1/2 octave bands center frequency (Hz)	1	2	4	8	16	31.5	63	90
Vertical modified vibration power level (dB)	-6	-3	0	0	-6	-12	-18	-21

the vehicle-track coupled model can be collected; the result is shown in Figures 8 and 9.

The result shows that the track vibration power level reduces nearly 23 dB when the stiffness of fastener increases from 0.5×10^7 N/m to 100×10^7 N/m, but vibration power level of the sleeper reduces less than 2 dB. Similarly, track vibration power level will decrease 6 dB when damping of the fastener increases from 0.5×10^4 N·s/m to 50×10^4 N·s/m and vibration power level of the sleeper reduces nearly 2 dB.

Changing stiffness and damping of the fastener have great influence on the vibration performance of rail, but the effect of the vibration of the sleeper damping is small. Meanwhile, stiffness change of the fastener has better consequence on vibration attenuation. However, it is bound to reduce deformation of the track caused by vibration and to restrict the development of the long wave acceleration if the stiffness of the fastener is blindly increased. In addition, the stiffness of the fastener that is increased will lead to the increment of the wheel-track coupling force and the generation of noise.

Figures 10 and 11 show that the track vibration power level reduces 25 dB and the sleeper vibration power level decreases more than 45 dB when the stiffness of the under sleepers' rubber pad also increases from 0.5×10^7 N/m to 100×10^7 N/m. At the same time, the vibration power level of the rail will be reduced nearly 7 dB and sleeper vibration power level will be lost about 4 dB when the damping of the rubber pad increased from 0.5×10^4 N·s/m to 50×10^4 N·s/m. Thus, it can be seen that increasing the stiffness of fastener and under sleeper rubber pad can significantly reduce the rail and sleeper vibration power level. The vibration of the subgrade is small in elastic supporting block ballastless track system, so the influence of the stiffness and damping of rubber pad which at the bottom of the system on the vibration characteristics is bigger.

Rail and sleeper vibration energy are basic agreement when the stiffness of the rubber pad is relatively small. The main reason is that the lower rigidity leads to large deformations of the rubber pad when the overlying load transfers to it and the stiffness increment of the fasteners cannot be able to play its role

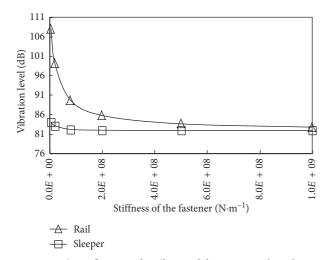


FIGURE 8: The influence of stiffness of fastener on the vibration power level.

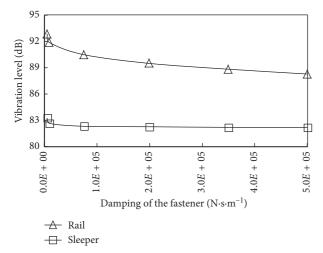


FIGURE 9: The influence of damping of fastener on the vibration power level.

in the system. The small stiffness of the rubber pad made the structure on it to form an integral whole when the large vibration load transfers from the rail to here.

In the whole vehicle-track system, the effect of the stiffness and damping of the fastener will gradually appear when the stiffness of the rubber pad increases, the difference of the rail and sleeper vibration energy amplitude gradually expend as shown in Figure 10. The deformation is small which is caused by the vehicle-track exciting force when the stiffness of the rubber pad is increased to a greater value under low frequency arrange. Thus, the vertical vibration speed of the sleeper will be decreased as the damping of the sleeper increased, which will also reduce strain velocity of the track and then affect its vibration energy change.

10. The Finite Element Modelling

Vibration will generate because of track irregularity during the metro operation. The vibration energy passes onto the soil via rail, sleeper, track ballast, and tunnel lining, and it

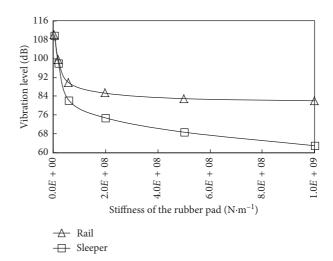


FIGURE 10: The influence of stiffness of the rubber pad on the vibration power level.

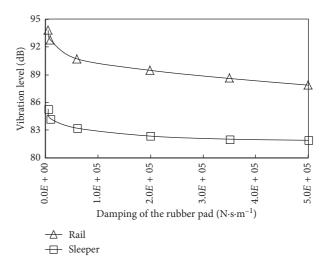


FIGURE 11: The influence of damping of the rubber pad on the vibration power level.

has great impact on the construction and residents' life when it transfers to the subway tunnel surface; therefore, the analysis of the change of damping and stiffness of the fastener and sleeper rubber pad is of great significance to the influence of vibration energy spreading to the surface.

The finite element method is used to calculate the acceleration of an arbitrary point in the soil due to an operation vehicle. The superiority of the finite element method is to analyze the interaction between the tunnel segments and the surrounding soft soil, and the subroutine can be used to simulate the soil to ensure the validity of the result calculated in the model.

According to the size of elastic supporting block ballastless track, the finite element model was established. Generally, the size of mesh must be at least 1/8th wavelengths to ensure calculated precision when meshing the finite element model [32]. The size of mesh should be around 2.4 m because the nature frequency of vibration in Nanjing soft soils is 10–80 Hz and the speed of stress wave is 190 m/s,

and the finite element model is set up as shown in Figure 12. The model boundary conditions are symmetrical layout along the tunnel axis, and at the bottom, the right-hand, and the left-hand, the viscous-spring boundary conditions are applied. The viscous-spring boundary conditions made the model seem like an infinite layered half-space, and the vibration energy will decay to zero and without any reflections. The connection between tunnel lining and subgrade is set as surface-to-surface contact, the normal behavior is "hard" contact, and the tangential behavior is friction contact, which may simulate the mechanical relationship between lining and subgrade well. The connection between surrounding soil and tunnel lining is set as Tie [33].

The exciting force is calculated by the vehicle-track coupled model shown in Figure 6. The load applied on the subgrade of the finite model systematically during the metro operation is shown in Figure 13, and the vibration acceleration of an arbitrary point can be computed during the vehicle operating.

The finite element model of the metro tunnel is made up of track bed slab, subgrad, and tunnel lining, and supposing these components are liner-elastic material. In the simulate calculation, the track bed slab and subgrad using C40 concrete which value is shown in Table 4, and the tunnel lining uses concrete labeled C55, and the value is shown in Table 5.

The clay is the soft soil of Nanjing of China for the finite element model calculation. The samples were sampled by thin-wall soil samples from the site of Nanjing metro 4 line, and the sampler is cylindrical for 30 cm high and 11 cm diameter, as shown in Figure 14. The dynamic triaxial tests are constructed by the GDS system shown in Figure 15. The GDS dynamic triaxial system can do the real-time monitoring during the tests; therefore, test data can be recorded and accessed in high speed. The calculation parameters of the soft soil for the segment-soil interaction-coupled model are measured under cyclic load of 75 kPa, 1 Hz frequency, and 5000 load cycles, and the specific value of the parameters are shown in Table 6.

According to the stress-strain curves based on the hyperbolic shape established by Hardin and Drnevich [34], setting up the functional relationships between the dynamic elastic modulus and dynamic strains is shown in Figure 16:

$$E_{\rm d} = \frac{E_0}{1 + (\varepsilon_{\rm d}/\varepsilon_{\rm r})}.$$
 (16)

According to the result of the experiment, we got the parameter values for Nanjing soft clay: $E_0 = 47.2$ and $\varepsilon_{\rm d} = 0.038$. Dynamic elastic modulus is used in the finite element software, and the quantitative influence of material parameters of fastener and under sleeper rubber pad on vibration energy transform in the soft soil to the surface of the earth is studied. The acceleration of the surface is calculated by the finite model is shown in Figure 17.

By changing the stiffness of the fastener and sleeper, the calculation results are shown in Figures 18 and 19, respectively.

The fact can be found that the surface vibration power level of the stiffness change of fastener and sleeper is obvious

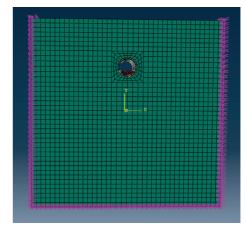


FIGURE 12: The finite model of the metro tunnel.

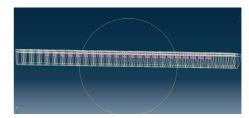


FIGURE 13: The load applied on the finite model.

TABLE 4: Track bed slab and subgrad parameter values.

Quantity	Young's modulus (E)	Poisson's ratio (ν)	Density (ρ)
Value	$3.25 \times 10^{10} \text{Pa}$	0.2	2450kg/m^3

more than the change of the damping of them from Figures 18 and 19. Meanwhile, the impact of changing the stiffness of sleeper rubber pad is the largest and the vibration power level of the surface reduces 2.5 dB when the stiffness increased from 0.5×10^7 N/m to 100×10^7 N/m, while the change of the other parameters is not significantly affected at the surface vibration power level.

Vibration energy continuously decays during the spread through rail, sleeper, ballast bed, lining, and the soil, as shown in Figure 20. It decays almost 9% when transferring from rail to sleeper and attenuates 20% when passing on to the tunnel lining, while vibration level reduces nearly 38% when vibration energy finally transfers to the surface of the ground.

11. Conclusion

The parameters of fastener and sleeper rubber pad influences on the system vibration characteristics are analyzed in this paper by establishing wheel-track nonlinear coupling dynamic model and the finite element model, specifically:

(1) The vibration energy indicator combined with human sensitivity is introduced to research the vibration characteristics of the system, and the results can be more intuitive to show the influence of various parameters on the system vibration characteristics.

TABLE 5: Tunnel lining parameter values.

Quantity	Young's modulus (E)	Poisson's ratio (ν)	Density (ρ)	Inner diameter (a)	Thickness of the tunnel shell (h)
Value	$3.45 \times 10^{10} \text{Pa}$	0.17	$2450 \mathrm{kg/m}^3$	2.7 m	0.3 m



FIGURE 14: Cylindrical samples.



FIGURE 15: GDS test system.

TABLE 6: The parameter of the soil.

Quantity	Poisson's ratio (ν)	Density (ρ)	Pressure wave velocity (c_1)	Shear wave velocity (c_2)	Volumetric damping $(\eta_{\rm K})$	Hysteretic loss factor (η_G)
Value	0.3	1859kg/m^3	524 m/s	190 m/s	0	0.06

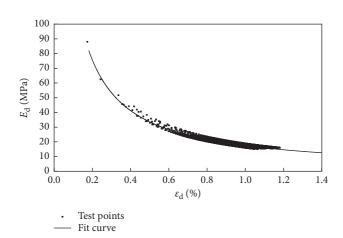


FIGURE 16: The relationship between dynamic elastic modulus and dynamic strains.

- (2) Increasing the stiffness and damping of fastener and under sleeper rubber pad can make a direct result of rail, sleeper vibration energy reduction, at the same time, the increasing stiffness of fastener and rubber pad can reduce the vibration energy, and the effect is higher than increasing the damping. Meanwhile, changing the stiffness of the sleeper rubber pad has the greatest impact on the vibration level of rail, sleeper, and the surface soil. The changing stiffness of the fastener has great influence on the vibration level of rail and sleeper, while a certain impact will happen on the vibration level of the system when the damping of the fastener and sleeper rubber pad changed, but it is relatively small to the change of stiffness.
- (3) During the operation of the metro vehicle, the vibration energy continuously decays pass through rail, sleeper, the tunnel lining, and finally the soil,

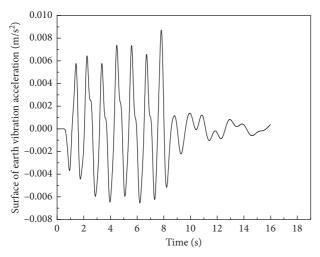


FIGURE 17: The time history of the acceleration.

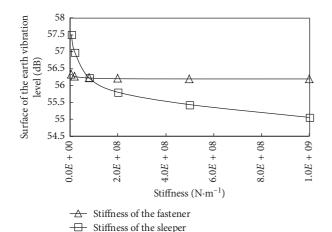
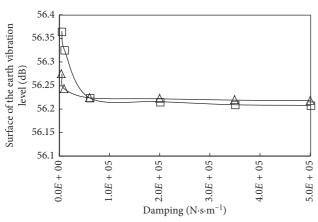


FIGURE 18: The influence of stiffness change on the vibration power level.



→ Damping of the fastener→ Damping of the sleeper

FIGURE 19: The influence of damping change on the vibration power level.

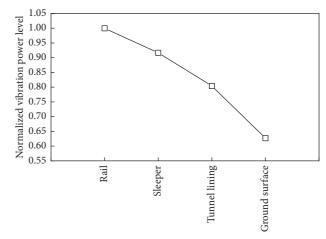


Figure 20: The attenuation of vibration energy in the system.

and eventually, vibration energy reaching the surface is only 62% of the rail vibration energy.

Data Availability

The data used to support the findings of this study are available from the corresponding author upon request.

Conflicts of Interest

The authors declare that they have no conflicts of interest.

Acknowledgments

The National Natural Science Foundation of China (no. 51278099) supported this work.

References

- [1] Z. M. Schrag, The Great Society Subway: A History of the Washington Metro, JHU Press, Baltimore, MD, USA, 2014.
- [2] S. Guo, H. Luo, and L. Yong, "A big data-based workers behavior observation in China metro construction," *Procedia Engineering*, vol. 123, pp. 190–197, 2015.
- [3] S. Timoshenko, "Method of analysis of statical and dynamical stresses in rail," in *Proceedings of the 2nd International Congress for Applied Mechanics*, pp. 12–17, Zurich, Switzerland, September 1926.
- [4] L. Xu, W. Zhai, and J. Gao, "A probabilistic model for track random irregularities in vehicle/track coupled dynamics," *Applied Mathematical Modelling*, vol. 51, pp. 145–158, 2017.
- [5] E. Aggestam, J. C. O. Nielsen, and R. Bolmsvik, "Simulation of vertical dynamic vehicle-track interaction using a twodimensional slab track model," *Vehicle System Dynamics*, vol. 56, no. 11, pp. 1633–1657, 2018.
- [6] P. Lopes, J. F. Ruiz, P. A. Costa, L. Medina Rodríguez, and A. Silva Cardoso, "Vibrations inside buildings due to subway railway traffic. Experimental validation of a comprehensive prediction model," *Science of the Total Environment*, vol. 568, pp. 1333–1343, 2016.
- [7] L. Ling, J. Han, X. Xiao, and X. Jin, "Dynamic behavior of an embedded rail track coupled with a tram vehicle," *Journal of Vibration and Control*, vol. 23, no. 14, pp. 2355–2372, 2017.

[8] Y. Qi, H. Dai, J. Yang, and K. Xu, "Dynamic analysis of vehicle track coupling based on double beam track model," *Shock and Vibration*, vol. 2018, Article ID 7469894, 10 pages, 2018.

- [9] L. Xu and W. Zhai, "A new model for temporal-spatial stochastic analysis of vehicle-track coupled systems," *Vehicle System Dynamics*, vol. 55, no. 3, pp. 427–448, 2017.
- [10] W. Zhai, K. Wang, and C. Cai, "Fundamentals of vehicle-track coupled dynamics," *Vehicle System Dynamics*, vol. 47, no. 11, pp. 1349–1376, 2009.
- [11] X. Lei and N. A. Noda, "Analyses of dynamic response of vehicle and track coupling system with random irregularity of track vertical profile," *Journal of Sound and Vibration*, vol. 258, no. 1, pp. 147–165, 2002.
- [12] Y. Q. Sun and M. Dhanasekar, "A dynamic model for the vertical interaction of the rail track and wagon system," *International Journal of Solids and Structures*, vol. 39, no. 5, pp. 1337–1359, 2002.
- [13] J. A. Forrest and H. E. M. Hunt, "A three-dimensional tunnel model for calculation of train-induced ground vibration," *Journal of Sound and Vibration*, vol. 294, no. 4, pp. 678–705, 2006.
- [14] X. Bian, W. Jin, and H. Jiang, "Ground-borne vibrations due to dynamic loadings from moving trains in subway tunnels," *Journal of Zhejiang University SCIENCE A*, vol. 13, no. 11, pp. 870–876, 2012.
- [15] S. Gupta, M. F. M. Hussein, G. Degrande, H. E. M. Hunt, and D. Clouteau, "A comparison of two numerical models for the prediction of vibrations from underground railway traffic," *Soil Dynamics and Earthquake Engineering*, vol. 27, no. 7, pp. 608–624, 2007.
- [16] W. Shi, L. Miao, Z. Wang, and J. Luo, "Settlement behaviors of metro tunnels during the metro operation," *Shock and Vi*bration, vol. 2015, Article ID 863961, 11 pages, 2015.
- [17] P. Amado-Mendes, P. Alves Costa, L. M. C. Godinho, and P. Lopes, "2.5D MFS-FEM model for the prediction of vibrations due to underground railway traffic," *Engineering* Structures, vol. 104, pp. 141–154, 2015.
- [18] A. El Kacimi, P. K. Woodward, O. Laghrouche, and G. Medero, "Time domain 3D finite element modelling of train-induced vibration at high speed," *Computers & Structures*, vol. 118, pp. 66–73, 2013.
- [19] W. Gardien and H. G. Stuit, "Modelling of soil vibrations from railway tunnels," *Journal of Sound and Vibration*, vol. 267, no. 3, pp. 605–619, 2003.
- [20] T. Ekevid, H. Lane, and N. E. Wiberg, "Adaptive solid wave propagation-influences of boundary conditions in high-speed train applications," *Computer Methods in Applied Mechanics* and Engineering, vol. 195, no. 4, pp. 236–250, 2006.
- [21] S. H. Ju, "Finite element investigation of traffic induced vibrations," *Journal of Sound and Vibration*, vol. 321, no. 3, pp. 837–853, 2009.
- [22] L. Andersen and C. J. C. Jones, "Coupled boundary and finite element analysis of vibration from railway tunnels—a comparison of two- and three-dimensional models," *Journal of Sound and Vibration*, vol. 293, no. 3–5, pp. 611–625, 2006.
- [23] T. Real, C. Zamorano, F. Ribes, and J. I. Real, "Train-induced vibration prediction in tunnels using 2D and 3D FEM models in time domain," *Tunnelling and Underground Space Technology*, vol. 49, pp. 376–383, 2015.
- [24] K. Vogiatzis, "Environmental ground borne noise and vibration protection of sensitive cultural receptors along the Athens Metro Extension to Piraeus," *Science of the Total Environment*, vol. 439, pp. 230–237, 2012.

[25] Y. Tang, H. Zhao, Y. Wang et al., "Characteristics of strain accumulation of reinforced soft clay around tunnel under subway vibration loading," *Journal of Tongji University*, vol. 39, no. 7, pp. 972–977, 2011.

- [26] S. G. Newton and R. A. Clark, "An investigation into the dynamic effects on the track of wheelflats on railway vehicles," *Journal of Mechanical Engineering Science*, vol. 21, no. 4, pp. 287–297, 1979.
- [27] S. Timoshenko, Vibration Problems in Engineering, John Wiley & Sons, Hoboken, NJ, USA, 4th edition, 1974.
- [28] Z. Shijian, J. Lou, and Q. He, Vibration Theory and Vibration Isolation Technology, National Defense Industry Press, Beijing, China, 2006.
- [29] Z. Y. Shen, J. K. Hedrick, and J. A. Elkins, "A comparison of alternative creep force models for rail vehicle dynamic analysis," *Vehicle System Dynamics*, vol. 12, no. 1–3, pp. 79–83, 1983.
- [30] J. A. Priest and W. Powrie, "Determination of dynamic track modulus from measurement of track velocity during train passage," *Journal of Geotechnical and Geoenvironmental Engineering*, vol. 135, no. 11, pp. 1732–1740, 2009.
- [31] International Standard, Mechanical Vibration and Shock Evaluation of Human Exposure to Whole-Body Vibration, ISO 2631-1, Vol. 5, International Organization for Standardization, Geneva, Switzerland, 1997.
- [32] X. Sun, Prediction of Environment Vibrations Induced by Metro Trains and Mitigation Measures Analysis, Beijing Jiaotong University, Beijing, China, 2008.
- [33] F. Kang and J. Zhang, The Application of ABAQUS in Geotechnical Engineering, China Water & Power Press, Beijing, China, 2010.
- [34] B. O. Hardin and V. P. Drnevich, "Shear modulus and damping in soils: design equations and curves," *Journal of Soil Mechanics and Foundations Division*, vol. 98, no. 7, pp. 667–692, 1972.

Hindawi Shock and Vibration Volume 2018, Article ID 6853047, 12 pages https://doi.org/10.1155/2018/6853047

Research Article

Wind-Induced Response of Inclined and Yawed Ice-Accreted Stay Cable Models

Songyu Cao, Himan Hojat Jalali , and Elena Dragomirescu

Correspondence should be addressed to Elena Dragomirescu; elndrag@uottawa.ca

Received 23 March 2018; Revised 1 August 2018; Accepted 5 September 2018; Published 9 October 2018

Academic Editor: Tai Thai

Copyright © 2018 Songyu Cao et al. This is an open access article distributed under the Creative Commons Attribution License, which permits unrestricted use, distribution, and reproduction in any medium, provided the original work is properly cited.

During the past decades, wind-induced vibrations of bridge stay cables were reported to occur under various incipient conditions. The ice formation on stay cables is one of these conditions, which causes the ice-accreted stay cables to alter their cross section geometry, thus modifying their aerodynamic characteristics. Wind tunnel tests and several CFD simulations were performed for ice-accreted inclined bridge stay cables with two ice-accretion profiles dimensions, 0.5D and 1D, where D is the diameter of the cable. Wind-induced vibrations were analyzed experimentally for cable models with yaw inclination angles of 0° , 30° , and 60° and vertical inclination angles of 0° and 15° , for Reynolds numbers of up to 4×10^{5} . The aerodynamic drag and lift coefficients of the cable models and the pressure coefficients were determined from the CFD-LES simulations. The experimental results indicated that the vertical and torsional vibrations of the ice-accreted stay cables increased with the increase of the vertical and yaw angles. Also, higher vertical and torsional vibration amplitudes were measured for the case with larger ice thickness, indicating the effect of the ice accretion profile on the cable wind-induced response.

1. Introduction

Cable-stayed bridges are among the most reliable and complex bridge structures, and their ability to support long spans make them an ideal solution for spanning large distances over bay or valley regions with high vehicular traffic. One of the main concerns when designing such bridges is related to the wind-induced effect on the bridge decks and towers. However, during the past decades, large-amplitude vibrations of stay cables have been reported [1-7]. These vibrations can tamper with the safety and serviceability of cable-stayed bridges and can cause unexpected fatigue failures at the cable anchor points. The causes for the stay cable vibrations vary in nature, such as rain-wind induced vibrations [5, 8], dry inclined cable galloping [2, 9-12], and high-speed vortex excitation [8, 13, 14]. Another type vibration has been reported in recent years for bridge stay cables with ice accretion, when sudden large-amplitude wind

and ice accretion-induced vibrations were noticed [15-18]. For this phenomenon, the ice accumulates on the stay cable surface under freezing rain, drizzle, and wet or dry snow conditions at low temperatures. The formed ice accretion changes the cross-sectional shape of the cables, which in turn can cause aerodynamic instability [19]. Several field studies reported vibrations of stay cables in freezing conditions, which caused the ice to detach from the cables and fall on the passing vehicles. The Port Mann Bridge in Canada was temporarily closed to traffic in 2012 because of the iceaccreted cable vibrations and due to the ice falling from the stay cables causing a hazard for the traffic and people on the bridge. The Tacoma Narrows Bridge in USA was temporarily closed in 2011, due to similar hazards caused by the falling ice from the cables. Similar phenomena of ice falling from cables were reported for other bridges as well, such as the Alex Fraser Bridge in 2016, Canada; the Great Belt East Bridge, Denmark [20]; and the Severn Bridge in UK [21].

¹Key Laboratory of Transportation Tunnel Engineering, Ministry of Education, Southwest Jiaotong University, Chengdu 610031, Sichuan, China

²Civil Engineering Department, University of Texas at Arlington, 425 Nedderman Hall, 416 Yates St., Arlington, TX 76019, USA ³Faculty of Engineering, University of Ottawa, 161 Louis Pasteur, Ottawa, ON K1N 6N5, Canada

In an attempt to clarify the onset conditions for the iceaccreted cable vibrations, Koss and Matteoni [22] conducted a wind tunnel experiment for determining the effect of ice accretion on the aerodynamic forces, recorded for full-scale cables under 0° angle of attack and Re numbers of up to 3.2×10^5 , using the FORCE/DTU climatic wind tunnel (CWT). Also Koss et al. [23] performed an experimental investigation for determining the shape of the ice accretion formed on cables of 0.0381 m and 0.089 m in diameter, that were oriented in horizontal and vertical directions, for different exposure times and air temperatures. They classified the regions of the ice accretion profiles into the core, center area, outer area, flow-out, flow-out accumulation, and runback. The effect of the ice accretion on the aerodynamics of the vertical bridge hangers was investigated by Gjelstrup et al. [20] using static and dynamic wind tunnel tests. The aerodynamic coefficients were determined for smooth and rough surfaces of the ice-accreted cables, under smooth and turbulent wind flow conditions. Furthermore, Koss and Lund [24] presented the results of a full-scale experimental study on horizontal 160 mm diameter bridge cables, under wet and dry ice accretion conditions, using an innovative spray system to determine the aerodynamic coefficients and to evaluate the galloping instability using the Den Hartog criterion. Moreover, Koss et al. [25] studied the formation of ice accretion on three full-scale horizontal bridge cables with plain, helical fillet, and indented high density polyethylene (HDPE) cover, under wet and dry climatic conditions, and they concluded that gravity plays a major role in the ice profile formation on the cables under the wet icing condition. Also, this study indicated that only the cable with plain HDPE cover was susceptible to galloping instability, as per the Den Hartog criterion. Demartino et al. [19] extended this study to full-scale HDPE vertical and inclined bridge cables, and they investigated the process of ice accretion formation, the final ice shape, and the corresponding aerodynamic drag, lift, and moment coefficients for different parameters such as temperature, wind speed, and yaw angle. Using the experimental data of Demartino et al. [19], Demartino and Ricciardelli [26] modelled different galloping vibrations for one degree of freedom (1-DOF) and multiple degrees of freedom (MDOF) cables, and they analyzed the stability of bridge cables with ice accretion. Results showed that the 1-DOF models usually generate conservative results, and the use of dynamic wind tunnel experiments was recommended to confirm the results of existing theoretical models, especially for the cases where no sufficient data are available.

However, the actual wind-induced vibrations for the inclined and yawed cables in regard to the wind direction, which are very often encountered in practise, with ice accretion attached to their surface, were not specifically investigated. The current study examines the aerodynamic behavior of yawed and inclined ice-accreted stay cables. The stay cable models had vertical inclination angles of 0° and 15° and yaw angles of 0°, 15°, 30°, and 60°, while the ice accretion profile thickness were 0.5D and 1.0D. Wind tunnel wind speeds between 1.5 m/s and 15 m/s were considered to identify the critical wind-induced cable vibrations.

2. Experimental Set-Up and Cable Model Configuration

The experimental program was performed in the suction wind tunnel facility of the University of Ottawa, Department of Mechanical Engineering (Figure 1(a)), which has a testing section of 61 cm \times 92 cm, and has three openings on each side of the testing section, used for installing the models and to coordinate the necessary vertical and yaw inclination angles for the cable models. The maximum wind speed which can be achieved in the wind tunnel is 30.0 m/s; however, for the current experiment, the ice-accreted cable was tested for wind speeds of up to 15.0 m/s, corresponding to a Reynolds number of 4.0×10^5 , considering the high amplitude vibrations developed beyond these testing conditions. The wind speed varied during the tests from 1.5 m/s to 15.0 m/s, in steps of 1.5 m/s. The blockage ratio was determined as the total area of the model normal to the free stream velocity divided by the total area of the test section and was found to be 0.368×10^{-3} and 0.736×10^{-3} , for the cable models with 1.0 cm and 2.0 cm ice profiles, respectively. According to West and Apelt [27], if the blockage ratio is lower than 6%, for smooth cylinders with aspect ratios in the range of 4 to 10, the Strouhal number is not affected and no correction is needed for the aerodynamic coefficients; hence, the turbulence intensity would not be a significant concern.

An important parameter which can significantly affect the wind-induced response of the cable models during the wind tunnel tests is the relative angle of attack between the wind direction and the cable axis. Therefore, the wind-cable relative angle, as defined by Cheng et al. [2], was employed in the current research, that is, $\theta = \cos^{-1}(\cos \alpha \cos \beta)$, where θ , α , and β represent the relative wind-cable angle, yaw, and vertical cable inclination angles, respectively (Figure 1(b)). To simulate the wind-induced vibrations of the cables, eight supporting springs, each of elastic constant k = 1.5 N/m, were installed symmetrically at the two ends of the cables along the vertical direction, as schematically represented in Figure 1(b). Also the position of the cable models was adjusted using the three circular openings in the wind tunnel lateral wall and by moving the entire spring support system installed outside the tunnel to adjust for different vertical and yaw angles of attack, as shown in Figures 2(a) and 2(b). For flow perpendicular to the cylinder at 0° yaw, the same location openings were used for installing the model (Figure 2(c)), while for bigger yaw and vertical angles, the cable model was installed between the middle and the last opening with an elevation difference between the spring support systems (Figure 2(d)).

The cable models were scaled to 1:45 from the prototype bridge cable used by Cheng et al. [2] for the full-scale wind tunnel experiments conducted for the smooth surface inclined and yawed cylinders. Ice accretion profiles with a thickness of 0.5D and 1D, where D is the diameter of the cable model, were added on one side of the cable models. These dimensions correspond, respectively, to a cable ice accretion thickness of 45 cm (0.5D) and 90 cm (1D), considering the 1:45 scale factor. According to Koss et al. [23] exposing the cable for 1,800 seconds to precipitations under freezing conditions, the ice accretion profile thickness can

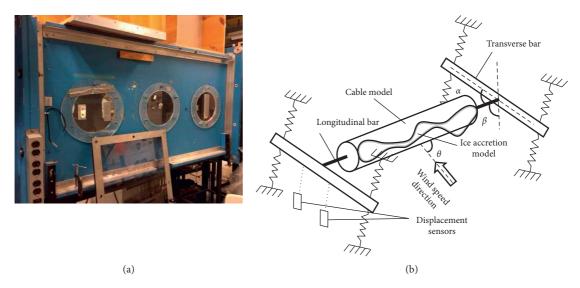


FIGURE 1: (a) Suction wind tunnel facility; (b) spring suspension system.

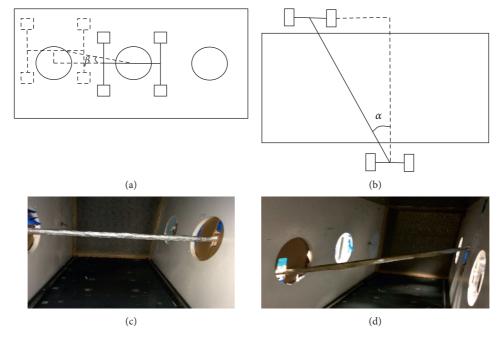


FIGURE 2: Cable models configuration in the wind tunnel facility: (a) front view; (b) top view; (c) $\alpha = \beta = 0^{\circ}$; (d) $\alpha = 60^{\circ}$ and $\beta = 15^{\circ}$.

reach up to 0.5D. The ice accretion profiles with thicknesses of 0.5D and 1.0D were both tested in the current experiment, for clarifying the critical ice-accreted cable response. In order to replicate the arbitrary aspect of the ice profile, expandable foam was applied on the cable model. The ice accretion simulated by foam showed good geometrical agreement with the models obtained from the climatic wind tunnels reported in the literature [23], especially for the troughs and crests of the ice accretion. However, the foam also developed small gaps and indentations; the entire ice profile was corrected by applying aluminium foil, and thus, the cable model and the foam ice accretion could better resemble the ice surface smoothness, as it can be seen in Figures 3(a) and 3(b).

Three cable models were tested for vertical and yaw inclinations between 60° and 15° as follows (Table 1): Cable Model 1 (CM1) was the cable perpendicular to the flow (0°) and had an aspect ratio of 46, a natural frequency of 0.395 Hz, and a Scruton number of 2.1. This model was also used for 15° yaw angle tests; Cable Model 2 (CM2) was used for vertical angles of 30° and 60° and for yaw angles of 0° and 15° ; this had an aspect ratio of 53.5, a natural frequency of 0.33 Hz, and a Sc = 5.1. For Cable Model 3 (CM3), the aspect ratio was 92, and the natural frequency was 0.29 Hz while the Sc number was 10.5. This cable model was used for tests with 0° , 30° , and 60° vertical angles and 0° and 15° yaw angles. The yaw and vertical inclination angles were varied by changing the location of the model, from the middle opening to the last or

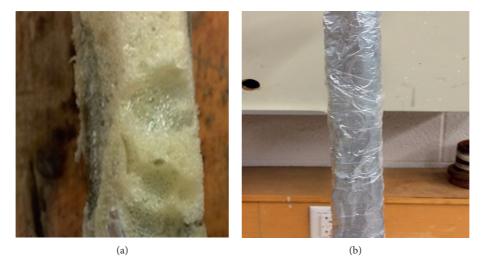


FIGURE 3: Bridge cable model with 1.0D ice accretion: (a) initial foam model; (b) foam and aluminium foil model.

Cable model	Yaw angle, α (°)	Vertical angle, β (°)	Relative angle, θ (°)	Ice thickness (D)	Damping ratio (%)	Frequency (Hz)	Scruton number	Aspect ratio
CM1	0	0	0	0.5D and 1.0D	0.76	0.395	2.1	46
CM1	0	15	15	0.5D and 1.0D	0.76	0.395	2.1	46
CM2	30	15	33	0.5D	2.4	0.330	5.1	53.5
CM2	30	0	30	0.5D and 1.0D	2.4	0.330	5.1	53.5
CM3	60	0	60	0.5D	3.8	0.290	10.5	92
CM3	60	15	61	0.5D	2 0	0.200	10.5	02

TABLE 1: Characteristics of the tested cable models.

first opening, as represented in Figure 3. Table 1 summarizes the experiments performed for different yaw and vertical inclination angles. The ice accretion profile of 0.5D was tested for all three cable models, at yaw inclination angles (α) of 0°, 30°, and 60° and vertical inclination angles (β) of 0° and 15°. Since 1.0D is considered as an extreme case of the ice accretion thickness, more tests were performed for the 0.5D ice accretion profile, which is more often encountered.

3. Vertical and Torsional Wind-Induced Vibrations of Ice-Accreted Cables

3.1. Effect of Ice Accretion Thickness. The torsional and vertical vibrations for the ice accreted cables were recorded for different wind speeds, from 1.5 m/s to 15 m/s at intervals of 1.5 m/s. Figure 4 shows the response time histories for the vertical and rotational vibrations, for the CM1 cable model at 0° relative angle, with an ice accretion thickness of 0.5D. The maximum vertical and torsional responses were measured as 23.92 mm and 2.63°, respectively. For the model CM1 at 0° relative angle, with 1.0D ice thickness, Figure 5 reports the vertical and torsional vibrations at 15 m/s, for which the maximum vertical displacement was 21.95 mm, while the maximum torsional displacement was 5.8°. It is interesting to note that despite the slight decrease in the maximum vertical displacements recorded for the CM1 at 0°, with 1.0D ice thickness, the maximum torsional response increased by a factor of 2.1, when compared with the CM1 model with 0.5D ice thickness.

Figure 6 presents the time histories of vertical and torsional response of the cable for model CM2, inclined at relative angle $\theta=30^\circ$, for the wind speed of 15 m/s. In this case, the maximum vertical displacements due to wind-induced vibration were recorded as 21.94 mm at 14.8 s; the maximum vibration amplitude for torsional displacement was 3.13° at 41 s. The torsional vibration was increasing steadily, but no strong fluctuations were noticed for this case. For higher ice accretion thickness, of 1.0D, the cable model CM2 registered vertical displacement with the maximum value of 27.3 mm, while the mean value for this case was 20.66 mm (Figure 7(a)). The maximum amplitude of the torsional vibration was 7.3°, as it can be noticed in Figure 7(b), and the average value for this case was 3.3°.

For clarifying the effect of the ice accretion effect on the mean vertical displacement of the tested cables for different wind speeds, the response of the same inclination models, but with 0.5D and 1.0D ice accretion thickness, was compared in Figures 8(a)–8(c). As expected, the vertical displacements of all models increased with the increase of wind speed; for lower wind speeds of up to 3.0 m/s for CM1 at θ =0° and CM2 at θ =30° and up to 4.5 m/s for CM1 at θ =15°, the vertical response for the 0.5D cable models was consistent with the response of the 1.0D cable models; however, a sudden decrease in amplitude was noticed for the models with 0.5D ice accretion at 4.5 m/s for CM1 at θ =0° and at 6 m/s for at CM1 at θ =15° and CM2 at θ =30°, respectively. The cable models with 1.0D encounter a small decay in amplitudes at low wind speeds of 4.5 m/s for CM2 at

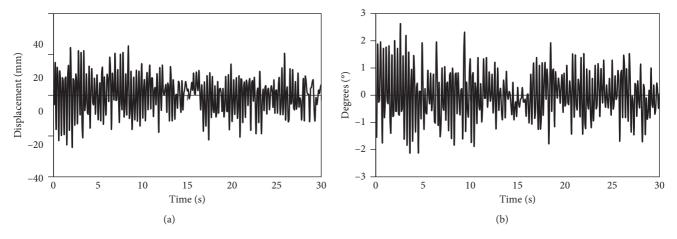


FIGURE 4: Time history responses for CM1, $\theta = 0^{\circ}$, 0.5(D), at 15 m/s: (a) vertical vibration; (b) torsional vibration.

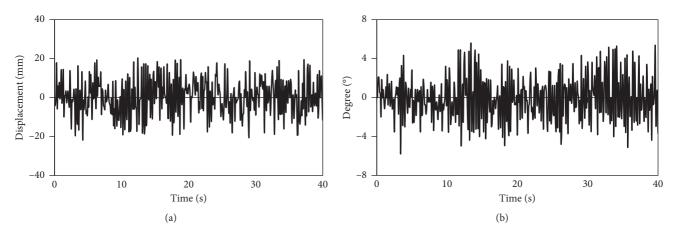


FIGURE 5: Time history responses for CM1, $\theta = 0^{\circ}$, 1.0(D), at 15 m/s: (a) vertical vibration; (b) torsional vibration.

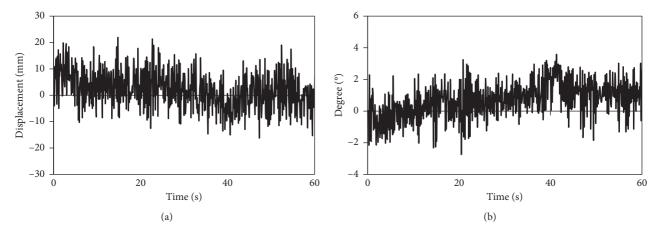


FIGURE 6: Time history responses for CM2, $\theta = 30^{\circ}$, 0.5(D), at 15 m/s: (a) vertical vibration; (b) torsional vibration.

 θ = 30° and at 7.5 m/s for CM1 at θ = 15°; however, for the cable model CM1 at θ = 0°, a sudden increase of amplitudes was noticed for 7.5 m/s. The vertical vibration response for the cables with 1.0D ice thickness was higher than that of the cable models with 0.5D ice thickness, especially for wind speeds higher than 9.0 m/s.

The mean torsional response for the cable model CM2 at $\theta = 30^{\circ}$ with 0.5D ice accretion thickness was more consistent with the mean torsional response of the same inclination cable model, CM2 at $\theta = 30^{\circ}$, but with 1.0D ice accretion, as it can be noticed in Figure 9(C); however, discrepancies were noticed for the other investigated cable models. For CM1 at

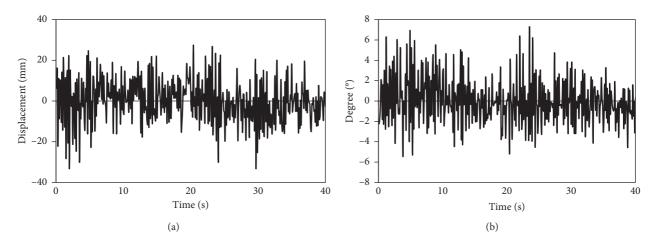


FIGURE 7: Time history responses for CM2, $\theta = 30^{\circ}$, 1.0(D), at 15 m/s: (a) vertical vibration; (b) torsional vibration.

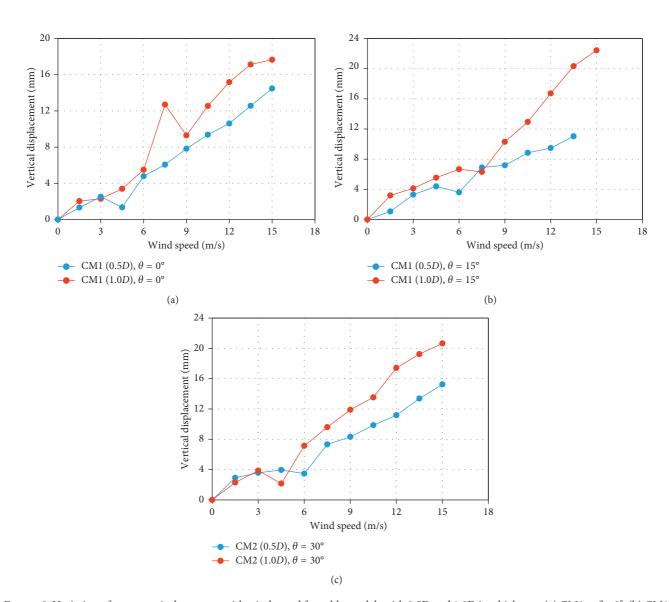


FIGURE 8: Variation of mean vertical response with wind speed for cable models with 0.5D and 1.0D ice thickness: (a) CM1 at $\theta = 0^{\circ}$; (b) CM1 at $\theta = 15^{\circ}$; (c) CM2 at $\theta = 30^{\circ}$.

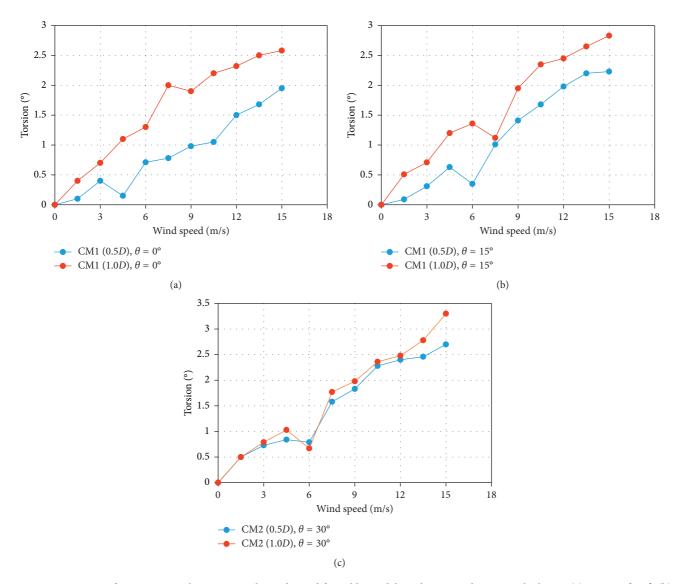


FIGURE 9: Variation of mean torsional response with wind speed for cable models with 0.5D and 1.0D ice thickness: (a) CM1 at $\theta = 0^{\circ}$; (b) CM1 at $\theta = 15^{\circ}$; (c) CM2 at $\theta = 30^{\circ}$.

 θ = 0° and CM1 at θ = 15°, the mean torsional response was higher for 1.0D ice accretion thickness, when compared with the 0.5D ice accretion models, for all the tested wind speeds (Figures 8(a) and 8(b)). Sudden decays in amplitude were still noticed for models with 0.5D ice thickness at lower wind speeds of 4.5 m/s and 6 m/s for the CM1 and CM2 models, respectively, while for 1.0D ice thickness models, the torsional response decay occurred at 7.5 m/s and 4.5 m/s for models CM1 and CM2, respectively.

3.2. Effect of Relative Angle. The average amplitudes for vertical and torsional vibrations were investigated for different relative angles of attack, θ , and it was noticed that the highest responses corresponded to the highest relative angles. For the cases with 0.5D ice accretion, the cable models CM3 at $\theta = 61^{\circ}$ and $\theta = 60^{\circ}$ showed the highest vertical and torsional responses (Figures 10(a) and 11(a)), which is similar to the critical cases reported by Cheng et al. [2] for

vertically and horizontally inclined stay cables, without ice accretion. Also for relative angles of 60° and 61°, the sudden decay of amplitude at lower wind speeds was not noticed. For the CM2 cable model, both vertical and torsional responses were smaller for wind speeds up to 3.0 m/s; however, from 4.5 m/s and up to 10.5 m/s, the responses for the model inclined at relative angle 33° were higher than the one registered for the model inclined at relative angle 30° (Figures 10(b) and 11(b)).

In general, for CM3 and CM2 models, the torsional and vertical mean responses were higher for higher relative angles; however, by comparing the magnitude of the recorded vibrations, it can be concluded that the vibrations were consistent with each other, for different wind speeds. For the CM1 model, the mean vertical response was higher for θ =0° at higher wind speeds between 9.0 m/s and 13.5 m/s and at 6 m/s (Figure 10(c)); the mean torsional response however was much higher for the CM1 model at θ =15° between wind speeds of 7.5 m/s and 15 m/s and at 6 m/s (Figure 11(c)).

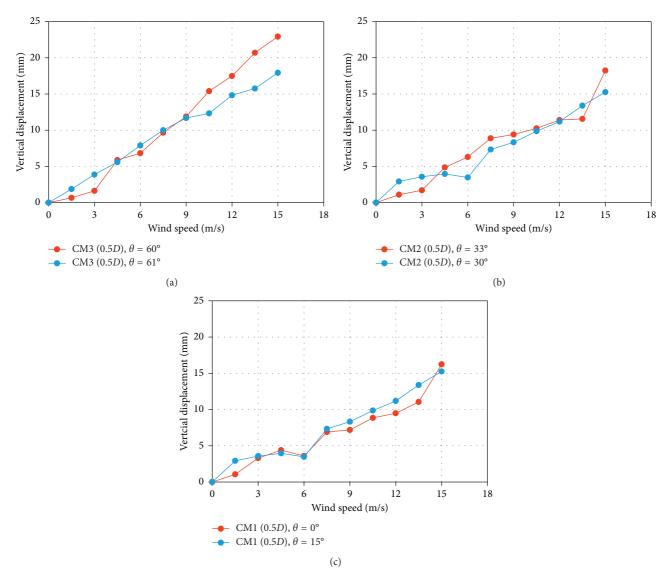


FIGURE 10: Variation of mean vertical response with wind speed for cable models with 0.5D ice thickness: (a) CM3 at $\theta = 60^{\circ}$ and $\theta = 61^{\circ}$; (b) CM2 at $\theta = 30^{\circ}$ and $\theta = 33^{\circ}$; (c) CM1 at $\theta = 0^{\circ}$ and $\theta = 15^{\circ}$.

3.3. Wind-Induced Response Frequency Analysis. In order to observe the variation of the response frequency under different wind speeds, Fast Fourier transform (FFT) was applied for the measured vertical vibrations and the dominant frequency for each response time history was identified. The spectral distribution obtained through the FFT analysis showed very small frequencies without a dominant peak for wind speeds lower than 3.0 m/s for CM1 at 0°, with 0.5D ice accretion, and for CM2 at 30°, with 1.0D ice accretion; frequencies difficult to identify were noticed for wind speeds lower than 4.5 m/s for models CM1 at 0° with 1.0D ice accretion and CM2 at 30° with 0.5D ice accretion, as represented in Figures 12(a) and 12(b).

The frequencies of the wind-induced response were higher for the models CM1 at 0° and CM2 at 30° models with higher ice accretion (1.0D), having a similar trend of slightly higher frequencies at 10.5 m/s and at 15 m/s. For 10.5 m/s wind speed, other peaks, of smaller intensity, were identified

in the FFT spectra, around frequencies of 0.025 Hz and 0.21 Hz for the model CM1 at 0° and 0.025 Hz for the model CM2 at 30°, both with 1.0D ice accretion (Figures 13(a) and 13(b)). For the 0.5D ice accretion, the two models, CM1 at 0° and CM2 at 30°, showed trends similar to each other, for the vertical response frequencies obtained at the wind speeds between 4.5 m/s and 15 m/s were (Figures 12(b)), with a slight increase at 6.0 m/s and a sudden decrease at 10.5 m/s, followed by an ascending frequency at 15 m/s, of up to 0.34 Hz for the model CM1 at 0° and up to 0.4 Hz for the model CM2 at 30°, both with 0.5D ice accretion. A second peak at 0.18 Hz was noticed only for the model CM2 at 30°, at 10.5 m/s (Figure 14(b)), while a single dominant frequency at 0.3303 Hz was signaled for the CM1 at 0° model.

Any changes of the frequency can indicate the change of the dynamic response of the cable model, under the effect of the increasing wind speed. As shown in Figures 8 and 10, a sudden decrease in the frequency response is observed at

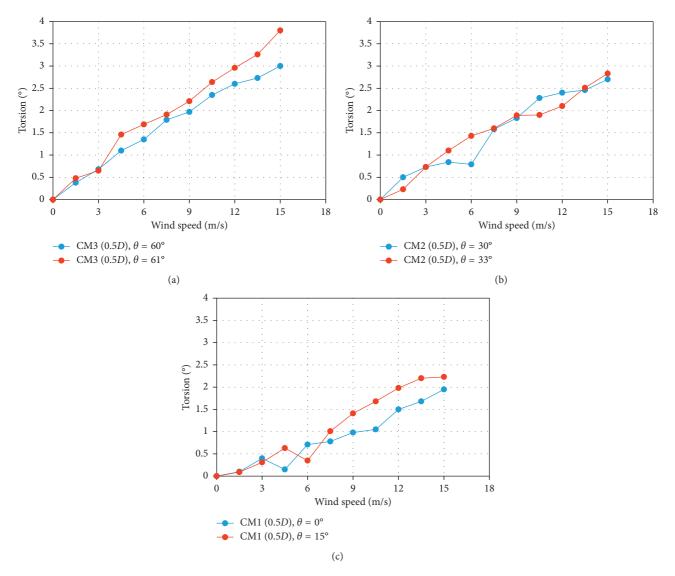


FIGURE 11: Variation of mean torsional response with wind speed for cable models with 0.5D ice thickness: (a) CM3 at $\theta = 60^{\circ}$ and $\theta = 61^{\circ}$; (b) CM2 at $\theta = 30^{\circ}$ and $\theta = 33^{\circ}$; (c) CM1 at $\theta = 0^{\circ}$ and $\theta = 15^{\circ}$.

4.5 m/s for the models CM1 at θ = 0°, 0.5D, CM2 at θ = 30°, 1.0D, which corresponds to a low frequency point in the vertical vibration FFT shown in Figures 12(a) and 12(b), for the same wind speed. Similarly, for other models, such as CM1 at θ = 15°, 0.5D and 1.0D, and CM2 at θ = 30°, 0.5D, the sudden decrease of the vertical response occurred at 6.0 m/s (Figures 8 and 10), which correspond to a low frequency point as well (Figure 12).

In order to compare the frequencies for the wind-induced response recorded at different wind speeds, for cable models with 0.5D and 1.0D ice accretion profiles, the variation of the Strouhal number for the aforementioned cases was investigated. The Strouhal number was determined as $St = fD_{\rm eq}/U$, where f, $D_{\rm eq}$, and U are the frequency of the vertical response, and the equivalent diameter of each cable model was exposed to the wind direction and the mean wind speed, respectively. It should be noted that the thickness of the ice accretion on the cable and the relative cable-wind direction angle were considered in estimating the equivalent

cable diameter, $D_{\rm eq}$, for the Strouhal number calculation, as shown in Equation (1). Also, $D_{\rm eq}$, in Equation (1), is the equivalent cable diameter considering the ice thickness and relative cable-wind direction angle; D_c and h_i are the cable diameter and mean thickness of the ice profile, respectively, while θ is the relative wind-cable direction angle:

$$D_{\text{eq}} = (D_c + h_i) \times \cos(\theta). \tag{1}$$

Figure 15 shows that despite the frequency variations indicated in Figure 10, the normalized frequencies (Strouhal numbers) for all the performed cases decreased with the increase of wind speed, as expected. Also Figure 15 shows that, for different relative wind-cable angles, the normalized frequencies for the cases with the same ice thickness were almost identical. According to Hao [28], the galloping divergent vibration can occur for Strouhal numbers lower than 0.05, the value corresponding to the horizontal dashed line in Figure 15, showing the incipient conditions from which the galloping divergent vibration

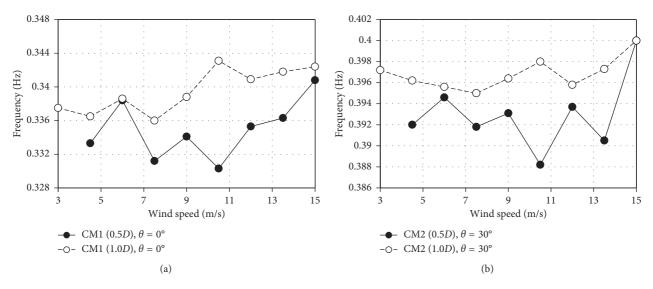


FIGURE 12: Vertical vibrations frequencies for models with 0.5D and 1.0D ice accretion: (a) CM1 (θ = 0°); (b) CM2 (θ = 30°).

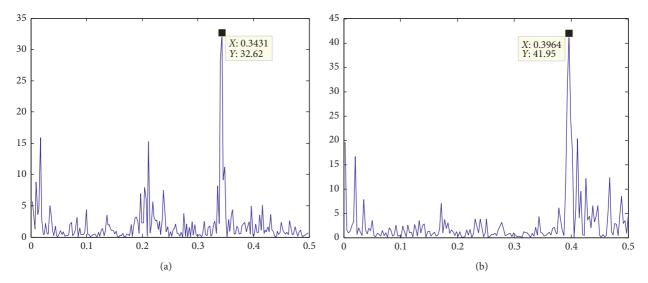


FIGURE 13: FFT distribution of frequencies for models with an ice thickness of 1.0D at 10.5 m/s for (a) CM1 ($\theta = 0^{\circ}$) and (b) CM2 ($\theta = 30^{\circ}$).

could occur, for both cable models, with 0.5D ice accretion and with 1.0D ice accretion, from wind tunnel wind speeds as low as 3.0 m/s.

The critical wind speed, after which galloping instability can be expected, for all cable models tested can be determined using Equation (2) [16, 29]. In Equation (2), $U_{\rm crit}$, f, D, and S_c are critical wind speed, natural frequency of the fundamental mode of vibration, cable diameter, and the Scruton number, respectively:

$$U_{\rm crit} = 40 f D \sqrt{S_c}.$$
 (2)

Using Equation (2), the critical wind speeds were determined spanned between 4.5 m/s and 10.5 m/s for the models CM1 at $\theta = 0^{\circ}$ with 0.5D and CM3 at $\theta = 61^{\circ}$ with 1.0D, respectively. These wind speeds coincide with the sudden changes in the vertical response frequencies presented in Figures 8 and 10, showing that the higher wind-induced response occurred at different wind speeds, depending on

the relative angle of attack and the thickness of the ice profile tested.

4. Conclusions

Cable-stayed bridges stability rely on all the structural members composing these massive structures, and the stay cables, which are the most flexible elements of the bridge, and have a significant role in the overall bridge design. The wind tunnel experiment performed for cables with ice accretion reported herewith clarifies some aspects related to the wind-induced response for the ice-accreted bridge yawed and inclined stay cables. Different parameters such as the vertical inclination angle (0° and 15°), yaw angle (0°, 15°, 30°, and 60°), ice accretion profile thickness (0.5D and 1.0D), and wind tunnel wind speed (1.5 to 15 m/s) were considered. The increase of ice accretion thickness was shown to increase the wind-induced response, especially for wind speeds higher

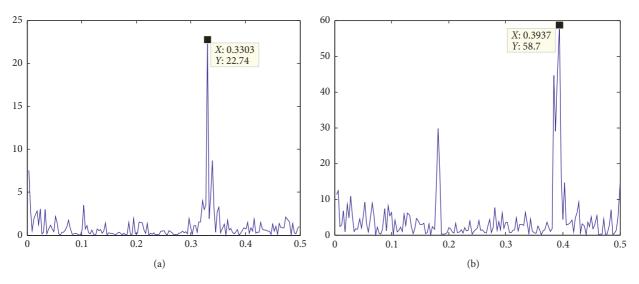


FIGURE 14: FFT distribution of frequencies for models with an ice thickness of 0.5D at 10.5 m/s for (a) CM1 ($\theta = 0^{\circ}$) and (b) CM2 ($\theta = 30^{\circ}$).

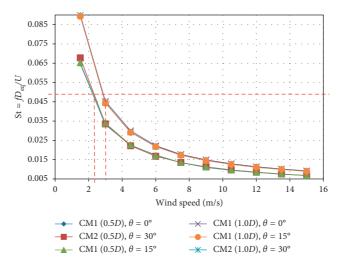


Figure 15: Normalized frequency (St = fD_{eq}/U) for the vertical vibrations.

than 4.5 m/s. Both vertical and torsional displacements increased with the increase of the relative angles of attack; however, the investigated angles did not determine a significant increase of the wind-induced response for the 0.5D and 1.0D ice-accreted stay cables. Also, at certain wind speeds, the vibration for the cables with higher inclination angles was smaller than the cases with lower inclinations; however, for wind speeds beyond 7.5 m/s, the response of the cables with higher inclination angles surpassed the case with lower inclination angles. A sudden decrease in the vertical vibration occurred for models CM1 at $\theta = 0^{\circ}$, 0.5D, CM2 at $\theta = 30^{\circ}$, 1.0D, and CM2 at $\theta = 33^{\circ}$, 1.0D, for wind tunnel wind speeds of 4.5 m/s, for which the frequency analysis showed lower frequency points. A similar decrease in response was noticed at wind speeds of 6.0 m/s and above, for models CM1 at $\theta = 15^{\circ}$, 0.5D and 1.0D, and CM2 at $\theta = 30^{\circ}$, 0.5D. The frequency analysis showed multiple vibration values for the vertical wind-induced response between wind speeds 4.5 m/s and 9.0 m/s for models with 0.5D ice accretion and between

wind speeds of 7.5 m/s and 15 m/s for models with 1.0D ice accretion, which can be an indication of an aerodynamic instability.

Data Availability

The data supporting the current research project can be found at CVG Department, University of Ottawa, and can be made available if necessary by the authors.

Conflicts of Interest

The authors declare that they have no conflicts of interest.

Acknowledgments

This work was supported by the Natural Sciences and Engineering Research Council of Canada (NSERC), Discovery Grant 06776, 2015.

References

- [1] M. Matsumoto, H. Shirato, T. Yagi, M. Goto, S. Sakai, and J. Ohya, "Field observation of th full-scale wind-induced cable vibration," *Journal of Wind Engineering and Industrial Aerodynamics*, vol. 91, no. 1-2, pp. 13–26, 1995.
- [2] S. Cheng, G. L. Larose, M. G. Savage, H. Tanaka, and P. A. Irwin, "Experimental study on the wind-induced vibration of a dry inclined cable–part I: phenomena," *Jour*nal of Wind Engineering and Industrial Aerodynamics, vol. 96, no. 12, pp. 2231–2253, 2008.
- [3] M. Raoof, "Free-bending fatigue life estimation of cables at points of fixity," *Journal of Engineering Mechanics*, vol. 118, no. 9, pp. 1747–1764, 1992.
- [4] J. Druez, S. Louchez, and P. McComber, "Ice shedding from cables," *Cold Regions Science and Technology*, vol. 23, no. 4, pp. 377–388, 1995.
- [5] D. Zuo and N. P. Jones, Stay-cable Vibration Monitoring of the Fred Hartman Bridge (Houston, Texas) and the Veterans Memorial Bridge (Port Arthur, Texas), Center for Transportation Research, Bureau of Engineering Research, University of Texas at Austin, Austin, TX, USA, 2005.
- [6] A. Davenport, "Buffeting of a suspension bridge by storm winds," *ASCE Journal of Structural Division*, vol. 88, no. 3, pp. 233–268, 1962.
- [7] D. H. Yeo and N. P. Jones, "Computational study on 3-D aerodynamic characteristics of flow around a yawed, inclined, circular cylinder," NSEL Report Series, Report No. NSEL-027, University of Illinois at Urbana-Champaign, Champaign, IL, USA, 2011.
- [8] M. Matsumoto, N. Shiraishi, and H. Shirato, "Rain-wind induced vibration of cables of cable-stayed bridges," *Journal of Wind Engineering and Industrial Aerodynamics*, vol. 43, no. 1–3, pp. 2011–2022, 1992.
- [9] M. Matsumoto, T. Yagi, H. Hatsudab, T. Shimac, M. Tanakad, and H. Naitoa, "Dry galloping characteristics and its mechanism of inclined/yawed cables," *Journal of Wind Engineering* and Industrial Aerodynamics, vol. 98, no. 6-7, pp. 317–327, 2010
- [10] Q. Liu, F. Zhang, M. Wenyong, and W. Yi, "Experimental study on Reynolds number effect on dry cable galloping of stay cables," in *Proceedings of the 13th International Con*ference on Wind Engineering, Amsterdam, Netherlands, July 2011.
- [11] J. H. G. Macdonald and G. L. Larose, "A unified approach to aerodynamic damping and drag/lift instabilities, and its application to dry inclined cable galloping," *Journal of Fluids and Structures*, vol. 22, no. 2, pp. 229–252, 2006.
- [12] M. S. Hoftyzer and E. Dragomirescu, "Numerical investigation of flow behaviour around inclined circular cylinders," in *Proceedings of the Fifth International Symposium on Computational Wind Engineering (CWE2010)*, Chapel Hill, NC, USA, May 2010.
- [13] M. Matsumoto, Y. Shigemura, Y. Daito, and T. Kanamura, "High speed vortex shedding vibration of inclined cables," in Proceedings of the Second International Symposium on Cable Dynamics, pp. 27–35, Tokyo, Japan, October 1997.
- [14] W. Martin, E. Naudascher, and I. Currie, "Streamwise oscillations of cylinders," *Journal of the Engineering Mechanics Division*, vol. 107, pp. 589–607, 1981.
- [15] H. Tabatabai, Inspection and Maintenance of Bridge Stay Cable Systems, NCHRP Synthesis 353, National Cooperative Research Program, Transportation Research Board, 2005.

[16] S. Kumarasena, N. P. Jones, P. Irwin, and P. Taylor, Wind-Induced Vibration of Stay Cables, US Department of Transportation, Federal Highway Association, Publication No. FHWA-RD-05-083, Washington, DC, USA, 2007.

- [17] N.J. Gimsing and C.T. Georgakis, Cable Supported Bridges: Concept and Design, Wiley, Chichester, England, 2011.
- [18] P. McComber and A. Paradis, "A cable galloping model for thin ice accretions," *Atmospheric Research*, vol. 46, no. 1-2, pp. 13–25, 1998.
- [19] C. Demartino, H. H. Koss, C. T. Georgakis, and F. Ricciardelli, "Effects of ice accretion on the aerodynamics of bridge cables," *Journal of Wind Engineering and Industrial Aerodynamics*, vol. 138, pp. 98–119, 2015.
- [20] H. Gjelstrup, C. T. Georgakis, and A. Larsen, "An evaluation of iced bridge hanger vibrations through wind tunnel testing and quasi-steady theory," Wind and Structures An International Journal, vol. 15, no. 5, pp. 385–407, 2012.
- [21] L. J. Vincentsen and P. Lundhus, *The Øresund and the Great Belt links—Experience and Developments*, IABSE SymposiumWeimar, Germany, 2007.
- [22] H. H. Koss and G. Matteoni, "Experimental investigation of aerodynamic loads on iced cylinders," in *Proceedings of 9th International Symposium on Cable Dynamics*, Shanghai, October 2011.
- [23] H. H. Koss, H. Gjelstrup, and C. T. Georgakis, "Experimental study of ice accretion on circular cylinders at moderate low temperatures," *Journal of Wind Engineering and Industrial Aerodynamics*, vol. 104–106, pp. 540–546, 2012.
- [24] H. H. Koss and M. S. M. Lund, "Experimental investigation of aerodynamic instability of iced bridge sections," in *Pro*ceedings of 6th European and African Conference on Wind Engineering, Robinson College, Cambridge, UK, July 2013.
- [25] H. H. Koss, J. F. Henningsen, and I. Olsenn, "Influence of icing on bridge cable aerodynamics," in *Proceedings of Fif*teenth International Workshop on Atmospheric Icing of Structures, St.John's, Newfoundland and Labrador, Canada, September 2013.
- [26] C. Demartino and F. Ricciardelli, "Aerodynamic stability of ice-accreted bridge cables," *Journal of Fluids and Structures*, vol. 52, pp. 81–100, 2015.
- [27] G. S. West and C. J. Apelt, "The effects of tunnel blockage and aspect ratio on the mean flow past a circular cylinder with Reynolds numbers between 104 and 105," *Journal of Fluid Mechanics*, vol. 114, no. 1, pp. 361–377, 1982.
- [28] H. Hao, "The galloping phenomenon and its control of bridges," Master's thesis, Chang'an University, Xi'an, China, 2010, in Chinese.
- [29] T. Saito, M. Matsumoto, and M. Kitazawa, "Rain-wind excitation of cables on cable- stayed Higashi-Kobe bridge and cable vibration control," in *Proceedings of the International Conference on Cable-Stayed and Suspension Bridges*, pp. 507–514, AFPC, Deauville, France, 1994.

Hindawi Shock and Vibration Volume 2018, Article ID 9106404, 12 pages https://doi.org/10.1155/2018/9106404

Research Article

Reliability and Random Lifetime Models of Planetary Gear Systems

Peng Gao (1), 1,2 Liyang Xie (1), 3 and Wei Hu⁴

Correspondence should be addressed to Peng Gao; gaopeng@lnpu.edu.cn

Received 26 April 2018; Revised 4 July 2018; Accepted 26 July 2018; Published 12 September 2018

Academic Editor: Mohammad A. Hariri-Ardebili

Copyright © 2018 Peng Gao et al. This is an open access article distributed under the Creative Commons Attribution License, which permits unrestricted use, distribution, and reproduction in any medium, provided the original work is properly cited.

Conventional reliability models of planetary gear systems are mainly static. In this paper, dynamic reliability models and random lifetime models of planetary gear systems are developed with dynamic working mechanism considered. The load parameters, the geometric parameters, and the material parameters are taken as the inputs of the reliability models and the random lifetime models. Moreover, failure dependence and dynamic random load redistributions are taken into account in the models. Monte Carlo simulations are carried out to validate the proposed models. The results show that the randomness of the load distribution is obvious in the system working process. Failure dependence has significant influences on system reliability. Moreover, the dispersion of external load has great impacts on the reliability, lifetime distribution, and redundancy of planetary gear systems.

1. Introduction

Planetary gear systems are widely used in technological systems, such as helicopters, cars, spacecraft, mining machineries, and so on, which have the advantages of compact structures, high transmission efficiency, and large transmission ratio. The load can be evenly distributed on planet gears to achieve the purpose of torque shunting. The normal operations of planetary gear systems are quite important for the safety and economy of technological systems. Hence, it is imperative to develop reliability models of planetary gear systems based on their practical working mechanism, environmental loads, and material properties.

Many efforts in reliability analysis of planetary gear systems have been made in the last few decades. Ye et al. developed a reliability-based optimization design method with stress and strength regarded as random variables. In their method, volume and efficiency were taken as the objective functions, while reliability and fatigue strength were set as boundary conditions. The reliability was calculated by the stress-strength interference (SSI) model [1–4]. Zhang

presented a reliability-based optimization design model, in which the design parameters were modeled as fuzzy variables and random variables [5]. Li et al. developed a reliability model of planetary gear systems in helicopters under the condition of partial loads with the effects of unequal load sharing considered [6]. Zhang introduced a method by combining floating-point encoding genetic algorithm with dynamic penalty function to improve the optimal design of planetary gear systems [7]. Wang developed a reliability model of planetary gear systems in wind power generators. In the literature, the SSI model was adopted with the contact force and the contact fatigue strength taken as the generalized stress and the generalized strength, respectively [8]. These innovative models provide a theoretical framework for reliability evaluation of planetary gear systems.

As a matter of fact, the operational process of a planetary gear system is dynamic and complex. At present, reliability models of planetary gear systems based on system working mechanisms are seldom reported. To analyze the reliability of planetary gear systems, the stress history and the strength degradation processes of the components in a system have to

¹School of Mechanical Engineering, Liaoning Shihua University, Liaoning 113001, China

²School of Mechanical Engineering and Automation, Zhejiang Sci-Tech University, Hangzhou 310018, China

³School of Mechanical Engineering and Automation, Northeastern University, Liaoning 110819, China

⁴Department of Industrial Design, Liaoning Shihua University, Liaoning 113001, China

be known. Currently, numerous dynamic models of planetary gear systems have been developed to analyze system motion characteristics. For instance, the spectral kurtosis technique was used by Barszcz and Randall to detect tooth cracks in a planetary gear system [9]. Kiracofe and Parker put forward compound analytical dynamic models for planetary gears [10]. Zhu et al. established dynamic models of planetary gear systems with both the flexibility of the pins and the gyroscopic effect taken into consideration [11]. These innovative models are quite effective for motion and dynamic characteristics analysis of planetary gear systems.

In general, many analytical dynamics models and dynamic simulation methods have been developed for dynamic analysis of planetary gears. Most of these models and methods are deterministic, which provide theoretical foundation for reliability analysis of planetary gears. However, they cannot be applied directly in reliability analysis. Many unique phenomena, such as failure dependence, stochastic strength degradation, and stochastic load redistribution, arise due to the emergence of dynamic random factors in the systems, which bring great difficulties in reliability modeling. Currently, reliability models of planetary gear systems are mainly static with components in a system regarded mutually statistically independent. The randomization of the data from deterministic dynamic models, associated with the mathematical treatments of these unique phenomena, has to addressed when developing dynamic reliability models of planetary gear systems. This is the reason why dynamic reliability models of planetary gears considering working mechanism are seldom reported. In this paper, we concentrate on constructing dynamic reliability models of planetary gear systems with their working mechanism taken into account by employing the existing dynamic simulation methods.

In addition, conventional lifetime estimation of planetary gear systems has to rely on material fatigue tests under stress with constant amplitude. It is quite difficult to consider the comprehensive effects including the randomness of load, structural and material parameters as well as the failure dependence, and random load distribution in lifetime assessment. These problems will be addressed via the proposed dynamic reliability models.

The structure of this paper is organized as follows: In Section 2, the system logic structure and the problems in modeling are introduced. The reliability and random lifetime models are derived in Section 3. Numerical examples are given in Section 4 to demonstrate the proposed models and identify key factors which have great influences on reliability and lifetime distribution of planetary gear systems. Conclusions are summarized in Section 5.

2. System Logic Structure and Stochastic Dynamic Stress

2.1. Stochastic Dynamic Stress. The structure of a typical planetary gear system is shown in Figure 1. A planetary gear system is usually composed of a sun gear, a carrier, a ring gear, and some planet gears. To obtain the component reliability, the SSI model is adopted with the static root stress computed by [12]

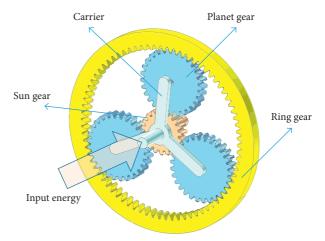


FIGURE 1: Structure of a planetary gear system.

$$s = \frac{2KT}{hd^2m} Y_1 Y_2 Y_3 Y_4,\tag{1}$$

where K, T, b, d, m, Y_1 , Y_2 , Y_3 , and Y_4 are load coefficient, torque on the gear, tooth width, diameter of dividing circle, normal modulus, tooth profile coefficient, stress correction coefficient, contact ratio factor, and helix angle coefficient, respectively. The equation is convenient in stress calculation. However, the working process of the planetary gear system is dynamic under fluctuant stress and the strength degrades under the dynamic stress. Therefore, the dynamic stress on each component should be calculated based the motion equations of the system and the material properties of the components.

The motion of the planetary gear systems is mainly analyzed via lumped parameter models as follows [13]:

$$M\ddot{X} + (C_1 + C_2 + 2wG)\dot{X} + KX = T,$$
 (2)

where X, M, C_1 , C_2 , $w \in K T$ represent the generalized coordinates of the system, the mass matrix, the support damping matrix, the meshing damping matrix, the angular velocity of the carrier, the gyro matrix, the system stiffness matrix including the support stiffness matrix, the meshing stiffness matrix and the centripetal stiffness matrix, and the external generalized load, respectively. Nevertheless, the stress on the components cannot be calculated directly in this way due to the lack of accurate geometric parameters of the components. Furthermore, despite the accuracy of the stress obtained via physical experiments, when considering the randomness of the load parameters and the material parameters, physical experiments are still infeasible for reliability estimation in practice. An alternative method to deal with this problem is to adopt the finite element method. In this paper, the stress is calculated by using the Adams software and the Ansys software [14]. The basic idea is to use the modal neutral file in the Ansys software to replace rigid bodies with flexible body in the Adams software [14]. Then the dynamic stress can be obtained via the simulations by using the Adams software. The motions of rigid bodies can be expressed as

$$M(q, t)\ddot{q} + \Phi \Xi_q^T(q, t)\lambda - Q(q, \dot{q}, t) = 0,$$

 $\Xi(q, t) = 0,$
(3)

where q is the generalized coordinate vector of the rigid bodies, λ is the lagrange multiplier, $Q(q, \dot{q}, t)$ is the generalized external forces on the rigid bodies, t is time, and Ξ is the constraint equations of the rigid bodies with respect to q. The motions of the flexible bodies can be calculated by [15]

$$M\ddot{q}_1 + \dot{M}\dot{q}_1 + Kq_1 + C\dot{q}_1 + \left[\frac{\partial\Omega}{\partial q_1}\right]^T q_1 - \frac{1}{2} \left[\frac{\partial M}{\partial q_1}\dot{q}_1\right] = Q_1,$$
(4)

where C is the mass matrix, q_1 is the generalized coordinate vector of the flexible bodies, Ω is the constraint equation of the flexible bodies with respect to q_1 , and Q_1 is the generalized external forces on the flexible bodies. The friction coefficient is expressed by [16]

$$\zeta = \begin{cases} \frac{b_1 + b_2}{2} + \frac{1}{2} \left[(b_2 - b_1) \cos \left(\pi \frac{|v_1| - v_2}{v_3 - v_2} \right) \right], & v_2 \le v_1 \le v_3, \\ b_1, & |v_1| > v_2, \\ b_2 \sin \left(\pi \frac{|v_1|}{2v_2} \right), & v_1 < v_2, \end{cases}$$
(5)

where v_1 , v_2 , and v_3 are the relative velocity, the stick-slip conversion velocity, and the static-sliding conversion velocity, respectively. b_1 and b_2 are the sliding friction coefficient and the static friction coefficient, respectively. The dynamic stress obtained after the simulations, which contributes to the fatigue failure of the gears in the system, is deterministic. In order to acquire the statistical characteristics of stress in each time interval, the following sample matrix has to be determined via a large number of simulations or tests:

$$\Gamma = \begin{bmatrix} \psi_{1}^{(1)} & \psi_{1}^{(2)} & \cdots & \psi_{1}^{(n)} \\ \psi_{2}^{(1)} & \psi_{2}^{(2)} & \cdots & \psi_{2}^{(n)} \\ \vdots & \vdots & \ddots & \vdots \\ \psi_{k}^{(1)} & \psi_{k}^{(2)} & \cdots & \psi_{k}^{(n)} \end{bmatrix},$$

$$\psi_{y}^{(y_{1})} = \begin{bmatrix} \psi_{y}^{(y_{1},1)}, & \psi_{y}^{(y_{1},2)}, & \dots, & \psi_{y}^{(y_{1},n_{1})} \end{bmatrix},$$

$$(y = 1, 2, \dots, k \cdot y_{1} = 1, 2, \dots, n),$$
(6)

where $\psi_y^{(y_1)}$ is the sample vector of the yth component in the y_1 th time interval and $\psi_y^{(y_1, y_2)}$ is the y_2 th stress sample of the yth component in the y_1 th time interval. Although the simulation method is much more efficient in sample acquisition than the method based on physical experiments, it is still quite time-consuming to obtain Γ considering the randomness of the input of the stress models, such as the input torque, input angular velocity, or the resistance torque on the output components. Nevertheless, provided that the

relationship between the inputs and the stress on each component is known, the process to gain Γ can be simplified. From the analysis above, it can be learnt that it is difficult to provide explicit mathematical equations to express the relationship. Thus, the response surface method [17] is used in this section to obtain Γ . The relationship between an input vector $\Theta = [\theta_1, \theta_2, \ldots, \theta_{k1}]$ ($\theta_{k1} = t$) and the stress s(t) on a component can be given by the following expression:

$$s(t) = \beta_0 + \sum_{i=1}^{k_1} \beta_i \theta_i + \sum_{i=1}^{k_1} \beta_{ii} \theta_i^2 + \sum_i \sum_j \beta_{ij} \theta_i \theta_j + \varepsilon.$$
 (7)

Equation (7) is a generalized expression of response surface methods. The stress in this paper refers to the Mises equivalent stress. Equation (7) is used to establish the relationship between the input vector $\Theta = [\theta_1, \ \theta_2, \ \dots, \ \theta_{k1}]$ and the output stress s(t) on a gear in a specified time interval. $\beta = [\beta_0, \ \beta_1, \ \dots, \beta_{k1}, \ \beta_{11}, \ \beta_{12}, \ \dots, \ \beta_{k1k1}]$ is the pending vector, which is obtained via the input samples of Θ and the corresponding output samples of s(t) by employing the dynamic simulations. ε is the higher-order omission item. The relationships between the input vector and the output stress on different gears have to be obtained separately by using Equation (7). After a limited number of simulations, this relationship can be determined through the regression method. Then, the stress distributions can be acquired directly via the distributions of the inputs as shown in Figure 2.

2.2. System Logic Structure. From the structures and the working mechanism of the planetary gear systems, it can be known that the failure of the sun gear, the carrier, or the ring gear could lead to the failure of the whole system. The remaining working duration of a planetary gear system after the failure of a planet gear depends on the material characteristics of the remaining planet gears, and the system can even work with less planet gears. In this case, the system can be viewed as a parallel system. However, the failure of a planetary gear system will speed up obviously after the failure of a planet gear due to the load redistribution. For the safety of the whole system, it is necessary to carry out maintenance or replacements after the partial failure of the system. Thus, the whole system is essentially a series-parallel system as shown in Figure 3.

In current reliability models or the models for reliabilitybased optimal design, the system reliability is always calculated according to classical reliability theory as follows:

$$R_{\text{sys}} = R_1 R_2 R_3 R_4, \tag{8}$$

where R_{sys} , R_1 , R_2 , R_3 and R_4 are the system reliability, the reliability of the ring gear, the reliability of the sun gear, the reliability of the parallel subsystem, and the reliability of the carrier, respectively. R_3 can be expressed by

$$R_3 = 1 - \prod_{i=1}^{K_1} (1 - R_{3i}), \tag{9}$$

where R_{3i} ($i = 1, 2, ..., K_1$) is the reliability of the ith planet gear in the parallel subsystem with K_1 planet gears. From the derivation of Equation (9), it can be seen that the

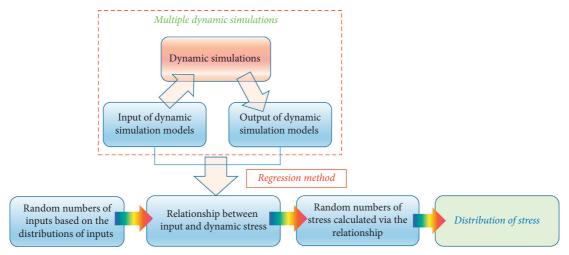


FIGURE 2: Method for distributions of stress.

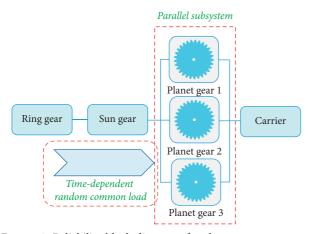


FIGURE 3: Reliability block diagram of a planetary gear system.

stress on each component in a system is mutually statistically correlative. Therefore, the components are statistically correlative, and the failure dependence should be taken into account in reliability modeling. As a matter of fact, failure dependence occurs under the condition of random common working environment, which significantly reduces the reliability of parallel systems. Under deterministic external load, failure dependence seldom takes place and the components seldom fail to work at the same time. However, the existence of random common load source greatly increases the possibility of simultaneous failure of components and reduces the effects of redundant designs, such as the wellknown phenomenon of common cause failure in nuclear power plants. When failure dependence happens, the parallel system reliability cannot be calculated according to classical reliability theory. Therefore, failure dependence brings great difficulties in reliability estimation of planetary gear systems. In this case, the reliability calculated according to Equations (8) and (9) could lead to large computational error. Moreover, considering the strength degradation, the correlation between different components could show obvious dynamic characteristics. Meanwhile, this dynamic characteristic of failure dependence also significantly increases the difficulty in random lifetime distribution modeling of planetary gear systems. It should be noted that failure dependence significantly affects the formulation of maintenance strategies and replacement strategies.

Besides, the components in parallel configuration in the subsystem share the same external load, and failure could take place on any component due to the randomness of the stress and the strength. Hence, a load redistribution could occur at any time and on any remaining components in the subsystem as shown in Figure 4. In Figure 4, t_1 and t_2 are random variables, and the load redistribution speeds up the strength degradation processes of the remaining components. The strength degradations of different components in the parallel subsystem are mutually dependent due to the stress dependence, and the load redistribution happens simultaneously on the remaining components. These problems in the subsystem have great influences on the failure dependence, dynamic reliability, and lifetime distribution of the whole system, which will be taken into consideration and analyzed in this paper.

3. Reliability Models and Lifetime Models

In practice, as an important component connecting the impeller and the generator in the wind generator, the gearbox always works with the highest failure rate in the wind generator under the harsh conditions of the external random wind load. The planetary gear is the most important part in the gearbox, which is crucial to the safe operation of the whole system. Besides, as important components, planetary gears are widely used in machine tools, automobiles, metallurgy, cranes, and aerospace products. Therefore, it is quite critical to investigate reliability models of planetary gears. Error, material parameters, and external load are key factors in the dynamics analysis of planetary gears. When considering the randomness of these factors, some new problems are encountered which bring large difficulties in reliability modeling of planetary gear systems. Current deterministic analytical dynamics models cannot be employed directly to solve these problems. For instance, the random external load causes

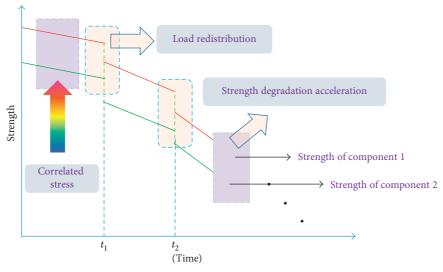


FIGURE 4: Strength degradation of components in a planetary gear system.

a random strength degradation. The random failure of the components results in the random load redistributions, which makes the mathematical expression of the stochastic strength degradation more difficult. Moreover, the dynamic failure dependence analysis of the components in a system, considering the random strength degradation and the random load redistribution, is seldom reported, which is quite important to the accurate reliability assessments of planetary gear systems. In this paper, dynamic reliability models of planetary gear systems are developed with the problems mentioned above taken into account.

Besides, analytical lifetime distribution models of planetary gear systems are further developed based on the proposed reliability models. The lifetime distribution models take the random load parameters, random geometric parameters, and random material parameters as the inputs. Furthermore, the lifetime distribution models consider the comprehensive effects of the random strength degradation, the random load distribution, and the dynamic failure dependence, which overcome the shortcomings of the lifetime assessment methods based on conventional fatigue tests and provide a theoretical framework for the random lifetime estimation of planetary gear systems. In practice, carriers are always designed with high strength and stiffness because of their important roles in energy transmission, and the system failure is mainly caused by other components in the systems. Therefore, in this section, we will concentrate on the behavior of the ring gear, the sun gear, and the parallel subsystem.

3.1. Reliability Models and Lifetime Distribution Models of the Subsystem. As mentioned above, the reliability analysis of the subsystem is the most complex compared with that of other components when considering the failure dependence and the random load redistributions. Thus, the dynamic reliability models of the subsystem will be established first. To consider the randomness of the input torque w_1 , input angular velocity w_2 , and the resistance torque w_3 in the jth

time interval, the stress associated its probability density function (PDF) on a planet gear is denoted by $T_j(w)$ and $f_{T_j(w)}(T_j(w))$ where $w = [w_1, w_2, w_3]$. Generally, the S-N curve model can be written as follows:

$$s^m N = C, (10)$$

where m and C are material parameters and N is the total cycles to failure under the stress s. In the failure mode of fatigue, when considering the strength degradation path dependence (SDPD), the equivalent residual strength can be given by [18]:

$$r(n) = \begin{cases} r_0 \left(1 - \sum_{j=1}^{n-1} \frac{\int_{-\infty}^{\infty} T_j(w)^m f_{T_j(w)}(T_j(w)) dT_j(w)}{C} \right)^a, & n > 1, \\ r_0, & n = 1, \end{cases}$$
(11)

where r_0 is initial strength, m and C are material parameters for S-N curve, and $f_{T_j(w)}(T_j(w))$ is the PDF of the stress $T_j(w)$ in the ith time interval. For description convenience, the function Φ is defined as follows:

$$\Phi(z_1, z_2, T_j(w)) = \int_{z_2}^{z_1} f_{T_j(w)}(T_j(w)) dT_j(w).$$
 (12)

The reliability of a component can be given by

$$R_{\text{com}}(n) = \prod_{h=1}^{n} \Phi(r(h), 0, T_h(w)).$$
 (13)

For a parallel system composed of k components, in which the minimum initial strength is denoted by r_{\min} , with identical material parameters and stress, after n time intervals, the reliability of the parallel system in the condition that the k components still work normally can be calculated by

$$R_k(n) = \prod_{h=1}^{n} \Phi(r_{\min}(h), 0, T_{h+1}(w)).$$
 (14)

For the k components with deterministic initial strength in ascending order denoted by r_{j2} (j2 = 1, 2, ..., k), when considering the failure history of the components within the

n time intervals, the reliability of the parallel system in the condition that the k2 components still work normally can be calculated by

$$R_{k2}(n) = \sum_{h_1=1}^{p_1} \sum_{h_2=1}^{p_2} \dots \sum_{h_{(k-k2)}=1}^{p_{(k-k2)}} \left(\prod_{z_3=1}^{k-k2} W_{z_3} \right) \prod_{\text{hr}=h_{(k-k2)}+1}^{n} \Phi\left(r_{k-k2+1}\left(\text{hr}\right), \ 0, \ T_{\text{hr}}\left(w\right)\right),$$

$$\left(h_{z_3-1} \le h_{z_3}, \ p_{z_3-1} \le p_{z_3} \le (n-1)\right),$$

$$W_1 = \begin{cases} \prod_{d_1=1}^{h_1-1} \Phi\left(r_1(d_1), \ 0, \ T_{d_1}\left(w\right)\right) \Big] \Big[1 - \Phi\left(r_2\left(h_1\right), \ r_1\left(h_1\right), \ T_{h_1}\left(w\right)\right)\Big], & h_1 \ge 2, \\ \left[1 - \Phi\left(r_2\left(h_1\right), \ r_1\left(h_1\right), \ T_{h_1}\left(w\right)\right)\right], & h_1 = 1, \end{cases}$$

$$W_{k3} = \begin{cases} \prod_{d_{k3}=h_{k3-1}+1}^{h_{k3}-1} \Phi\left(r_{k3}\left(d_{k3}\right), \ 0, \ T_{d_{k3}}\left(w\right)\right)\Big] \Big[1 - \Phi\left(r_{k3+1}\left(h_{k3}\right), \ r_{k3}\left(h_{k3}\right), \ T_{h_{k3}}\left(w\right)\right)\Big], & h_{k3} \ge 2, \\ \left[1 - \Phi\left(r_{k3+1}\left(h_{k3}\right), \ r_{k3}\left(h_{k3}\right), \ T_{h_{k3}}\left(w\right)\right)\Big], & h_{k3} = 1, \end{cases}$$

$$(15)$$

when $h_{x1} = h_{x2} = \ldots = h_{xj}$,

$$\prod_{z3=x1}^{xj} W_{z3} = \begin{cases}
\prod_{dk3=h_{x_{1-1}+1}}^{h_{x_{1}}-1} \Phi\left(r_{x_{1}}(dk3), 0, T_{dk3}(w)\right) \left[1 - \Phi\left(r_{x_{j+1}}(h_{x_{1}}), r_{x_{1}}(h_{x_{1}}), T_{h_{x_{1}}}(w)\right)\right], & h_{x_{1}} \geq 2, \\
\left[1 - \Phi\left(r_{x_{j+1}}(h_{x_{1}}), r_{x_{1}}(h_{x_{1}}), T_{h_{x_{1}}}(w)\right)\right], & h_{x_{1}} = 1.
\end{cases}$$
(16)

The reliability models above are derived under the assumption that the initial strength of each component is deterministic. When considering the randomness of these initial strength, provided that the PDFs of r_{j2} (j2 = 1, 2, ..., k) are identical, which are denoted by $f_1(r_{j2})$ (j2 = 1, 2, ..., k), the reliability above can be further modified as follows:

$$R_{k}(n) = k! \int_{-\infty}^{\infty} f_{1}(r_{k}) \int_{r_{-\infty}}^{r_{k}} f_{1}(r_{k-1}) \dots \int_{-\infty}^{r_{2}} f_{1}(r_{1}) \cdot \left[\prod_{h=0}^{n-1} \Phi(r_{1}(h), 0, T_{h+1}(w)) \right] dr_{1} dr_{2} \dots dr_{k},$$
(17)

$$R_{k2}(n) = k! \int_{-\infty}^{\infty} f_1(r_k) \int_{r_{-\infty}}^{r_k} f_1(r_{k-1}) \dots \int_{-\infty}^{r_2} f_1(r_1) \cdot \left\{ \sum_{h_1=1}^{p_1} \sum_{h_2=1}^{p_2} \dots \sum_{h_{(k-k2)}=1}^{p_{(k-k2)}} \prod_{z,3=1}^{k-k2} W_{z,3} \right\} \times \left[\prod_{h_1=h_{(k-k2)}+1}^{n} \Phi(r_{k-k2+1}(h_1), 0, T_{h_1}(w)) \right] \cdot dr_1 dr_2 \dots dr_k,$$

$$(18)$$

The total reliability of the parallel system can be computed by

$$R_{s}(n) = \sum_{k3=1}^{k} R_{k3}(n).$$
 (19)

In the dynamic reliability models of planetary gear systems derived above, all possible failure processes of the system are considered. Moreover, the possibility that a parallel system works with a specified number of components is calculated on the basis of the possibility that the parallel system works with more components, which simplifies the calculation and saves the computing cost. Besides, it should be noted that in Equation (18) that $R_{k3}(n)$ represents the reliability of the parallel system under the condition that the k3 components still work normally, rather than the reliability of Component k3.

Define the gth-order lifetime PDF of the parallel system as the PDF of the lifetime within which g components work normally. Then, the gth-order discrete lifetime PDF can be given by

$$f_{k}(n) = k! \int_{-\infty}^{\infty} f_{1}(r_{k}) \int_{r_{-\infty}}^{r_{k}} f_{1}(r_{k-1}) \dots \int_{-\infty}^{r_{2}} f_{1}(r_{1}) \\ \cdot \left\{ \prod_{h=0}^{n-1} \Phi(r_{1}(h), 0, T_{h+1}(w)) \right] \\ \times \left[1 - \Phi(r_{1}(n), 0, T_{h+1}(w)) \right] \right\} dr_{1} dr_{2} \dots dr_{k},$$

$$f_{k2}(n) = k! \int_{-\infty}^{\infty} f_{1}(r_{k}) \int_{r_{-\infty}}^{r_{k}} f_{1}(r_{k-1}) \dots \int_{-\infty}^{r_{2}} f_{1}(r_{1}) \\ \cdot \left\{ \sum_{h_{1}=1}^{p_{1}} \sum_{h_{2}=1}^{p_{2}} \dots \sum_{h_{(k-k2)}=1}^{p_{(k-k2)}} \prod_{z,3=1}^{k-k2} W_{z,3} \right.$$

$$\times \left[\prod_{hr=h_{(k-k2)}+1}^{n} \Phi(r_{k-k2+1}(hr), 0, T_{hr}(w)) \right]$$

$$- \sum_{h_{1,a}=1}^{p_{1,a}} \sum_{h_{2,a}=1}^{p_{2,a}} \dots \sum_{h_{(k-k2),a}=1}^{p_{(k-k2),a}} \prod_{z,3=1}^{k-k2} W_{z,3,a}$$

$$\times \left[\prod_{hr=h_{(k-k2),a}+1}^{n+1} \Phi(r_{k-k2+1}(hra), 0, T_{hra}(w)) \right]$$

$$\cdot dr_{1} dr_{2} \dots dr_{k},$$

$$\left(h_{z,3a-1} \leq h_{z,3a}, p_{z,3a-1} \leq p_{z,3a} \leq n \right),$$

$$(20)$$

3.2. Reliability Models and Lifetime Distribution Models of the Planetary Gear System. In Section 3.1, the reliability models

and the lifetime distribution models are developed, in which the failure dependence among each planet gear is taken into account. As stated in Section 2.2, the reliability of the ring gear $R_1(n)$ and the reliability of the sun gear $R_2(n)$ are also statistically dependent with $R_s(n)$. The residual strength of the ring gear and the residual strength of the sun gear are denoted by $u_1(n)$ and $u_2(n)$, respectively. From Equation (7), it can be known that the stress on the ring gear $s_1(j, w)$ and the stress on sun gear $s_2(j, w)$ can be mathematically expressed by

$$s_1(j, w) = N_1(j)T_j(w),$$

 $s_2(j, w) = N_2(j)T_j(w),$
(21)

where $N_1(j)$ and $N_2(j)$ can be obtained by Equation (7). The equivalent residual strength of the ring gear and the sun gear can be written as

$$u_{11}(j) = \frac{u_1(j)}{N_1(j)},$$

$$u_{22}(j) = \frac{u_2(j)}{N_2(j)}.$$
(22)

The PDF of the initial strength of the ring gear and that of the sun gear are denoted by $f_{u_{10}}(u_{10})$ and $f_{u_{20}}(u_{20})$, respectively. Then, the system reliability can be calculated by

$$R_T(n) = \sum_{T=1}^k R_{\text{ST1}}(n), \tag{23}$$

where
$$R_{Sk}(n) = \int_{-\infty}^{\infty} f_{u_{10}}(u_{10}) \int_{-\infty}^{\infty} f_{u_{20}}(u_{20})k! \int_{-\infty}^{\infty} f_1(r_k) \int_{r_{-\infty}}^{r_k} f_1(r_{k-1}) \dots \int_{-\infty}^{r_2} f_1(r_1) \\
\times \left[\prod_{h=0}^{n-1} \Phi\left(\min(r_1(h), u_{11}(h), u_{22}(h)), 0, T_{h+1}(w) \right) \right] dr_1 dr_2 \dots dr_k du_{10} du_{20},$$

$$R_{Sk2}(n) = \int_{-\infty}^{\infty} f_{u_{10}}(u_{10}) \int_{-\infty}^{\infty} f_{u_{20}}(u_{20})k! \int_{-\infty}^{\infty} f_1(r_k) \int_{r_{-\infty}}^{r_k} f_1(r_{k-1}) \dots \int_{-\infty}^{r_2} f_1(r_1) \left\{ \sum_{h_1=1}^{p_1} \sum_{h_2=1}^{p_2} \dots \sum_{h_{(k-k2)}=1}^{p_{(k-k2)}} \prod_{k=3}^{k-k2} W_{Sk3} \right\} \\
\times \left[\prod_{h=h_{(k-k2)}+1}^{n} \Phi\left(\min(r_{k-k2+1}(hr), u_{11}(hr), u_{22}(hr)), 0, T_{hr}(w) \right) \right] dr_1 dr_2 \dots dr_k du_{10} du_{20},$$

$$W_{S1} = \begin{cases} \prod_{l=1}^{h_1-1} \Phi\left(\min(r_1(d1), u_{11}(d1), u_{22}(d1)), 0, T_{d1}(w) \right) \\
\times \left[1 - \Phi\left(\min(r_2(h_1), u_{11}(h_1), u_{22}(h_1)), \min(r_1(h_1), u_{11}(h_1), u_{22}(h_1)), T_{h_1}(w) \right) \right], \quad h_1 \geq 2, \\
\left[1 - \Phi\left(\min(r_2(h_1), u_{11}(h_1), u_{22}(h_1)), \min(r_1(h_1), u_{11}(h_1), u_{22}(h_1)), T_{h_1}(w) \right) \right], \quad h_1 = 1, \end{cases}$$

$$W_{Sk3} = \begin{cases} \prod_{l=1}^{h_{23}-1} \Phi\left(\min(r_{k3}(dk3), u_{11}(dk3), u_{22}(dk3)), 0, T_{dk3}(w) \right) \\
\times \left[1 - \Phi\left(\min(r_{k3+1}(h_{k3}), u_{11}(h_{k3}), u_{22}(h_{k3}) \right), \min(r_{k3}(h_{k3}), u_{11}(h_{k3}), u_{22}(h_{k3})), T_{h_{k3}}(w) \right) \right], \quad h_{k3} \geq 2, \\
\left[1 - \Phi\left(\min(r_{k3+1}(h_{k3}), u_{11}(h_{k3}), u_{22}(h_{k3}) \right), \min(r_{k3}(h_{k3}), u_{11}(h_{k3}), u_{22}(h_{k3})), T_{h_{k3}}(w) \right) \right], \quad h_{k3} = 1, \\
(K3 \geq 2), \tag{24}$$

when $h_{x1} = h_{x2} = \ldots = h_{xj}$,

TARIE 1.	Structural	narameters	and	material	parameters.
IABLE I.	Structurar	parameters	and	materiai	parameters.

Parameters	Value	Unit
Pressure angle	20	Degree
Helix angle	0	Degree
Tooth thickness	3	Mm
Density of gears	7.8^*10^3	kg/m ³
Number of teeth of sum gear	36	_
Number of teeth of planet gear	36	
Number of planet gears	3	
Modulus	2	mm
Angular velocity of sun gear	60	Degree/second
Elastic modulus	$2*10^5$	MPa
Length of a time interval	1	Н
m	3	
C	10^{8}	MPa^2
Mean value of total resistance torque	30	N⋅m
Standard deviation of total resistance torque	1.5	N⋅m
Mean value of initial strength of a planet gear	300	MPa
Standard deviation of initial strength of a planet gear	30	MPa
Mean value of initial strength of sun gear	250	MPa
Standard deviation of initial strength of sun gear	30	MPa
Mean value of initial strength of ring gear	250	MPa
Standard deviation of initial strength of ring gear	30	MPa

$$\prod_{z3=x1}^{xj} W_{z3} = \begin{cases}
& \left[\prod_{dk_3=h_{x_{1-1}+1}}^{h_{x_{1}-1}} \Phi\left(\min\left(r_{x_{1}}(dk_{3}), u_{11}(dk_{3}), u_{22}(dk_{3})\right), 0, T_{dk_{3}}(w)\right) \right] \\
& \times \left[1 - \Phi\left(\min\left(r_{x_{j+1}}(h_{x_{1}}), u_{11}(h_{x_{1}}), u_{22}(h_{x_{1}})\right), \min\left(r_{x_{1}}(h_{x_{1}}), u_{11}(h_{x_{1}}), u_{22}(h_{x_{1}})\right), T_{h_{x_{1}}}(w)\right) \right], \quad h_{x_{1}} \geq 2, \\
& \left[1 - \Phi\left(\min\left(r_{x_{j+1}}(h_{x_{1}}), u_{11}(h_{x_{1}}), u_{22}(h_{x_{1}})\right), \min\left(r_{x_{1}}(h_{x_{1}}), u_{11}(h_{x_{1}}), u_{22}(h_{x_{1}})\right), T_{h_{x_{1}}}(w)\right) \right], \quad h_{x_{1}} = 1.
\end{cases} \tag{25}$$

The lifetime PDF can be given by

$$f_S(n) = \sum_{k_3=1}^k f_{sk_3}(n), \tag{26}$$

where

where
$$f_{sk}(n) = \int_{-\infty}^{\infty} f_{u_{10}}(u_{10}) \int_{-\infty}^{\infty} f_{u_{20}}(u_{20}) k! \int_{-\infty}^{\infty} f_1(r_k) \int_{r_{-\infty}}^{r_k} f_1(r_{k-1}) \dots \int_{-\infty}^{r_2} f_1(r_1) \times \left\{ \left[\prod_{h=0}^{n-1} \Phi\left(\min\left(r_1(h), u_{11}(h), u_{22}(h)\right), 0, T_{h+1}(w)\right) \right] \right\} dr_1 dr_2 \dots dr_k du_{10} du_{20}.$$

$$(27)$$

For $k3 \neq k$

$$f_{sk3}(n) = \int_{-\infty}^{\infty} f_{u_{10}}(u_{10}) \int_{-\infty}^{\infty} f_{u_{20}}(u_{20})k! \int_{-\infty}^{\infty} f_{1}(r_{k}) \int_{r_{-\infty}}^{r_{k}} f_{1}(r_{k-1}) \dots \int_{-\infty}^{r_{2}} f_{1}(r_{1}) \left\{ \sum_{h_{1}=1}^{p_{1}} \sum_{h_{2}=1}^{p_{2}} \dots \sum_{h_{(k-k)}=1}^{p_{(k-k)}} \prod_{z \ni 1}^{k-k} W_{Sz3} \right\}$$

$$\times \left[\prod_{hr=h_{(k-k)}+1}^{n} \Phi\left(\min\left(r_{k-k3+1}(hr), u_{11}(hr), u_{22}(hr)\right), 0, T_{hr}(w)\right) \right] - \sum_{h_{1}=1}^{p_{1}} \sum_{h_{2}=1}^{p_{2}} \dots \sum_{h_{(k-k)}=1}^{p_{(k-k)}} \prod_{z \ni 1}^{k-k} W_{Sz3}$$

$$\times \left[\prod_{hr=h_{(k-k)}+1}^{n+1} \Phi\left(\min\left(r_{k-k3+1}(hra), u_{11}(hra), u_{22}(hra)\right), 0, T_{hra}(w)\right) \right] dr_{1} dr_{2} \dots dr_{k} du_{10} du_{20}.$$

$$(28)$$

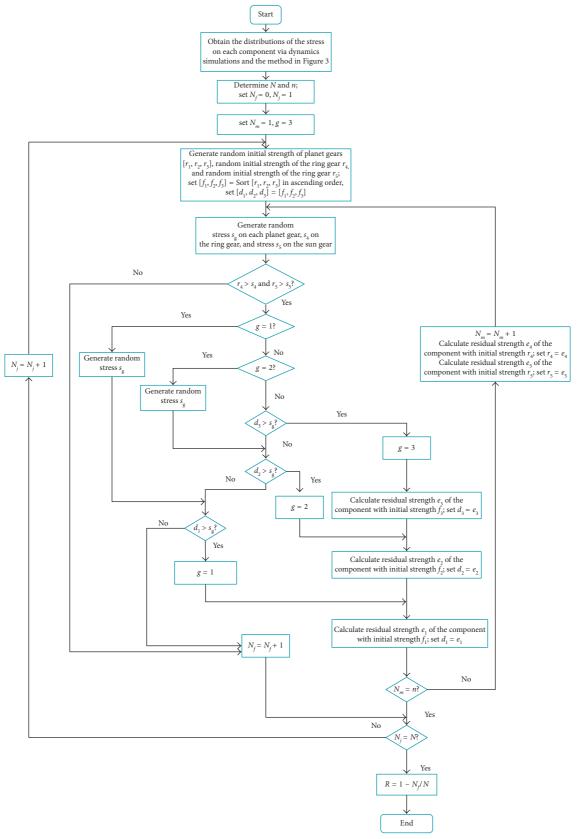


FIGURE 5: Flowchart for MCS of subsystem reliability.

4. Numerical Examples

Consider a planetary gear system with the structural and material parameters of its components listed in Table 1. In this numerical example, the sun gear operates at a constant angular velocity. The randomness of the output torque due to the uncertainty of the working environment is taken into account. The sum of the resistance torque on each planet gear is assumed to follow the normal distribution at each time interval. To validate the proposed models, Monte Carlo simulations (MCSs) are carried out in this section with the flowchart shown in Figure 5. The system reliability from the proposed models and the results from MCSs are shown in Figure 6. In addition, when the ring gear and the sun gear, whose reliability are calculated by Equation (12), are assumed to be independent to the subsystem, the system reliability from Equation (8) is plotted in Figure 6. In Table 1, pressure angle, helix angle, tooth thickness, density of gears, no. of teeth of sun gear, no. of teeth of planet gear, no. of planet gears, modulus, elastic modulus, angular velocity of sun gear, and length of a time interval are used for geometric modeling and material parameter input of planetary gear systems in the dynamic simulations. m and C are material parameters for S-N curve models. These two parameters and the parameter of initial strength are used to model the equivalent strength degradation paths of components. Moreover, the mean value and the standard deviation of a normal random variable are used to characterize the statistical distribution of the random variable. The stress is generated by the motion and mechanical parameters, such as the angular velocity of sun gear and the total resistance torque. The randomness of the stress comes from the randomness of these parameters. Hence, the stress distributions are obtained from the distribution of these parameters listed in Table 1 and dynamic simulations.

From Figure 6, it can be learnt that the reliability from the proposed models and that from MSCs show good agreement. The proposed analytical reliability models are effective for reliability evaluation of the planetary gear systems. The stress on each component is mutually statistically correlative because of the common external load. In the proposed models, the failure dependence between the planet gears and the failure dependence among the ring gear, the sun gear, and the parallel subsystem are taken into consideration. Besides, random load distributions are also considered in the models. The system reliability calculated under the assumption that the components are mutually independent is obviously lower than that calculated with failure dependence considered. Therefore, attention should be paid in the reliability assessment for mechanical systems which are mainly dependent system due to the working mechanism. At the early stage, the reliability is high, which seems almost invariable. Hence, a small change of reliability could lead to a sharp decrease in the failure rate. In the accidental failure period, on the one hand, the reliability decreases faster compared with that at the early stage. On the other hand, the reliability is obviously lower compared with that at the early stage. Thus, the failure rate shows a low descent speed in the accidental failure period as seen in the bathtub curve.

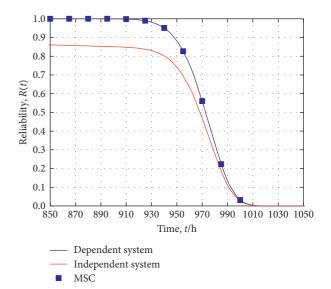


FIGURE 6: Reliability of independent system and dependent system and results from MSC.

To analyze the dispersion of the resistance torque on the system reliability, in the case where the standard deviations are $1.5 \,\mathrm{N} \cdot \mathrm{m}$ and $0.75 \,\mathrm{N} \cdot \mathrm{m}$, respectively, the system reliability is shown in Figure 7. In addition, the third-order lifetime PDF, the second-order lifetime PDF, and the first-order lifetime PDF of the parallel system in the case of different dispersions of the resistance torque are shown in Figures 8–10, respectively.

From Figure 7, it can be seen that although the mean value of the resistance torque keeps constant, the system reliability is significantly affected by the dispersion of the resistance torque. In general, large dispersion of the resistance torque results in low system reliability, because large dispersion increases the possibility of large stress which always causes the common cause failure and reduces the effects of redundant design. Hence, in the design of planetary gear systems, besides the deterministic design stress, the practical stress dispersion caused by the uncertainty of external loads, dimensional error, and material parameters should also be paid enough attentions.

In addition, from Figures 8-10, it can be learnt that random load redistributions exist in the operational duration of the planetary gear systems, which is seldom reported in current reliability models of planetary gear systems. Due to the randomness of the external load, the failure of each component is stochastic, which results in the randomness of the load redistribution. In general, the decrease in the dispersion of external load causes the improvement of the mean value of the system lifetime and reduces the dispersion of the system lifetime in each order, which is beneficial for the usage of the planetary gear systems. In addition, with the increase of the number of the redundant components, the mean value of the system lifetime is raised and the dispersion of the system lifetime is decreased. Furthermore, these effects are more obvious with the increase of the number of the redundant components in a system. Hence, the proposed

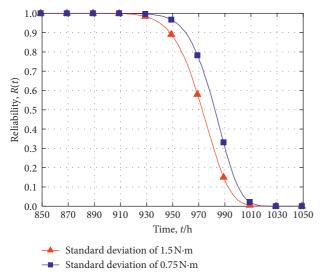


FIGURE 7: System reliability with different resistance torque dispersions.

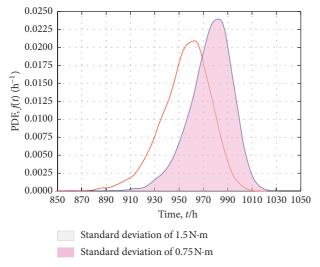


FIGURE 8: The third-order lifetime PDF with different resistance torque dispersions.

models are helpful for the design and the draw-up of maintenance strategies of the planetary gear systems.

5. Conclusions

Reliability and random lifetime models of planetary gear systems are developed in this paper. Conventional reliability models of planetary gear systems are mainly static models without detailed information about the stress and strength in the models. In this paper, the dynamic working mechanism is considered when establishing the dynamic system reliability models. Besides, conventional lifetime models are constructed based on fatigue test under constant stress, which cannot be used in the situation of dynamic random stress. In this paper, the lifetime distribution models of planetary gear systems are derived based on the proposed dynamic reliability models with the load parameters, the

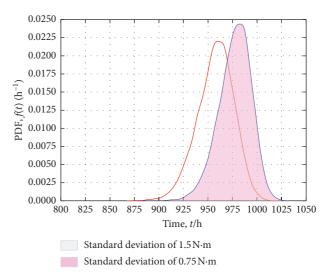


FIGURE 9: The second-order lifetime PDF with different resistance torque dispersions.

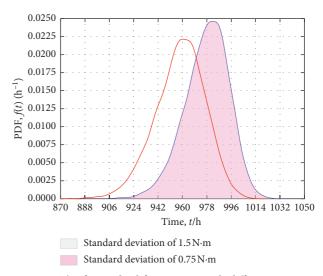


FIGURE 10: The first-order lifetime PDF with different resistance torque dispersions.

geometric parameters, and the material parameters taken as the inputs. Furthermore, failure dependence of components in a planetary gear system and the random dynamic load redistributions are taken into account in the reliability models and the lifetime distribution models. MCSs are performed in this paper to validate the proposed models. The results in numerical examples show that the randomness of the load distribution is obvious in the system working process. Failure dependence has significant influences on system reliability. Moreover, the dispersion of external load has great impacts on the reliability, the lifetime distributions, and the redundancy of the planetary gear systems.

Data Availability

The data used to support the findings of this study are available from the corresponding author upon request.

Conflicts of Interest

The authors declare that there are no conflicts of interest regarding the publication of this paper.

Acknowledgments

This work was supported by National Natural Science Foundation of China (Grant no. 51505207), Program for Liaoning Innovative Talents in University (Grant no. LR2017070), Liaoning Provincial Natural Science Foundation of China (Grant no. 2015020152), and Open Foundation of Zhejiang Provincial Top Key Academic Discipline of Mechanical Engineering (Grant no. ZSTUME02A01)

References

- [1] B. Ye, Y. Zhao, G. Yu et al., "Multi-objective reliability optimization design of tractor's NGW type planetary gear final transmission," *Transactions of the Chinese Society of Agricultural Engineering*, vol. 24, no. 11, pp. 89–94, 2008.
- [2] B. Ye, G. Wu, G. Yu et al., "Optimized design and tests on rice potted seedling transplanting mechanism of planetary gear train with non-circular gears," *Transactions of the Chinese Society for Agricultural Machinery*, vol. 48, no. 11, 2016.
- [3] B. L. Ye, G. H. Yu, and Y. Zhao, "Multi-objective fuzzy reliability optimization design of tractor's final transmission," *Transactions of the Chinese Society for Agricultural Machinery*, vol. 41, no. 4, pp. 95–100, 2010.
- [4] B. Ye, Z. Hao, G. Yu et al., "Dynamics analysis and tests of rotary transplanting mechanism for rice pot-seedling," *Transactions of the Chinese Society for Agricultural Machinery*, vol. 47, no. 5, 2016.
- [5] S. Zhang, "Fuzzy reliability optimal design of cycloidal pinwheel planetary gear speed reducer," *Journal of Mechanical Strength*, vol. 24, no. 3, pp. 458–462, 2002.
- [6] M. Li, L. Xie, and L. Ding, "Load sharing analysis and reliability prediction for planetary gear train of helicopter," Mechanism and Machine Theory, vol. 115, pp. 97–113, 2017.
- [7] D. Zhang, "Application of improved genetic algorithm in reliability optimization design of NGW planetary gear transmission," *Journal of Mechanical Transmission*, vol. 37, no. 2, pp. 44–46, 2013.
- [8] C. Wang and S. Yue, "Reliability assessment of wind power growth planetary gear train based on dynamics," in Proceedings of International Conference on Mechanical Materials and Manufacturing Engineering, Savannah, GA, USA, May 2016.
- [9] T. Barszcz and R. B. Randall, "Application of spectral kurtosis for detection of a tooth crack in the planetary gear of a wind turbine," *Mechanical Systems and Signal Processing*, vol. 23, no. 4, pp. 1352–1365, 2009.
- [10] D. R. Kiracofe and R. G. Parker, "Structured vibration modes of general compound planetary gear systems," *Journal of Vibration and Acoustics*, vol. 129, no. 1, pp. 511–526, 2007.
- [11] C. Zhu, X. Xu, and H. Wang, "Modal prediction and sensitivity analysis of wind-turbine planetary gear system with flexible planet pin," *Journal of Computational and Theoretical Nanoscience*, vol. 4, no. 3, pp. 1219–1224, 2011.
- [12] R. Guo, Foundation of Mechanical Design, Tsinghua University Press, Beijing, China, 2001.

[13] E. Zhu, S. Wu, X. Wang et al., "Study on nonlinear dynamic model of planetary gear train sets with friction force," *Journal* of Vibration and Shock, vol. 29, no. 8, pp. 217–220, 2010.

- [14] Q. Ye and H. Xue, "Dynamic simulation of planetary gear mechanism for 1.5 MW wind turbine," *Journal of Mechanical Manufacturing*, vol. 51, no. 6, pp. 17–19, 2013.
- [15] L. Chen, Mechanical System Dynamics Analysis and ADAMS Application, Tsinghua University Press, Beijing, China, 2005.
- [16] J. Wu, S. Yan, and M. Zuo, "Evaluating the reliability of multibody mechanisms: a method considering the uncertainties of dynamic performance," *Reliability Engineering and System Safety*, vol. 149, pp. 96–106, 2016.
- [17] W. J. Roux, N. Stander, and R. T. Haftka, "Response surface approximations for structural optimization," *International Journal for Numerical Methods in Engineering*, vol. 42, no. 3, pp. 517–534, 2015.
- [18] P. Gao, L. Xie, and F. Liu, "Dynamic reliability analysis of series mechanical systems considering strength degradation path dependence of components," *Journal of Advanced Mechanical Design, Systems and Manufacturing*, vol. 9, no. 5, pp. 1–13, 2015.

Hindawi Shock and Vibration Volume 2018, Article ID 6839062, 8 pages https://doi.org/10.1155/2018/6839062

Research Article

A New Erosion Model for Wind-Induced Structural Vibrations

Keqin Yan , Yi Zhang , and Tao Cheng and Tao Cheng

Correspondence should be addressed to Yi Zhang; zhang_yi87@163.com

Received 16 March 2018; Revised 7 June 2018; Accepted 17 July 2018; Published 10 September 2018

Academic Editor: Aly Mousaad Aly

Copyright © 2018 Keqin Yan et al. This is an open access article distributed under the Creative Commons Attribution License, which permits unrestricted use, distribution, and reproduction in any medium, provided the original work is properly cited.

In recent years, computational fluid dynamics (CFD) method has been widely utilized in simulating wind-induced snow drifting. In the simulating process, the erosion flux is the main controlling factor which can be calculated by the product of erosion coefficient and the differences between the flow stress and threshold stress. The erosion coefficient is often adopted as an empirical constant which is believed not to change with time and space. However, in reality, we do need to consider the influences of snow diameter, density, and wind speed on the erosion coefficient. In this technical note, a function of air density, sow particle density, snow particle radius, and snow particle strength bond is proposed for the erosion coefficient. Based on an experiment study, the effects of these parameters in erosion coefficient is analyzed and discussed. The probability distribution and value range of erosion coefficient are also presented in this technical note. The applicability of this approach is also demonstrated in a numerical study for predicting the snow distributions around a cube structure. The randomness of the structural vibrations is studied with details.

1. Introduction

In heavy snow areas, wind-induced snow drifting causes unbalanced snowdrift around buildings/on roofs. It is not only difficult to remove but also causes trouble for vehicles and pedestrians. Roof collapse occurs for unbalanced snow distribution

Wind-induced snow drifting belongs two-phase flow. There are many parameters affecting the result of this phenomenon: wind speed, friction velocity, threshold friction velocity, snow particle radius, density, and cohesion. At present, there are four kinds of research methods for this phenomenon: theoretical analysis, field investigation, wind tunnel (water flume) experiment, and numerical simulation. Field investigation can obtain first hand data, and it is the basis of all other methods. But the field investigation is usually constrained by natural conditions, is time-consuming, and can only obtain the result under certain conditions. Therefore, it is not easy to reveal the inherent law of this phenomenon. Wind tunnel test can change parameters and can make up the shortage of field measurement to some extent. But only a few wind tunnels can carry out this

kind of test. Furthermore, similarity criterion is difficult to satisfy due to reduced model. Many former researches have been done on the topic of wind-induced snow drifting through either field experiment [1-8] or numerical simulation [9-13]. Most researchers tried to combine theoretical analysis with empirical formulas from results of field investigations and use it in the numerical simulations [5, 9-13]. In an early works of the authors [14], a new method is developed to measure the air velocity profile surrounding an existing building structure considering snow effects. The snow particle size and its distribution are considered in plotting the velocity profile. In this method, the experiment was conducted based on a simple wind tunnel powered by a fan in the lab. The influences from the field such as the potential damages that might be caused to the equipment due to snow particles are not considered. Different snow size effects are also not catered. Obviously, the input from the field results has a significant influence on the reliability of the analysis. Among these, the modeling of erosion flux is one of the most dominant factors in numerical analysis. Plenty of studies on determining the erosion flux have been carried out in recent years [15].

¹School of Civil Engineering, Hubei Polytechnic University, Huangshi, Hubei 435003, China

²Department of Civil Engineering, Tsinghua University, Beijing 100084, China

³Geodätisches Institut, Leibniz Universität Hannover, 30167 Hannover, Germany

In these pioneering works, the erosion flux is found to be dependent on the difference between the friction flow stress and threshold friction stress. The erosion flux can be calculated based on the product of a coefficient γ and the stress difference. The determination of the value of γ is based on field experiments. For instance, Schmidt [16] had once carried out experimental tests in a wind tunnel to investigate behavior of drifting spherical glass microbeads, which has a diameter of 350 μ m and density of 2.5 g/cm³. From the experiment, it was found that when flow friction velocity is $0.5~\mathrm{ms^{-1}}$, γ has a value around $5 \times 10^7~\mathrm{N^{-1} \cdot s^{-1}}$. It is also reported that the value of coefficient γ increases as the particle diameter decreases. For instance, Anderson [17] carried out investigations with mineral particles in size of sand and found out that the value of γ should be in orders of $10^5 \,\mathrm{N}^{-1} \cdot \mathrm{s}^{-1}$. Therefore, the particle size is an influential factor in determining the value of γ . In fact, there are more factors that need to be considered in the estimate of γ . The authors believe that it depends on snow conditions.

Since 1990s, computational fluid dynamics (CFD) theory has been brought into the simulation of snow drifting. Similar to the model of Andersen [16], Naaim [11] suggested that the erosion flux of snow can be computed by the product of two factors. The first factor is the difference between the square of flow friction velocity and the square of threshold friction velocity. The second factor is a coefficient ρA , or so-called erosion coefficient $A_{\rm ero}$, which usually takes a value of $7 \times 10^{-4} \,\mathrm{kg \cdot m^{-3}}$. Because of its simplicity, many research works have adopted this concept and taken this value for the erosion coefficient in their CFD simulations [18]. Very limited studies have been carried out to discuss about the value range of this coefficient. And studies on which factors can affect this coefficient are also lacking. Thus, a comprehensive study on the attributes for an erosion coefficient is quite demanding.

The objective of this study was to investigate the value range of erosion coefficient and to derive an expression of erosion coefficient in terms of the dominant factors. Realizing this, the paper is organized as follows. After the introduction, Section 2 will first discuss the dominant factors that are influential to erosion coefficient. Based on these factors, an expression of erosion coefficient is derived. After this, the value range of erosion coefficient is investigated in Section 3. The domain of the dominant factors is considered in this evaluation. The applicability of the developed approach is further demonstrated in a case study carried out in Section 4. The final conclusions drawn from this study are summarized in Section 5.

2. Derivation of the Formula for Erosion Coefficient

As mentioned in many of the literature, coefficient γ , which characterizes the bond strength of snow particles, has the same physical meaning as erosion coefficient $A_{\rm ero}$ in the CFD method [19]. Herein, a short discussion on the relationship between these two coefficients is provided as follows.

In most literature on the topic of wind-induced snow drifting, the snow surface erosion flux is calculated as follows [20]:

$$q_{\text{ero}} = \rho A (u_*^2 - u_{*t}^2) = A_{\text{ero}} (u_*^2 - u_{*t}^2),$$
 (1)

where $A_{\rm ero}$ is the erosion coefficient, u_* is the friction velocity, and u_{*t} is the threshold friction velocity of snow particles. In most former works, the value of $A_{\rm ero}$ is suggested to be 0.0005 or 0.0007.

Later on, Anderson analyzed the characteristics of surface force and suggested that drifted snow particle number should be calculated as follows [9, 17]:

$$N = \gamma (\tau - \tau_t), \tag{2}$$

where γ is a coefficient characterized by the bond strength between snow particles which usually takes a value of $10^5~{\rm N}^{-1}\cdot{\rm s}^{-1}$, τ represents the surface shear stress caused by flow, and $\tau_{\rm t}$ indicates the threshold shear stress. By combining Equations (1) and (2), the relationship between γ and $A_{\rm ero}$ can be revealed.

The relationship between surface shear stress τ and surface friction velocity u_* can be described by the following equation:

$$u_* = \sqrt{\frac{\tau}{\rho_a}},\tag{3}$$

where ρ_a is the air density (the value usually adopts a value of 1.25 kg·m⁻³ for normal air).

By substituting Equation (3) into Equation (2), we can obtain the following equation for computing the snow particle number:

$$N = \rho_{\rm a} \gamma (u_*^2 - u_{*t}^2). \tag{4}$$

Once the snow particle number is estimated, it can then be used to calculate the erosion flux. Snow surface erosion flux $q_{\rm ero}$ is the drifted snow particle quantity in unit area per unit time. Since drifted snow contains snow particles with different radius, $q_{\rm ero}$ can be expressed as a function of the particle sizes as the following equation:

$$q_{\text{ero}} = \sum_{i=1}^{n} N \rho_{\text{p}i} V_{\text{p}i} = \sum_{i=1}^{n} \frac{\pi d_{\text{p}i}^{3}}{6} \rho_{\text{p}i} \rho_{\text{a}} \gamma \left(u_{*}^{2} - u_{*\text{t}i}^{2}\right)$$

$$= \sum_{i=1}^{n} \frac{4\pi r_{\text{p}i}^{3}}{3} \rho_{\text{p}i} \rho_{\text{a}} \gamma \left(u_{*}^{2} - u_{*\text{t}i}^{2}\right),$$
(5)

where ρ_p is the snow particle density, V_p is the snow particle volume, d_p is the snow particle diameter, r_p is the snow particle radius, and i represents the i_{th} snow particle $(i=1,2,\ldots,n)$. For simplicity, threshold friction velocity is assumed to be the constant for all snow particles. Thus, Equation (5) can be further revised as follows:

$$q_{\rm ero} = \sum_{i=1}^{n} \frac{4\pi r_{\rm pi}^{3}}{3} \rho_{\rm pi} \rho_{\rm a} \gamma \left(u_{*}^{2} - u_{*t}^{2}\right). \tag{6}$$

Therefore, by substituting Equation (6) into Equation (1), the equation for computing the erosion coefficient can be derived as follows:

$$A_{\rm ero} = \sum_{i=1}^{n} \frac{\pi d_{\rm pi}^{3}}{6} \rho_{\rm pi} \rho_{\rm a} \gamma = \sum_{i=1}^{n} \frac{4\pi r_{\rm pi}^{3}}{3} \rho_{\rm pi} \rho_{\rm a} \gamma. \tag{7}$$

As can be observed from Equation (7), erosion coefficient $A_{\rm ero}$ is a function of snow particle radius and density, coefficient γ , and air density. It is a much more complicated factor which should be quite random depending on snow particle properties. In the following, the influence of different parameters on the erosion coefficient in Equation (7) will be elucidated below.

3. Value Range of Erosion Coefficient

3.1. Randomness of Snow Particle Radius. Wind-induced snow drifting contains snow particles with different radius. Budd [3] analyzed the particle radius distribution through field investigation. He suggested that the drifted snow particle radius obeys two-parameter gamma distribution and gave out the distribution of snow radius along the height Schmidt et al. [21, 22]. A specific formula for this distribution function is given as follows Schmidt [21]:

$$f(r_{\rm p}) = \frac{r_{\rm p}^{(\alpha-1)} e^{\left(-r_{\rm p}/\beta\right)}}{\beta^{\alpha} \Gamma(\alpha)},\tag{8}$$

$$\Gamma(\alpha) = \int_0^\infty x^{\alpha - 1} \exp(-x) \, dx,\tag{9}$$

$$\alpha = 4.08 + 12.6z,\tag{10}$$

where $f(r_p)$ represents the probability density function of snow particle radius, α is the shape parameter of gamma distribution which is proportional to height z from snow surface, β is the scale parameter of gamma distribution, and Γ is a gamma distribution.

It can be seen that α and β are related to average snow radius $r_{\rm m}$ and height z. The relationship among these parameters can be further described by the following equations:

$$\beta = \frac{r_{\rm m}}{\alpha},\tag{11}$$

$$r_m = 4.6 \times 10^{-5} z^{-0.258}. (12)$$

It is easy to see from the equation that average snow particle radius $r_{\rm m}$ will decrease as the height z from snow surface increases.

3.2. Randomness of Erosion Coefficient. From the above analysis, we can see the distribution of particle size is highly depending on the height z from snow surface. Snow particle radius varies inversely with z. Tabler's work indicated that when the 10 m height wind speed is less than 12 m/s, saltation is predominant transportation [23]. Bagnold [24] suggested that the height should be within 0.1 meter.

Therefore, based on these concerns, in the following part, we only investigate the value range of $A_{\rm ero}$ at three selected heights, namely, z = 0.02 m, 0.05 m, and 0.1 m.

To determine the value range of A_{ero} , the calculation is split into four steps. Firstly, based on the surface height value z (0.02 m, 0.05 m, and 0.1 m), the values of α and β are calculated from Equations (10)–(12). Second, based on the values of α and β , the gamma distribution function for the snow particle radius is constructed. Thirdly, substitute the distribution function for snow particle radius $f(r_p)$ into Equation (7). By utilizing the kernel smoothing density estimation, probability density distribution function of A_{ero} can be directly obtained (Figure 1(a)). Finally, the cumulative distribution function for erosion coefficient can be derived based on the density function (Figure 1(b)). The comparison between the investigated erosion coefficients at different heights and the reported results in the literature is also illustrated in Figure 1. The estimated statistical parameter values in Figure 1 are recorded in Table 1.

Figure 1(a) shows that the value of $A_{\rm ero}$ concentrates at a value around 1.0×10^{-4} . The probability of values of $A_{\rm ero}$ higher than 2.5×10^{-4} is very small. From the observation of Figure 1(b), we can see that the proposed distribution model has a larger prediction value of erosion coefficient compared to the field experiment results. And this prediction tends to decrease with the increase of surface height. In fact, the model for erosion coefficient at a surface height of 0.05 m has a perfect fit to the results reported in Schmidt [13]. However, on the other hand, results reported in Budd (1966) are more closer to the model predictions for erosion coefficient at a surface height of 0.1 m. This shows how the value of $A_{\rm ero}$ changes with the surface height while considering the randomness in snow particle size.

Besides the effects from randomness of snow particle radius, the erosion coefficient is also largely affected by the snow density $\rho_{\rm p}$ and coefficient γ . Here, a short parametric study is also provided to investigate the influences from these two parameters. In order to have a fair comparison, the surface height in this case is assumed to be unchanged. The values of the gamma distribution parameters are assumed to be constant; for example, $\alpha = 5$ and $\beta = 20$ are adopted in this case, Table 2. Based on Equation (7), a comparison of erosion coefficient for using different snow particle density and snow particle radius is shown in Figure 2. The compared value is the 95 percentile in the distribution function of A_{ero} . It is seen from the figure that when $\rho_{\rm p}$ varies between 300 kg·m⁻³ and 900 kg·m⁻³ and $r_{\rm p}$ varies between 50 μ m and 150 μm (common assumption), the value range of $A_{\rm ero}$ is $1.96 \times 10^{-4} \sim 1.6 \times 10^{-3}$. The influence of γ to $A_{\rm ero}$ is also shown in Figure 3. It can be seen from Figure 3 that the influence of coefficient γ to erosion coefficient A_{ero} is quite significant which should not be ignored. However, we have to point out the inherent relationship among snow particle radius, density, and coefficient γ is still not clear yet. In reality, these factors could be dependent on each other. The value range of the erosion coefficient could be enlarged considering a positive dependence in the parameters. Therefore, the results presented here have its limitations. The results are assuming an independent relationship among the

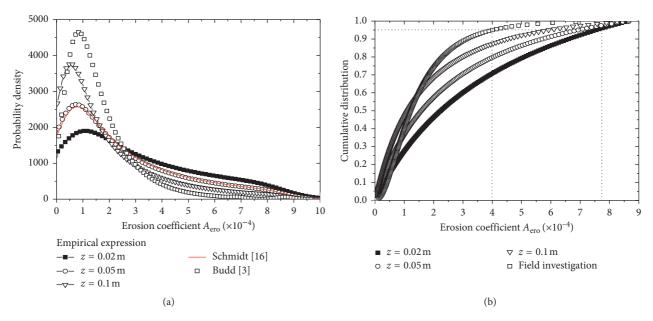


Figure 1: (a) Probability density distribution of A_{ero} and (b) cumulative distribution of A_{ero} .

TABLE 1: Parameter values in Figure 1.

D	Surface height z (m)			D., 11 [2]	C-l: 14 [12]
Parameter	0.02	0.05	0.1	Budd [3]	Schmidt [13]
α(m)	4	4.7	6	15	5
β	30	21	15	4	20
$r_{\rm m}$ (μ m)	120	100	90	80	100

Note: $\rho_{\rm a} = 1.25 \, {\rm kg \cdot m^{-3}}, \; \rho_{\rm p} = 500 \, {\rm kg \cdot m^{-3}}, \; \gamma = 10^5 \, {\rm N^{-1} \cdot s^{-1}}, \; r_{\rm p} = (1 \sim 150) \, \mu {\rm m}.$

TABLE 2: Parameter values in Figures 2 and 3.

$\alpha(m)$	β	$r_{ m m}\left(\mu{ m m}\right)$	$\rho_{\mathrm{p}}(\mathrm{kg}\!\cdot\!\mathrm{m}^{-3})$	$\rho_{\rm a}({\rm kg}{\cdot}{\rm m}^{-3})$	$\gamma(N^{-1}\cdot s^{-1})$	$r_{\rm p} (\mu {\rm m})$
5	20	50~150	300~900	1.25	$10^5 \sim 10^7$	50~150

considered parameters. It should be further validated through field investigation while considering all physical reasons about the parameter interactions.

4. Case Study: Prediction of Snow Distribution around Cube Structure

To demonstrate the applicability of the proposed model for erosion coefficient, this section will conduct a case study on a real engineering snow problem. In this case study, the objective is to predict the snow distribution around a cube structure when there is snow drifting. As discussed in the former section, erosion coefficient changes with different snow conditions. Therefore, herein, we considered two different snow conditions, namely, fresh snow condition and old snow condition, in the analysis. The field experiment has already been carried out by authors in 2009 in Harbin [7, 25]. These results will be used as a reference to compare with the numerical analysis in this paper.

4.1. Numerical Model Analysis. In order to put in the model of erosion coefficient, the numerical model for the problem is established first. The computational domain and meshing are constructed at a model scale which is exactly corresponding to the field investigation. The dimensions of the cube structure model are $0.2 \times 0.2 \times 0.2 \text{m}^3$ (H = 0.2 m). The dimension of the simulation domain is $3.2 \times 1.2 \times 1.2 \text{m}^3$. The meshing of the model includes 2096000 hexahedral elements. The minimum volume of the elements is $1.357 \times 10^{-6} \, \text{m}^3$, while the maximum volume of the element is $2.26 \times 10^{-6} \, \text{m}^3$. The details of the meshing are illustrated in Figure 4.

The inlet of the simulation domain adopted velocity inlet boundary. The wind-velocity profile inside the simulation domain is defined based on the logarithmic law as follows:

$$u(z) = \frac{u_*}{k} In\left(\frac{z + z_0}{z_0}\right),\tag{13}$$

where z_0 is the roughness height which can be determined from the field experiment (in this case, $z_0 = 0.2 \text{ mm}$) and u_*

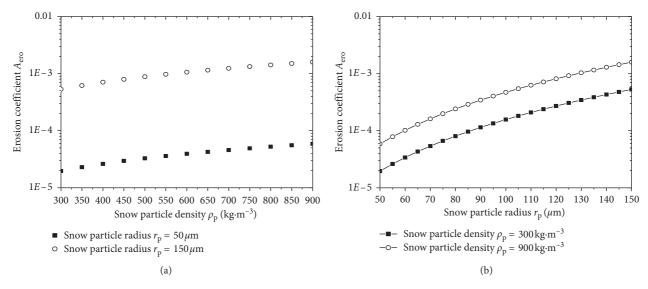


Figure 2: (a) Relationship between $A_{\rm ero}$ (95 percentile) and $\rho_{\rm p}$ and (b) relationship between $A_{\rm ero}$ (95 percentile) and $r_{\rm p}$.

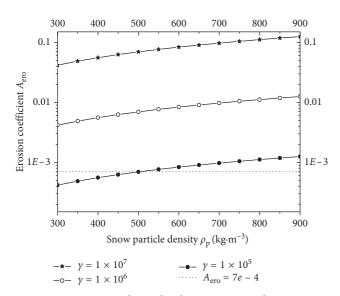


Figure 3: Relationship between $A_{\rm ero}$ and γ .

is the friction velocity which can be determined based on the values of $u_{\rm ref}$ and $z_{\rm ref}$ (0.2 m) from the field experiment. Furthermore, k is the von Karman constant (0.42) and z is the height coordinate. The turbulent kinetic energy K is calculated from the mean wind speed and the measured turbulence intensity using the following equation:

$$K(z) = \alpha \left[I_{11}(z)u(z) \right]^2, \tag{14}$$

where $I_{\rm u}$ is the measured streamwise turbulence intensity and α is a parameter ranging from 0.5 to 1.5 [14]. In this study, a value of 1.5 is adopted for α . The turbulence dissipation rate ε can be estimated by the following equation:

$$\varepsilon = \frac{u_*^3}{k(z + z_0)}. (15)$$

Therefore, based on the model, the vertical profiles of u(z) and I_u inside the simulation domain and around the

cube structure (incident profiles) are simulated and calculated (Figure 5).

The simulation domain is assumed to be symmetric along the vertical and horizontal directions. The surface of the cube structure is assumed to be stationary walls. The commercial CFD code, ANSYS Fluent 15, is used to perform the simulations. UDF files are added to simulate snow drifting. The 3D steady Reynolds-averaged Navier–Stokes (RANS) equations are solved in combination with the $k-\varepsilon$ model. The SIMPLE algorithm is used for pressure-velocity coupling. The pressure interpolation applied here is second order. Convergence is assumed to be obtained when all the scaled residuals leveled off and reached a minimum of 10^{-6} for x, y, and z momentum, 10^{-4} for k and ε .

4.2. Results and Discussion

Figure 6 shows the results of numerical simulation and field investigation for the investigated problem with consideration of fresh snow. The values of parameters for this simulation are shown in Table 3. Figure 7 shows the results of numerical simulation and field investigation for the same problem with consideration of old snow condition which was compressed by wind. The values of parameters for this simulation are shown in Table 4.

The values of snow radius, density, and threshold friction velocity in Tables 3 and 4 are based on field investigation [7]. The value of γ is taken from the suggested value provided by Schmidt and Shoa [15, 16]. Therefore, erosion coefficient can be calculated based on these parameters and the developed method. In this study, erosion coefficient for fresh and dry snow is about 10^{-3} and 7×10^{-4} for old and wind compressed snow. The results showed that the numerical predictions can accurately depict the real phenomenon. The difference of snow distribution between numerical simulation and field investigation is quite small, indicating the applicability of the proposed approach. Meanwhile, from the observation of Figures 6 and 7,

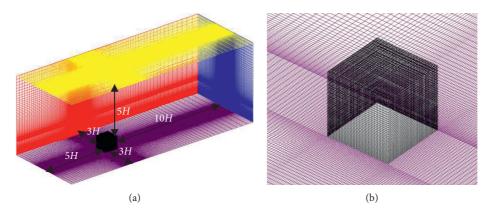


FIGURE 4: Perspective view and meshing of simulation domain and cube structure: (a) perspective view of the simulation domain and (b) meshing around the cube structure.

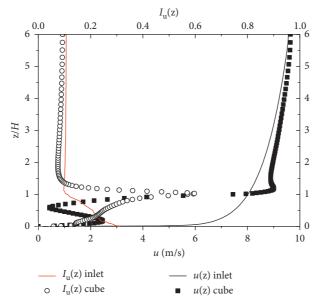


FIGURE 5: Profiles of the mean wind speed (u) and turbulent kinetic energy (K).

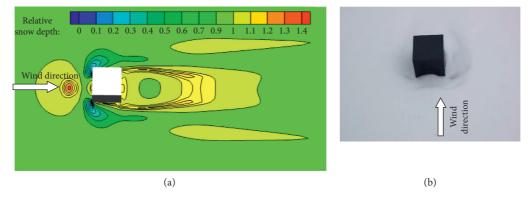


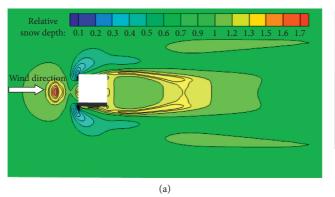
FIGURE 6: (a) Numerical simulation and (b) field investigation of snow distribution around a cube structure with fresh and dry snow.

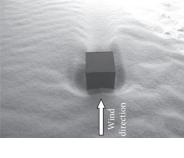
it should be noticed that the snow condition has a significant influence on the snow distribution. This is mainly due to the differences in erosion coefficient. The value of erosion

coefficient is largely depending on the snow property parameters. It further proves that we should not use the same erosion coefficient for different snow conditions.

TABLE 3: Parameter	17011100	for	cimulating	frach	and	dry	CHOTA
TABLE 5: Parameter	varues	101	simulating	rresn	and	ary	snow.

Parameters	r (μm)	$\rho_a (kg/m^3)$	$\rho_{\rm p}({\rm kg/m^3})$	$\gamma(N^{-1}\cdot s^{-1})$	u_{*t} (m/s)	t (s)
Value	100	1.25	170	10^{6}	0.2	240





(b)

FIGURE 7: (a) Numerical simulation and (b) field investigation of snow distribution around a cube structure with old and wind exposed

TABLE 4: Parameter values for simulating old and wind compressed snow.

Parameters	r(µm)	$\rho_{\rm a}({\rm kg/m^3})$	$\rho_{\rm p}({\rm kg/m^3})$	$\gamma(N^{-1}\cdot s^{-1})$	<i>u</i> _{*t} (m/s)	t (s)
Value	150	1.25	400	10^{5}	0.35	3600

5. Conclusion

In this technical note, a study on the determination of erosion coefficient is provided. Several parameters which are quite influential to erosion coefficient are being investigated. This includes air density ρ_a , snow particle density ρ_p snow radius r_p , and experiment coefficient γ . An equation of calculating the erosion coefficient for considering these important parameters is derived. By considering the randomness of snow radius, the randomness and value range of erosion coefficient are presented. A case study is conducted to demonstrate the applicability of the proposed approach. It was found that the developed approach can give a perfect prediction of the snow distribution when it is compared to the field investigation. And results showed that the erosion coefficient is very sensitive to the snow conditions. However, the dependences among snow parameters are not considered in this paper. The conclusions and results drawn from this technical note have to be used in view of these limitations. Future work should be put on the investigation of the importance of parameter dependences to the erosion coefficient.

Notations

$A_{\rm ero}$:	Snow surface erosion coefficient (kg·m 3)
$d_{\mathfrak{p}}$:	Diameter of snow particle (m)
g:	Acceleration of gravity (m⋅s ⁻²)
N_a :	Drifting snow particles in unit horizontal
	area per unit time $(m^{-2} \cdot s^{-1})$

$q_{\text{ero}}(x)q_{\text{dep}}(x)$:	Erosion/deposition flux (kg⋅m ⁻² s ⁻¹)
$r_{\rm p}$:	Radius of snow particles (m)
u_{10}^{r} :	10 m wind velocity (m⋅s ⁻¹)
u_{ref} :	Average wind velocity at reference height
101	$(m \cdot s^{-1})$
u_*, u_{*t} :	Friction velocity and threshold friction
	velocity of surface (m·s ⁻¹)
$V_{\mathfrak{p}}$:	Volume of snow particle (m ³)
$w_{\mathrm{f}}^{\mathrm{r}}$:	Settle velocity of snow particle (m·s ⁻¹)
α:	Shape parameter of gamma distribution
	(m)
β:	Length scale parameter of gamma
	distribution (dimensionless)
Γ:	Gamma distribution
ρ_a :	Air density (kg⋅m ⁻³)
ρ_{p} :	Snow particle density (kg⋅m ⁻³)
τ :	Shear stress of snow surface $(N \cdot m^{-2})$
τ_{t} :	Threshold shear stress of snow surface
-	$(N \cdot m^{-2})$
v:	Viscosity coefficient of air motion $(m^2 \cdot s^{-1})$
μ :	Aerodynamic coefficient of viscosity
•	$(kg \cdot m^{-2}s^{-1})$
γ:	Experimental constant $(N^{-1} \cdot s^{-1})$.

Data Availability

The data used to support the findings of this study are available from the corresponding author upon request.

Conflicts of Interest

The authors declare that there are no conflicts of interest regarding the publication of this paper.

Acknowledgments

This research was supported by the Innovation Foundation in Youth Science and Technology Team of Hubei Province (no. T201823), 2017 Provincial Teaching Reform Research Project (no. 2017A09), Hubei Polytechnic University Talent Introduction Project (no. 13xjz07R), Natural Science Fund of Hubei Province (2012FKC14201 and 2013CFC103), Scientific Research Fund of Hubei Provincial Educational Department (no. D20134401), and Innovation Foundation in Youth Team of Hubei Polytechnic University (no. Y008).

References

- [1] R. A. Bagnold, *The Physics of Blown Sand and Desert Dunes*, Methuen, London, UK, 1941.
- [2] J. H. M. Beyers, P. A. Sundsbø, and T. M. Harms, "Numerical simulation of three-dimensional, transient snow drifting around a cube," *Journal of Wind Engineering & Industrial Aerodynamics*, vol. 92, no. 9, pp. 725–747, 2004.
- [3] W. F. Budd, *The Drifting of Nonuniform Snow Particles, Studies in Antarctic Meteorology*, American Geophysical Union, Washington, DC, USA, 2013.
- [4] P. Delpech, P. Palier, and J. Gandemer, "Snowdrifting simulation around Antarctic buildings," *Journal of Wind Engi*neering and Industrial Aerodynamics, vol. 74–76, pp. 567–576, 1998.
- [5] R. S. Anderson and P. K. Haff, "Wind modification and bed response during saltation of sand in air," *Acta Mechanica Supplementum*, vol. 1, no. 1, pp. 21–51, 1991.
- [6] Y. Zhang, C. W. Kim, M. Beer, H. Dai, and C. G. Soares, "Modeling multivariate ocean data using asymmetric copulas," *Coastal Engineering*, vol. 135, pp. 91–111, 2018.
- [7] Y. Shoa, "Numerical modelling of saltation in the atmospheric surface layer boundary-layer meteorology layer," *Boundary-Layer Meteorology*, vol. 91, no. 2, pp. 199–225, 1999.
- [8] F. Naaim-Bouvet, H. Bellot, K. Nishimura et al., "Detection of snowfall occurrence during blowing snow events using photoelectric sensors," *Cold Regions Science and Technology*, vol. 106-107, pp. 11–21, 2014.
- [9] F. Naaim-Bouvet and P. Mullenbach, "Field experiments on "living" snow fences," *Annals of Glaciology*, vol. 26, pp. 217–220, 1998.
- [10] M. Naaim, F. Naaim-Bouvet, and H. Martinez, "Numerical simulation of drifting snow: erosion and deposition models," *Annals of Glaciology*, vol. 26, pp. 191–196, 1998.
- [11] M. O'rourke, A. Degaetano, and J. D. Tokarczyk, "Snow drifting transport rates from water flume simulation," *Journal* of Wind Engineering & Industrial Aerodynamics, vol. 92, no. 14-15, pp. 1245–1264, 2004.
- [12] T. Okaze, Y. Takano, A. Mochida, and Y. Tominaga, "Development of a new k–ε model to reproduce the aerodynamic effects of snow particles on a flow field," *Journal of Wind Engineering and Industrial Aerodynamics*, vol. 144, pp. 118–124, 2015.
- [13] R. Schmidt, "Vertical profiles of wind speed, snow concentration, and humidity in blowing snow," *Boundary-Layer Meteorology*, vol. 23, no. 2, pp. 223–246, 1982.

[14] K. Yan, T. Cheng, and Y. Zhang, "A new method in measuring the velocity profile surrounding a fence structure considering snow effects," *Measurement*, vol. 116, pp. 373–381, 2018.

- [15] R. A. Schmidt, "Estimates of threshold windspeed from particle sizes in blowing snow," Cold Regions Science and Technology, vol. 4, no. 3, pp. 187–193, 1981.
- [16] R. A. Schmidt, "Measuring particle size and snowfall intensity in drifting snow," *Cold Regions Science and Technology*, vol. 9, no. 2, pp. 121–129, 1984.
- [17] Y. Shao and A. Li, "Numerical modelling of saltation in the atmospheric surface layer," *Boundary-Layer Meteorology*, vol. 91, no. 2, pp. 199–225, 1999.
- [18] P.-A. Sundsbø, "Numerical simulations of wind deflection fins to control snow accumulation in building steps," *Journal of Wind Engineering and Industrial Aerodynamics*, vol. 74–76, pp. 543–552, 1998.
- [19] R. D. Tabler, Snow Fence Handbook: (Release 1.1), Tabler & Associates, Niwot, CO, USA, 1988.
- [20] T. K. Thiis, "Large scale studies of development of snowdrifts around buildings," *Journal of Wind Engineering and In*dustrial Aerodynamics, vol. 91, no. 6, pp. 829–839, 2003.
- [21] Y. Tominaga, A. Mochida, R. Yoshie et al., "AIJ guidelines for practical applications of CFD to pedestrian wind environment around buildings," *Journal of Wind Engineering and In*dustrial Aerodynamics, vol. 96, no. 10-11, pp. 1749–1761, 2008.
- [22] Y. Tominaga, T. Okaze, and A. Mochida, "CFD modeling of snowdrift around a building: an overview of models and evaluation of a new approach," *Building and Environment*, vol. 46, no. 4, pp. 899–910, 2011.
- [23] T. Uematsu, T. Nakata, K. Takeuchi, Y. Arisawa, and Y. Kaneda, "Three-dimensional numerical simulation of snowdrift," *Cold Regions Science and Technology*, vol. 20, no. 1, pp. 65–73, 1991.
- [24] B. R. White and J. C. Schulz, "Magnus effect in saltation," Journal of Fluid Mechanics, vol. 81, no. 3, pp. 497–512, 1977.
- [25] A. Winstral, D. Marks, and R. Gurney, "Simulating windaffected snow accumulations at catchment to basin scales," *Advances in Water Resources*, vol. 55, pp. 64–79, 2013.

Hindawi Shock and Vibration Volume 2018, Article ID 5460362, 15 pages https://doi.org/10.1155/2018/5460362

Research Article

Experimental Study of the Debris Flow Slurry Impact and Distribution

Haixin Zhao,¹ Lingkan Yao ,¹,¹,²,³ Yong You ,⁴ Baoliang Wang ,¹ and Cong Zhang¹

Correspondence should be addressed to Lingkan Yao; yaolk@swjtu.edu.cn

Received 13 March 2018; Revised 3 July 2018; Accepted 5 August 2018; Published 5 September 2018

Academic Editor: Elena Dragomirescu

Copyright © 2018 Haixin Zhao et al. This is an open access article distributed under the Creative Commons Attribution License, which permits unrestricted use, distribution, and reproduction in any medium, provided the original work is properly cited.

In this study, we present a new method to calculate debris flow slurry impact and its distribution, which are critical issues for designing countermeasures against debris flows. There is no unified formula at present, and we usually design preventive engineering according to the uniform distribution of the maximum impact force. For conducting a laboratory flume experiment, we arrange sensors at different positions on a dam and analyze the differences on debris flow slurry impact against various densities, channel slopes, and dam front angles. Results show that the force of debris flow on the dam distributes unevenly, and that the impact force is large in the middle and decreases gradually to the both sides. We systematically analyze the influence factors for the calculation of the maximum impact force in the middle point and give the quantitative law of decay from the middle to the sides. We propose a method to calculate the distribution of the debris flow impact force on the whole section and provide a case to illustrate this method.

1. Introduction

Debris flow impact force includes slurry impact and huge rock impact, which provide the mechanical bases for checking engineering structures, including calculations for antisliding and anti-overturning [1-4]. The magnitude of the slurry impact force is one of the most important parameters for the Sabo dam design determining the movement of debris flow and its impact on the dam, especially for debris flow without huge rocks. Many formulas have been proposed to calculate the debris flow impact. Fei and Shu [5] conducted theoretical analysis and many simulation experiments on impact force and established a calculation model of the debris flow impact, according to different particle movement types. He et al. [6] proposed several methods for calculating the impact force of the large rock mass on the basis of elastoplastic theory. Chen et al. [7, 8] simplified the debris flow as solid-liquid two-phase flow and

established the calculation of the two phases of the debris flow based on the theory of phase flow velocity as well as debris flow impact time. Armanini and Scotton [9] proposed a formula for the impact force based on a momentum conservation analysis to study the impact force of debris flow. Zeng [10] systematically studied differences in the vertical distribution of the impact force of debris flow and evaluated building vulnerability.

The formulas to calculate the impact force of debris flow are given in Table 1.

The formulas in Table 1 are modified by the theoretical formula based on the energy method. The correction coefficient which is empirically based varies according to the factors considered. The theory of the energy method is derived by hydraulics, which is suitable for the general uniform flow, such as water, but it is not suitable for nonuniform flow [16–18], such as debris flow. A debris flow is a rapid, gravity-driven mass movement that involves

¹School of Civil Engineering, Southwest Jiaotong University, Chengdu 610031, China

²MOE Key Laboratory of High-Speed Railway Engineering, Chengdu 610031, China

³National Engineering Laboratory for Technology of Geological Disaster Prevention in Land Transportation, Chengdu 610031, China

⁴Institute of Mountain Hazards and Environment, CAS, Chengdu 610041, China

TABLE 1: Debris flow slurry impact formulas.

Number	Formula for debris flow impact	Reference
1	$P = \rho_{\rm s} \cdot H \cdot v^2 / g$	Mizuyama [1]
2	$P = \lambda \cdot \gamma_{\rm c} \cdot v^2 / g \cdot \sin \beta$	Chen [11]
3	$P = \rho_{\rm s} \cdot A \cdot v^2 \cdot \sin \beta$	Hungr et al. [12]
4	$P = k \cdot \gamma_c \cdot v^2/g$	Li [13] and Zhou [14]
5	$P = 5 \cdot \rho_{\rm s} \cdot v^{0.8} \cdot (g \cdot H)^{0.6}$	Hübl and Holzinger [15]
6	$P = 5.3 \cdot F_r^{-1.45} \cdot \rho_s \cdot v^2$	Zeng [10]

P is the debris flow impact force; ρ_s is the debris flow density; H is the mud depth; ν is the mean velocity of the debris flow; g is the acceleration of gravity; λ is the shape correction coefficient; γ_c is the gravity density of the debris flow; β is the impact angle; A is the cross-sectional area; k is the empirical coefficient; F_r is the Froude number.

water-charged, predominantly coarse-grained inorganic and organic materials. A positive correlation does not necessarily exist between the impact force of debris flow and the square of the mean velocity. Simply adding the correction coefficient does not guarantee the accuracy of the formula; as such, further discussion and improvement of the current methods are required.

Conversely, we usually take the debris flow impact force on the prevention engineering as a uniform distribution according to the maximum impact force. This makes the predicted overall structure resistance much larger than the actual overall structure resistance. Meanwhile, to ensure the safety of the weakest part, we also waste the construction material on the safer part such as the both sides of the top edge of the dam. Some scholars have studied the distribution of the impact force of the debris flow through an inhomogeneous distribution of flow velocity [19, 20]. Han et al. [21] presented a new approach for exploring the debris flow velocity distribution in a cross section that used an iteration algorithm based on the Riemann integral method to search an approximate solution to the unknown flow surface. In fact, their work emphasized the effect of terrain on the distribution of velocity and the impact force but did not consider internal interactions of debris flow and external interactions to the both sides of the channel.

In this paper, we arrange sensors at different positions on the dam and analyze the different debris flow slurry impact on the dam with various densities, channel slopes, and dam front angles through the laboratory flume experiment test. This study shows that the force of debris flow on the dam is unevenly distributed, and the impact force is large in the middle and small at both ends. We systematically analyzed the factors influencing the calculation of the maximum impact force in the middle point and give the quantitative law of decay from the middle to the sides. We propose a method for calculating the distribution of the debris flow impact force on the whole section and provide a case to illustrate this method.

2. Physical Model

We conducted our experiments in a debris flow simulation laboratory at the Institute of Mountain Hazards and

Environment, which belongs to the Chinese Academy of Sciences (CAS). The flume consists of seven parts: hopper, flume, tailings poll, dam model, camera, gate, and acquisition instrument. Figure 1 is a schematic illustration of the model experiment. The cube hopper is 60 cm in length, 60 cm in width, and 80 cm in height. It has the capacity of 0.1 m³, and it is affixed to the flume and controlled the discharge from the gate. We conducted our experiments in a flume with a length of 400 cm, a width of 30 cm, and a height of 40 cm. The gradient of the flume was adjustable from 0° to 20°. We placed a dam model at the bottom of the flume. The dam modeled has a surface slope of 63°. We used the tailings pool to recycle the debris flow.

The distance between the front edge of the dam model and the gate is 6 m, which helps to stabilize the debris flow velocity and prevents rapid changes at the impact location. We installed eight sensors on the surface of the model dam. Figure 2 shows the size of the surface of the dam, the surface size of the sensor, and the location of the sensor arrangement.

In this study, we used a piezoelectric-type sensor whose range is 0–100 kPa with a sensitivity of 0.1%. The acquisition frequency is 2 kHz, and the sampling duration is 32 s. We opened the gate, and the debris quickly flowed out and affected the model dam under the action of gravity. Sensors installed on the dam can quickly collect the impact force of debris flow on the dam. We obtained impact force data by computer processing. Figure 3 shows the impact of debris flow on the dam. The experimental process does have errors, including electromagnetic interference and improper operation. We completed three repetitions to obtain intermediate data to minimize these errors.

We collected experimental material samples from sites located in Gan Gully, which is the Level 1 tributary canal of the Yinchang Gully in the upper stream of the Qian River in the Longmen mountain town of Pengzhou, Sichuan Province. This location experienced an outbreak of large-scale debris flow at the night of August 18, 2012. The specific sampling sites were located on the eastside of the alluvial fan. The maximum particle size of the experimental materials was 20 mm. We took five random samples for grain-size distribution analysis before conducting the experiments. Figure 4 shows the grain-size distribution of the experimental materials.

We mainly considered the effect of debris flow densities and channel slopes on the impact force. Meanwhile, the mass volume of debris flow was a major factor for designing countermeasures against debris flows in the field. In addition, we explored whether the dam front angles affected the impact force. Therefore, we designed three tests groups. Group A mainly analyzed the influence of debris flow density and channel slope on impact force. Group B mainly analyzed the influence of dam front angles on the impact force combined with Group A. Group C mainly analyzed the influence of debris flow mass volume on the impact force combined with Group A. After setting up the experimental apparatus and preparing the experimental materials, we carried out 33 group tests according to the experimental scheme shown in Tables 2 and 3.

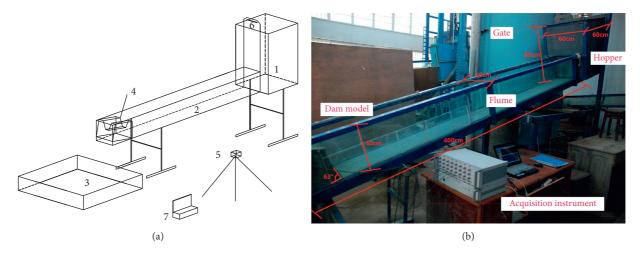


FIGURE 1: Experimental apparatus. 1: hopper; 2: flume; 3: tasilings poll; 4: dam model; 5: camera; 6: gate; 7: acquisition instrument.

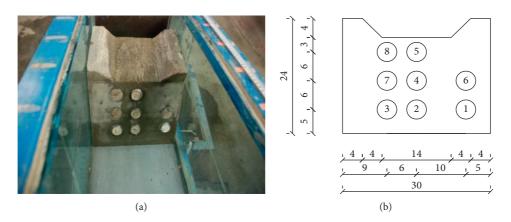


FIGURE 2: Size of the surface of the dam, surface size of the sensor, and location of the sensor arrangement.

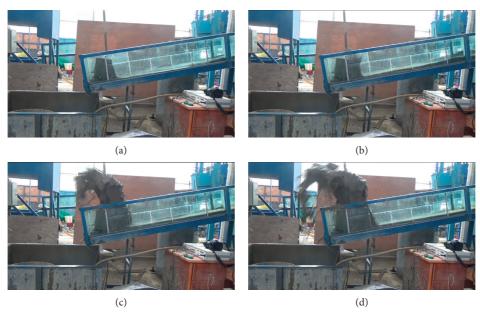


FIGURE 3: Continued.

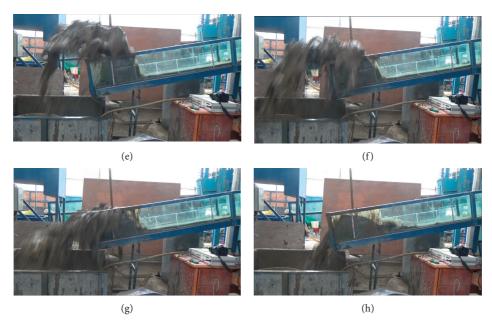


FIGURE 3: The phenomenon of the impact of debris flow on the dam. Time-series photos of (a) debris flow accelerating; (b) the front of the debris flow touching the dam; (c)–(f) debris flow affecting the dam and the dam changing the debris flow pattern; (g) the impact mitigation; (h) the swing back of silt.

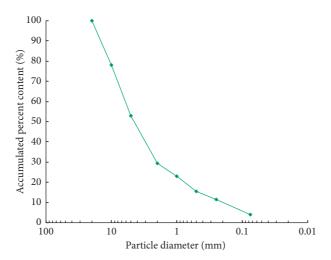


Figure 4: Particle gradation of the materials used in the experiment.

TABLE 2: The experimental conditions	for the 33 performed laboratory tests.
	V 1:4:

Tanta	Tooto Too	Various experimental conditions					
Tests group	Tests Tag number	Debris flow density (kN/m³)	Debris flow mass volume (L)	Channel slope (°)	Dam model front angles (°)		
A	Case 1 to 25	13, 15, 17, 19, 21	60	7, 10, 11, 13, 15	63		
В	Case 26 to 29	13, 17	60	9	77,90		
С	Case 30 to 33	17, 19	90, 120	13	63		

3. Characteristics of Debris Flow Maximum Impact Force

3.1. Maximum Impact Force Compared with Former Formula. The impact force collected by sensors 1, 2, and 3 is obviously greater than the other sensors. This is mainly because sensors

1, 2, and 3 are located in the bottom of the dam (as seen in Figure 2), and these positions are directly affected by the impact of debris flow. The first three sensors are arranged within the depth of the mud, whereas the others are arranged upon the mud depth (as seen in Figure 2). Through theoretical analysis, we know that the greater the velocity in the range

TABLE 3: The experimental conditions and results for 33 laboratory tests.

	Tests		ī	Mass	Dam model Impact Impact I		Impact							
Tests group	Tag number	Density (kN/m^3)	Flume slope (°)	volume (L)	front slope (°)	ν (m/s)	force 1# (kPa)	force 2# (kPa)	force 3# (kPa)	force 4# (kPa)	force 5# (kPa)	force 6# (kPa)	force 7# (kPa)	force 8# (kPa)
	1	13	7	09	64	2.321	4.558	5.022	4.625	2.963	1.055	1.507	2.704	0.669
	2	15		09	64	2.115	2.880	3.216	2.904	1.026	0.740	0.384	1.672	0.332
	3	17		09	64	2.000	2.005	2.301	2.265	1.950	0.506	0.003	1.290	0.180
	4	19	7	09	64	1.146	1.096	1.211	1.200	0.263	0.000	0.103	0.713	0.000
	5	21	7	09	64	1.058	1.382	1.509	1.497	1.151	0.000	0.260	0.898	0.000
	9	13	6	09	64	2.500	3.610	4.750	4.000	2.993	1.140	1.456	2.200	0.710
	^	15	6	09	64	2.080	2.490	3.610	3.050	2.238	0.830	0.850	1.640	0.529
	∞	17	6	09	64	1.786	3.770	4.150	3.850	2.656	0.913	1.564	2.520	0.643
	6	19	6	09	64	1.563	3.870	4.030	3.900	2.620	0.846	1.639	2.090	0.492
	10	21	6	09	64	1.441	3.610	4.180	3.800	2.550	0.000	1.436	2.430	0.000
	11	13	11	09	64	2.625	5.060	5.980	5.550	3.767	1.435	2.783	3.030	0.434
	12	15	11	09	64	2.386	4.150	4.570	4.200	3.879	1.005	1.833	2.240	0.194
А	13	17	11	09	64	2.188	3.600	4.120	3.880	1.896	1.056	1.520	2.078	0.150
	14	19	11	09	64	1.750	4.280	4.550	4.300	4.067	0.741	1.884	2.330	0.211
	15	21	11	09	64	1.710	4.130	4.550	4.440	2.821	1.171	1.792	2.424	0.205
	16	13	13	09	64	3.250	7.380	8.180	8.100	4.908	1.550	3.569	4.310	1.427
	17	15	13	09	64	2.954	5.140	6.480	5.820	3.823	1.716	2.279	2.932	1.029
	18	17	13	09	64	2.500	5.200	5.420	5.320	3.415	1.142	2.313	2.622	0.944
	19	19	13	09	64	1.204	5.810	090'9	5.990	3.515	1.573	2.650	3.014	1.018
	20	21	13	09	64	1.548	6.360	6.450	6.430	3.806	1.419	2.943	3.268	1.113
	21	13	15	09	64	4.063	8.340	9.840	089.6	6.199	2.045	3.987	4.998	1.666
	22	15	15	09	64	3.250	7.410	8.300	8.040	5.229	2.326	3.466	4.004	1.387
	23	17	15	09	64	2.954	6.460	7.240	006.9	4.561	2.193	2.933	3.310	0.653
	24	19	15	09	64	2.708	12.700	13.800	13.400	8.556	3.936	6.415	7.200	2.278
	25	21	15	09	64	2.167	14.480	15.720	15.650	9.904	4.458	5.964	8.540	2.861
	26	13	13	09	77	3.250	7.520	8.950	8.000	6.739	2.238	3.336	3.980	1.560
а	27	17	13	09	77	2.500	3.056	3.909	3.472	3.563	0.977	0.961	1.833	0.690
a	28	13	13	09	06	3.250	7.440	8.645	8.400	6.546	1.988	3.192	4.230	1.228
	29	17	13	09	06	2.500	4.500	5.523	5.000	4.579	1.160	2.275	2.760	0.750
	30	17	15	06	64	3.611	9.885	12.191	10.191	086.6	4.682	4.597	5.535	1.782
	31	19	15	06	64	3.250	12.854	14.119	13.090	11.395	4.106	6.720	7.164	2.265
)	32	17	15	120	64	4.063	13.650	17.068	15.380	14.053	4.755	7.248	8.508	2.645
	33	19	15	120	64	3.611	15.520	18.514	17.010	14.964	5.573	7.956	9.356	2.912

of the mud depth, the greater the impact force. Therefore, the impact at the surface of debris flow is supposed to be the maximum. Above this mud depth, the impact force is caused by the debris flow superelevation, which is obviously smaller than the force in the range of the mud depth [10]. Meanwhile, data from sensor 2 is the largest among the first three sensors, and we selected the data from sensor 2 to analyze the maximum impact force. We used a high-resolution camera to measure the average velocity of debris flow and applied formulas 2, 4, and 6 in Table 1. We compared the results with the data from sensor 2 (as shown in Figure 5). The red lines in Figure 5 represent the linear fitting of the experimental values and the calculated values of the impact force of debris flow.

Figure 5 shows that the correlation coefficient between our experimental results and the calculation formulas of Chen [11], Li [11] and Zhou [14], and Zeng [10] are 0.57, 0.56, and 0.79, respectively. The results of the calculation by Li [11] and Zhou [14] are obviously larger than the experimental results. This difference is due to their correction being based on the integration of actual measurement data in the field, including the impact of large stones. The results of Chen's (1983) calculation are in the same range as the experimental results, but the correlation coefficient is poor. The calculated results by Zeng [10] are best fitting the experimental results, but Zeng still used average velocity. In fact, the velocity distribution is not uniform, and the maximum impact force should be related to surface velocity, which is the maximum velocity. Therefore, this paper tries to find the relationship between the surface maximum velocity and the maximum impact force and proposes a new method to calculate the impact force of the maximum debris flow.

3.2. The Influence of Debris Flow Density on Impact Force. We used the same dam model for the upstream slope that we used to determine the maximum impact force. In this case, we analyzed the various debris flow impact force with various debris flow densities under the same scale of debris flow (quality) and the same channel characteristics (flume slope). The experimental results show that when the channel characteristics (flume slope), the dam model upstream slope ratio and the debris flow scale (quality), are the same, the value of the debris impact force does not necessarily increase along with the debris flow density. Figure 6 shows that when the flume slope is 15°, the debris flow impact force decreases gradually, with debris flow density changing from 13 kN/m³ to 17 kN/m³. Although the debris flow impact force increases gradually, the debris flow density changes from 17 kN/m³ to 21 kN/m³. The main cause for this phenomenon is that the velocity of debris flow is obviously reduced as debris flow density increases from 13 kN/m³ to 17 kN/m³, which can be observed in the experiment. When the density changes from 17 kN/m³ to 21 kN/m³, the effect of density on impact force is more significant than that of velocity, although it is still reducing. As the flume slope is bigger, bending becomes more obvious and looks like a "hook," as shown in Figure 6.

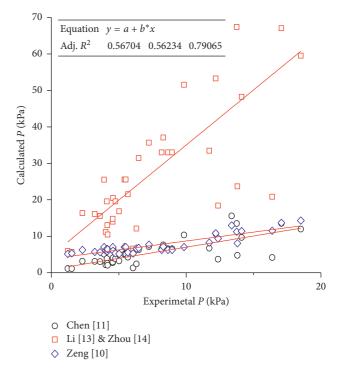


FIGURE 5: Maximum impact force compared with former formula.

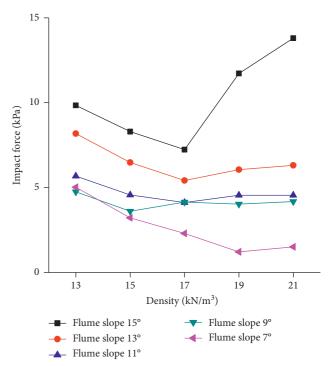


FIGURE 6: The relationship between maximum impact force and density.

3.3. The Influence of Flume Slope on Impact Force. Similarly, we used the same method to analyze the influence of the channel slope on impact force. We used the same dam model for the upstream slope. In this case, we analyzed various debris flow impact forces with various flume slopes under the same scale of debris flow (mass volume) and the

same property of debris flow (density). The experimental results show that the steeper the flume slope, the bigger the impact force. This is because the flume slope directly affects the velocity of debris flow. Figure 7 shows the relationship between the maximum impact force and the flume slope, where γ_c is the density of the debris flow. Corresponding to the density for all five slopes, the greater the slope, the greater the impact value. As density increases, this increasing trend becomes more obvious.

3.4. The Influence of Dam Model Upstream Slope on Impact Force. We used the same mass volume of debris flow (60 L) and flume slope (13°) and selected the density of 13 kN/m³ and $17 \, \text{kN/m}^3$ to analyze the relationship between the maximum impact and the dam model upstream slopes, which are 63°, 76°, and 90°, respectively. Figure 8 shows the experimental result. Our study indicates that the effect of the dam model upstream slope on impact force is not obvious. When the debris flow density was 13 kN/m³, the maximum impact force was 8.2 kPa, 9 kPa, and 8.7 kPa for the upstream slope ratios of 63°, 76°, and 90°, respectively. When the debris flow density was 17 kN/m³, the maximum impact force was 5.4 kPa, 5.3 kPa, and 5.5 kPa for the upstream slopes of 64°, 77°, and 90°, respectively. The change of the impact value is within 10%. This phenomenon is mainly related to the inhomogeneity of the material composition of the debris flow, which results in a different impact direction of the internal particles. These particles are randomly distributed, and a relationship does not necessarily exist between debris flow impact value and dam model upstream slope. Therefore, we do not use the model dam upstream slope in the calculation of the maximum impact force.

3.5. The Influence of Debris Mass Volume on the Impact Force. We used the model dam upstream slope of 64°, selected the debris flow density as 17 kN/m³ and 19 kN/m³, and used the flume slope of 15°. We changed only the debris flow mass volume (60 L, 90 L, and 120 L) and analyzed the impact force. Figure 9 shows the experimental result. Experimental data shows that the impact force of debris flow has a linear positive correlation with the mass volume of debris flow, and the greater the mass volume, the greater the impact. As shown in Figure 9, when the debris flow density was 17 kN/m³, the debris flow impact force increased by 5 kPa and 5.5 kPa, respectively, and the debris flow mass volume increased from 60 L to 90 L and then to 120 L. When the debris flow density was 19 kN/m³, the debris flow impact force increased by 2 kPa and 4 kPa, respectively, and the debris flow mass volume increased from 60 L to 90 L and then to 120 L. The reason for this phenomenon is that the flow mass volume would change the mud depth, which is related to the velocity of the debris flow. Table 4 provides the measured results of the mud depth of the debris flow varying with the mass volume.

3.6. The Influence of Debris Flow Velocity on the Impact Force. Compared with the analysis of the influence of debris flow density, flume slope, model dam upstream slope, and debris

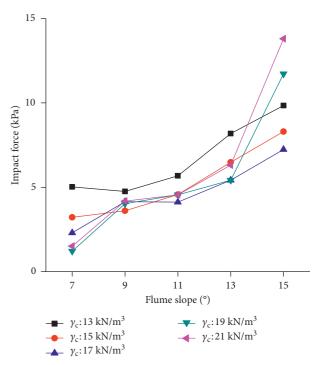


FIGURE 7: The relationship between the maximum impact force and the flume slope.

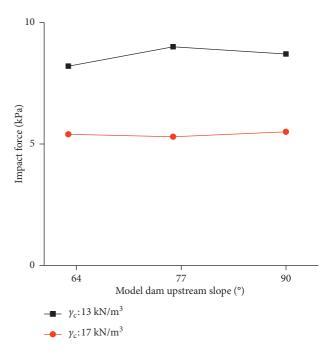


FIGURE 8: The relationship between the maximum impact force and the model dam upstream slope.

flow mass volume, we found that the effects of these factors on impact force are all related to debris flow velocity. Therefore, Zeng [10] used the Froude number to calculate the impact, which had good compatibility with the experimental data, and used mean velocity to calculate the Froude number. The velocity of debris flow is unevenly distributed

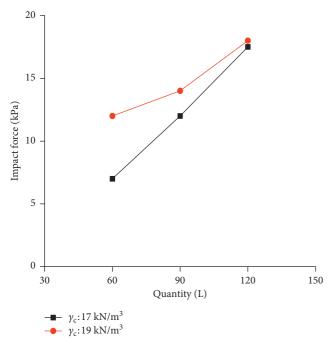


FIGURE 9: The relationship between the maximum impact force and the mass volume.

TABLE 4: Mud depth varies with the mass volume.

Debris flow mass volume (L)	Mud depth with a density of 17 kN/m³ (cm)	Mud depth with a density of 19 kN/m³ (cm)
60	3.93	4.05
90	5.28	5.32
120	6.15	6.18

in the range of mud depth, and surface velocity is much larger, which may introduce an error in the calculation. Furthermore, we studied the relationship between impact force and debris flow surface velocity using this experimental method. Figure 10 shows the experimental results.

The experimental results show that the larger the debris flow surface velocity, the larger the impact force. As density increases, this trend becomes more obvious. As shown in Figure 10, a bigger density corresponds to a larger debris flow surface velocity and a greater increase in the impact force. This finding is different from that given in Section 3.2; changing the density not only changes the impact force but also changes the debris flow surface velocity. Additionally, both the debris flow surface velocity and density will affect the impact force. Furthermore, we define the following three dimensionless parameters in Equations (1)–(3) to show this trend of change:

dimensionless debris flow impact
$$\eta_0 = \frac{P}{\rho_w \cdot v_s^2}$$
, (1)

debris flow Froude number
$$F_{\rm r} = \frac{v_{\rm s}}{\sqrt{gH}}$$
, (2)

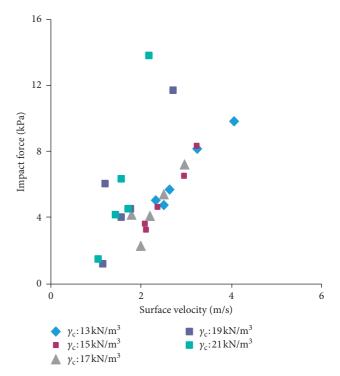


FIGURE 10: The relationship between maximum impact force and debris flow velocity.

dimensionless debris flow density
$$\gamma_0 = \frac{\gamma_c}{\gamma_w}$$
. (3)

Based on this dimensionless analysis, the relationship between these 3 dimensionless parameters is defined in Equation (4):

$$\eta_0 = f(F_r, \gamma_0). \tag{4}$$

Using this method, we established the empirical equation using nonlinear multiple regression analysis. We indicated that the relationship among these three dimensionless numbers depends on a series of experimental data, as shown in Equation (5):

$$\eta_0 = 0.18 \cdot F_{\rm r}^{0.0052} \gamma_0^{1.8142}. \tag{5}$$

The correlation coefficient between the measured value and predicted value is 0.87, and the maximum deviation is $\pm 29\%$. Figure 11 shows the comparison between the measured and predicted $P/(\rho_{\rm w}v_{\rm s}^2)$ by Equation (5). The fitting results show that using the debris flow surface velocity for the dimensionless parameter analysis, the positive proportional relationship between the impact and the surface velocity squared is obvious and the scale coefficient is related to debris flow density. The new formula fully embodies the characteristics of debris flow and is directly related to the debris flow surface velocity, which is the reference value of the maximum debris flow impact force

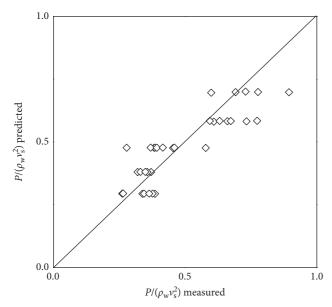


FIGURE 11: Comparison between measured and predicted $P/(\rho_{\rm w}v_{\rm s}^2)$ computed with Equation (5).

4. The Lateral Distribution of Debris Flow Impact and Surface Velocity

After the analysis of the calculation of the maximum impact force of debris flow, we focus on the difference on the collected data between sensor 2 and sensors 1 and 3, namely, the lateral distribution of debris flow impact. We set one end of the dam as the origin of the coordinate and assume that the distribution of the impact force of the debris flow is symmetrical in the center of the dam model. Figure 12 shows the experimental results for debris flow density of 13 kN/m. The horizontal ordinate is the ratio of the distance between the measuring points to the sidewall and the width of the whole dam. The longitudinal coordinate is the relative impact value compared with the maximum impact force. The experimental results show that the force of debris flow on the dam is distributed unevenly. Debris flow velocity is greater in the middle and decreases gradually to the both sides. At the same time, the velocity of debris flow at the sidewall is 0, and the impact force of the debris flow at the sidewall is 0. For the magnitude of the impact force values of different debris flow positions, we fit the curve equation of the relative impact force between the relative position and the relative impact force and found that the logarithmic fitting curve better reflected the experimental results. Therefore, we propose a logarithmic model to calculate the lateral distribution of the impact force of the debris flow as follows:

$$k_{\rm F} = \kappa_1 \, \ln\left(a\right) + \kappa_2,\tag{6}$$

where $k_{\rm F}$ is the dimensionless reduction coefficient, namely, $k_{\rm F} = P_x/P_{\rm m}$, and a is the dimensionless calculating distance a = x/(B/2).

Using the analysis in Equation (6), we find that it is an increasing function, and the range of the independent

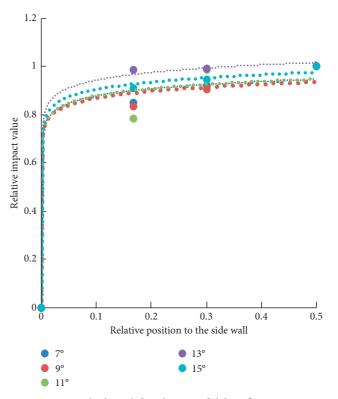


FIGURE 12: The lateral distribution of debris flow impact.

variable is 0 to 0.5. This indicates the lateral impact force of debris flow and the reduction characteristic of the middle to the sidewall. The velocity quickly decreases to zero when approaching the both sidewalls. The defect of this model is that when calculating the location of the sidewall, the independent variable cannot reach 0 and only can obtain the minimum value approaching 0. At the same time, when the independent variable is 0.5, the calculation result may be slightly larger than that of 1, but the error is quite small, which can meet the needs of actual debris flow prevention and control engineering.

Furthermore, we analyzed the coefficients κ_1 and κ_2 , which are the two essential parameters in Equation (6). We established an empirical equation using nonlinear multiple regression analysis and analyzed the relationship between κ_1 , κ_2 and three dimensionless parameters ($F_{\rm r}$, γ_0 , and s) on a series of experimental data as shown in the following equations:

$$\kappa_1 = 0.041 \cdot F_{\rm r}^{-0.0144} \cdot \gamma_0^{0.0746} \cdot s^{-0.0076},$$
(7)

$$\kappa_2 = 0.9454 \cdot F_{\rm r}^{-0.0152} \cdot \gamma_0^{0.0777} \cdot s^{-0.0067},$$
(8)

where s is a dimensionless parameter obtained by dividing mud depth H by unit length. The correlation coefficient between the $k_{\rm F}$ measured and $k_{\rm F}$ predicted is 0.94, and the maximum deviation is $\pm 12\%$. Figure 13 shows the comparison between the measured and predicted $k_{\rm F}$ by Equation (6). Our method provides a basis for quantifying the lateral distribution of the impact force.

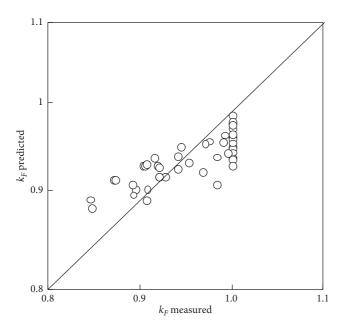


FIGURE 13: Comparison between measured and predicted $k_{\rm F}$ computed with Equation (6).

We assumed that impact and surface velocity are positively correlated and that the scale coefficient is related to the debris flow density from Equations (1) and (5). Therefore, we used a reduction coefficient k_v to show the decreasing trend of debris flow surface velocity and obtained the distribution of debris flow surface velocity as Equation (9) from Equations (6)–(8), as follows:

$$k_{\rm v} = k_{\rm F}^{0.5} = \frac{v_{\rm x}}{v_{\rm m}} = \sqrt{\kappa_1 \ln(a) + \kappa_2}.$$
 (9)

Note that we obtained the surface velocity distribution derived from Equation (6) without considering the variation of mud depth. In Section 5, we will analyze the distribution of debris flow velocity at any point in the debris flow section.

5. The Calculation Method of the Distribution of Debris Flow Impact on a Section

In this paper, we used the Bingham model to calculate the velocity of debris flow [22–26]. In the Bingham model, it is understood that velocity is not evenly distributed vertically; however, a uniform section of velocity is referred to as "plug." Plug is the scope of h_0 in Figure 14. Below the plug, the velocity of the debris flow decreases quickly and the bottom velocity is zero. The shear force τ in the Bingham model is

$$\tau = \tau_{\rm B} + \eta \frac{\partial u}{\partial y},\tag{10}$$

where η is the coefficient of the viscosity and $\tau_{\rm B}$ is Bingham limit shear stress.

The shear force is

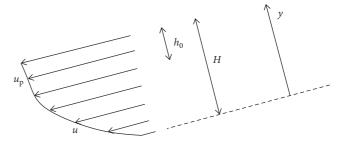


FIGURE 14: The Bingham model.

$$\tau = \gamma_c (H - y)J,\tag{11}$$

where γ_c is the bulk density, H is the mud depth, and J is the slope of the gully. By combining Equations (10) and (11), we were able to obtain the velocity below the plug, based on vertical integration, as follows:

$$u = \frac{y}{2\eta} \left(2\gamma_{\rm c} J - \gamma_{\rm c} J y - 2\tau_{\rm B} \right). \tag{12}$$

The thickness of the plug is

$$h_0 = \frac{\tau_{\rm B}}{\gamma_c J}.\tag{13}$$

The velocity at the top of the "nonplug" is equal to the velocity in the plug section, and the surface velocity is the velocity in the plug section, as follows:

$$v_{\rm s} = \frac{\gamma_{\rm c} H^2 J}{2\eta} \left(1 - \frac{\tau_{\rm B}}{\gamma_{\rm c} H J} \right)^2. \tag{14}$$

Furthermore, we put forward a calculated method for the debris flow impact distribution, which uses mass conservation [20] and takes the difference of velocity in the horizontal direction into account. A debris flow section is shown in Figure 15. We set the lowest point as O point and the horizontal line at O point as the baseline and the elevation of O point is O. Take the appropriate number of points as P_1, P_2, \ldots, P_n with transverse coordinates of x_1, x_2, \ldots, x_n , and the elevation values are h_1, h_2, \ldots, h_n . These n+1 known point $(O, O), (x_1, h_1), (x_2, h_2), \ldots, (x_n, h_n)$ can fit polynomial h(x) or piecewise linear function h(x)', whose independent variable span is $x_a \le x \le x_d$.

Furthermore, we established the following equation:

$$h(x) = H - \frac{\tau_{\rm B}}{\gamma_{\rm c} J}.$$
 (15)

Then, we are able to get two points $(x_b, h_0 - h')$ and $(x_c, h_0 - h')$ as shown in Figure 15.

We divide the section into n parts along the x direction. When n tends to infinity, each part is nearly a rectangular section whose elevation is h(x), length is dx, and mud depth is $h_0 - h(x)$. For the position of the maximum mud depth, it is generally the center of the debris flow section, and the longitudinal velocity distribution using the Bingham model is

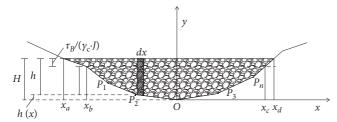


FIGURE 15: Cross section and coordinate representation of debris

$$v_{y} = \begin{cases} \frac{y}{2\eta} \left(2\gamma_{c}hJ - \gamma_{c}yJ - 2\tau_{B} \right), & y \leq H - \frac{\tau_{B}}{\gamma_{c}J}, \\ \frac{\gamma_{c}h^{2}J}{2\eta} \left(1 - \frac{\tau_{B}}{\gamma_{c}hJ} \right)^{2}, & H - \frac{\tau_{B}}{\gamma_{c}J} \leq y \leq H. \end{cases}$$

$$(16)$$

By combing Equations (9) and (16), we are able to obtain the velocity at any position on the debris flow section:

$$v_{x,y} = k_{y} \cdot v_{y}. \tag{17}$$

For a microunit of the section $(x_b \le x \le x_c)$, the debris flow discharge can be calculated as follows:

$$\Delta Q = \int_{h(x)}^{H} v_{x,y} \, dy. \tag{18}$$

TABLE 5: Analysis of the rheological properties of the debris flow.

Density	Coefficient of	Bingham limit
Density (kN/m³)	viscosity η (Pa·s)	shear stress $\tau_{\rm B}$ (Pa)
19.00	0.49	2.10
20.00	0.62	4.90
21.00	1.00	15.00

Sum these *n* microunits, and we obtain the whole section discharge as follows:

$$Q = \sum_{j=1}^{j} Q_{j} = \int_{x_{a}}^{x_{d}} \Delta Q \ dx.$$
 (19)

The relationship between section discharge Q and maximum mud depth H can be deduced by Equation (19), Bingham limit shear stress τ_B , debris bulk density γ_c , and the slope of the gully J; we measured the coefficient of the viscosity η by a field investigation and rheological experiment of debris flow.

By combining Equations (16)–(19), we obtain the velocity distribution on a section by the following equation:

$$v(x, y) = \begin{cases} k_{v} \frac{y - h(x)}{2\eta} \left(2\gamma_{c} [H - h(x)] J - \gamma_{c} [y - h(x)] J - 2\tau_{B} \right), & x_{b} \leq x \leq x_{c}, y \leq h_{0} - \frac{\tau_{B}}{\gamma_{c} J}, \\ k_{v} \frac{\gamma_{c} [H - h(x)]^{2} J}{2\eta} \left(1 - \frac{\tau_{B}}{\gamma_{c} [H - h(x)] J} \right)^{2}, & x_{a} \leq x \leq x_{d}, h_{0} - \frac{\tau_{B}}{\gamma_{c} J} \leq y \leq h_{0}. \end{cases}$$

$$(20)$$

We take the value of v(x, y) in Equation (5) to calculate the impact force at any point on the section and obtain the distribution of impact force by the following equation:

$$F_{\delta} = 0.18 \cdot \left(\frac{\gamma_{\rm s}}{\gamma_{\rm w}}\right)^{1.842} \cdot F_{\rm r}^{0.0052} \cdot \rho_{\rm w} \nu_{\rm s}^2.$$
 (21)

We selected the data of the impact force of the debris flow in the range of $19 \, \text{kN/m}^3$ and $21 \, \text{kN/m}^3$ and the flume slope of 7° to 13° . The debris flow in this range was more consistent with the Bingham model [22–26]. Table 5 provides the results of the rheological properties of the debris flow [27–28].

We used Equations (14)–(21) to calculate the impact force of debris flow at three locations in Figure 2 (numbers 1, 2, and 3) and compared it with the actual measurement results. Figure 16 shows the results of the comparison

between measured and predicted P, and its correlation coefficient is 0.91.

6. Case Study

The considered debris flow gully is a valley with an altitude of $1820\,\mathrm{m}{\sim}3500\,\mathrm{m}$ and a basin area of $12.2\,\mathrm{km}^2$. Debris flows have been produced many times, which seriously threatens the local people's lives and property. To reduce the debris flow disaster, we proposed to build a debris dam in the circulation area of the debris flow. We used the following steps to design the spatial distribution of the debris flow impact load at the proposed dam:

(1) By measuring a large-scale topographic map, we determined that the debris flow gully had an average longitudinal slope *J* of 0.09.

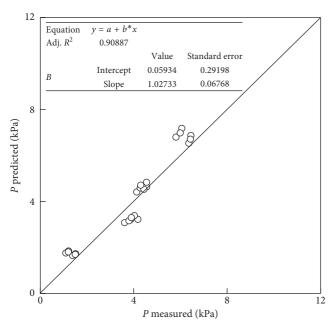


FIGURE 16: Comparison between measured and predicted P.

- (2) According to the actual sample measurements, we determined that the bulk density of the debris flow γ_c was $21 \, \text{kN/m}^3$.
- (3) Based on the rheological experiments on the debris flow and considering the effect of large particles in the field, we determined that the debris flow viscous coefficient η was 50 Pa. We also determined that the debris flow yield stress $\tau_{\rm B}$ was 190 Pa.
- (4) We selected the computed section, which is perpendicular to the movement direction and the

- ground. The design discharge of the debris flow Q was $132 \,\mathrm{m}^3/\mathrm{s}$.
- (5) We used a trial calculation method to determine the maximum mud depth H: assume H'=1 m; then, on the debris flow section (in Figure 17), we set the lowest point as O point with the horizontal line at O point as the baseline, and the elevation of O point is O. Take the appropriate number of points as O point as O point as O point as the appropriate number of points as O point as O

We used the five points measured previously and fit the piece-wise linear function h(x) = -0.05x, $x \le 0$ and h(x) = 0.05x, $x \ge 0$, whose independent variable span is $-20 \text{ m} \le x \le 20 \text{ m}$.

The thickness of the plug h_0 is 0.1 m according to Equation (13), and the corresponding $x_{\rm b}$ is -18 and $x_{\rm c}$ 18.

Use Equations (6)–(9) to determine the form of k_v as follows:

$$k_{\rm v} = 0.042 \ln \left(\frac{20 - |x|}{20} \right) + 0.978.$$
 (22)

Next calculate the section discharge Q' of $132 \,\mathrm{m}^3/\mathrm{s}$ by Equations (16)–(19) and make the calculated Q' equal to the design discharge Q. Then, determine the maximum mud depth $H = H' = 1 \,\mathrm{m}$.

(6) Taking the *H* obtained from step 5 into Equation (20), we obtained the velocity at any point on the section.

$$v(x, y) = \begin{cases} k_{\rm v} \cdot \frac{y - h(x)}{2\eta} \left(2\gamma_{\rm c} [H - h(x)] J - \gamma_{\rm c} [y - h(x)] J - 2\tau_{\rm B} \right), & x_{\rm b} \le x \le x_{\rm c}, y \le h_0 - \frac{\tau_{\rm B}}{\gamma_{\rm c} J}, \\ k_{\rm v} \cdot \frac{\gamma_{\rm c} [H - h(x)]^2 J}{2\eta} \left(1 - \frac{\tau_{\rm B}}{\gamma_{\rm c} [H - h(x)] J} \right)^2, & x_{\rm a} \le x \le x_{\rm d}, h_0 - \frac{\tau_{\rm B}}{\gamma_{\rm c} J} \le y \le h_0, \\ \left(0.042 \ln \left(\frac{20 - |x|}{20} \right) + 0.978 \right) \times \frac{y - 0.05 |x|}{2 \times 50} \left(2 \times 21000 \times [1 - 0.05 |x|] \times 0.09 - 21000 \right) \\ \times \left[y - 0.05 |x| \right] \times 0.09 - 2 \times 190), & |x| < 18, y < 0.9, \\ \left(0.042 \ln \left(\frac{20 - |x|}{20} \right) + 0.978 \right) \times \frac{21000 \left[1 - 0.05 |x| \right]^2 \times 0.09}{2 \times 50} \left(1 - \frac{190}{21000 \left[1 - 0.05 |x| \right] \times 0.09} \right)^2, |x| < 20, 0.9 \le y \le 1, \\ = \begin{cases} (0.042 \ln (20 - |x|) + 0.852) \times (y - 0.05 |x|) \times (34 - 0.945 |x| - 18.9y), & |x| < 18, y < 0.9, \\ (0.794 \ln (20 - |x|) + 16.103) \times (0.9 - 0.05 |x|)^2, & |x| < 20, 0.9 \le y \le 1, \end{cases}$$

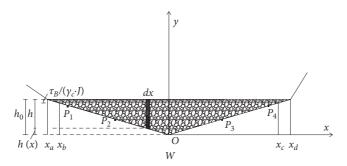


FIGURE 17: Cross section of one debris flow.

(7) Taking v(x, y) obtained from step 6 into Equation (5), we obtained the impact force at any point on the section.

$$\begin{split} P &= 0.18 \cdot \left(\frac{\gamma_s}{\gamma_w}\right)^{1.842} \cdot F_r^{0.0052} \cdot \rho_w v_s^2 \\ &= 721 \times v_s^2 \\ &= \begin{cases} 721 \times \left[(0.042 \ln{(20 - |x|)} + 0.852) \times (y - 0.05|x|) \times (34 - 0.945|x| - 18.9y) \right]^2, & |x| < 18, y < 0.9, \\ 721 \times \left[(0.794 \ln{(20 - |x|)} + 16.103) \times (0.9 - 0.05|x|)^2 \right]^2, & |x| < 20, 0.9 \le y \le 1, \end{cases} \end{split}$$

Figure 18 shows the calculated results of the distribution of debris flow impact on a section.

7. Discussion

7.1. The Weakness of Our Proposed Method. Although we carried out some experiments on impact force and drew some conclusions, the proposed method still has some weakness. First, there is an error in the measurement of the maximum impact force of debris flow. Through theoretical analysis, we can conclude that the maximum impact force of debris flow should occur at the mud depth where the surface velocity is the largest. Under different experimental combinations, the mud depth of debris flow will change, whereas the position of the sensors remains fixed. Therefore, it is difficult to ensure that the center point of the sensor surface remains in the mud depth position of the debris flow. Therefore, only the area near the mud depth position and the measured impact value deviate slightly. The result of the bottom sensor only can be approximated to be the maximum impact force.

Second, the calculation method of the distribution of debris flow impact on a section performs better for viscous debris flow, which obeys the rheology of the Bingham model. For other types of debris flow, a similar method can be used to calculate the distribution of debris flow impact on a section.

7.2. Future Plan to Improve the Current Study. In our future study, we plan to use a flat panel collector to measure the

impact force of debris flow. The advantage of the flat plate collector is that it can collect the maximum impact force within the section area even though the mud depth is changed. The temporal and spatial distribution of the impact process can be well reconstructed.

In addition, we plan to set up the sensors used in the field to measure the impact force data and the distribution of the debris flow under actual conditions and to compare these findings with experimental results to optimize the calculation method of the debris flow slurry impact and distribution.

8. Conclusion

We proposed a new method to calculate the maximum slurry impact force and the distribution through a laboratory flume experiment with various debris flow densities, mass volume, flume slopes, and dam front angles. We summarize the following conclusions from the results of the study:

- (1) Our new calculation method for the maximum impact force of debris flow considers the characteristics of debris flows and gullies, which are directly related to the debris flow instantaneous velocity and relative bulk density, and provides the basis for the calculation of the distribution of the impact force of debris flow.
- (2) We consider the influence of debris flow channel sidewall as well as internal interactions and deduce the transverse distribution under the same mud depth. We propose a new method to calculate the reduction from the middle to the ends.

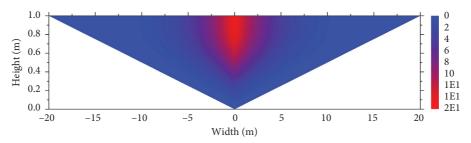


Figure 18: Calculated results of the distribution of debris flow impact on a section.

- (3) We propose a calculation method for the distribution of the debris flow impact force on preventive engineering considering the sidewall effect and longitudinal mud depth and give an example to illustrate this calculation.
- (4) Our calculation method is based on the Bingham model, which is appropriate for the calculation of viscous debris flow but inadequate for other diluted debris flow. Additional methods and calculations will need to be developed to address this issue.

Our new calculation method is better to calculate the impact and velocity distribution of viscous debris flow. Moreover, our calculation method can be beneficial to improve preventive engineering efforts, resulting in improved safety and less loss of life and farmland.

Notations

- P: Debris flow impact force (kPa)
- P_x : Impact force at x position (kPa)
- $P_{\rm m}$: Impact force in the middle of the dam (kPa)
- x: The distance from one point to the near end (m)
- ρ_s : Debris flow density (kg/m³)
- $\rho_{\rm w}$: Water density (kg/m³)
- γ_c : Gravity density of debris flow (kN/m³)
- $\gamma_{\rm w}$: Gravity density of water (kN/m³)
- H: Mud depth (m)
- v: The mean velocity of debris flow (m/s)
- v_s : The surface velocity of debris flow (m/s)
- g: Acceleration of gravity (m/s²)
- λ : Shape correction coefficient (-)
- β : Impact angle (°)
- A: Cross-sectional area (m²)
- *k*: Empirical coefficient (–)
- $k_{\rm F}$: Reduction coefficient of impact force (-)
- $k_{\rm v}$: Reduction coefficient of velocity (-)
- F_r : Froude number (–)
- B: Dam width (m)
- $\tau_{\rm B}$: Bingham limit shear stress
- *J*: Slope of the gully (–)
- η : Coefficient of viscosity.

Data Availability

The acquisition of experimental data is obtained by the physical model experiment conducted in a debris flow simulation laboratory at the Institute of Mountain Hazards and Environment, which is part of the Chinese Academy of Sciences (CAS). The experimental results are repeatable. Relevant scholars can use similar experimental models or visit Institute of Mountain Hazards and Environment to further verify the reliability of the experimental data.

Conflicts of Interest

The authors declare that they have no conflicts of interest.

Acknowledgments

This research was supported by the National Program on Key Research Project of China (Grant no. 2016YFC0802206) and the National Natural Science Foundation of China (Grant no. 41571004). The authors would like to thank LetPub for providing linguistic assistance during the preparation of this manuscript.

References

- [1] T. Mizuyama, "Computational method and some considerations on impulsive force of debris flow acting on Sabo dams," *Japan Society of Erosion Control Engineering*, vol. 112, pp. 40–43, 1979, in Japanese.
- [2] G. Zanchetta, R. Sulpizio, M. T. Pareschi, F. M. Leoni, and R. Santacroce, "Characteristics of May 5-6, 1998 volcaniclastic debris flows in the Sarno area (Campania, southern Italy): relationships to structural damage and hazard zonation," *Journal of Volcanology and Geothermal Research*, vol. 133, no. 1–4, pp. 377–393, 2004.
- [3] Q. Wang, H. E. Si-Ming, and J. Y. Zhang, "Theoretical method for calculating impact force on debris flow protection piers," *Journal of Disaster Prevention and Mitigation Engineering*, vol. 29, no. 4, pp. 423–427, 2009.
- [4] S. He, W. Liu, and X. Li, "Prediction of impact force of debris flows based on distribution and size of particles," *Environ*mental Earth Sciences, vol. 75, no. 4, p. 298, 2016.
- [5] X. J. Fei and A. P. Shu, Movement Mechanism and Disaster Control for Debris Flow, Tsinghua University Press, Beijing, China, 2004, in Chinese.
- [6] S. M. He, X. P. Li, and Y. Wu, "Calculation of impact force of outrunner blocks in debrisflow considering elastoplastic deformation," *Chinese Journal of Rock Mechanics and Engineering*, vol. 26, no. 8, pp. 1664–1669, 2007.
- [7] H. K. Chen, H. M. Tang, and S. F. Wu, "Research on abrasion of debris flow to high-speed drainage structure," *Applied Mathematics and Mechanics*, vol. 25, no. 11, pp. 1257–1264, 2004.

[8] H. K. Chen and H. M. Tang, "Method to calculate impact force and impact time of two phase debris flow," *China Journal of Highway and Transport*, vol. 3, no. 19, pp. 19–23, 2006, in Chinese.

- [9] A. Armanini and P. Scotton, "On the dynamic impact of a debris flow on structures," in *Proceedings of XXV Congress of IAHR. Technical Session B, Debris Flows and Landslides*, pp. 203–210, Tokyo, Japan, 1993.
- [10] C. Zeng, Vulnerability Assessment of Building to Flow Hazard, University of Chinese Academy of Sciences, Beijing, China, 2014, in Chinese.
- [11] G. X. Chen, *Debris Flow Disaster Prevention*, China Railway Publishing House, Beijing, China, 1983, in Chinese.
- [12] O. Hungr, G. C. Morgan, and R. Kellerhals, "Quantitative analysis of debris torrent hazards for design of remedial measures," *Canadian Geotechnical Journal*, vol. 21, no. 4, pp. 663–667, 1984.
- [13] D. J. Li, *Theory and Practice for Hazard Reduction of Debris Flow*, Science Press, Beijing, China, 1997, in Chinese.
- [14] B. F. Zhou, *Debris-Flow Prevention Guide*, Science Press, Beijing, China, 1991, in Chinese.
- [15] J. Hübl and G. Holzinger, Entwicklung von Grundlagen zur Dimensionierung kronenoffener Bauwerke für die Geschiebebewirtschaftung in Wildbächen: Kleinmassstäbliche Modellversuche zur Wirkung von Murbrechern, WLS Report 50 Band 3, Institut of Mountain Risk Engineering, Vienna, Austria, 2003.
- [16] M. Watanabe and H. Ikeya, "Investigation and analysis of volcanic mud flows on Mount Sakurajima, Japan," *Erosion Sediment Transport Measurement*, vol. 33, pp. 245–256, 1981.
- [17] S. Zhang, "A comprehensive approach to the observation and prevention of debris flow in China," *Natural Hazards*, vol. 7, no. 1, pp. 1–23, 1993.
- [18] B. Zanuttigh and A. Lamberti, "Instability and surge development in debris flows," *Reviews of Geophysics*, vol. 45, no. 3, 2007.
- [19] P. R. Tecca, A. M. Deganutti, R. Genevois, and A. Galgaro, "Velocity distributions in a coarse debris flow," *Debris*, vol. 2, pp. 905–916, 2003.
- [20] Z. Han, G. Chen, Y. Li et al., "A new approach for analyzing the velocity distribution of debris flows at typical cross-sections," *Natural Hazards*, vol. 74, no. 3, pp. 2053–2070, 2014.
- [21] Z. Han, G. Chen, Y. Li, W. Wang, and H. Zhang, "Exploring the velocity distribution of debris flows: an iteration algorithm based approach for complex cross-sections," *Geomorphology*, vol. 241, pp. 72–82, 2015.
- [22] T. Takahashi, "Mechanical characteristics of debris flow," Journal of the Hydraulics Division, vol. 104, no. 8, pp. 1153– 1169, 1978.
- [23] T. Takahashi, "Debris flow on prismatic open channel," *Journal of the Hydraulics Division*, vol. 106, no. 3, pp. 381–396, 1980.
- [24] R. M. Iverson, "The physics of debris flows," *Reviews of Geophysics*, vol. 35, no. 3, pp. 245–296, 1997.
- [25] M. Drago, "A coupled debris flow-turbidity current model," *Ocean Engineering*, vol. 29, no. 14, pp. 1769–1780, 2002.
- [26] H. X. Zhao, Y. You, J. F. Liu, and L. K. Yao, "Superelevation calculation of debris flow climbing ascending slopes," *Mathematical Problems in Engineering*, vol. 2017, Article ID 9578928, 9 pages, 2017.
- [27] I. M. Krieger and T. J. Dougherty, "A mechanism for non-newtonian flow in suspensions of rigid spheres," *Transactions of the Society of Rheology*, vol. 3, no. 1, pp. 137–152, 1959.
- [28] M. Mooney, "The viscosity of concentrated suspension of spherical particles," *Journal of Colloid Science*, vol. 6, no. 2, pp. 162–170, 1951.

Hindawi Shock and Vibration Volume 2018, Article ID 9824631, 13 pages https://doi.org/10.1155/2018/9824631

Research Article

Theoretical Study of Synchronous Behavior in a Dual-Pendulum-Rotor System

Fang Pan , Hou Yongjun , Dai Liming , and Du Mingjun

¹School of Mechanical Engineering, Southwest Petroleum University, Chengdu, China ²University of Regina, Regina, Canada

Correspondence should be addressed to Fang Pan; ckfangpan@126.com and Hou Yongjun; hyj2643446@126.com

Received 27 March 2018; Revised 16 May 2018; Accepted 4 June 2018; Published 9 July 2018

Academic Editor: Aly Mousaad Aly

Copyright © 2018 Fang Pan et al. This is an open access article distributed under the Creative Commons Attribution License, which permits unrestricted use, distribution, and reproduction in any medium, provided the original work is properly cited.

A dual-pendulum-rotor system widely appears in aero-power plant, mining screening machines, parallel robots, and the like of the other rotation equipment. Unfortunately, the synchronous behavior related to the dual-pendulum-rotor system is less reported. Based on the special backgrounds, a simplified mechanical model of the dual-pendulum-rotor system is proposed in the paper, and the intrinsic mechanisms of synchronous phenomenon in the system are further revealed with employing the Poincaré method. The research results show that the spring stiffness, the installation angular of the motor, and rotation direction of the rotors have a large influence on the existence and stability of the synchronization state in the coupling system, and the mass ratios of the system are irrelevant to the synchronous state of the system. It should be noted that to ensure the implementation of the synchronization of the system, the values of the parameters of the system should be far away to the two "critical points".

1. Introduction

"Synchronization phenomenon" widely exists in nature and daily life. The so-called synchronization phenomenon refers to self-adjusting different frequencies of oscillating objects to a unified frequency relying on their internal weak couplings [1, 2]. In recent years, the study of synchronization phenomenon is involved in the fields of physics, chemistry, and biology, such as the practical application on complex dynamic network systems [3–5], nonlinear coupled chaotic systems [6, 7], coupled pendulum system [8–12], and rotor system [1, 13– 19]. Nevertheless, the latter two systems can be categorized as synchronous problem of mechanics system in detail. In the synchronous study of the pendulum system, antiphase selfsynchronization of clock pendulum is firstly discovered by Huygens in 1665. In the modern computation and analysis, the difference of spring stiffness influenced on the synchronous state is concerned, and the synchronization in inphase and anti-phase state for Huygens model is analyzed. Meanwhile, the derivatizations of Huygens model, including two coupled double pendula, coupling pendula under elastic forces, and pendula connected with linear springs, have

attracted many scholars' attention. In the self-synchronous study of the rotor system, I.I.Blekhman proposed Poincaré method to explore the synchronous mechanism in multirotor systems. Nowadays, the Poincaré method is still widely used in modern engineering design. Based on the foundation of I.I.Blekhman's method, many scientists proposed the other approaches to study self-synchronization of the rotor system. Wen Bangchun introduced an averaging method to calculate the synchronization and stability between multiple coupled rotors [13]. Zhao Chunyu [14, 15] gave a revised small parameter method to describe the synchronous process of rotor system, which greatly simplifies the solving process of synchronization problem in rotor system. Sperling presented a two-plane automatic balancing device for equilibration of rigid-rotor unbalance, on which the synchronization of the rigid rotors is determined with numerical method. Similarly, Balthazar [16] examined self-synchronization of four nonideal exciters in nonlinear vibration system via numerical simulations. Djanan. A. A. N [17] explored the system, three motors working on the same plate; the synchronous state depends on the physical characteristics of the motors and the

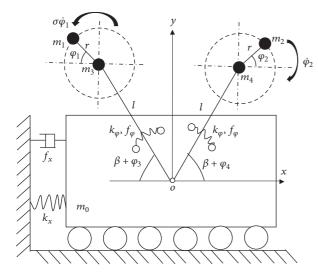


FIGURE 1: The dual-pendulum-rotor system.

The objects of the above-mentioned researches are mainly synchronization of the coupled pendula or the coupled rotors; however, the synchronization of the pendulumrotor system is less concerned. The extensive application of the pendulum-rotor system in aero-power plant, mining screening machines, parallel robots, and the like of the other rotation equipment is important for our industrial production and daily life [20-22]. The aim of this paper is to investigate a system composed of two unbalanced rotors coupled with two pendula in a horizontal plane. But mass of the motor and the rotor, which can be relatively heavy or light, may affect the system motion. Therefore, the proposed problem is different from the dynamics of classical pendulum systems presented in papers [8-11] and classical rotor systems presented in papers [12-20, 23-27]. We consider an ideal source of energy supply to asynchronous motors, which drag the unbalanced rotors. We also investigate selected aspects of the synchronization phenomenon. There are different synchronization states possible in mechanical systems. We will search for a complete synchronization when the rotors perform rotation with the difference direction or for the synchronous state when the phase differences between the rotors are stabilized.

2. Dynamic Model

A simplified dual-pendulum-rotor system is shown in Figure 1. This system consists of a rigid oscillating body of mass m_0 [Kg] elastically supported via a linear damping spring with stiffness k_x [N/m] and damping f_x [Ns/m]. Unbalanced rotor i actuated by an asynchronous motor is modelled by a point mass m_i [Kg] (for i=1,2) and attached at the end of a massless rod of length r [m]; the rotation angle of the rotors is defined by $\varphi_i \in S^1$ (for i=1,2) in [rad]. It should be noted that all the motors are installed rigid vibrating body by linear torsion springs with stiffness k_φ [N/rad] and damping $f_\varphi[\mathrm{N}\cdot\mathrm{m}/(\mathrm{rad/s})]$. Thus, small oscillating should exist in the two motors when the motors are operated in steady state; the

oscillating angle is denoted by $\varphi_j \in S^1$ (for j=3,4) in [rad]. Therefore, the oscillating characteristics of the motors are just like a pendulum or pendula with length l and lumped mass (equal to the mass of the motors) m_j [Kg] (for j=3,4). The angular installation of the motors is denoted by $\beta \in S^1$ in [rad]; x represents oscillation of centroid of the system in x-direction, respectively. σ is the rotation direction of the rotors; l [m] is distance between pivot of the motor and centroid O of the system.

In rotating coordinate o'x''y'', the rotating centers of the rotors Φ_1'', Φ_2'' can be expressed as

$$\Phi_{1}^{"} = \begin{pmatrix} \sigma r \cos \varphi_{1} - l \cos (\varphi_{3} + \beta) \\ r \sin \varphi_{1} + l \sin (\varphi_{3} + \beta) \end{pmatrix},$$

$$\Phi_{2}^{"} = \begin{pmatrix} r \cos \varphi_{2} + l \cos (\varphi_{4} + \beta) \\ r \sin \varphi_{2} + l \sin (\varphi_{4} + \beta) \end{pmatrix}.$$
(1)

And the rotating center of the motors Φ_3'' and Φ_4'' is represented as

$$\Phi_{3}^{"} = \begin{pmatrix} -l\cos(\beta + \varphi_{3}) \\ l\sin(\beta + \varphi_{3}) \end{pmatrix},
\Phi_{4}^{"} = \begin{pmatrix} l\cos(\beta + \varphi_{4}) \\ l\sin(\beta + \varphi_{4}) \end{pmatrix}.$$
(2)

In fixed coordinate *oxy*, coordinates Φ_1 , Φ_2 , Φ_3 , Φ_4 can be obtained by

$$\Phi_i = \Phi_0 + \Phi_i''. \quad (i = 1, 2, 3, 4)$$
 (3)

where Φ_0 is displacement vector of the vibrating base, $\Phi_0 = [x, 0]^T$.

According to kinetic theory, kinetic energy T of the dual-pendulum-rotor system should be written as follows:

$$T = \frac{1}{2}m_0\dot{x} + \frac{1}{2}\sum_{i=1}^{4}m_i\dot{\boldsymbol{\Phi}}_i^{\mathrm{T}}\dot{\boldsymbol{\Phi}}_i + \frac{1}{2}\sum_{i=1}^{2}J_i\dot{\varphi}_i^2. \tag{4}$$

 J_1 and J_2 are the rotational inertia of the rotors, and symbols ($\dot{\bullet}$) and ($\ddot{\bullet}$) denote $d(\dot{\bullet})/dt$ and $d^2(\dot{\bullet})/dt^2$, respectively.

In addition, potential energy V of the dual-pendulum-rotor system can be expressed by

$$V = \frac{1}{2}k_x x^2 + \frac{1}{2}k_{\varphi}\varphi_3^2 + \frac{1}{2}k_{\varphi}\varphi_4^2$$
 (5)

Moreover, dissipated energy D of the system can be obtained by

$$D = \frac{1}{2} f_x \dot{x}^2 + \frac{1}{2} f_1 \dot{\varphi}_1^2 + \frac{1}{2} f_2 \dot{\varphi}_2^2 + \frac{1}{2} f_3 \dot{\varphi}_3^2 + \frac{1}{2} f_4 \dot{\varphi}_4^2$$
 (6)

According to the Lagrange equation

$$\frac{d}{dt}\left(\frac{\partial T}{\partial \dot{q}}\right) - \frac{\partial \left(T - V\right)}{\partial q} + \frac{\partial D}{\partial q} = Q_i,\tag{7}$$

the dynamic equation of the dual-pendulum-rotor system can be derived. In the system, coordinate matrix $\mathbf{q} = [x, \varphi_1, \varphi_2, \varphi_3, \varphi_4]^{\mathrm{T}}$ is considered as the generalized coordinate matrix; meanwhile, the generalized force matrix of the system is assumed as

$$\begin{bmatrix} Q_{x} & Q_{\varphi_{1}} & Q_{\varphi_{2}} & Q_{\varphi_{3}} & Q_{\varphi_{4}} \end{bmatrix}^{T}$$

$$= \begin{bmatrix} 0 & M_{e1} - R_{e1} & M_{e2} - R_{e2} & 0 & 0 \end{bmatrix}^{T}$$
(8)

Substituting (4), (5), (6), and (8) into (7) and, meanwhile, considering $m_1, m_2 \ll m_0$, $\sum_{k=0}^4 m_k = M$. As J_1 and J_2 are sums of rotational inertia of motor's rotor about spin axis and that of eccentric lump, compared with $m_1 r^2$ and $m_1 r^2$, the rotational inertia of motor's rotor about spin axis is too small to be neglected; i.e., $J_1 \approx m_1 r^2$, $J_2 \approx m_2 r^2$, and the dynamic equation of the dual-pendulum-rotor system is written by

$$J_1 \ddot{\varphi}_1 = M_{e1} - R_{e1} + \sigma m_1 r \sin \varphi_1 \ddot{x}$$
$$- m_1 r l \ddot{\varphi}_3 \cos (\beta + \sigma \varphi_1)$$
$$+ m_1 r l \dot{\varphi}_3^2 \sin (\beta + \sigma \varphi_1)$$
(9a)

$$J_{2}\ddot{\varphi}_{2} + J_{2}\ddot{\varphi}_{2} = M_{e2} - R_{e2} + m_{2}r\sin\varphi_{2}\ddot{x}$$
$$- m_{2}rl\ddot{\varphi}_{4}\cos(\beta - \varphi_{2})$$
$$+ m_{2}rl\dot{\varphi}_{4}^{2}\sin(\beta - \varphi_{2})$$
(9b)

$$M\ddot{x} + f_{x}\dot{x} + k_{x}x$$

$$= \sigma m_{1}r \left(\ddot{\varphi}_{1} \sin \varphi_{1} + \dot{\varphi}_{1}^{2} \cos \varphi_{1} \right)$$

$$+ m_{2}r \left(\ddot{\varphi}_{2} \sin \varphi_{2} + \dot{\varphi}_{2}^{2} \cos \varphi_{2} \right) \qquad (9c)$$

$$- \left(m_{1} + m_{3} \right) l \left(\ddot{\varphi}_{3} \sin \beta + \dot{\varphi}_{3}^{2} \cos \beta \right)$$

$$+ \left(m_{2} + m_{4} \right) l \left(\ddot{\varphi}_{4} \sin \beta + \dot{\varphi}_{4}^{2} \cos \beta \right)$$

$$(m_1 l^2 + m_3 l^2) \ddot{\varphi}_3 + f_{\varphi} \dot{\varphi}_3 + k_{\varphi} \varphi_3$$

$$= -(m_1 + m_3) l \sin \beta \ddot{x}$$

$$- m_1 lr \left[\ddot{\varphi}_1 \cos (\beta + \sigma \varphi_1) - \sigma \dot{\varphi}_1^2 \sin (\beta + \sigma \varphi_1) \right]$$
(9d)

$$(m_2 l^2 + m_4 l^2) \ddot{\varphi}_4 + f_{\varphi} \dot{\varphi}_4 + k_{\varphi} \varphi_4$$

$$= (m_2 + m_4) l \sin \beta \ddot{x}$$

$$- m_2 lr \left[\ddot{\varphi}_2 \cos (\beta - \varphi_2) + \dot{\varphi}_2^2 \sin (\beta - \varphi_2) \right]$$

$$(9e)$$

where

σ

$$= \begin{cases} 1, & \text{the two rotor rotate in the same direction,} \\ -1, & \text{the two rotor rotate in the opposite direction.} \end{cases}$$
 (10)

It can be seen that the terms of $\dot{\varphi}_3^2$ and $\dot{\varphi}_4^2$, nonlinear terms owing to the small periodic vibration in synchronous state, are included in (9c). The terms related to $\dot{\varphi}_3^2$ and $\dot{\varphi}_4^2$ can be rewritten as Poincaré style with small parameter μ . Meanwhile, damping coefficient of this system is very small, and so the terms with damping coefficient can be rearranged as Poincaré style. In synchronous state, velocity of the motors is fluctuated slightly and periodically; hence, the acceleration of the rotors is also considered as a small term. Therefore, introducing small parameter μ , the Poincaré style of (9a), (9b),(9c), (9d), (9e) is given as follows [27]:

$$J_1 \ddot{\varphi}_1 = \mu \Phi_1 \tag{11a}$$

$$J_2 \ddot{\varphi}_2 = \mu \Phi_2 \tag{11b}$$

$$M\ddot{x} + k_{x}x = \sigma m_{1}r \left(\ddot{\varphi}_{1} \sin \varphi_{1} + \dot{\varphi}_{1}^{2} \cos \varphi_{1} \right)$$

$$+ m_{2}r \left(\ddot{\varphi}_{2} \sin \varphi_{2} + \dot{\varphi}_{2}^{2} \cos \varphi_{2} \right) - \left(m_{1} + m_{3} \right) l \ddot{\varphi}_{3}$$

$$\cdot \sin \beta + \left(m_{2} + m_{4} \right) l \ddot{\varphi}_{4} \sin \beta - \mu \left[f_{x} \dot{x} \right]$$

$$+ \left(m_{1} + m_{3} \right) l \dot{\varphi}_{3}^{2} \cos \beta - \left(m_{2} + m_{4} \right) l \dot{\varphi}_{4}^{2} \cos \beta \right]$$
(11c)

$$\begin{split} \left(m_1 l^2 + m_3 l^2\right) \ddot{\varphi}_3 + k_{\varphi} \varphi_3 \\ &= -\left(m_1 + m_3\right) l \sin \beta \ddot{x} - m_1 l r \ddot{\varphi}_1 \cos \left(\beta + \sigma \varphi_1\right) \\ &- \mu \left[f_{\varphi} \dot{\varphi}_3 - \sigma m_1 l r \dot{\varphi}_1^2 \sin \left(\beta + \sigma \varphi_1\right) \right] \end{split} \tag{11d}$$

$$(m_2 l^2 + m_4 l^2) \ddot{\varphi}_4 + k_{\varphi} \varphi_4$$

$$= (m_2 + m_4) l \sin \beta \ddot{x} - m_2 l r \ddot{\varphi}_2 \cos (\varphi_2 - \beta) \qquad (11e)$$

$$- \mu \left[f_{\varphi} \dot{\varphi}_4 + m_2 l r \dot{\varphi}_2^2 \sin (\varphi_2 - \beta) \right]$$

where

$$\mu \Phi_1 = M_{e1} - R_{e1} + \sigma m_1 r \sin \varphi_1 \ddot{x}$$
$$- m_1 r l \ddot{\varphi}_3 \cos (\beta + \sigma \varphi_1)$$
$$+ m_1 r l \dot{\varphi}_3^2 \sin (\beta + \sigma \varphi_1)$$
 (12a)

$$\mu \Phi_2 = M_{e2} - R_{e2} + m_2 r \sin \varphi_2 \ddot{x}$$
$$- m_2 r l \ddot{\varphi}_4 \cos (\beta - \varphi_2)$$
$$+ m_2 r l \dot{\varphi}_4^2 \sin (\beta - \varphi_2)$$
 (12b)

Based on Zhao's method [15], the electromagnetic torque of the asynchronous motor is linearized at stable point $\dot{\varphi}_i = \omega_s$ when the two motors are synchronously operated; i.e.,

$$M_{ei} = n_p \frac{L_{mi}^2 U_{S0}^2}{L_{::}^2 \omega_{...} R_{ri}} \left(\omega_s - n_p \omega_m \right) \quad (i = 1, 2)$$
 (13)

where L_{mi} is coefficient of mutual asynchronous in the *i*th motor; L_{si} is the *i*th coefficient of stator inductance in the *i*th motor; n_p is pole-pairs of the motors; ω_m is synchronous velocity of the motors; R_{ri} is rotor resistance in the *i*th motor; U_{SO} is amplitude of stator voltage.

3. Approximate Solution

From formulas (9a) to (9e), it can be seen that the vibration characteristics of the system are coupled related to DOFs $\varphi_1, \varphi_2, x, \varphi_3$, and φ_4 . Neglecting the terms of small parameters, introduce the dimensionless parameter as follows:

$$\frac{r}{l} = r_{l},$$

$$\frac{m}{M} = r_{m},$$

$$\frac{m_{i}}{m} = \eta_{i} \quad (i = 1, 2, 3, ..., 4),$$

$$\omega_{x} = \sqrt{\frac{k_{x}}{M}},$$

$$\omega_{\phi} = \sqrt{\frac{k_{\phi}}{m_{1}l^{2}} + m_{3}l^{2}},$$

$$\omega_{\phi} = \sqrt{k_{\phi}/m_{1}l^{2} + m_{3}l^{2}},$$

$$f_{1}(t) = r_{m}r_{l}(\sigma\eta_{1}\cos\varphi_{1} + \eta_{2}\cos\varphi_{2}),$$

$$f_{2}(t) = \frac{\eta_{1}r_{l}}{(\eta_{1} + \eta_{3})}\sin(\varphi_{1} + \sigma\beta),$$

$$f_{3}(t) = \frac{\eta_{2}r_{l}}{(\eta_{2} + \eta_{4})}\sin(\varphi_{2} - \beta).$$
(14)

In addition, velocities $\dot{\varphi}_1$ and $\dot{\varphi}_2$ of the two motors approached to a constant are represented by ω_m in the steady state; therefore, the accelerations of the two motors should be equal to zero; i.e., $\ddot{\varphi}_1 = 0$ and $\ddot{\varphi}_2 = 0$. In this case, (11c) -(11e) can be simplified as the dimensionless style:

$$\ddot{x} + \omega_x^2 x = \omega_m^2 l f_1(t) - (\eta_1 + \eta_3) r_m l \sin \beta \ddot{\varphi}_3 + (\eta_2 + \eta_4) r_m l \sin \beta \ddot{\varphi}_4,$$
(15a)

$$\ddot{\varphi}_3 + \omega_{\varphi}^2 \varphi_3 = -\frac{\sin \beta}{l} \ddot{x} + \omega_m^2 f_2(t),$$
 (15b)

$$\ddot{\varphi}_4 + \omega_{\varphi}^2 \varphi_4 = \frac{\sin \beta}{l} \ddot{x} + \omega_m^2 f_3(t).$$
 (15c)

For simplifying the solution procedure, consider that the natural frequencies of the torsion spring are quasi-identical; thus, parameter ω_{ω} should be replaced by ω_{φ} .

Applying Laplace transformation in (16a), (16b), (16c), the coupling terms can be decoupled. Therefore, we have

$$s^{2}X + \omega_{x}^{2}X = \omega_{m}^{2}lF_{1}(s) - (\eta_{1} + \eta_{3})r_{m}ls^{2}\sin\beta\phi_{3} + (\eta_{2} + \eta_{4})r_{m}ls^{2}\sin\beta\phi_{4}$$
(16a)

$$s^{2}\phi_{3} + \omega_{\varphi}^{2}\phi_{3} = -\frac{s^{2}\sin\beta}{l}X + \omega_{m}^{2}F_{2}(s)$$
 (16b)

$$s^2 \phi_4 + \omega_{\varphi}^2 \phi_4 = \frac{s^2 \sin \beta}{I} X + \omega_m^2 F_3(s)$$
 (16c)

From formulas (16a)-(16c), the approximate solutions of the system in complex domain can be given by

$$X = \frac{\omega_{m}^{2} l}{G_{1}(s)} F_{1}(s) - \frac{(\eta_{1} + \eta_{3}) \omega_{m}^{2} r_{m} l s^{2} \sin \beta}{G_{1}(s)} F_{2}(s) + \frac{(\eta_{2} + \eta_{4}) \omega_{m}^{2} r_{m} l s^{2} \sin \beta}{G_{1}(s)} F_{3}(s)$$
(17a)

$$\phi_{3} = -\frac{s^{2} \sin \beta \omega_{m}^{2}}{G_{1}(s)} F_{1}(s)$$

$$+ \left[\frac{\omega_{m}^{2}}{G_{2}(s)} + \frac{\omega_{m}^{2} (\eta_{1} + \eta_{3}) r_{m} s^{4} \sin^{2} \beta}{G_{1}(s) G_{2}(s)} \right] F_{2}(s) \quad (17b)$$

$$- \frac{\omega_{m}^{2} (\eta_{2} + \eta_{4}) r_{m} s^{4} \sin^{2} \beta}{G_{1}(s) G_{2}(s)} F_{3}(s)$$

$$\phi_{4} = \frac{\omega_{m}^{2} s^{2} \sin \beta}{G_{1}(s)} F_{1}(s)$$

$$- \frac{\omega_{m}^{2} (\eta_{1} + \eta_{3}) r_{m} s^{4} \sin^{2} \beta}{G_{1}(s) G_{2}(s)} F_{2}(s)$$

$$+ \left[\frac{\omega_{m}^{2}}{G_{2}(s)} + \frac{\omega_{m}^{2} (\eta_{2} + \eta_{4}) r_{m} s^{4} \sin^{2} \beta}{G_{1}(s) G_{2}(s)} \right] F_{3}(s)$$
(17c)

where $G_1(s) = (s^2 + \omega_x^2)(s^2 + \omega_{\varphi}^2) - (\eta_1 + \eta_3 + \eta_2 + \eta_4)r_m s^4 \sin^2 \beta$, $G_2(s) = s^2 + \omega_{\varphi}^2$.

Then, the numerators and denominators of (17a), (17b), (17c) in the right are divided by divisor $\omega_{\varphi}^{\ 4}\omega_{x}^{\ 2}$; moreover, introduce frequency ratios

$$n_x = \frac{\omega_m}{\omega_x},$$

$$n_{\varphi} = \frac{\omega_m}{\omega_{\varphi}}$$
(18)

into (17a)-(17c). In this case, the coefficients of spring stiffness k_x and k_{φ} are converted into the frequency ratios n_x and n_{φ} in light of (14), respectively.

Finally, through applying the inverse Laplace transformation to (18), the approximate solutions of the system in time domain can be obtained by

$$x = \mu_{11} l f_1(t) + \mu_{12} (\eta_1 + \eta_3) l r_m f_2(t) + \mu_{13} (\eta_2 + \eta_4) l r_m f_3(t),$$
(19a)

$$\varphi_{3} = \mu_{21} f_{1}(t) + \mu_{22} (\eta_{1} + \eta_{3}) r_{m} f_{2}(t) + \mu_{23} (\eta_{2} + \eta_{4}) r_{m} f_{3}(t),$$
(19b)

$$\varphi_4 = \mu_{31} f_1(t) + \mu_{32} (\eta_1 + \eta_3) r_m f_2(t) + \mu_{33} (\eta_2 + \eta_4) r_m f_3(t),$$
(19c)

where

$$\mu_{11} = \frac{n_x^2 \left(1 - n_\varphi^2\right)}{g},$$

$$\mu_{12} = \mu_{21} = \frac{n_x^2 n_\varphi^2 \sin \beta}{g},$$

$$\mu_{13} = \mu_{31} = -\frac{n_x^2 n_\varphi^2 \sin \beta}{g},$$

$$\mu_{22} = \mu_{33} = \frac{n_x^2 n_\varphi^4 \sin^2 \beta}{\left(1 - n_\varphi^2\right) g} + \frac{n_\varphi^2}{\left(1 - n_\varphi^2\right) \left(\eta_1 + \eta_3\right) r_m},$$

$$\mu_{23} = \mu_{32} = -\frac{n_x^2 n_\varphi^4 \sin^2 \beta}{\left(1 - n_\varphi^2\right) g},$$

$$g = \left(1 - n_x^2\right) \left(1 - n_\varphi^2\right)$$

$$-\left(\eta_1 + \eta_3 + \eta_2 + \eta_4\right) r_m n_x^2 n_\varphi^2 \sin^2 \beta$$

In light of functions $f_1(t)$, $f_2(t)$, and $f_3(t)$ in (14), the approximate solutions of the system can be rearranged as the following:

$$x = \sigma \mu_{11} \eta_{1} r r_{m} \cos \varphi_{1} + \mu_{11} \eta_{2} r r_{m} \cos \varphi_{2}$$

$$+ \mu_{12} \eta_{1} r r_{m} \sin (\varphi_{1} + \sigma \beta)$$

$$+ \mu_{13} \eta_{2} r r_{m} \sin (\varphi_{2} - \beta) ,$$

$$\varphi_{3} = \sigma \mu_{21} \eta_{1} r_{m} r_{l} \cos \varphi_{1} + \mu_{21} \eta_{2} r_{m} r_{l} \cos \varphi_{2}$$

$$+ \mu_{22} \eta_{1} r_{l} r_{m} \sin (\varphi_{1} + \sigma \beta)$$

$$+ \mu_{23} \eta_{2} r_{l} r_{m} \sin (\varphi_{2} - \beta) ,$$

$$\varphi_{4} = \mu_{31} r_{m} r_{l} (\sigma \eta_{1} \cos \varphi_{1} + \eta_{2} \cos \varphi_{2})$$

$$+ \mu_{32} \eta_{1} r_{l} r_{m} \sin (\varphi_{1} + \sigma \beta)$$

$$+ \mu_{33} \eta_{2} r_{l} r_{m} \sin (\varphi_{1} - \beta) .$$

$$(21a)$$

$$(21b)$$

$$+ \mu_{33} \eta_{2} r_{l} r_{m} \sin (\varphi_{1} - \beta) .$$

$$(21c)$$

4. Synchronization

Based on the approximate solutions above, the synchronization and stability of the system can be determined with Poincaré method [20, 25–27]. In addition, the phase angle of the rotors can be assumed by

$$\varphi_1 = \omega_m t + \alpha_1
\varphi_2 = \omega_m t + \alpha_2$$
(22)

Substituting (22) into (21a), (21b), (21c), the approximate solutions of the system can be written by

$$x = \mu_{11} r r_m \left[\sigma \eta_1 \cos \left(\omega_m t + \alpha_1 \right) + \eta_2 \cos \left(\omega_m t + \alpha_2 \right) \right]$$

$$+ \mu_{12} r r_m \eta_1 \sin \left(\omega_m t + \alpha_1 + \sigma \beta \right)$$

$$+ \mu_{13} r r_m \eta_2 \sin \left(\omega_m t + \alpha_2 - \beta \right),$$
(23a)

$$\varphi_{3}$$

$$= \mu_{21} r_{m} r_{l} \left[\sigma \eta_{1} \cos \left(\omega_{m} t + \alpha_{1} \right) + \eta_{2} \cos \left(\omega_{m} t + \alpha_{2} \right) \right]$$

$$+ \mu_{22} r_{l} r_{m} \eta_{1} \sin \left(\omega_{m} t + \alpha_{1} + \sigma \beta \right)$$

$$+ \mu_{23} r_{l} r_{m} \eta_{2} \sin \left(\omega_{m} t + \alpha_{2} - \beta \right),$$
(23b)

 Ψ_{4} $= \mu_{31} r_{m} r_{l} \left[\sigma \eta_{1} \cos \left(\omega_{m} t + \alpha_{1} \right) + \eta_{2} \cos \left(\omega_{m} t + \alpha_{2} \right) \right]$ $+ \mu_{32} \eta_{1} r_{l} r_{m} \sin \left(\omega_{m} t + \alpha_{1} + \sigma \beta \right)$ $+ \mu_{33} \eta_{2} r_{l} r_{m} \sin \left(\omega_{m} t + \alpha_{2} - \beta \right).$ (23c)

As the values of the phase difference of the rotors may be different when the asynchronous motors are operated in the steady state, the phase difference between the rotors is noted by

$$\alpha = \alpha_1 - \alpha_2 \tag{24}$$

The second derivatives of x, φ_3 , and φ_4 with respect to time t can be obtained. Substituting \ddot{x} , $\ddot{\varphi}_3$, and $\ddot{\varphi}_4$ into (12a) and (12b), and then integrating and averaging these equations related to t over period T, respectively, we can obtain

$$P_{1} = \frac{1}{T} \int_{0}^{T} \mu \Phi_{1} dt = \overline{M}_{e1} - \overline{R}_{e1} + \frac{1}{2}$$

$$\cdot \eta_{1} \eta_{2} m r^{2} \omega_{m}^{2} r_{m} \begin{cases} -\sigma \mu_{11} \sin \alpha + \sigma \mu_{12} \cos (\alpha + \beta) \\ +\mu_{21} \cos (\alpha + \sigma \beta) - \mu_{23} \sin [\alpha + (\sigma + 1) \beta] \end{cases}$$

$$(25)$$

$$P_{2} = \frac{1}{T} \int_{0}^{T} \mu \Phi_{2} dt = \overline{M}_{e2} - \overline{R}_{e2} + \frac{1}{2}$$

$$\cdot \eta_{1} \eta_{2} m r^{2} \omega_{m}^{2} r_{m} \begin{cases} -\sigma \mu_{11} \sin \alpha + \sigma \mu_{12} \cos (\alpha + \beta) \\ +\mu_{21} \cos (\alpha + \sigma \beta) - \mu_{23} \sin [\alpha + (\sigma + 1) \beta] \end{cases}$$
(26)

 P_1 and P_2 represent the averaging residual torque of the first and second motor in single period T, respectively. As we all know, when the motors are operated in synchronous state, μ is a small parameter approached to zero. Therefore, the residual torque in the motors is approximated to zero; i.e.,

$$P_1 \approx P_2 \approx 0 \tag{27}$$

Substituting (27) into (25) and (26), the balanced torques of the motor are written by

$$\overline{M}_{e1} - \overline{R}_{e1} = \frac{1}{2} \eta_1 \eta_2 m r^2 \omega_m^2 r_m \left\{ \sigma \mu_{11} \sin \alpha - \sigma \mu_{12} \cos \left(\alpha + \beta \right) - \mu_{21} \cos \left(\alpha + \sigma \beta \right) + \mu_{23} \sin \left[\alpha + (\sigma + 1) \beta \right] \right\}$$
(28a)

$$\overline{M}_{e2} - \overline{R}_{e2} = \frac{1}{2} \eta_1 \eta_2 m r^2 \omega_m^2 r_m \left\{ -\sigma \mu_{11} \sin \alpha + \sigma \mu_{12} \cos (\alpha + \beta) + \mu_{21} \cos (\alpha + \sigma \beta) - \mu_{23} \sin \left[\alpha + (\sigma + 1) \beta \right] \right\}$$
(28b)

 \overline{M}_{ei} , \overline{R}_{ei} (i=1,2) represent average electromagnetic and friction torque in the motors over period T, respectively. When the two rotors are operated synchronously, the vibrating system transmits electromagnetic torque between the two

motors to overcome the differences of output torque for the two rotors by adjusting the phase difference between two rotors. The differences of output torque ΔM between the motors can be expressed as

$$\Delta M = \overline{M}_{e1} - \overline{R}_{e1} - \left(\overline{M}_{e2} - \overline{R}_{e2}\right) = \eta_1 \eta_2 m r^2 \omega_m^2 r_m \begin{cases} \sigma \mu_{11} \sin \alpha - \sigma \mu_{12} \cos \left(\alpha + \beta\right) - \mu_{21} \cos \left(\alpha + \sigma \beta\right) \\ \sigma \mu_{12} \cos \left(\alpha + \beta\right) + \mu_{21} \cos \left(\alpha + \sigma \beta\right) \end{cases}$$
(29)

As the parameter of the two asynchronous motors is identical, the differences of output torque should be zero. Therefore, to implement synchronous operation, the values of the parameters in the system must satisfy the following equation:

$$-\sigma\mu_{11}\sin\alpha + \sigma\mu_{12}\cos(\alpha + \beta) + \mu_{21}\cos(\alpha + \sigma\beta)$$
$$-\mu_{23}\sin[\alpha + (\sigma + 1)\beta] = 0$$
 (30)

which is called balance equation of synchronous state. Obviously, the phase difference is influenced by the rotation direction of the motors, the coupling coefficients between rotor and pendula, and the installation location of the motors. According to (30), we can determine phase difference α with numerical computations. With trigonometric function, the equation above can be expanded as

 $\cot \alpha$

$$= \frac{\sigma \mu_{11} + \sigma \mu_{12} \sin \beta + \sigma \mu_{21} \sin \beta + \mu_{23} \cos \left[(\sigma + 1) \beta \right]}{\sigma \mu_{12} \cos \beta + \mu_{21} \cos \beta - \mu_{23} \sin \left[(\sigma + 1) \beta \right]}$$
(31)

If some solutions of phase difference α exist in (31), the denominator of this equality in the right should be nonzero. Define the denominator of this equality with a symbol D; i.e.,

$$D = \sigma \mu_{12} \cos \beta + \mu_{21} \cos \beta - \mu_{23} \sin [(\sigma + 1) \beta]$$
 (32)

It can be known that denominator D is a function related to variables $\sigma, \mu_{12}, \mu_{21}, \mu_{23}$, and β , but parameter σ indicates the rotation directions of the motors independent of nonzero solution of denominator D. Therefore, we will discuss zero solution of parameter D related to installation angle and coupling coefficients. There are two cases causing the zero solution of denominator D.

(1) Parameter β represents installation angle of the motors. Thus, parameter β with a particular value leads to D being zero. The first "critical point" is

$$\beta = k\pi - \pi, \quad (k = 1, 2, 3...).$$
 (33)

When the installation angles of the motors are approximated or equal to this point, the absent-synchronization of the system will be implemented. In this situation, the vibrating characteristics of the oscillating body are unascertainable.

(2) According to (20), coupling coefficients μ_{12} , μ_{21} , and μ_{23} are fractions; thus parameters n_x and n_φ with particular values lead to D being zero. The second "critical point" is

$$n_x = 1 \text{ or } n_{\varphi} = 1.$$
 (34)

The second "critical point" means that the excitation frequency of the motors is identical to the natural frequency of the springs. In this case, strong resonance exists in such value of the frequency ratios. However, frequency ratios n_x and n_φ are the function related to stiffness coefficients k_x and k_φ of the springs, which indicates that stiffness coefficients are the key parameters to determine phase difference α .

Clearly, to ensure the synchronization and stability of the system, the value of frequency ratios n_x and n_{φ} should be far away from 1. In light of different value of n_{φ} and n_{φ} , the coupling type of the system can be defined as follows:

Type 1: system of before-resonance coupled before-resonance (0.1 < n_x < 1 and 0.1 < n_ω < 1).

Type 2: system of after-resonance coupled before-resonance (0.1 < n_x < 1 and 1.0 < n_{φ} < 7, or 1.0 < n_x < 7 and 0.1 < n_{φ} < 1).

Type 3: system of after-resonance coupled after-resonance (1.0 < n_{φ} < 7 and 1.0 < n_{x} < 7).

Eliminating the two kinds of "critical point", the phase difference between the two rotors can be calculated:

α

$$= \operatorname{arccot} \frac{\sigma \mu_{11} + \sigma \mu_{12} \sin \beta + \sigma \mu_{21} \sin \beta + \mu_{23} \cos \left[(\sigma + 1) \beta \right]}{\sigma \mu_{12} \cos \beta + \mu_{21} \cos \beta - \mu_{23} \sin \left[(\sigma + 1) \beta \right]}.$$
 (35)

Obviously, the value of the phase difference is related to the coupling coefficients (μ_{11} , μ_{12} , μ_{21} , and μ_{23}) and the installation angle. Coupling coefficients represent the mutual coupling ability among the oscillating body, rotors, and pendula through the springs. The larger the coupling coefficients are, the stronger the coupling ability of the system is. Obviously, coupling coefficients μ_{12} , μ_{21} , and μ_{23} contain $\sin \beta$; thus the absence of the coupling ability appears when $\beta=0$. In this situation, the rotors cannot implement synchronous operation. It should be noted that coupling coefficients are the functions of parameters n_x , n_φ , β , and r_m , and these parameters may influence the value of phase difference α .

5. Synchronous Stability

From (35), some values of phase difference can be obtained; however, the stability of these values should be determined as I.I.Blekhman's method [1, 2]. If a certain constant $\alpha = \alpha^*$ satisfies equation

$$\frac{\partial \left(P_1 - P_2\right)}{\partial \alpha} - \chi = 0,\tag{36}$$

TABLE 1: Parameter values.

Unbalanced rotor for $i = 1, 2$	Vibroplatform	Pendulum rod	Asynchronous motor
$m_i = 2 [kg]$	$m_0 = 100 [\mathrm{kg}]$	l = 0.3 [m]	$m_3 = m_4 = 14 [\text{kg}]$
r = 0.05 [m]	$k_x = 246490000 - 50307 [N/m]$	$k_{\varphi} = 4980 - 24402510 [\text{Nm/rad}]$	$L_{mi} = 0.13 [H]$
$\omega_m = 152 - 157 [rad/s]$	$f_x = 1064[\text{Ns/m}]$	$f_{\varphi} = 15 \left[\text{Nm/(rad/s)} \right]$	$L_{si} = 0.1 [\mathrm{H}]$
-	-	$\beta = 0 - 5\pi/12 [\text{rad}]$	$n_p = 2$
-	-	-	$R_{ri}=0.54[\Omega]$
_	-	-	$U_{S0} = 220 [V]$

(b) Parameter values according to dimensionless equations (11a), (11b), (11c), (11d), (11e)

$$\eta_1 = 0.2, 1$$
 $\eta_2 = 1$
 $\eta_3 = \eta_4 = 12$
 $\sigma = -1, 1$
 $r_m = 0.02$
 $n_x = 0.1 \sim 7$
 $n_{\varphi} = 0.1 \sim 7$

phase difference α^* is stable under the condition that the value of χ is negative.

Thus, the residual torque difference can be obtained by

$$\begin{split} P_{1} - P_{2} &= \left\langle \mu \Phi_{1} \right\rangle = \overline{M}_{e1} - \overline{R}_{e1} - \left(\overline{M}_{e2} - \overline{R}_{e2} \right) \\ &+ \eta_{1} \eta_{2} m r^{2} \omega_{m}^{2} r_{m} \left\{ \begin{matrix} -\sigma \mu_{11} \sin \alpha + \sigma \mu_{12} \cos \left(\alpha + \beta \right) \\ +\mu_{21} \cos \left(\alpha + \sigma \beta \right) - \mu_{23} \sin \left[\alpha + \left(\sigma + 1 \right) \beta \right] \right\} \end{split} \tag{37}$$

As \overline{M}_{ei} , \overline{R}_{ei} (i=1,2) are irrelevant to phase difference α , in light of (33), the criterion of synchronous stability is expressed

$$\chi = \frac{\partial (P_1 - P_2)}{\partial \alpha}$$

$$= \eta_1 \eta_2 m r^2 \omega_m^2 r_m \left\{ -\sigma \mu_{11} \cos \alpha - \sigma \mu_{12} \sin (\alpha + \beta) - \mu_{21} \sin (\alpha + \beta) - \mu_{23} \cos [\alpha + (\sigma + 1)\beta] \right\}$$

$$< 0. \tag{38}$$

Rearranging the equation above, the criterion of synchronous stability is simplified by

$$\sigma \mu_{11} \cos \alpha + \sigma \mu_{12} \sin (\alpha + \beta) + \mu_{21} \sin (\alpha + \sigma \beta)$$

$$+ \mu_{23} \cos [\alpha + (\sigma + 1) \beta] > 0$$
(39)

The formula above shows that synchronous stability of the system is also determined by rotation direction of the rotors, coupling coefficients, and installation location of the motors. Only should parameters of the system satisfy the balance equation (30) and the synchronous stability criterion (39), the synchronous operation of the rotors can be implemented. In this case, the phase difference between the rotors is called the stable phase difference.

6. Numerical Analysis

The above-mentioned sections have given some theoretical discussions in the simplified form on synchronization problem for the vibration system that the unbalanced rotors are coupled with pendulum. In this section, we will employ some numerical analysis to discuss the stable phase difference, which can be calculated according to (30) and (39). The phase difference is determined by rotation direction of the rotors, coupling coefficients, and installation location of the motors. However, the coupling coefficients are the function of frequency ratios $(n_x n_\varphi)$, mass ratios (r_m, η_i) , and motor installation angle (β) . Therefore, it can be included that the stable phase difference may be influenced by the parameters above. The parameter values corresponding to general engineering application are as given in Table 1.

6.1. The Rotors Operated in Opposite Direction. The stable phase difference is determined by considering the different values of parameters β , η_i (i = 1, 2), n_x , and n_{φ} . Moreover, in light of (35) and (39), the rotation direction of the two rotors is opposite, and the stable phase difference between the two rotors is shown in Figure 2. According to (20) and (30), we have $(-\mu_{11} + \mu_{23}) \sin \alpha = 0$ when $\sigma = -1$, and the synchronous balance condition as in (17a), (17b), (17c) is simply expressed as $\sin \alpha = 0$. Similarly, the synchronous stability criterion can be rewritten by $(-\mu_{11} + \mu_{23}) \sin \alpha > 0$. It then follows that the value of the phase difference is stabilized at 0 [rad] in the blue area, which describes that the synphase motion is stable and the antiphase motion is unstable ([1] describes that the motion, as the existence of $\alpha \in (-\pi/2, \pi/2)$, is called synphase synchronization; and the motion, as the existence of $\alpha \in (\pi/2, 3\pi/2)$, is called antiphase synchronization). On the contrary, the brown area represents that the synphase synchronization is unstable and the antiphase synchronization is stable. Firstly, installation angle β and mass ratio r_m are

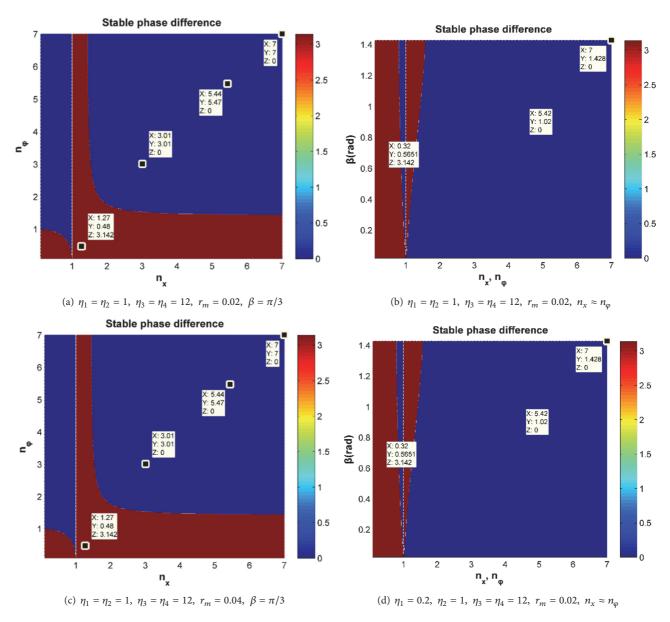


FIGURE 2: Stable phase difference when $\sigma = -1$.

fixed at $\pi/3$ and 0.02, respectively, and the mass ratios (η_1, η_2) are equal to 1.0. In such values of the parameters, the stable phase difference is shown in Figure 2(a). It is indicated that the stable phase difference is related to frequency ratios n_x and n_{ω} ; in other words, the phase difference is dependent on the stiffness of the torque spring in the pendulum and the pressure spring in the vibrating body. Secondly, mass ratio r_m is fixed at 0.02, and the frequency ratios n_x and n_{φ} are considered identical. Figure 2(b) describes that the stable phase difference is changed with the installation angle β . It can be seen that the synchronous state of the system is locked in the synphase synchronization when n_x and $n_{\varphi} > 1.5$, and the variation of installation angle β has little influence on the stable phase difference. However, the synchronous state is changed in region of n_x and n_{φ} < 1.5. Finally, the effect of mass ratios r_m , η_1 , and η_2 on the phase difference needs to be discussed. Thus, the parameter values in Figure 2(c) are identical to Figure 2(a) except for r_m . And the parameter values in Figure 2(d) are identical to Figure 2(b) except for η_1 . Comparing Figures 2(c) and 2(d) with Figures 2(a) and 2(b), respectively, it can be found that the values of the stable phase difference are independent of the mass ratios. Therefore, the mass variations of rotors and vibration body would not affect the synchronous motion when the two rotors operate in the opposite direction.

6.2. The Rotors Operated in the Same Direction. In the following calculations, the two rotors rotating in the same direction are considered according to (35) and (39). Firstly, the parameter values in Figure 3(a) are the same as Figure 2(a) except for rotation direction σ . From Figure 3(a), it follows that two rotors may synchronize either synphase or antiphase,

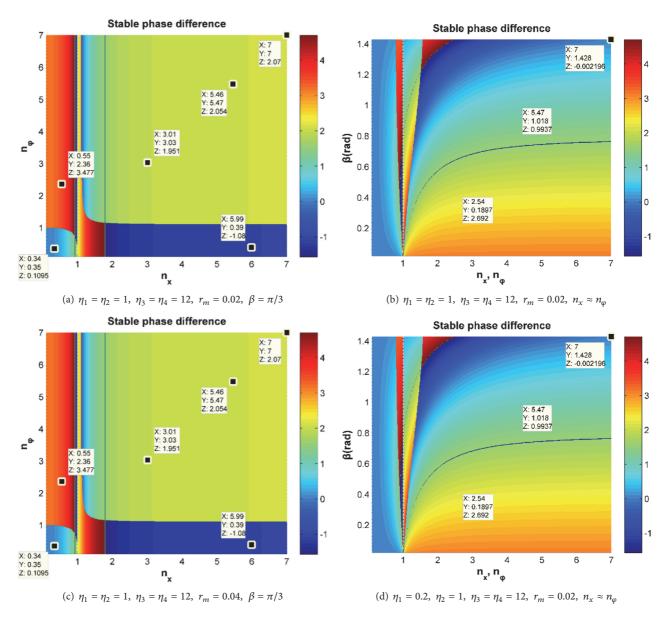


FIGURE 3: Stable phase difference when $\sigma = 1$.

also depending on the values of n_x and n_{φ} . The obtained results reveal that, in the interval of $0.1 < n_x' < 1$ and 0.1 < n_{φ} < 1, synphase synchronization is implemented between the rotors; in the interval of 0.1 $< n_x < 1$ and $1 < n_{\omega} < 1$ 7, antiphase synchronization is implemented between the rotors; in the interval of $1 < n_x < 7, 0.1 < n_{\varphi} < 1$ and $1 < n_x < 1$ 7, $1 < n_{\varphi} < 7$, both antiphase and synphase synchronization collectively remained; in the interval of $1 < n_r < 7$ and for $1 < n_{\varphi} < 7$, the two rotors will be synchronously operated in synphase state. Figure 3(b) shows the variation of the stable phase difference with the installation angle. It is indicated that the synchronous state of the system is obviously influenced by β . Finally, the effect of mass ratios r_m , η_1 , and η_2 on the phase difference is discussed. Thus, the parameters in Figure 3(c) are identical with Figure 3(a) except for r_m , and the parameters in Figure 3(d) are identical with Figure 3(b)

except for η_1 . Comparing Figures 3(c) and 3(d) with Figures 3(a) and 3(b), respectively, it can be found that the stable phase difference is also independent of the mass ratios. In other words, synchronous state is less influenced by mass of the rotors when the two rotors operate in the same direction.

7. Sample Verifications

7.1. For $\sigma=-1$, $n_x=6$, $n_\varphi=6$, $\eta_1=\eta_2=1$, $\eta_3=\eta_4=12$, $r_m=0.02$, and $\beta=\pi/3$. This subsection refers to the case that the system of after-resonance is coupled with the after-resonance; i.e., $n_x=6$, $n_\varphi=6$. The mass of the two rotors operated in opposite direction is identical; i.e., $\eta_1=\eta_2=1$. In the simulation model, the coefficients of the spring stiffness are $k_x=65969[{\rm N/m}]$ and $k_\varphi=1053[{\rm N\cdot m/rad}]$, and the other parameter is identical with Table 1(a). The numerical

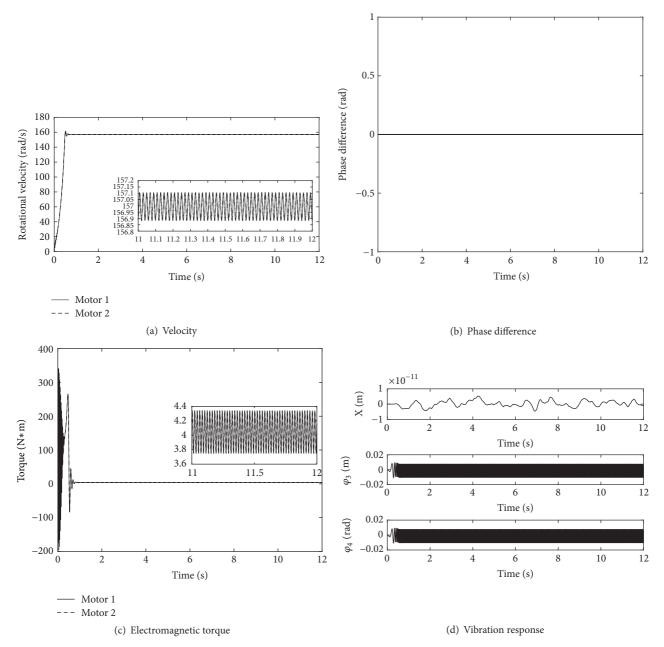


FIGURE 4: The dynamic characteristics when the rotors rotate in the opposite direction.

results of this sample can be calculated through (9a), (9b), (9c), (9d), (9e). When the two motors are supplied by the electric source at the same time, the velocities of the two rotors are compatible (in Figure 4(a)). When the angular velocities of the motors reach the nominal velocity, then the motors oscillate steadily with the identical responses. At this moment, the coupling torques (in Figure 4(c)), making the phase difference α stabilized nearby 0 [rad], are fluctuated. In this case, the two motors rotate stably in synphase synchronization. From Figure 4(c), it follows the displacements of the vibration body and the two motors. It is clear that when the rotation velocity of the two rotors passes through the resonant region of the coupling system, the

resonant responses of the system in the φ_3 - and φ_4 -directions appear in the starting process. In the synchronous state, the displacements of the vibrating body and the motors are stable, and the amplitudes of them are 0[m], 0.01[rad], and 0.01[rad], respectively. Comparing simulation results with Figures 2(a) and 2(b), the stable phase difference obtained by the computer simulation is consistent with the theoretical computation (i.e., the stable phase difference in Figures 3(a) and 3(b) is equal to 0 [rad]; here, the stable phase difference is fluctuated near 0 [rad]).

7.2. For $\sigma = 1$, $n_x = 6$, $n_{\varphi} = 0.3$, $\eta_1 = \eta_2 = 1$, $\eta_3 = \eta_4 = 12$, $r_m = 0.04$, and $\beta = \pi/3$. Simulation results obtained by (9a), (9b),

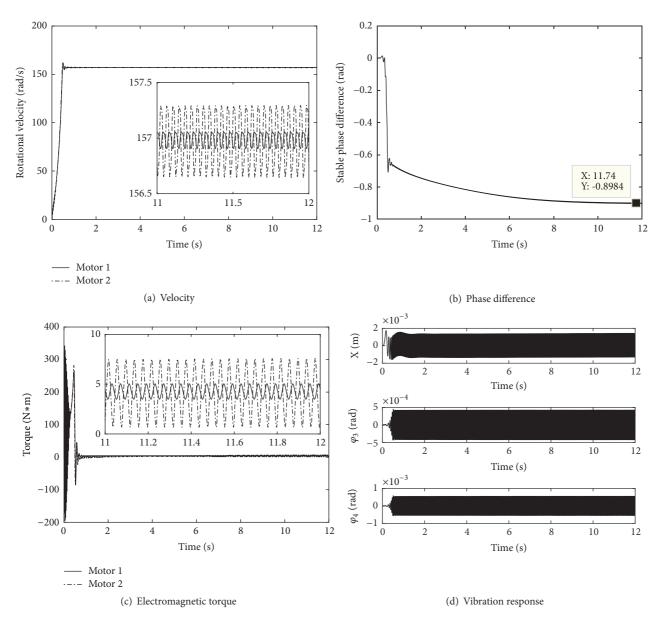


FIGURE 5: The dynamic characteristics when the rotors rotate in the same direction.

(9c), (9d), (9e) are shown in Figure 5 when $\sigma=1$, $n_x=6$, $n_{\varphi}=0.3$, $\eta_1=\eta_2=1$, $\eta_3=\eta_4=12$, $r_m=0.04$, and $\beta=\pi/3$. Here, the coefficients of spring stiffness are $k_x=65969[{\rm N/m}]$ and $k_{\varphi}=976100[{\rm N\cdot m/rad}]$, and the rotors are operated in the same direction. The coupling type of the system belongs to type 2. When the two motors are supplied by the electric source at the same time, the angular accelerations of the two rotors are compatible (in Figure 5(a)). The reason is that the inertia moments of the rotors are identical and the spring stiffness is extremely stronger. During the staring process of the system, the velocity difference exists between the two rotors, which leads to the phase difference instability, shown as in Figure 5(b). However, when the angular velocities of the motors reach the rated speed and the motor oscillate steadily, the synchronization phenomenon occurs. It should

be noted that the velocity fluctuation of the motors is smaller than that of Section 7.1, because the vibration of the motors is feebler. At this moment, the average coupling torques (in Figure 5(c)), making the phase difference α stabilized at -0.8984 [rad], are approximated to 4.08[N · m]. In this case, the two motors rotate stably in the synphase synchronization, and the synchronous velocity is 157 [rad/s]. From Figure 5(d) it follows the displacements of the vibrating body and the two motors. It can be seen that the displacement responses of the vibrating body and the two motors are stable, and the amplitudes of them are 1.5×10^{-3} [m], 4.1×10^{-4} [rad] and 7.3×10^{-4} [rad], respectively. Comparing simulation results with Figure 3(b), it should be noted that the value of the stable phase difference is in agreement with the results obtained for the case of the theoretical solutions (i.e., the stable phase

difference of such parameters in Figure 3(a) is equal to -1.08 [rad]; here, the stable phase difference is equal to -0.8984 [rad]).

8. Conclusions

In this paper, the dual-pendulum-rotor system is concerned. The research results show that the spring stiffness, the installation angular of the motor, and rotation direction of the rotors have a large influence on the existence and stability of the synchronization state in the coupling system, and the mass ratios of the system are irrelevant to the synchronous state of the system. It should be noted that to ensure the implementation of the synchronization of the system, the values of the parameters of the system should be far away to the two "critical points". To verify the correctness of the theoretical computations, some example simulations are preformed, and the results of theoretical computation are in accordance with that of example simulations.

The dual-pendulum-rotor system widely appears in aero-power plant, mining screening machines, parallel robots, and the like of the other rotation equipment. However, the dynamic characteristics and performance accuracy of the dual-pendulum-rotor system are mainly influenced by synchronous behavior between the rotors. In the early stage, for the developing and understanding the internal characteristics of the system, we only consider the vibrating body under the assumption of horizontal displacement. What is synchronization state of the system that the vibrating body simultaneously vibrates in the pitch and vertical directions? We believe that finding the answer to this question is the next step in challenging task of getting a complete understanding of synchronization in such system.

Data Availability

The data used to support the findings of this study are available from the corresponding author upon request.

Conflicts of Interest

The authors declare that there are no conflicts of interest regarding the publication of this paper.

Acknowledgments

This study is supported by National Natural Science Foundation of China (Grant no. 51705437), scientific research starting project of SWPU (no. 2017QHZ009), and the plan of science and technology of Sichuan province (no. 2016RZ0059).

References

- [1] I. I. Blekhman, Synchronization in science and technology, ASME Press, New York, USA, 1988.
- [2] I. I. Blekhman, Selected Topics in Vibrational Mechanics World scientific, Singapore, 2002.

[3] C. Murguia, R. H. B. Fey, and H. Nijmeijer, "Synchronization of identical linear systems and diffusive time-delayed couplings," *IEEE Transactions on Circuits and Systems I: Regular Papers*, vol. 61, no. 6, pp. 1801–1814, 2014.

- [4] A. Arenas, A. Dì az-Guilera, J. Kurths, Y. Moreno, and C. Zhou, "Synchronization in complex networks," *Physics Reports*, vol. 469, no. 3, pp. 93–153, 2008.
- [5] M. A. Barrón and M. Sen, "Synchronization of four coupled van der Pol oscillators," *Nonlinear Dynamics*, vol. 56, no. 4, pp. 357– 367, 2009.
- [6] R. Yamapi and P. Woafo, "Dynamics and synchronization of coupled self-sustained electromechanical devices," *Journal of Sound and Vibration*, vol. 285, no. 4-5, pp. 1151–1170, 2005.
- [7] J. F. Totz, R. Snari, D. Yengi, M. R. Tinsley, H. Engel, and K. Showalter, "Phase-lag synchronization in networks of coupled chemical oscillators," *Physical Review E: Statistical, Nonlinear, and Soft Matter Physics*, vol. 92, no. 2, Article ID 022819, 2015.
- [8] A. Pikovsky, M. Rosenblum, and J. Kurths, Synchronization: A Universal Concept in Nonlinear Sciences, Cambridge unversity press, Cambridge, UK, 2001.
- [9] P. Koluda, P. Perlikowski, K. Czolczynski, and T. Kapitaniak, "Synchronization configurations of two coupled double pendula," *Communications in Nonlinear Science and Numerical* Simulation, vol. 19, no. 4, pp. 977–990, 2014.
- [10] R. Dilão, "Anti-phase synchronization and ergodicity in arrays of oscillators coupled by an elastic force," *The European Physical Journal Special Topics*, vol. 223, no. 4, pp. 665–676, 2014.
- [11] L. Marcheggiani, R. Chacón, and S. Lenci, "On the synchronization of chains of nonlinear pendula connected by linear springs," *The European Physical Journal Special Topics*, vol. 223, no. 4, pp. 729–756, 2014.
- [12] R. A. O. Signeul, "Vibrating device for a directed vibratory effected by means of rotatable vibratory members," United states patent, No.2,531,706, 1950.
- [13] B. C. Wen, J. Fan, and C. Y. Zhao, Synchronization and controled sychronization in engineering, Science press, Beijing, China, 2009
- [14] C. Zhao, B. Wen, and X. Zhang, "Synchronization of the four identical unbalanced rotors in a vibrating system of plane motion," *Science China Technological Sciences*, vol. 53, no. 2, pp. 405–422, 2010.
- [15] C. Y. Zhao, H. T. Zhu, R. Z. Wang, and B. C. Wen, "Synchronization of two non-identical coupled exciters in a non-resonant vibrating system of linear motion. Part I: theoretical analysis," *Shock and Vibration*, vol. 16, no. 5, pp. 505–515, 2009.
- [16] J. M. Balthazar, J. L. Felix, and R. M. Brasil, "Some comments on the numerical simulation of self-synchronization of four nonideal exciters," *Applied Mathematics and Computation*, vol. 164, no. 2, pp. 615–625, 2005.
- [17] A. A. N. Djanan, B. R. N. Nbendjo, and P. Woafo, "Effect of self-synchronization of DC motors on the amplitude of vibration of a rectangular plate," *The European Physical Journal Special Topics*, vol. 223, no. 4, pp. 813–825, 2014.
- [18] X. L. Zhang, B. C. Wen, and C. Y. Zhao, "Synchronization of three non-identical coupled exciters with the same rotating directions in a far-resonant vibrating system," *Journal of Sound* and Vibration, vol. 332, no. 9, pp. 2300–2317, 2013.
- [19] X. Zhang, B. Wen, and C. Zhao, "Theoretical study on synchronization of two exciters in a nonlinear vibrating system with multiple resonant types," *Nonlinear Dynamics*, vol. 85, no. 1, pp. 141–154, 2016.

[20] P. Fang and Y. Hou, "Synchronization characteristics of a rotor-pendula system in multiple coupling resonant systems," Proceedings of the Institution of Mechanical Engineers, Part C: Journal of Mechanical Engineering Science, vol. 232, no. 10, pp. 1802–1822, 2017.

- [21] L. Tang, X. Zhu, and J. Li, "Effects of the Synchronous Variation of the Static and the Kinetic Friction Coefficients on Stick–Slip Vibration of Drillstring," *Iranian Journal of Science and Technology, Transactions of Mechanical Engineering.*
- [22] W. Craig, D. Yeo, and D. A. Paley, "Dynamics of a rotorpendulum with a small, stiff propeller in wind," in *Proceedings of* the ASME 2016 Dynamic Systems and Control Conference, DSCC 2016, USA, October 2016.
- [23] X. Zhang, B. Wen, and C. Zhao, "Vibratory synchronization transmission of a cylindrical roller in a vibrating mechanical system excited by two exciters," *Mechanical Systems and Signal Processing*, vol. 96, pp. 88–103, 2017.
- [24] P. Fang, Y. Hou, Y. Nan, and L. Yu, "Study of synchronization for a rotor-pendulum system with Poincare method," *Journal of Vibroengineering*, vol. 17, no. 5, pp. 2681–2695, 2015.
- [25] P. Fang, Y. Hou, L. Zhang, M. Du, and M. Zhang, "Synchronous behavior of a rotor-pendulum system," *Acta Physica Sinica*, pp. 254–265, 2016.
- [26] Y. Hou and P. Fang, "Investigation for Synchronization of a Rotor-Pendulum System considering the Multi-DOF Vibration," *Shock and Vibration*, vol. 2016, Article ID 8641754, 22 pages, 2016.
- [27] Y. Hou, M. Du, P. Fang, and L. Zhang, "Synchronization and stability of an elastically coupled tri-rotor vibration system," *Journal of Theoretical and Applied Mechanics (Poland)*, vol. 55, no. 1, pp. 227–240, 2017.

Hindawi Shock and Vibration Volume 2018, Article ID 3958016, 11 pages https://doi.org/10.1155/2018/3958016

Research Article

A Copula-Based and Monte Carlo Sampling Approach for Structural Dynamics Model Updating with Interval Uncertainty

Xueqian Chen (1), 1,2 Zhanpeng Shen, 1,2 and Xin'en Liu 1,2

¹Institute of Systems Engineering, China Academy of Engineering Physics (CAEP), Mianyang Sichuan 621999, China ²Shock and Vibration of Engineering Materials and Structures Key Laboratory of Sichuan Province, Mianyang Sichuan 621999, China

Correspondence should be addressed to Xueqian Chen; cxqdd127@sohu.com

Received 23 March 2018; Revised 29 May 2018; Accepted 4 June 2018; Published 9 July 2018

Academic Editor: Aly Mousaad Aly

Copyright © 2018 Xueqian Chen et al. This is an open access article distributed under the Creative Commons Attribution License, which permits unrestricted use, distribution, and reproduction in any medium, provided the original work is properly cited.

As the uncertainty is widely existent in the engineering structure, it is necessary to study the finite element (FE) modeling and updating in consideration of the uncertainty. A FE model updating approach in structural dynamics with interval uncertain parameters is proposed in this work. Firstly, the mathematical relationship between the updating parameters and the output interesting qualities is created based on the copula approach and the vast samples of inputs and outputs are obtained by the Monte Carlo (MC) sampling technology according to the copula model. Secondly, the samples of updating parameters are rechosen by combining the copula model and the experiment intervals of the interesting qualities. Next, 95% confidence intervals of updating parameters are calculated by the nonparameter kernel density estimation (KDE) approach, which is regarded as the intervals of updating parameters. Lastly, the proposed approach is validated in a two degree-of-freedom mass-spring system, simple plates, and the transport mirror system. The updating results evidently demonstrate the feasibility and reliability of this approach.

1. Introduction

Finite element (FE) models that numerically solve various engineering problems can aid virtual prototyping, reduce product development cycle, and cut down the cost of performing the physical tests. However, the reliability of the simulation results by finite element modeling is not always guaranteed since FE models are the approximations of real world phenomena based on various assumptions. These assumptions may detract from the quality and accuracy of simulation results. In order to improve the accuracy of FE simulating to serve the structural design better, the FE model updating techniques are needed to develop. In the past few decades, various kinds of FE model updating approaches have been widely investigated based on the actually observed behaviors of the system. Additionally, experimental modal and vibration data are often used in FE model updating in the field of structural dynamics [1–6].

In most model updating approaches, the simulations are usually deterministic where each of the updating parameters is considered to have one "true" value and the purpose of the updating procedure is to provide a deterministic estimation.

In reality, there are always uncertainties in nominally identical structures, such as the structural parameter uncertainty (physical material properties, geometric parameters), the assembly joints uncertainty, and the experiment uncertainty (measurement noise, modal identification techniques, etc.). As a result, the FE model updating approaches with uncertainty have received great attentions recently. Studies have shown that the simulation results are more reliable when the uncertainties are taken into account [7], suggesting that it is necessary to consider the uncertainties during modeling and simulating [8].

In FE model updating approaches with uncertainty, the updated parameters are no longer deterministic and are described as random variables. Usually, the FE model updating approaches with uncertainty can be classified into two major categories: probabilistic and nonprobabilistic approaches. In the earlier works, a probabilistic approach proposed incorporated the measurement noise into model updating [9]. Subsequently, Bayesian statistical frameworks were adopted to estimate the posterior probabilities of uncertain parameters [10–12]. However, high computational

costs due to a large amount of samples required for a satisfactory estimation greatly restrain the applications of Bayesian updating approaches. As a result, surrogate models such as the Gaussian process model with the perturbation approaches and sensitivity analysis approaches have been employed in stochastic model updating to improve the efficiency [13–16]. Though, the surrogate model approaches own the superiority of computational efficiency over Monte Carlo (MC) based methods. Nevertheless, the prerequisite of small uncertainties, together with the Gaussian distribution assumption, also limits the applications to complex problems. Moreover, perturbation based predictions are sensitive to the initial estimates of parameters. Recently, an approach with the response surface models and MC simulation has been developed, which decomposed a stochastic updating process into a series of deterministic ones [17]. On the other hand, the accuracy of the probabilistic approaches depends on the estimation of the probability distribution characteristics of the structural parameters and the responses. The establishment of an accurate probability distribution function (PDF) needs lots of experiment data in the probabilistic approaches, which greatly limits its application in engineering.

In nonprobabilistic approaches, the interval approach has been intensively investigated. By comparison, the experiment samples are not strictly needed in the FE model updating with interval analysis as was proposed. In the field of interval model updating (IMU), the inclusion theorem was employed to establish an interval inverse problem. And the convergence was achieved when measured responses fall into numerically predicted intervals [18-22]. Considering the easy implementation, IMU problems are usually solved within a deterministic framework where the upper and lower bounds of parameters are sought separately. For example, an IMU problem was decomposed into two deterministic constrained optimization processes where the midpoints and interval radii of parameters were separately estimated [19]. Alternatively, the vertex solution theorem is effective and cost-efficient for IMU due to its easy implementation [20], particularly in the solution of Eigen value problems [21]. But the vertex solution was valid only for particular parameterization of an FE model without the involvement of eigenvectors, which highly limits its further applications. Due to this drawback, global optimization algorithms were taken into account for more general solutions. Surrogate models such as the Kriging predictor and interval response surface were used to improve the efficiency of gradient computation and facilitate the convergence [23, 24]. So far most of IMU problems are solved within a deterministic framework since direct interval arithmetic operations are difficult to implement during inverse solutions. Therefore the upper and lower bounds of parameters should be sought separately through a deterministic inverse procedure. Additionally, global optimization of interval variables is difficult to realize due to the fact that the interval arithmetic is quite different with the traditional mathematical arithmetic.

Though several probabilistic and interval model updating approaches have been developed in the past years, most of them are still complicated for implementation. Additionally, these approaches with uncertainty suffer from the challenges

such as ill-condition, nonuniqueness and local optimal solution, etc. To overcome such inconvenience, an IMU approach is developed in this work based on the copula model and MC sampling. In the proposed approach, the copula model between the updating parameters and the interesting qualities is constructed firstly. Then a large amount of samples is obtained according to the copula model, and the samples are rechosen based on experiment intervals of interesting qualities. Lastly, the updating intervals of parameters are obtained by estimating on the rechosen samples with kernel density estimation (KDE). The remainder of the paper is organized as follows. In Section 2, the copula-based FE model updating approach and procedure with interval uncertainty are presented. In Section 3, three examples are provided to validate the accuracy and reliability of the proposed approach. Conclusions are presented in Section 4.

2. Identification of Interval Parameters

The FE model updating problems are classic inverse problems in structural mechanics where the standard "forward" relationship between input and output variables of a model is inverted. The key in solving a FE model updating problem is to construct the mathematical relationship between the updating parameters and the output interesting qualities. The copula function is one of the most effective mathematical tools to determine this relationship, which expediently characterizes the correlation between the marginal functions of multivariables and the joint distribution function.

2.1. Brief Introduction of the Copula Function. A copula function is a general function in statistics to formulate a multivariate distribution with various statistical dependence patterns, which was presented by Sklar in 1959 [25]. Formally, a copula is a joint distribution function of standard uniform random variables. According to the Sklar's theorem, there exists a two-dimensional copula C such that variables x_1 and x_2 in a real random space.

$$F(x_1, x_2) = C(F_1(x_1), F_2(x_2))$$
 (1)

where $F(x_1, x_2)$ is a two-dimensional distribution function with marginal functions $F_1(x_1)$ and $F_2(x_2)$ and $C(F_1(x_1), F_2(x_2))$ is the copula cumulative distribution function (CDF).

Equation (1) can be spread for m-dimensional variables easily, that is,

$$F(x_1, x_2, ..., x_m) = C(F_1(x_1), F_2(x_2), ..., F_m(x_m))$$
 (2)

Consequently, the m-dimensional PDF is as follows:

$$f(x_1, x_2, ..., x_m) = \frac{\partial^m F(x_1, x_2, ..., x_m)}{\partial x_1 \partial x_2 ... \partial x_m}$$

$$= \frac{\partial^m C(F_1(x_1), F_2(x_2), ..., F_m(x_m))}{\partial x_1 \partial x_2 ... \partial x_m}$$

$$= c(F_1(x_1), F_2(x_2), ..., F_m(x_m)) \times \prod_{i=1}^m f_i(x_i)$$
(3)

where $c(F_1(x_1), F_2(x_2), ..., F_m(x_m))$ is the copula PDF, $f(x_1, x_2, ..., x_m)$ is the united PDF for m-dimensional random variables, and $f_i(x_i)$ is the PDF of the *i*th random variable.

At present, the general copula function types include the Gaussian copula function, t-copula function, and Archimedean copula function [26, 27]. Among them, the Gaussian copula is widely utilized because most of the parameters in the engineering satisfy the normal distribution. In the study, the Gaussian copula is adopted for the FE model. Specifically, the Gaussian copula function is constructed by multidimensional Gaussian distribution and the linear correlation parameters, and its distribution function is as follows:

$$C_{Ga}(u_{1}, u_{2}, ..., u_{m}; \boldsymbol{\rho})$$

$$= \Phi_{\rho}(\Phi^{-1}(u_{1}), \Phi^{-1}(u_{2}), ..., \Phi^{-1}(u_{m}))$$
(4)

where Φ_{ρ} is the distribution function of the standard normal function for d-dimensional with the correlation matrix ρ , Φ^{-1} is the inverse function of the distribution function of the standard normal function, and $u_i = F_i(x_i)$, i = 1, 2, ..., m.

2.2. Copula-Based Approach for Model Updating with Interval Uncertainty. Firstly, the original design spaces of updating parameters x_i , $j = 1, 2, \dots, m$, are assumed, and a few samples are obtained by design of experiment (DOE) approach and subsequent deterministic FE analysis on samples according to DOE. Then, the samples of the output interesting qualities y_k , $k = 1, 2, \dots, n$, are obtained from the FE analysis results. Secondly, the copula model is constructed according to the samples of updating parameters and output interesting qualities, and resampling is performed to get large samples with number N for updating parameters and interesting response qualities based on the copula model. The samples falling into the experiment data space are considered to characterize the input-output relationship of the physical structure believably, and unuseful samples are needed to remove. Next, the samples of updating parameters x_i are rechosen according to the experiment intervals of interesting qualities, as follows:

$$x_{j} = \left\{ x_{j} = f\left(y_{1}, \dots, y_{n}\right) \mid y_{k} \in R, y_{k}^{-} \leq y_{k} \leq y_{k}^{+} \right\},\$$

$$j = 1, 2, \dots, m, \ k = 1, 2, \dots, n$$
(5)

where R is the real space and y_k^+ and y_k^- are the upper and lower bounds of the kth output interesting quality which can be obtained from the experiment results.

In practical model updating, the measured data are only a few samples in general. Reasonable interval estimation on experiment data is the precondition to obtain the reliable updated FE model. However, the KDE allows for the capture of the observed distributional structure for the random variables, without having to assume a particular parametric distribution form.

Following [28], the kernel density estimator for variable x has the form

$$\widehat{f}_h = \frac{1}{nh} \sum_{i=1}^n K\left(\frac{x - X_i}{h}\right) \tag{6}$$

where n is the number of observations used to construct the estimate, $K(\cdot)$ is a kernel function, X_i is the ith observation, and h is the window width, or bandwidth. A typical choice for the kernel $K(\cdot)$ is the standard normal density and is implemented here. The choice of the window width h is usually based on the optimization of some scoring function. A least-square cross-validation score function is adopted for this work [28].

The empirical CDF and 95% confidence interval (CI) $[y_{e,95}^- y_{e,95}^+]$ of the random variable x can be obtained by KDE in Matlab that is regarded as the interval of the random variable in this work.

Considering the fact that the estimation on the original intervals of the updating parameters may be inaccurate, the reliable intervals are not identified through one copula-based FE model updating procedure. In order to overcome this problem, the idea of the adaptive response surface technique is adopted for this work [29]. That is, in order to get the final updating results, multiloop on the copula-based model updating procedures may be performed.

In the FE model updating procedure, the convergent criterion is that the difference of the updating parameter intervals between the (i + 1)th iteration step and the ith iteration step is less than a small value, or the difference of the output interesting quality intervals between the ith iteration step results and the experiment results is less than a critical value.

In order to improve the efficiency and the validity of model updating, the renewal strategy of updating parameters is as follows in each iteration step. The current intervals of updating parameters are updated according to the results of the previous iteration step, and the interval medians of the previous step are regarded as the current interval medians, and about 80% of the interval width of the previous step is regarded as the current interval width. Also, the Latin Hypercube Sample (LHS) method is suggested in the DOE, and the number of samples is not less than ten.

The copula-based model updating procedure is repeated until the convergent criterion is satisfied. The flow chart for the copula-based FE model updating is outlined in Figure 1.

3. Case Studies

3.1. Example 1: A Two-Degree-of-Freedom Mass-Spring System. A two degree-of-freedom mass-spring system is shown in Figure 2. The deterministic parameters in the system are $m_1 = m_2 = 1 \text{ kg}$ and $k_1 = 1 \text{ N/m}$. The uncertain interval parameters are $k_2 = [0.8 \ 1.2] \text{ N/m}$ and $k_3 = [0.9 \ 1.1] \text{ N/m}$.

For simplicity, it is assumed that the uncertain parameters are uniformly distributed. To create such kind of uncertainty, the LHS method is used to generate twenty experiment samples. Afterwards, the experiment results of the first two natural frequencies are obtained according

	<i>f</i> ₁ (Hz)	f_2 (Hz)	f ₃ (Hz)	f_4 (Hz)	f ₅ (Hz)
mean	24.12	66.92	77.65	131.97	158.80
interval	[23.94 24.4]	[66.5 67.53]	[76.24 78.91]	[131.31 133.03]	[156.31 160.94]
Std.	0.11	0.25	0.57	0.42	0.97

TABLE 1: Statistical properties of the measured frequencies of the plates.

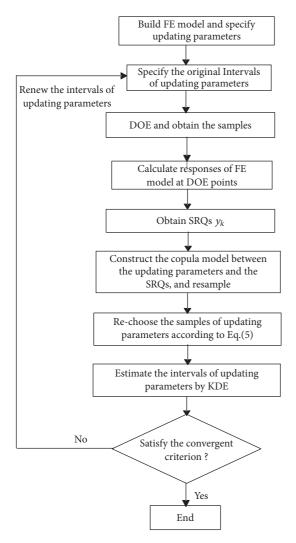


FIGURE 1: Flow chart of the copula-based FE model updating.

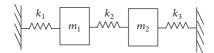


FIGURE 2: A two degree-of-freedom mass-spring system.

to the samples. Considering the effect of small sample, the 95% CI of experiment results are estimated by KDE and the estimated results are [0.9646 1.0338] rad.s⁻¹ and [1.5789 1.8875] rad.s⁻¹, respectively, which are regarded as the intervals of experimental results.

Assume that the original intervals of k_2 and k_3 are the same as [1.2 2.2] N/m, and the first two natural frequencies are regarded as the output interesting qualities. The intervals of k_2 and k_3 are identified according to the copula-based model updating flow with interval uncertainty in Figure 1. The updating results are convergent after three iteration steps.

Figure 3 is the scatter map between the updating parameters and the output interesting qualities when the updating results are convergent, which shows that there is strong correlation between k_3 and f_1 and between k_2 and f_2 and weak correlation between k_2 and f_1 and between k_3 and f_2 .

Then, the updated intervals of k_2 and k_3 are obtained by KDE for the resample in Figure 3, which are [0.775 1.230] N/m and [0.882 1.133] N/m, respectively. The comparison between the original uncertain interval and the updated interval of updating parameters is shown in Figure 4, which shows that the updated interval matches the real interval better. Because the effect of small samples on experiment data is considered in the model updating procedure, the updated interval is bigger than the real interval and the result is reasonable.

In order to validate the updating results on the interval uncertain parameters, the copula models are reconstructed according to the original and the updated intervals of k_2 and k_3 . As a result, 5000 samples of k_2 , k_3 , and the first two frequencies of the system are resampled by the copula models constructed just now. The scatter map between the simulating and the experimental results is shown in Figure 5, which indicates that the frequencies of the updated model are agreement with the experimental results better.

3.2. Example 2: Interval Model Updating in Simple Plates. Impact hammer modal testing with free-free boundary conditions was conducted on thirty-three nominally identical steel plates in [30]. The nominal geometric dimensions of the plates are $564 \, \mathrm{mm}(\mathrm{length}) \times 110 \, \mathrm{mm}(\mathrm{width}) \times 1.45 \, \mathrm{mm}(\mathrm{thickness})$. And the nominal material properties are Young's modulus of 210 GPa, the shear modulus of 83 GPa, and the mass density of $7860 \, \mathrm{kg/m^3}$. The statistical properties of the first five measured natural frequencies of the plates are given in Table 1.

The FE model of the plate is created by the SHELL181 element in ANSYS, which has 300 shell elements. The boundary is free-free in the model. The material properties of the original FE model are the nominal values. The FE model and the first five mode shapes of simulation are shown in Figure 6.

After investigation, the uncertainty of rectangular plates can be characterized by Young's modulus *E*, the shear modulus *G*, and the thick *T* in the FE model. The model updating

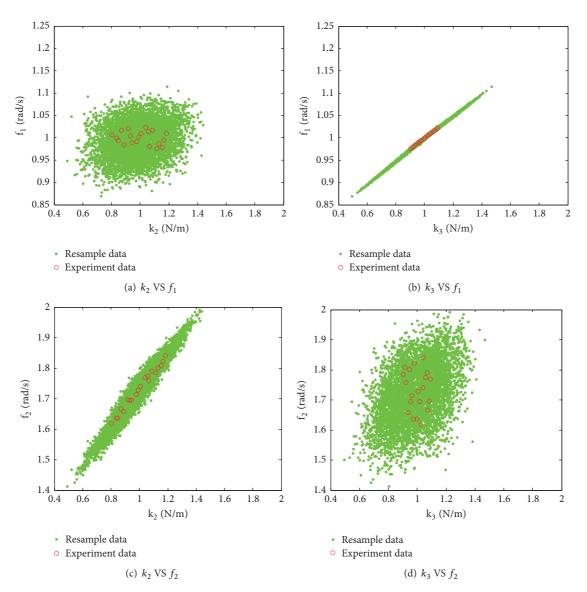


FIGURE 3: Scatter map between the updating parameters and the output quantities of mass-spring system.

is to identify the interval of these three uncertain parameters E, G, and T by the experiment results.

Firstly, the intervals of the first five modal frequencies are estimated by KDE according to the experiment data in Ref. [30]. Secondly, it is assumed that the original intervals of E, G, and T are [195 220] GPa, [78 87] GPa, and [1.30 1.60] mm, respectively, and intervals of E, G, and T are identified according to the copula-based model updating flow with interval uncertainty in Figure 1. There are 20 experimental design data in each iteration step, i.e., 20 determined FE simulations in each iteration step. The model updating of the plate is convergent after four iteration steps with the convergent indices $\varepsilon_1 = 0.002$ and $\varepsilon_2 = 0.002$.

After updating, the estimated intervals of the three parameters were $E = [203.21 \ 205.98]$ GPa, $G = [82.75 \ 85.20]$ GPa, and $T = [1.44 \ 1.46]$ mm, respectively. The comparison between the original uncertain interval and

the updated interval of the three parameters is shown in Figure 7, which shows that the updated intervals of these three parameters are much less than their original uncertain interval.

In order to validate the updating results on the interval uncertain parameters, the copula models are reconstructed on the original and the updated intervals of E, E, and E. The 5000 samples of E, E, and the first five natural frequencies of plates are obtained by MC sampling. The scatter plots for the simulation and the experimental results the first five natural frequencies of plates are shown in Figure 8. The comparisons on the natural frequencies between the simulation and the experimental results are listed in Table 2. It can be seen from Table 2 and Figure 8 that the frequencies of the updated model are in better agreement with the experimental results and the mean errors of frequencies decrease from the initial [12.51 12.62]% to [0.72 0.24]%.

Mode	Experimental interval/Hz	Original interval/Hz	Error /%	Updated interval/Hz	Error /%
1	[23.94 24.4]	[21.06 27.55]	[-12.05 12.92]	[23.71 24.44]	[-0.95 0.15]
2	[66.5 67.53]	[58.61 76.53]	[-11.86 13.32]	[66.84 67.83]	[-0.99 0.44]
3	[76.24 78.91]	[65.81 87.80]	[-13.68 11.26]	[75.93 78.67]	[-0.41 -0.30]
4	[131.31 133.03]	[116.34 151.62]	[-11.40 13.98]	[130.37 134.26]	[-0.71 0.92]
5	[156.31 160.94]	[135.12 179.67]	[-11.59 8.55]	[155.51 160.95]	[-0.51 0.01]
mean			[12.51 12.62]		[0.72, 0.24]

TABLE 2: Comparison on the natural frequencies of plates between the simulation and the experimental results.

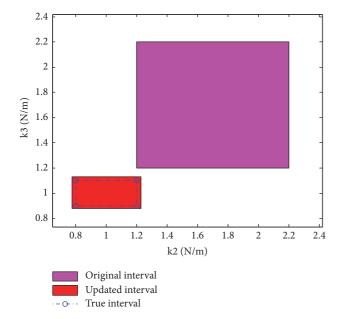
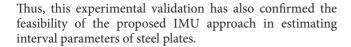


FIGURE 4: Patch plots for the updating parameters of mass-spring system.



3.3. Example 3: Interval Model Updating in Transport Mirror System. The ShenGuangIII (SGIII) facility is designed for inertial confinement fusion (ICF) high energy experiments with 48 laser beams exactly transported and oriented to target. Figure 9 is the view of the beam transport system in SGIII facility target area. There are 276 transport mirror systems in the facility, and the dynamic response under ambient vibration is a key factor to affect the stability of the SGIII facility [31]. A classic transport mirror system is shown in Figure 10, which consists of mirror component and support frame.

The material of the support frame is steel with nominal Young's modulus 200 Gpa, nominal Poisson's ratio 0.3, and the nominal density $7850 \, \text{kg/m}^3$. The material of the mirror is K9 class with nominal Young's modulus 80 Gpa, nominal Poisson's ratio 0.21, and the nominal density $2510 \, \text{kg/m}^3$. The transport mirror system is about 1.32 m in height.

The uncertainty exists in the transport mirror system because of the installation fluctuation and the welding

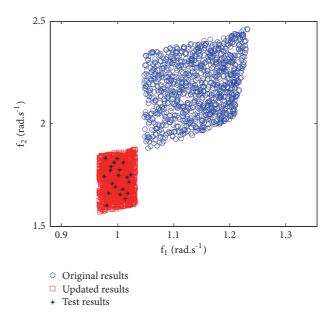


FIGURE 5: Scatter plots for the first two natural frequencies of massspring system.

technology fluctuation about the support frame, which induces the uncertainty of the vibration characteristics. In order to study how these uncertain factors affect the natural frequencies of the transport mirror system, impact hammer modal testing with fixed boundary conditions was conducted on ten nominally identical transport mirror systems. The experiment mount of the transport mirror system is shown in Figure 11. Three natural frequencies in the interesting frequency range were found to significantly influence the response of the transport mirror system under the work condition. Then, the first three natural frequencies of the transport mirror system should be updated before calculating the response. The corresponding natural frequencies were obtained by the modal experiments, as listed in Table 3. It is observed that the frequency variations become more obvious with the increase of the mode order.

Generally, the bolts are ignored in the structural dynamic analysis model generally, and the FE model of the transport mirror system is established by the SOLID185 and SHELL181 element in ANSYS, which is shown in Figure 12. A fully fixed bottom of the support frame is used as the boundary condition. The material properties of the original FE model are the nominal values. The first three simulation mode shapes are shown in Figure 13.

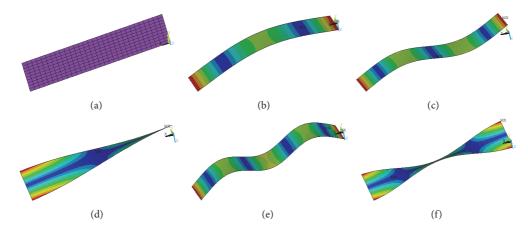


FIGURE 6: The FE model and mode shapes of steel plates: (a) FE model; (b) mode 1; (c) mode 2; (d) mode 3; (e) mode 4; (f) mode 5.

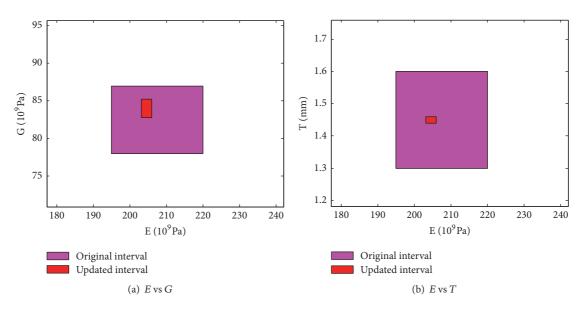


Figure 7: Patch plots for the updating parameters of steel plates.

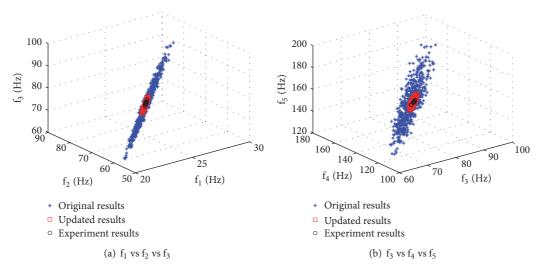


Figure 8: Scatter plots for the first five natural frequencies of steel plates.

								-		
Case	1	2	3	4	5	6	7	8	9	10
f_1/Hz	21.573	21.642	21.675	21.472	21.583	21.683	21.657	21.797	21.644	21.462
f_2/Hz	22.213	22.223	22.31	22.087	22.168	22.293	22.283	22.407	22.232	22.121
f_2/Hz	41.328	41.432	41.58	41.203	41.416	41.56	41.557	41.807	41.497	41.237

Table 3: Experiment results of the first three natural frequencies of the transport mirror system.

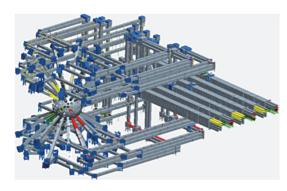


FIGURE 9: A view of the beam transport system in SGIII facility target area, which is reproduced from Chen X J et al. (2014).

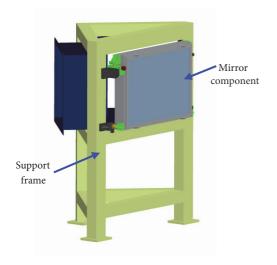


FIGURE 10: Sketch map of the transport mirror system.

Theoretical analysis finds that the installation uncertainty of the transport mirror system can be characterized by Young's modulus E_1 of the bottom part of the support frame, and the weld uncertainty of the support frame can be characterized by Young's modulus E_2 of the upper part of the support frame. The goal of FE model updating is to identify the interval of E_1 and E_2 .

Firstly, the intervals of the first three modal frequencies are estimated by KDE according to the experiment data in Table 3, which are [21.41 21.83] Hz, [22.03 22.45] Hz, and [41.09 41.88] Hz, respectively.

Secondly, assuming that the original intervals of E_1 and E_2 are [100 150] GPa and [160 200] GPa, respectively, the intervals of E_1 and E_2 are identified according to the copula-based



FIGURE 11: Experiment setup of the transport mirror system.

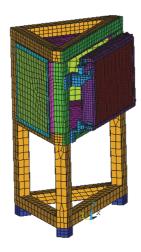


Figure 12: FE model of the transport mirror system.

model updating flow with interval uncertainty in Figure 1. There are 12 experimental design data in each iteration step, i.e., 12 determined FE simulations in each iteration step. The model updating of the transport mirror system is convergent after four iteration steps with the convergent indices $\varepsilon_1 = 0.005$ and $\varepsilon_2 = 0.005$.

After updating, the estimated intervals of the three parameters were $E_1 = [104.46\ 114.65]$ GPa and $E_2 = [104.46\ 114.65]$ GPa, respectively. The comparison between the original uncertain interval and the updated interval of the updating parameters is shown in Figure 14, indicating that the updated intervals of the updating parameters are much less than their original uncertain interval.

m 40 : 1 : 10	. (.1	. 11 . 1	1.1 1
TABLE 4: Comparison on the natural free	duencies of the transport mirror of	system between the simillation an	d the experimental results
TABLE 1. Comparison on the natural ne	queneres of the transport militor s	ystem between the simulation an	d the experimental results.

Mode	Experimental interval/Hz	Original interval/Hz	Error /%	Updated interval/Hz	Error /%
1	[21.46 21.80]	[22.06 24.24]	[2.77 11.20]	[21.38 22.91]	[-0.36 0.52]
2	[22.09 22.41]	[22.68 24.94]	[2.69 11.31]	[22.00 22.54]	[-0.38 0.59]
3	[41.20 41.81]	[42.03 45.98]	[2.01 9.97]	[40.92 41.85]	[-0.68 0.09]
mean			[2.49 10.83]		[0.47 0.40]

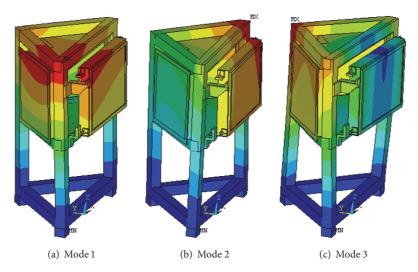


Figure 13: Mode shapes of the transport mirror system.

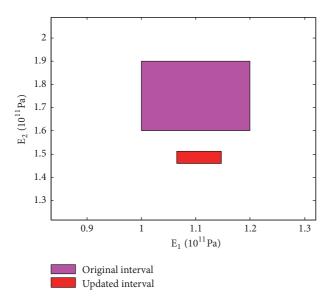
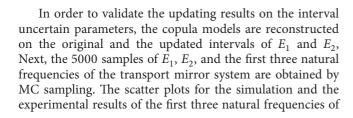


FIGURE 14: Patch plots for the updating parameters of transport mirror system.



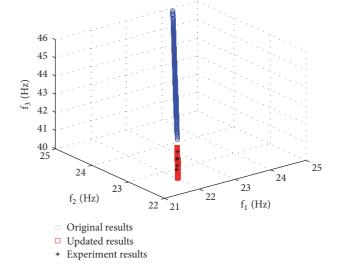


FIGURE 15: Scatter plots for the first three natural frequencies of transport mirror system.

the transport mirror system are shown in Figure 15. The comparisons on the natural frequencies between the simulation and the experimental results are listed in Table 4. It can be seen from Table 4 and Figure 15 that the frequencies of the updated model agree with the experimental results better and the mean errors of frequencies decrease from the initial [2.49 10.83]% to [0.47 0.40]%. As a result, this experimental validation has also proved the feasibility of the proposed

IMU approach in estimating the interval parameters of the transport mirror system.

4. Conclusions

In summary, a copula-based and MC sampling FE model updating approach in the structural dynamics with interval uncertainty is presented. Because the proposed FE model updating approach is based on the copula model of inputoutput parameters and MC sampling, the optimization difficulty caused by the interval algorithm is avoided in the proposed FE model updating approach with interval uncertainty, and the questions of ill-condition, nonuniqueness, and local optimal solution can be avoided also. Unlike other metal-based model updating approaches, the copula-based model updating approach can deal with the nonlinear relativity between the multi-input qualities and the multioutput qualities even if the multioutput qualities are correlated. In order to get a better copula model of input-output parameters for identifying the interval parameters, the LHS approach is suggested in the DOE and the number of samples is not less than ten in the proposed FE model updating approach. Besides, the proposed approach also considers the effect of small samples and estimates the interval of experiment samples by KDE in advance, which makes the updated model more reliable for the predictions on structural dynamic responses. Three examples were used to validate the FE model updating approach proposed in the study. The updating results have proved the feasibility and reliability of this approach.

The total time consumption of the FE model updating is mainly the time of the FE model simulation. For example, the FE model updating of the transport mirror system was completed after four iteration steps, and there were 12 FE model simulations in each iteration step, so only 48 deterministic FE simulations were carried out in the whole model updating with interval uncertainty. But, more than hundreds of FE simulations are needed in a determined model updating without the surrogate model, and the number of FE simulations in the model updating with uncertainty is far more than that of a deterministic model updating. Then, the model updating method proposed with interval uncertainty is efficient in the paper. Besides, after updating the FE model, the difference of the first few natural frequencies between the calculated interval and the experimental interval is less than 1%. In conclusion, the copula-based and MC sampling concept expands the application range of IMU and is useful for fast and accurate estimation of interval parameters in the FE model.

Data Availability

The data for Example 1 are included in the Supplementary Material file associated with this manuscript. The data for Example 2 are reported in [30] but are also included in the Supplementary Information file for completeness. The data for Example 3 are included within the article. Other data are available from the corresponding author upon request.

Conflicts of Interest

The authors declare that they have no conflicts of interest.

Acknowledgments

This work was supported by Science Challenge Project (Grant no. TZ2018007), the National Natural Science Foundation of China (Grant no. 11472256), and the National Key Research and Development Program of China (Grant no. 2016YFB0201005)

Supplementary Materials

Supplementary Table 1. Statistical properties of the measured frequencies of the plates in example 1. Supplementary Table 2. Statistical properties of the measured frequencies of the plates in example 2. (Supplementary Materials)

References

- [1] J. E. Mottershead and M. I. Friswell, "Model updating in structural dynamics: A survey," *Journal of Sound and Vibration*, vol. 167, no. 2, pp. 347–375, 1993.
- [2] C.-P. Fritzen, D. Jennewein, and T. Kiefer, "Damage detection based on model updating methods," *Mechanical Systems and Signal Processing*, vol. 12, no. 1, pp. 163–185, 1998.
- [3] Y. Ren and C. F. Beards, "Identification of effective linear joints using coupling and joint identification techniques," *Journal of Vibration and Acoustics*, vol. 120, no. 2, pp. 331–338, 1998.
- [4] W. L. Li, "A new method for structural model updating and joint stiffness identification," *Mechanical Systems and Signal Processing*, vol. 16, no. 1, pp. 155–167, 2002.
- [5] P. G. Bakir, E. Reynders, and G. De Roeck, "Sensitivity-based finite element model updating using constrained optimization with a trust region algorithm," *Journal of Sound and Vibration*, vol. 305, no. 1-2, pp. 211–225, 2007.
- [6] S.-S. Jin and H.-J. Jung, "Sequential surrogate modeling for efficient finite element model updating," *Computers & Structures*, vol. 168, pp. 30–45, 2016.
- [7] W. L. Oberkampf and C. J. Roy, Verification and Validation in Scientific Computing, Cambridge University Press, Cambridge, UK, 2010.
- [8] E. Simoen, G. De Roeck, and G. Lombaert, "Dealing with uncertainty in model updating for damage assessment: a review," *Mechanical Systems and Signal Processing*, vol. 56-57, pp. 123–149, 2015.
- [9] M. I. Friswell, "The adjustment of structural parameters using a minimum variance estimator," *Mechanical Systems and Signal Processing*, vol. 3, no. 2, pp. 143–155, 1989.
- [10] J. L. Beck and L. S. Katafygiotis, "Updating models and their uncertainties. I: Bayesian statistical framework," *Journal of Engineering Mechanics*, vol. 124, no. 4, pp. 455–461, 1998.
- [11] J. L. Beck and S.-K. Au, "Bayesian updating of structural models and reliability using Markov chain Monte Carlo simulation," *Journal of Engineering Mechanics*, vol. 128, no. 4, pp. 380–391, 2002.
- [12] M. C. Kennedy and A. O'Hagan, "Bayesian calibration of computer models," *Journal of the Royal Statistical Society: Series* B (Statistical Methodology), vol. 63, no. 3, pp. 425–464, 2001.

[13] H. P. Wan and W. X. Ren, "Stochastic model updating utilizing Bayesian approach and Gaussian process model," *Mechanical Systems and Signal Processing*, vol. 70-71, pp. 245–268, 2016.

- [14] H. H. Khodaparast, J. E. Mottershead, and M. I. Friswell, "Perturbation methods for the estimation of parameter variability in stochastic model updating," *Mechanical Systems and Signal Processing*, vol. 22, no. 8, pp. 1751–1773, 2008.
- [15] N. Abu Husain, H. Haddad Khodaparast, and H. Ouyang, "Parameter selection and stochastic model updating using perturbation methods with parameter weighting matrix assignment," *Mechanical Systems and Signal Processing*, vol. 32, pp. 135–152, 2012.
- [16] X. G. Hua, Y. Q. Ni, Z. Q. Chen, and J. M. Ko, "An improved perturbation method for stochastic finite element model updating," International Journal for Numerical Methods in Engineering, vol. 73, no. 13, pp. 1845–1864, 2008.
- [17] S. E. Fang, W. X. Ren, and R. Perera, "A stochastic model updating method for parameter variability quantification based on response surface models and Monte Carlo simulation," *Mechanical Systems and Signal Processing*, vol. 33, pp. 83–96, 2012
- [18] S. S. Rao and L. Berke, "Analysis of uncertain structural systems using interval analysis," *AIAA Journal*, vol. 35, no. 4, pp. 727–735, 1997.
- [19] S. L. Li, H. Li, and J. P. Ou, "Model updating for uncertain structures with interval parameters," in *Proceedings of the Asia-Pacific Workshop on Structural Health Monitoring*, Yokohama, Japan, 2006.
- [20] C. Jiang, X. Han, and G. R. Liu, "Optimization of structures with uncertain constraints based on convex model and satisfaction degree of interval," *Computer Methods Applied Mechanics and Engineering*, vol. 196, no. 49–52, pp. 4791–4800, 2007.
- [21] Z. P. Qiu, X. J. Wang, and M. I. Friswell, "Eigenvalue bounds of structures with uncertain-but-bounded parameters," *Journal of Sound and Vibration*, vol. 282, no. 1-2, pp. 297–312, 2005.
- [22] S. Gabriele and C. Valente, "An interval-based technique for FE model updating," *International Journal of Reliability and Safety*, vol. 3, no. 1–3, pp. 79–103, 2009.
- [23] H. H. Khodaparast, J. E. Mottershead, and K. J. Badcock, "Interval model updating with irreducible uncertainty using the Kriging predictor," *Mechanical Systems and Signal Processing*, vol. 25, no. 4, pp. 1204–1226, 2011.
- [24] S. E. Fang, Q. H. Zhang, and W.-X. Ren, "An interval model updating strategy using interval response surface models," *Mechanical Systems and Signal Processing*, vol. 60, pp. 909–927, 2015.
- [25] M. Sklar, "Fonctions de répartition à n dimensions et leurs marges," *Publications de l'Institut de Statistique de l'Université de Paris*, vol. 8, pp. 229–231, 1959.
- [26] J.-D. Fermanian, "Goodness-of-fit tests for copulas," *Journal of Multivariate Analysis*, vol. 95, no. 1, pp. 119–152, 2005.
- [27] C. Genest and L.-P. Rivest, "Statistical inference procedures for bivariate Archimedean copulas," *Journal of the American Statistical Association*, vol. 88, no. 423, pp. 1034–1043, 1993.
- [28] B. W. Silverman, Density Estimation for Statistics and Data Analysis, Chapman & Hall, London, UK, 1986.
- [29] G. G. Wang, "Adaptive response surface method using inherited Latin hypercube design points," *Journal of Mechanical Design*, vol. 125, no. 2, pp. 210–220, 2003.
- [30] N. A. Husain, H. H. Khodaparast, and J. H. Ouyang, "Parameter selections for stochastic uncertainty in dynamic models

- of simple and complicated structures," in *Proceedings of the* 10th International Conference on Recent Advances in Structural Dynamics, University of Southampton, 2010.
- [31] X. J. Chen, M. C. Wang, W. K. Wu, and X. H. Que, "Structural design of beam transport system in SGIII facility target area," *Fusion Engineering and Design*, vol. 89, no. 12, pp. 3095–3100, 2014

Hindawi Shock and Vibration Volume 2018, Article ID 3013684, 10 pages https://doi.org/10.1155/2018/3013684

Research Article

Remaining Useful Life Prediction Method of Rolling Bearings Based on Pchip-EEMD-GM(1, 1) Model

Fengtao Wang (b), Xiaofei Liu (b), Chenxi Liu (b), Hongkun Li (b), and Qingkai Han (b)

School of Mechanical Engineering, Dalian University of Technology, Dalian, China

Correspondence should be addressed to Fengtao Wang; wangft@dlut.edu.cn

Received 18 January 2018; Revised 16 May 2018; Accepted 21 June 2018; Published 8 July 2018

Academic Editor: Mohammad A. Hariri-Ardebili

Copyright © 2018 Fengtao Wang et al. This is an open access article distributed under the Creative Commons Attribution License, which permits unrestricted use, distribution, and reproduction in any medium, provided the original work is properly cited.

A trend prediction method based on the Pchip-EEMD-GM(1,1) to predict the remaining useful life (RUL) of rolling bearings was proposed in this paper. Firstly, the dimension of the extracted features was reduced by the KPCA dimensionality reduction method, and the WPHM model parameters were estimated via the kernel principal components. Secondly, the hazard rate was calculated at each time, and the Pchip interpolation method was used to obtain the uniformly spaced interpolation data series. Then the main trend of signal was obtained through the EEMD method to fit the GM(1,1) prediction model. Finally, the GM (1,1) method was used to predict the remaining life of the rolling bearing. The full life test of rolling bearing was provided to demonstrate that the method predicting the hazard data directly has the higher accuracy compared with predicting the covariates, and the results verified the feasibility and effectiveness of the proposed method for predicting the remaining life.

1. Introduction

Rolling bearings are critical components that determine the remaining lifetime of machinery [1]. The bearings are important parts in rotating machinery, and bearing failure may lead to catastrophic accidents [2]. Previous analysis has shown that faults caused by vibration accounted for 70% of all mechanical faults. Furthermore, faulty rolling bearings accounted for 30% of the faults caused by vibration [3]. The CBM uses modern sensing technology to provide the maintenance decisions before the equipment becomes faulty by real-time updated degradation information of the equipment [4]. The CBM is more effective when determining equipment maintenance based on the vibration data, rather than the traditional maintenance strategies. The CBM initially establishes exact correspondence between the condition parameters of equipment and reliability in order to provide accurate maintenance decisions [5]. Effective maintenance strategies reduce the maintenance downtime and cost, while simultaneously ensuring the normal operation of the equipment [6, 7]. Improving the prediction accuracy of the residual life plays an important role in making correct maintenance decisions that are based on the running status of the equipment.

The life prediction theory based on condition monitoring is an important research as continuous improvements are made in the measuring and the testing techniques. The proportional hazards model (PHM) [8] is a statistic analysis model of the lifetime data. It is applicable in models with no special requirements for data distribution or residual distribution. The PHM analyzes censored data, which establishes the failure model based on equipment condition monitoring and historical life data. This method is commonly used for predicting equipment life. Ding F. et al. [9] set the root mean square (RMS) and the kurtosis as the covariant and then used the Weibull proportional hazards model (WPHM) to assess the reliability of the rolling bearings on railway wheels. Zimroz R et al.[10] used the load-dependent feature processing to diagnose the wind turbine bearings in strong operating and nonstationarity conditions. Liao H. T. et al. [11] set the RMS and the kurtosis as a covariant, where the logistic regression model and the PHM were used to predict the remaining useful life of single equipment. Zhang Q. et al. [12] used the mixed WPHM to predict the remaining life of a mechanical system that contained multiple failure modes. Chi K. R. L. et al. [13] used the state-space Switching Kalman Filter (SKF) method for predicting the remaining life and providing

maintenance decisions based on the degradation model. In real life applications, the trend prediction is a key component of the remaining life prediction. By improving the accuracy of trend prediction, the accuracy of the remaining life is confirmed.

The trend prediction uses historical time-series vibration data and conjecture data variations from future data to establish the prediction model. Current trend prediction methods include the curve-fitting methods, the time-series methods, the neural network methods, the support vector machine methods, and the grey model methods. The computational process of the curve-fitting methods is simple; however, the prediction accuracy is low. The standard time-series prediction methods are based on the autoregressive model and the autoregressive moving average model. The prediction accuracy is low, and the methods are only suitable for short-term prediction. The neural network methods and the support vector machine methods require trained data, which cannot be used in the trend prediction of small datasets. The grey system theory [14] demonstrated the evolution law of things based on the analysis of lacking systematic characteristics, operating mechanism, and behaviors. Liu S. D. et al. [15] normalized the weighted time domain parameters and used the grey model to predict the life trend, which resulted in a high prediction accuracy. Yang J. T. et al. [16] used a multivariable grey prediction model to predict the development of mechanical failure, which overcame the disadvantages of the traditional fault prediction methods by considering each characteristic parameter separately. Liu E. L. et al. [17] used the vibration signals of rolling bearings to adopt the GM(1, 1) model, which predicted the life trend based on two typical characteristic indicators (RMS and kurtosis). Tabaszewski M. [18, 19] used the moving method applied to GM(1,1) model for estimating the model parameters to develop the method based on the weighted mean forecast. The life trend reflects the performance degradation process and became the foundation for subsequent RUL prediction. The grey model methods require less data and the prediction accuracy is high. This paper proposed a modified grey model knew as the Pchip-EEMD-GM(1, 1) model to predict the trend based on WPHM.

2. The Fundamental Theory

2.1. WPHM. The WPHM established the mathematical relationship between the running status of the equipment and the reliability. The current hazard rate was obtained based on the real-time running status. The hazard function of the WPHM is defined as follows:

$$h(t, \mathbf{z}_t) = \frac{\beta}{\eta} \left(\frac{t}{\eta}\right)^{\beta - 1} \exp\left(\gamma \cdot \mathbf{z}_t\right) \tag{1}$$

where $\beta > 0$ is the parameter shape of the Weibull distribution and $\eta > 0$ is the scale parameter of the Weibull distribution. $\mathbf{z}_t = [z_1, z_2, \dots, z_n]^{\mathrm{T}}$ is a column vector that is composed of a covariant, which have time-varying characteristics. The degree to which the selected covariant could accurately reflect the performance degradation process is imperative to the accuracy of the model. $\gamma = [\gamma_1, \gamma_2, \dots, \gamma_n]$ is a row vector

composed of the regression parameters of the corresponding covariant.

The reliability and the failure probability density are estimated with

$$R(t, \mathbf{z}_t) = \exp\left[-\int_0^t h(t, \mathbf{z}_t) dt\right]$$
 (2)

The rotating rolling bearing is considered to be in failure when the reliability $R(T, \mathbf{z}_T)$ of time T is lower than the preset threshold. The failure time is defined as follows:

$$T(R_0) = \inf \{T : R(T, \mathbf{z}_T) \le R_0, T > 0\}$$
 (3)

where R_0 is the failure threshold or the characteristic life when it is equal to e^{-1} [20].

The error of the RUL prediction is defined as

$$E = \left| \frac{T_p - T_a}{T_a} \right| \times 100\% \tag{4}$$

where T_p is the predicted RUL and T_a is the actual RUL.

2.2. GM(1, 1) Model. The grey system theory revealed a variation law of research objects with less data and insufficient information based on the analysis of systematic characteristics. The theory uses small samples and insufficient information to establish the prediction model [21]. The GM(1, 1) model is the most widely used prediction model of the grey system theory, where the specific modeling process is described as follows.

 $X^{(0)} = [x^{(0)}(1), x^{(0)}(2), ..., x^{(0)}(n)]$ is set as the original nonnegative data series. $X^{(1)} = [x^{(1)}(1), x^{(1)}(2), ..., x^{(1)}(n)]$ is described as the generation data series. The relationship between $X^{(1)}$ and $X^{(0)}$ can be described as (5), which is referred to as the accumulated generating operation:

$$x^{(1)}(k) = \sum_{i=1}^{k} x^{(0)}(i); \quad k = 1, 2, ..., n$$
 (5)

The accumulated generating operation effectively eliminates the volatility and the randomness of the original data series, aiming at building an ascending series. The new-generation data series $X^{(1)}$ is roughly the exponential growth. Then, the differential coefficient equation can be established as

$$\frac{dx^{(1)}}{dt} + \alpha x^{(1)} = u \tag{6}$$

which is referred to as the winterization equation of GM(1, 1) model. a and u are unknown parameters, denoted as $\Phi = [a\ u]^T$. The parameter of vector Φ can be solved through the least square method. The discrete solutions of $\overset{\wedge}{\alpha}$ and \hat{u} can be described in

$$\hat{x}^{(1)}(k+1) = \left(x^{(1)}(1) - \frac{\hat{u}}{\overset{\wedge}{\alpha}}\right)e^{-\overset{\wedge}{\alpha}k} + \frac{\hat{u}}{\overset{\wedge}{\alpha}}$$
(7)

Finally, the grey prediction series $x^{(0)}$ of the original data can be described as

$$\hat{x}^{(0)}(k+1) = \hat{x}^{(1)}(k+1) - \hat{x}^{(1)}(k) \tag{8}$$

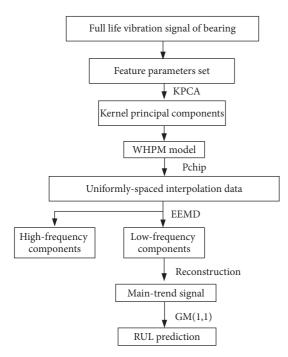


FIGURE 1: The flowchart of the proposed method.

3. Method and Steps

This paper extracted the kernel principal elements to establish the WPHM model and used Pchip-EEMD method to preprocess the obtained hazard rate data directly and fit the requirements of the GM(1,1) prediction model. Figure 1 showed the flow chart of this method.

The specific steps are as follows.

- (1) Extraction of the kernel principal components: the feature parameters were extracted from the full life vibration data, and the KPCA method was used to reduce the dimension of the feature set and obtain the kernel principal elements.
- (2) Establishing the WPHM: the WHPM parameters were estimated based on the obtained kernel principal components and the hazard rate was calculated at the corresponding time.
- (3) Data preprocessing: the Pchip interpolation method was used to get the uniformly spaced interpolation data series, and the main trend was reconstructed by removing the high-frequency signal through the EEMD decomposition method to fit the GM(1,1) model.
- (4) RUL prediction: the GM (1,1) model was used to predict the trend of hazard rate data, and the reliability was calculated to predict the remaining life of the bearing.

4. Experiment Verification

4.1. The Features Extraction. The rolling bearing life cycle datasets for this experiment were provided by the Center for Intelligent Maintenance Systems (IMS), University of Cincinnati [22]. The experimental datasets were generated from bearing run-to-failure tests under load conditions on a specially designed test rig as shown in Figure 2.

TABLE 1: Parameters of WPHM.

Parameters	β	η	γ_1	γ_2	γ_3
Estimates	1.074	36.04	0.4626	0.1142	0.06485

There were four test double row bearings (Rexnord ZA-2115) on a single shaft within the bearing test rig. The shaft was driven by an AC motor and coupled with rub belts. A 6,000 lb radial load was added to the shaft and the bearings via a spring mechanism. The rotation speed was kept constant at 2,000 rpm throughout the experiment. A magnetic plug was installed in the oil feedback pipe in order to collect the oil debris as evidence of bearing degradation. The test was stopped when the accumulated debris that had adhered to the magnetic plug exceeded a certain level, which caused an electrical switch to close. The vibration data was collected every 20 minutes with a National Instruments DAQCard-6062E data acquisition card (data sampling rate 20 kHz and data length 20,480 points). The data collection was conducted in the National Instruments LabVIEW program.

Figure 3 displays the vibration signal of a tested bearing during its entire lifecycle. The results show that the amplitudes of vibration signals are steady during the early stage, but the amplitude has significantly increased compared to the normal standard amplitude in the end of the bearing life, which indicates that the vibration signals contain the bearing performance degradation. Figure 4 shows the pictures of bearing components after a test; the bearing failure in different forms. From the vibration signal, 11 features that could reflect the degradation process are selected to form a feature set [23]. The features were as follows:

- (1) Time domain: RMS, kurtosis, peak to peak value, and peak factor.
- (2) Frequency domain: spectral mean, the root mean square value of the spectrum, and spectral variance.
- (3) Time-frequency domain: the third band normalized wavelet packet energy spectrum of 3-level wavelet packet decomposition (E3), the seventh band normalized wavelet packet energy spectrum (E7), the entropy of the third band of the 3-level wavelet packet decomposition (S3), and the seventh band samples entropy value (S7).

Figure 5 shows the degradation trend in full life cycle of the selected features over time, which are suitable for RUL prediction of the rolling bearing.

4.2. The GM(1,1) Model Application. The KPCA was used to reduce the dimension of the bearing feature set and to select the first three-dimensional kernel principal components, whose cumulative contribution rate was greater than 85%. The WPHM parameters were estimated and shown in Table 1 [23].

The hazard rate was calculated by using the variation data series of the KPC1, the KPC2, and the KPC3. The different degradation stages [23] were used to select the data from four time periods in order to predict the trend with the GM(1,1) model. The characteristics of the data were shown by amplifying and marking each time period in Figure 6.

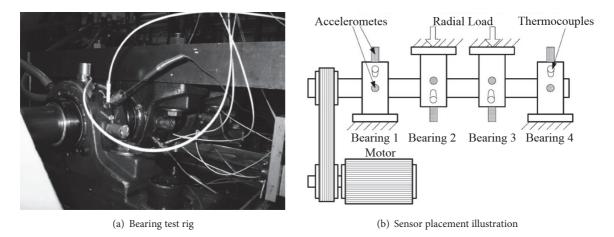


Figure 2: Bearing test rig and sensor placement illustration.

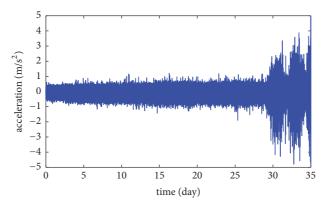


FIGURE 3: Bearing 3 run-to-failure vibration signals.

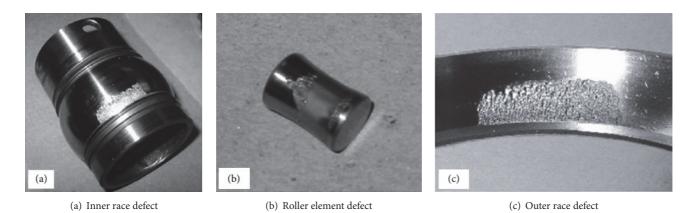


FIGURE 4: Components of failure bearing.

Figure 6 shows that the data was collected with the unequal interval sampling method. The GM(1, 1) model required the use of the equal interval data series when predicting the trend. Thus, equally spaced interpolation was required. The MATLAB toolkit provided a variety of interpolation methods, including the Pchip interpolation and the Spline interpolation. These methods were compared by

using the data from day 30.2 to day 31.0 (period (a)), as well as the data from day 32.1 to day 33.1 (period (c)). Figures 7 and 8 showed the results of the two interpolation methods. The performance is nearly the same in period (a) of Figure 7, because the data was approximately the same interval with no large gaps, but the intervals between data points were large and uneven in period (c) of Figure 8; the

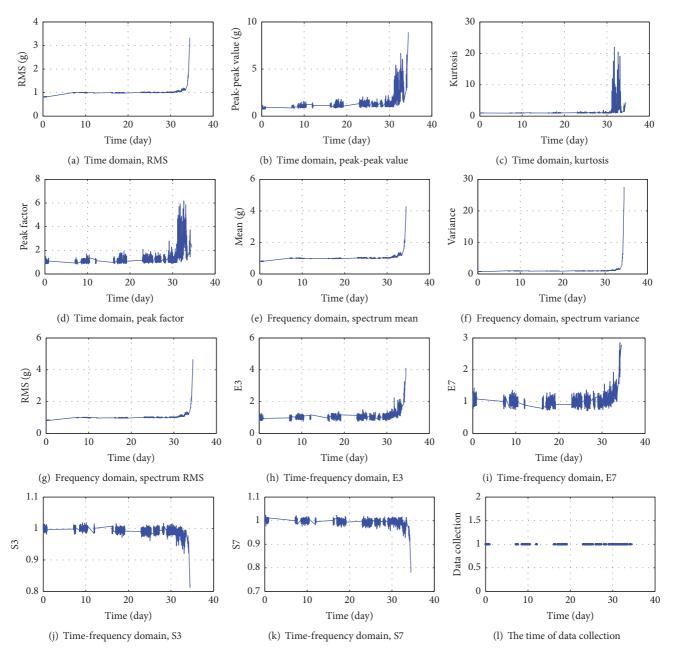


Figure 5: The 11 features extracted from the bearing full life data.

transient overshoot in the interpolated line between the two points throughout the Spline interpolation method was more obvious than in the Pchip interpolation method. So, the Pchip interpolation method performed better in terms of shape preserving especially dealing with the data that has large spacing and are uneven.

The data series adopted interpolation processing, although the oscillation still existed within the data points. The oscillation had a passive influence on trend prediction according to the GM(1, 1) model. The influence of the transient overshoot component among data points need to be reduced in order to achieve a smoother trend component of the data. This was accomplished by dividing the data series

into a dozen signals using the ensemble empirical mode decomposition (EEMD). The first several signals that contained the high-frequency oscillation component were omitted in order to reconstruct the main trend of data series based on the remaining component signals.

Figures 9 and 10 show the interpolation curve and the main trend curve of periods (a) and (c), and Figures 11 and 12 show the comparison results of the trend prediction curve of periods (a) and (c). As seen in Figures 11 and 12, the proposed Pchip-EEMD-GM(1, 1) model (the hazard rate prediction method) was used to predict the trend that would effectively eliminate high-frequency oscillation throughout the data series. This substantially decreased the influence of discrete

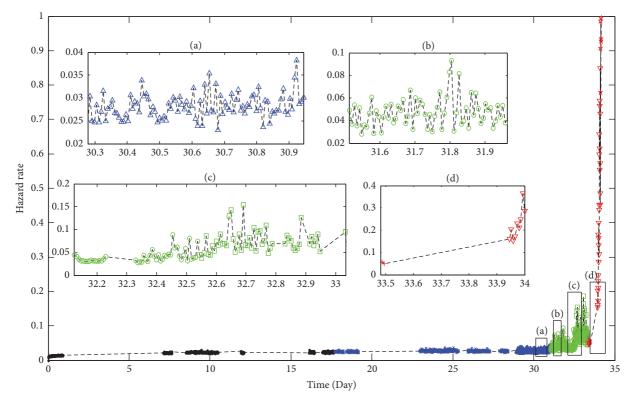


FIGURE 6: The four time periods.

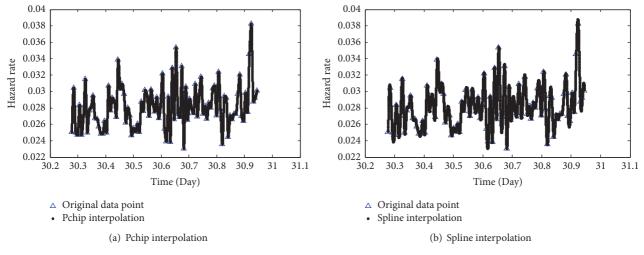


FIGURE 7: The comparison of interpolation results of period (a).

points selection and obtained a more stable and more reliable trend prediction result.

4.3. RUL Prediction. Previous research verified that the kernel principal components could reflect the degradation process of the rolling bearings as the covariants, and it included more bearing life cycle data than RMS values or kurtosis [23]. Both the covariate and the hazard rate trends can be predicted using the proposed method. However, the hazard rate prediction method can optimize the prediction

steps and reduce the amount of model calculation. To verify the effectiveness of the proposed method, the first three KPCs and the hazard rate were used to predict the main trend, respectively, and then predict the remaining life. The results were compared to the actual URL to verify the accuracy of the two methods. Figure 13 showed the variation of the kernel components and the hazard rate over the entire life of the bearing; the three KPCs curves were unstable and oscillated more while the hazard rate obtained from the KPCs was relatively stable with less turbulence. The reconstructed data

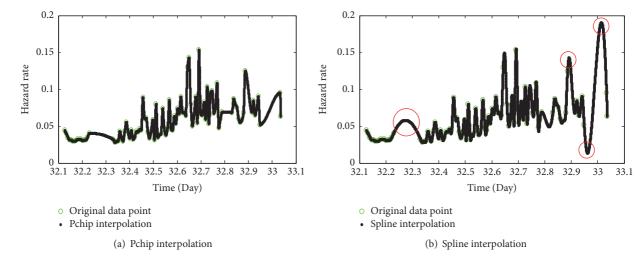
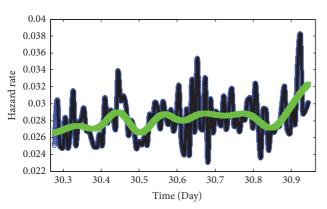
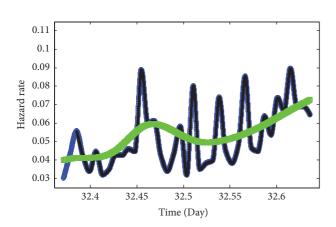


FIGURE 8: The comparison of interpolation results of period (c).



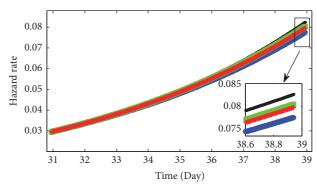
- o Interpolation curve (30.27d-30.94d)
- Interpolation curve (30.28d-30.94d)
- □ Reconstructed signal curve

FIGURE 9: The interpolation curve and the main trend of period (a).



- o Interpolation curve (32.37d-32.63d)
- Interpolation curve (32.38d-32.63d)
- □ Reconstructed signal curve

FIGURE 10: The interpolation curve and the main trend of period (c).



- o Trend prediction curve based on data from 30.27d-30.94d
- Trend prediction curve based on data from 30.28d-30.94d
- □ Trend prediction curve based on reconstructed signal data from 30.27d-30.94d
- Trend prediction curve based on reconstructed signal data from 30.28d-30.94d

FIGURE 11: The comparison results of trend prediction curve of period (a).

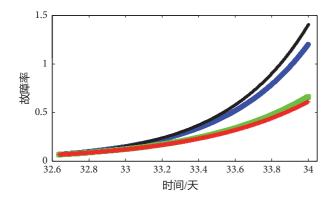
series from the four periods ((a), (b), (c), and (d)) were used to predict the future trend periods through the covariant prediction method and the hazard rate prediction method.

Figures 14–17 show the trend prediction results of the covariates and the hazard rate method throughout different degradation stages of the rolling bearings. The predicted values were closer to the actual values as time progressed. The RUL accuracy of the prediction methods was verified through the threshold of reliability, which is typically set by statistical experience. The reliability value of the tested rolling bearing at the severe wear stage was around e^{-1} [23]; we set the reliability value of e^{-1} as the moment of complete failure of the bearing; the bearing operating time was taken as the bearing life. The prediction results of RUL are presented in Table 2.

The prediction errors of the two RUL prediction methods were calculated using (4). The results were shown in

TABLE 2: KUL	prediction.

Day	Normal working stage	Early failure stage	Healing stage	Medium wear stage
Actual RUL	3.2091	2.1883	1.1181	0.1667
Hazard prediction method	6.6262	2.7499	1.2736	0.1831
Covariatesprediction method	8.1662	1.5184	0.8871	0.1259



- o Trend prediction curve based on data from 32.27d-32.63d
- Trend prediction curve based on data from 32.28d-32.63d
- ☐ Trend prediction curve based on reconstructed signal data from 32.27d-32.63d
- Trend prediction curve based on reconstructed signal data from 32.28d-32.63d

FIGURE 12: The comparison results of trend prediction curve of period (c).

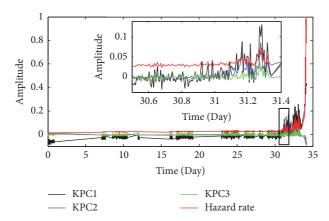
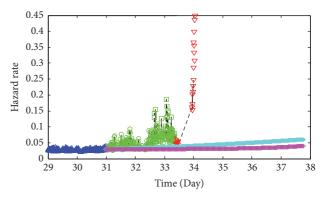


FIGURE 13: The KPCs and the hazard rate throughout the entire life of the bearing.

Figure 18. The prediction error continued to decrease as the rolling bearings degenerated. As seen in Table 2, the proposed method achieved a better performance than the covariates prediction method throughout the four stages with smaller error. And the predicted RUL was quite different from the actual RUL of the tested rolling bearing during the normal working stage. This may cause by accident the damage of the rolling bearings; the trend of the hazard varied nonlinearly, which led to larger errors at the normal working stage. The accumulation of the new degradation characteristics at the early failure stage led to the predicted RUL becoming closer



- △ Actual hazard rate of 28.99d-31.05d
- o Actual hazard rate of 31.05d-32.53d
- ☐ Actual hazard rate of 32.53d-33.34d
- + Actual hazard rate of 33.34d-33.49d
- ▼ Actual hazard rate of 33.49d-34.04d
- Predicted hazard rate of hazard rate prediction method from 30.94d
- Predicted hazard rate of covariant prediction method from 30.94d

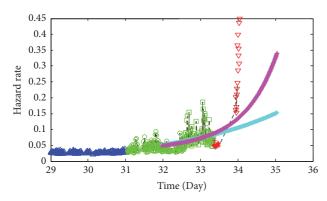
Figure 14: The trend prediction result of period (a).

to the actual RUL. The accuracy degree reached 90.16% (1-error rate 9.84% = 90.16%) at the medium wear stage. The result showed that the hazard rate prediction method of the Pchip-EEMD-GM(1, 1) model accurately predicted the rolling bearing's RUL with less computational amount than the covariates prediction method, as well as providing timely and effective maintenance decisions.

5. Conclusion

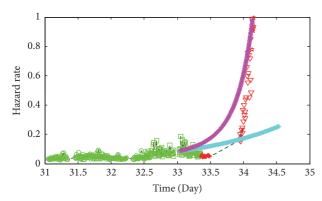
In this study, the Pchip-EEMD-GM(1, 1) model successfully and accurately predicted the variation trend and the RUL of the rolling bearings based on the vibration data. Pchip-EEMD was used to extract the main trend of data change. It overcame the shortcomings of the traditional trend predicting methods with large fluctuations and low prediction accuracies. The proposed method improved the prediction accuracy more effectively. The advantages of the proposed method were listed as follows.

- (1) The original data adopts interpolation processing by the Pchip interpolation method. This method has a good form of conformality and prevention of overshoot, maintains the trend characteristics of the original signal, and helps to improve the reliability of RUL prediction results.
- (2) The EEMD method is used to extract the main trend of the data; it reduces data fluctuations to fit the the GM



- △ Actual hazard rate of 28.99d-31.05d
- o Actual hazard rate of 31.05d-32.53d
- □ Actual hazard rate of 32.53d-33.34d
- + Actual hazard rate of 33.34d-33.49d
- ▼ Actual hazard rate of 33.49d-34.04d
- Predicted hazard rate of hazard rate prediction method from 31.96d
- Predicted hazard rate of covariant prediction method from 31.96d

FIGURE 15: The trend prediction result of period (b).



- o Actual hazard rate of 31.05d-32.53d
- ☐ Actual hazard rate of 32.53d-33.43d
- + Actual hazard rate of 33.34d-33.49d
- ▼ Actual hazard rate of 33.49d-34.11d
- ★ Actual hazard rate of 34.11d-34.17d
- Predicted hazard rate of hazard rate prediction method from 33.03d
- Predicted hazard rate of covariant prediction method from 33.03d

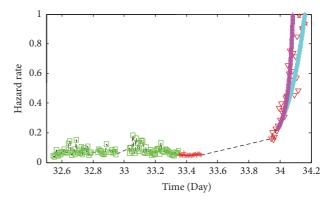
Figure 16: The trend prediction result of period (c).

(1,1) prediction model, which helps to improve the model prediction accuracy.

(3) The WPHM was used to calculate the hazard rate in the bearing life cycle, and the hazard rate was predicted directly, which reduced the error of prediction and the amount of calculation, optimized the prediction steps, and improved the prediction accuracy.

Data Availability

The data used to support the findings of this study are available from the corresponding author upon request.



- ☐ Actual hazard rate of 32.53d-33.43d
- + Actual hazard rate of 33.34d-33.49d
- ▼ Actual hazard rate of 33.49d-34.11d
- ★ Actual hazard rate of 34.11d-34.17d
- Predicted hazard rate of hazard rate prediction method from 33.98d
- + Predicted hazard rate of covariant prediction method from 33.98d

FIGURE 17: The trend prediction result of period (d).

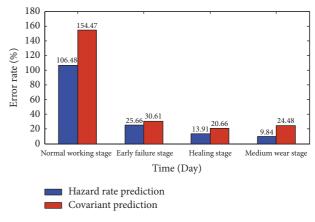


FIGURE 18: The prediction error of RUL.

Conflicts of Interest

The authors declare that they have no conflicts of interest.

Acknowledgments

This work was supported by the National Natural Science Foundation of China (no. 51375067).

References

- [1] L. Cui, J. Huang, and F. Zhang, "Quantitative and localization diagnosis of a defective ball bearing based on vertical-horizontal synchronization signal analysis," *IEEE Transactions on Industrial Electronics*, vol. 64, no. 11, pp. 8695–8706, 2017.
- [2] L. Cui, N. Wu, C. Ma, and H. Wang, "Quantitative fault analysis of roller bearings based on a novel matching pursuit method with a new step-impulse dictionary," *Mechanical Systems and Signal Processing*, vol. 68-69, pp. 34–43, 2016.

[3] Z. J. He and Z. Y. Huang, Selection of Mechanical Fault Diagnosis, Xi'an Jiaotong University Press, Xian, China, 1991.

- [4] H. P. Zhuo, J. Cai, and H. W. Wang, The Theory and Methods of Maintenance Strategies, Aviation Industry Press, Beijing, China, 2008.
- [5] H. F. Zuo, H. J. Li, and X. Rong, "Condition based aero-engine maintenance decisionmethod using proportional hazards model," *Journal of Aerospace Power*, vol. 21, pp. 716–721, 2006.
- [6] W. Guo and P. W. Tse, "A novel signal compression method based on optimal ensemble empirical mode decomposition for bearing vibration signals," *Journal of Sound and Vibration*, vol. 332, no. 2, pp. 423–441, 2013.
- [7] F. Cong, J. Chen, G. Dong, and M. Pecht, "Vibration model of rolling element bearings in a rotor-bearing system for fault diagnosis," *Journal of Sound and Vibration*, vol. 332, no. 8, pp. 2081–2097, 2013.
- [8] D. R. Cox, "Regression models and life-tables," *Journal of the Royal Statistical Society*, vol. 34, pp. 187–220, 1972.
- [9] F. Ding, "Reliability Assessment Based on Equipment Condition Vibration Feature Using Proportional Hazards Model," *Journal of Mechanical Engineering*, vol. 45, no. 12, p. 89, 2009.
- [10] R. Zimroz, W. Bartelmus, T. Barszcz, and J. Urbanek, "Diagnostics of bearings in presence of strong operating conditions non-stationarity A procedure of load-dependent features processing with application to wind turbine bearings," *Mechanical Systems and Signal Processing*, vol. 46, no. 1, pp. 16–27, 2014.
- [11] H. Liao, W. Zhao, and H. Guo, "Predicting remaining useful life of an individual unit using proportional hazards model and logistic regression model," in *Proceedings of the Annual Reli*ability and Maintainability Symposium, pp. 127–132, Newport Beach, Calif, USA, January 2006.
- [12] Q. Zhang, C. Hua, and G. H. Xu, "A mixture Weibull proportional hazard model for mechanical system failure prediction utilizing lifetime and monitoring," *Mechanical Systems Signal Processing*, vol. 43, pp. 103–112, 2014.
- [13] C. K. R. Lim and D. Mba, "Switching Kalman filter for failure prognostic," *Mechanical Systems and Signal Processing*, vol. 52-53, no. 1, pp. 426–435, 2015.
- [14] J. L. Deng, "A review of grey system," World Science, vol. 7, pp. 1–5, 1983.
- [15] S. D. Liu, L. B. Zhang, and Z. H. Wang, "Forecasting diagnosis of rolling bearing by GM model," *Lubrication Engineering*, vol. 2, pp. 38-39, 2002.
- [16] J. T Yang and W. L. Ye, "Application of grey model to machinery faults prediction," *Journal of Mechanical Strength*, vol. 23, pp. 277–279, 2001.
- [17] E. L. Liu, Research on rolling bearing life prediction method based on WPHM model [Ph.D. thesis], Dalian University of Technology, Dalian, China, 2014.
- [18] M. Tabaszewski, "Prediction of diagnostic symptom values using a set of models GM(1,1) and a moving window method," *Diagnostyka*, vol. 15, no. 3, pp. 65–68, 2014.
- [19] M. Tabaszewski and C. Cempel, "Using a set of GM(1,1) models to predict values of diagnostic symptoms," *Mechanical Systems and Signal Processing*, vol. 52-53, no. 1, pp. 416–425, 2015.
- [20] Z. H. Zhang, Theory and Engineering Applications of Reliability, Science Press, Beijing, China, 2012.
- [21] Y. Li, Research and application of the grey forecast model [Ph.D. thesis], Zhejiang Sci-Tech University, Zhejiang, China, 2012.

- [22] H. Qiu, J. Lee, J. Lin, and G. Yu, "Wavelet flter-based weak signature detection method and its application on rolling element-bearing prognostics," *Journal of Sound Vibration*, vol. 289, pp. 1066–1090, 2006.
- [23] F. Wang, X. Chen, B. Dun, B. Wang, D. Yan, and H. Zhu, "Rolling bearing reliability assessment via kernel principal component analysis and weibull proportional hazard model," *Shock and Vibration*, vol. 2017, Article ID 6184190, 11 pages, 2017.

Hindawi Shock and Vibration Volume 2018, Article ID 1784203, 14 pages https://doi.org/10.1155/2018/1784203

Review Article

Response Surface Method for Material Uncertainty Quantification of Infrastructures

Mohammad Amin Hariri-Ardebili , 1,2 S. Mahdi Seyed-Kolbadi, and Mohammad Noori , 3,4

Correspondence should be addressed to Mohammad Amin Hariri-Ardebili; mohammad.haririardebili@colorado.edu

Received 15 March 2018; Accepted 16 May 2018; Published 5 July 2018

Academic Editor: Roberto Palma

Copyright © 2018 Mohammad Amin Hariri-Ardebili et al. This is an open access article distributed under the Creative Commons Attribution License, which permits unrestricted use, distribution, and reproduction in any medium, provided the original work is properly cited.

Recently, probabilistic simulations became an inseparable part of risk analysis. Managers and stakeholders prefer to make their decision knowing the existing uncertainties in the system. Nonlinear dynamic analysis and design of infrastructures are affected by two main uncertainty sources, i.e., epistemic and aleatory. In the present paper, the epistemic uncertainty is addressed in the context of material randomness. An old ultra-high arch dam is selected as a vehicle for numerical analyses. Four material properties are selected as random variables in the coupled dam-reservoir-foundation system, i.e., concrete elasticity, mass density, compressive (and tensile) strength, and the rock modulus of elasticity. The efficient Box-Behnken experimental design is adopted to minimize the required simulations. A response surface metamodel is developed for the system based on different outputs, i.e., displacement and damage index. The polynomial-based response surface model is subsequently validated with a large number of simulations based on Latin Hypercube sampling. Results confirm the high accuracy of proposed technique in material uncertainty quantification.

1. Introduction

With the recent advances in computational tools, the probabilistic numerical simulations became an important aspect in risk analysis and risk management. Nowadays, decision-making is based on the uncertainties in the system and not a deterministic simulation. Nonlinear dynamic response of concrete dams can be affected by two main uncertainty sources: epistemic and aleatory [1].

The aleatoric uncertainty stems from intrinsic randomness of a phenomenon. Uncertainty in the seismic hazard (e.g., intensity, time, and return period) is the most dominant one. On the other hand, the epistemic uncertainty is due to lack of knowledge. Uncertainty in material characteristics (e.g., modulus of elasticity and strength) is the main source in this category. Both these uncertainties can be incorporated in

the numerical simulations, which results in the uncertainty propagation though the model, Figure 1. Ground motion record-to-record variability is usually presented as a fragility function. A comprehensive state-of-the-art review on the fragility analysis of concrete dam can be found in [2]. Material uncertainties were also studied in few cases [3–5].

Having all the tools for the probabilistic simulations, still it is computationally expensive to perform a large set of non-linear dynamic analyses on 3D model of dam-foundation-reservoir coupled system. Thus, it is important to look for methods which efficiently reduce the sample size. In the case of fragility curves, such a method is proposed by Azarbakht and Dolšek [7] which reduces the total number of required ground motions for an incremental dynamic analysis (IDA). In the case of material and modeling uncertainty, response surface method (RSM) is found to be a good solution [8]. The

¹Department of Civil Environmental and Architectural Engineering, University of Colorado, Boulder, USA

²X-Elastica, LLC, Boulder, USA

³College of Engineering, California Polytechnic State University, California, USA

⁴International Institute for Urban Systems Engineering, Southeast University, Nanjing, China

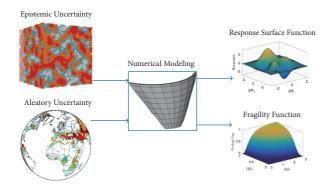


FIGURE 1: General framework for uncertainty quantification.

computational cost in RSM is significantly reduced compared to the crude Monte Carlo Simulation (MCS). Moreover, the explicit nature of response surface makes is useful for future assessments.

The primary goal of this paper is to develop a response surface to calculate the probabilistic nonlinear seismic response of the arch dams, Figure 1. Although the RSM is a well-established method, it has been applied to limited number of geostructures such as rock-fills [9], concrete-faced rock-fill dams [10], slope stability reliability analysis [11–13], and concrete gravity dams [14, 15].

The main objective of this paper is to focus on the epistemic random variables (RVs). First, the concept of experimental design is studied in Section 2, followed by response surface method, Section 3. Fundamentals of smeared crack in the mass concrete are reviewed in Section 4. Next, the case study and its finite element model are discussed in Section 5. Finally, the results of metamodeling are provided in Section 6 and validated.

2. Design of Experiment

A Design of Experiment (DOE) refers to a statistical procedure that systematically defines the efficient number of sampling data points to optimize the computed responses [16]. A DOE includes a "Factor" and "Level". Factor is a parameter over which the designer or analyzer has direct control on an experiment. Moreover, level is the number of different values a factor can be assigned based on its discretization. In this section some DOE techniques are briefly presented.

Randomized Complete Block Design (RCBD) is a procedure based on blocking and is used when the analyzer wants to focus on one or more particular factors. The number of required experiments for a RCBD is $N_{DOE} = \prod_{i=1}^k L_i$, where k refers to factors and L represents levels.

Latin Square Experimental Design (LSED) is similar to RCBD while it requires less samples. It performs single experiment in each block and requires some conditions that are needed to implement this technique. The sample size is $N_{DOE} = L^2$.

Full Factorial Design (FFD) is a widely used technique in developing the metamodels and is usually constructed on a two-level or three-level basis. The samples are given by all the possible combination of the factors. Therefore, the sample size is $N_{DOE} = L^k$.

Fractional Factorial Design (FrFD) is a subset of FFD which reduces the total number of experiments/simulations. In this method, the sample size is usually one-half, one-third, or one-quarter of FFD. It is important to select the samples in a way that they be balanced. The sample size is $N_{DOE} = L^{k-p}$, where p is related to the fraction of design.

Star Experimental Design (SED) contains two axial points on the axis of each factor with a physical distance δ from the center. Also, it includes the center point with all the factors in their mean value. The sample size is $N_{DOE} = 2k + 1$.

Central Composite Design (CCD) is a combination of a two-level FFD and a SED. Therefore, the sample size is $N_{DOE} = k^2 + 2k + 1$. This method is capable of estimating the curvature of the design space. Depending on location of star points (δ) , CCD can take different forms:

- (i) Central Composite Circumscribed (CCC): if $\delta = 1$.
- (ii) Central Composite Faced (CCF) and Inscribed (CCI): if $\delta = 1/\sqrt{k}$.
- (iii) Central Composite Scaled (CCS): if δ is arbitrarily selected to be either > 1 or < $1/\sqrt{k}$.

Box-Behnken Experimental Design (BBED) is an incomplete three-level FFD. It is supposed to reduce the sample size as the number of parameters grows; however, it is still sufficient to estimate the coefficients of a 2nd-degree least squares polynomial. Specific tables are available to construct the BBED models [17].

Plackett-Burman Experimental Design (PBED) includes a set of economical designs with the run number a multiple of four and they are appropriate for screening purposes. It is constrained with the condition that $N_{DOE} = k + 1$. Sample size is $N_{DOE} = k + 4 - MOD(k, 4)$, in which MOD is modulo operation.

Taguchi Experimental Design (TED) is based on distinction between the controllable and noise factors to reduce the sensitivity of the problem to the variations in uncontrollable factors. Sample size is $N_{DOE} = L^{k_i + k_o}$, in which the subscripts i and o refer to the inner and outer factors, respectively.

Random Experimental Design (RED) relies on different techniques for filling uniformly the design space. RED is not based on the concept of levels and does not require discretization. Sample size, N_{DOE} , is selected independently.

Quasi Random Sequences (QRS) are generated from a completely deterministic, low-discrepancy process and possess no inherent statistical properties. Discrepancy is a metric for the degree of nonuniformity of numbers in a sequence [18]. Two main sequences are Halton and Sobol.

Latin Hypercube Sampling (LHS) reduces the variance in the crude Monte Carlo Simulation (MCS) [19]. In LHS, first the given range, [0,1], is divided into N equal intervals 1/N. Then, a point is randomly selected from each interval.

3. Response Surface Method

Response surface method (RSM) has been used for a variety of problems in structural reliability and optimization [8, 20–27]. The fundamental idea is to use the results of a DOE to create an approximation of the response parameters. This approximation, which is called the response surface or "metamodel" (model of the model), can be constructed for different engineering demand parameters (EDPs).

Since the response surface provides an analytical or explicit function, the further operations (e.g., reliability or optimization) on the system will be very fast and do not require extra experiments or simulations. Assuming that the response variable, y, is an unknown function of the input parameters, \mathbf{x} , then the response surface \hat{y} is an approximation of this function:

$$y = f(\mathbf{x}) = \hat{f}(\mathbf{x}) + \epsilon(\mathbf{x}) \Longrightarrow$$

$$\hat{y} = \hat{f}(\mathbf{x})$$
(1)

where $\epsilon(\mathbf{x})$ is the error in the estimated response.

The outcome of a DOE with N_{DOE} experiments or simulations can be collected as $N_{DOE}(\mathbf{x}_i, y_i)$ couples in which any EDP y_i is associated with a point \mathbf{x}_i in the design space. The response surface is said to be *interpolating* if for each sample point $y_i = \hat{f}(\mathbf{x}_i)$ holds, or *approximating* if $\epsilon(\mathbf{x}_i) \neq 0$ [16]. There are different techniques in order to approximate a response surface, e.g., least squares method, optimal RSM, shepard and K-Nearest, Kriging, Gaussian processes, radial basis functions, and artificial neural networks.

In this paper, the least squares method (LSM) is used to construct the response surface. This method is originally developed by Gauss [28]. It is based on adjusting the coefficients in the response surface metamodel so that it best fits an observed data set (from experiments or simulations). The *model function* is defined as $\widehat{f}(\mathbf{x}, \boldsymbol{\beta})$, where $\boldsymbol{\beta} = [\beta_1, \dots, \beta_m]^T$ is the vector of m unknown coefficients to be found and $\mathbf{x} = [x_1, \dots, x_k]^T$ is the vector of k input parameters. The data set consists of $\langle \mathbf{x}_i, y_i \rangle$ pairs, $i = 1, \dots, N$, where \mathbf{x}_i is the input parameters of the ith simulation, whose EDP is y_i . In LSM, the coefficients, β_j , $j = 1, \dots, m$, are estimated by minimizing the S function (i.e., the sum of squared residuals at the points in the data set):

$$S = \sum_{i=1}^{N_{DOE}} \epsilon_i^2 \tag{2}$$

where the residuals are the difference between the actual responses and the predicted ones at the locations \mathbf{x}_i and can be written as $\epsilon_i = y_i - \hat{f}(\mathbf{x}_i, \boldsymbol{\beta}), i = 1, ..., N$. The minimum of S can be easily found by setting the gradient equal to zero:

$$\frac{\partial S}{\partial \beta_{j}} = 2 \sum_{i=1}^{N_{DOE}} \epsilon_{i} \frac{\partial \epsilon_{i}}{\partial \beta_{j}} = -2 \sum_{i=1}^{N_{DOE}} \left[y_{i} - \widehat{f} \left(\mathbf{x}_{i}, \boldsymbol{\beta} \right) \right] \frac{\partial \widehat{f} \left(\mathbf{x}_{i}, \boldsymbol{\beta} \right)}{\partial \beta_{j}}$$

$$= 0, \quad j = 1, \dots, m$$
(3)

Least squares problems are divided into two groups: linear and nonlinear. The following provides insight into each solution technique.

Linear problems have a closed-form (analytical) solution; however, they are not quit accurate and they only provide the general trends of the EDPs over the design space. For a problem with N_{DOE} simulations/experiments and k parameters, the metamodel function takes the following form:

$$\widehat{f}(\mathbf{x}, \boldsymbol{\beta}) = \beta_0 + \beta_1 x_1 + \dots + \beta_k x_k$$

$$\widehat{f}(\mathbf{x}_i, \boldsymbol{\beta}) = \beta_0 + \sum_{i=1}^k x_{i,j} \beta_j$$
(4)

or the form of matrix notation,

$$y = X\beta + \epsilon, \tag{5}$$

where

$$\mathbf{y} = \begin{bmatrix} y_1 \\ y_2 \\ \vdots \\ y_N \end{bmatrix},$$

$$\mathbf{X} = \begin{bmatrix} 1 & x_{1,1} & \cdots & x_{1,k} \\ 1 & x_{2,1} & \cdots & x_{2,k} \\ \vdots & \vdots & \ddots & \vdots \\ 1 & x_{N,1} & \cdots & x_{N,k} \end{bmatrix},$$

$$\boldsymbol{\beta} = \begin{bmatrix} \beta_1 \\ \beta_2 \\ \vdots \\ \beta_N \end{bmatrix},$$

$$\boldsymbol{\epsilon} = \begin{bmatrix} \epsilon_1 \\ \epsilon_2 \\ \vdots \\ \vdots \end{bmatrix}$$

$$\boldsymbol{\epsilon} = \begin{bmatrix} \epsilon_1 \\ \epsilon_2 \\ \vdots \\ \vdots \end{bmatrix}$$

$$\boldsymbol{\epsilon} = \begin{bmatrix} \epsilon_1 \\ \epsilon_2 \\ \vdots \\ \vdots \end{bmatrix}$$

Subsequently, (2) can be written as

$$S = \boldsymbol{\epsilon}^T \boldsymbol{\epsilon} = (\mathbf{y} - \mathbf{X}\boldsymbol{\beta})^T (\mathbf{y} - \mathbf{X}\boldsymbol{\beta})$$
$$= \mathbf{y}^T \mathbf{y} - 2\boldsymbol{\beta}^T \mathbf{X}^T \mathbf{y} + \boldsymbol{\beta} \mathbf{X}^T \mathbf{X} \boldsymbol{\beta}$$
 (7)

Deriving (7), equating to zero, and solving in β yield

$$\frac{\partial S}{\partial \boldsymbol{\beta}} = -2\mathbf{X}^T \mathbf{y} + 2\mathbf{X}^T \mathbf{X} \boldsymbol{\beta} = 0 \Longrightarrow$$

$$\boldsymbol{\beta} = \left(\mathbf{X}^T \mathbf{X}\right)^{-1} \mathbf{X}^T \mathbf{y}$$
(8)

and the EDP of the estimated (fitted) metamodel is

$$\widehat{\mathbf{y}} = \mathbf{X}\boldsymbol{\beta} \tag{9}$$

Nonlinear problems should be solved iteratively. In this method, first the initial values for the coefficients, $\beta^{(1)}$, are chosen. Then, it is updated iteratively (it is known as Gauss-Newton algorithm):

$$\boldsymbol{\beta}^{(k+1)} = \boldsymbol{\beta}^{(k)} + \Delta \boldsymbol{\beta}^{(k)} \tag{10}$$

where $\Delta \pmb{\beta}^{(k)}$ refers to the shift vector. This vector can be updated using an iterative model by approximation to a first-order Taylor series expansion about $\pmb{\beta}^{(k)}$

$$\widehat{f}\left(\mathbf{x}_{i}, \boldsymbol{\beta}^{(k+1)}\right) = \widehat{f}\left(\mathbf{x}_{i}, \boldsymbol{\beta}^{(k)}\right) + \sum_{j=1}^{m} \underbrace{\frac{\partial \widehat{f}\left(\mathbf{x}_{i}, \boldsymbol{\beta}^{(k)}\right)}{\partial \beta_{j}} \left(\beta_{j}^{(k+1)} - \beta_{j}^{(k)}\right)}_{\mathbf{J}_{i}^{(k)} \Delta \beta_{i}^{(k)}}$$
(11)

where **J** is a $N \times m$ Jacobian matrix of \hat{f} with respect to β . This equation can be written in the form of matrix notation

$$\mathbf{y} = \hat{\mathbf{y}}^{(k)} + \boldsymbol{\epsilon}^{(k)} = \hat{\mathbf{y}}^{(k+1)} + \boldsymbol{\epsilon}^{(k+1)}$$
$$= \hat{\mathbf{y}}^{(k)} + \mathbf{J}^{(k)} \Delta \boldsymbol{\beta}^{(k)} + \boldsymbol{\epsilon}^{(k+1)}$$
(12)

Subsequently, derivative of *S* with respect to β takes the following form:

$$\frac{\partial S}{\partial \boldsymbol{\beta}} = -2\mathbf{J}^{(k)T} \boldsymbol{\epsilon}^{(k)} + 2\mathbf{J}^{(k)T} \mathbf{J}^{(k)} \Delta \boldsymbol{\beta}^{(k)}$$
(13)

Solving in $\Delta \boldsymbol{\beta}^{(k)}$ yields

$$\Delta \boldsymbol{\beta}^{(k)} = \left(\mathbf{J}^{(k)}^T \mathbf{J}^{(k)} \right)^{-1} \mathbf{J}^{(k)}^T \boldsymbol{\epsilon}^{(k)}$$
 (14)

Both linear and nonlinear problems can be used in the context of the complete or incomplete polynomials. The number of required coefficients, m, for a nth-degree polynomial, with k variables, can be calculated as

$$m = \binom{k+n}{n} = \frac{(k+n)!}{n!k!} \tag{15}$$

and, subsequently, the general expression for the *n*th-degree polynomial can be written as

$$\widehat{f}_{(n)^{th}}(\mathbf{x}, \boldsymbol{\beta}) = \widehat{f}_{(n-1)^{th}} + n\text{th order terms}$$
 (16)

Majority of the real-world civil engineering problems can be estimated using one of the following expressions for the linear and quadratic forms:

$$\widehat{f}_{1st}(\mathbf{x}, \boldsymbol{\beta}) = \beta_0 + \sum_{i=1}^k \beta_i x_i$$

$$\widehat{f}_{2nd}(\mathbf{x}, \boldsymbol{\beta}) = \widehat{f}_{1st} + \sum_{i=1}^k \sum_{i=1}^i \beta_{i,j} x_i x_j$$
(17)

The goodness-of-fit (GOF) in an approximation can be estimated by regression parameters which varies between 0.0 and 1.0. The higher the GOF is, the better the model is expected to be. A widely used GOF is

$$R^{2} = 1 - \frac{\sum_{i=1}^{N} (y_{i} - \widehat{y}_{i})^{2}}{\sum_{i=1}^{N} (y_{i} - \overline{y})^{2}};$$

$$\overline{y} = \frac{1}{N} \sum_{i=1}^{N} y_{i}$$
(18)

4. Smeared Crack Model

In concrete dam engineering, the nonlinearity is originated mainly from two sources: continuum crack model and discrete crack model. The latter one is usually used when the location and direction of a potential crack or joint are already known. This model has been successfully used for modeling the contraction joints in arch dams [6]. The former one itself can be divided into two major groups, i.e., the damage mechanics approach [29–31] and the smeared crack approach [32–34].

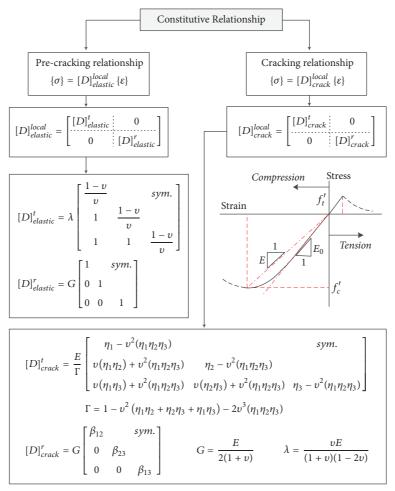
The nonlinear response of the case study dam in this paper is modeled by smeared crack approach. Thus, this section briefly reviewed the main formulation of this technique. Smeared cracks are convenient when the crack orientations are not known beforehand. It does not require a remeshing or new degrees of freedom. A coaxial rotating model is used to simulate the concrete crack under the dynamic loading. In this model, the precracked constitutive relation is replaced by the cracked one where the reference axis is aligned with the fracture direction. The main assumptions are as follows: (1) the concrete is initially linear isotropic until it reaches the ultimate strength, (2) the concrete modulus of elasticity is taken as the average instead of the linear actual one, and (3) during the softening phase, an anisotropic modulus matrix is considered for material.

Figure 2 shows the smeared crack-based precracked and cracked constitutive relationships. Cracking occurs when the principal stresses, in any direction, lie outside the failure surface. In this model, cracking is permitted at each Gaussian point and in three orthogonal directions.

Next, a failure criterion (e.g., yielding, load carrying capacity, and initiation of cracking) is required to quantify the ultimate strength surface. In the present paper, Willam and Warnke [35] failure criterion is used to identify the initiation and propagation of the cracks in mass concrete. Since this formulation is not the main scope of this paper, only a brief formulation is illustrated in Figure 3.

5. Numerical Example

An ultra-high arch dam is selected as a vehicle for the numerical examples [6]. The finite element model of the dam, the foundation, and the reservoir are prepared in ANSYS [36] software, Figure 4. The model consists of 792 and 3,770 solid brick elements for dam and foundation, and 3,660 fluid brick elements for the reservoir domain.



Notes: *E*: modulus of elasticity; *G*: shear modulus of elasticity; *v*: Poisson's ratio, λ : Lame constant; f'_c : compressive strength; f'_t : tensile strength; η_1, η_2, η_3 : ratio of the softened Young's modulus in three directions; $\beta_{12}, \beta_{23}, \beta_{31}$: shear transfer factors in three directions; $[\sigma]$: stress vector; $\{\varepsilon\}$: strain vector

FIGURE 2: Constitutive model for the concrete based on coaxial rotating smeared crack model; adopted from [6].

Notes: $Y(\theta)$: elliptic trace; θ : Lode angle; f_{cb} : biaxial compressive strength; f_t : tensile strength; $\sigma_1, \sigma_2, \sigma_3$: principal stress components; I_1, I_2, I_3 : stress invariants; I_1, I_2, I_3 : deviatoric stress invariants; I_1, I_2, I_3 : position vectors of meridians

FIGURE 3: Formulation of failure criterion for concrete; adopted from [6].

TABLE 1: Material properties for the finite element model.
--

Overtites	Symbol	Unit	DOE			UQ			
Quantity	Symbol	Ollit	Mean (0)	Variation	Lower (-1)	Upper (+1)	Model	COV	Truncation
Concrete modulus of elasticity	E_c	MPa	40,000	15%	34,000	46,000	Normal	0.08	[34,000 46,000]
Concrete Poisson's ratio	ν_c	-	0.2	-	-	-	-	-	-
Concrete mass density	$ ho_c$	kg/m³	2,400	10%	2,160	2,640	Normal	0.06	[2,160 2,600]
Concrete compressive strength	f_c'	MPa	35.0	20%	28.0	42.0	Normal	0.10	[25.0 40.0]
Concrete tensile strength	f_f'	MPa	3.5	20%	2.8	4.2	Normal	0.10	[2.5 4.0]
Foundation modulus of elasticity	E_f	MPa	20,000	25%	15,000	25,000	Normal	0.10	[15,000 25,000]
Foundation Poisson's ratio	$ u_f$	-	0.25	-	-	-	-	-	-
Foundation mass density	$ ho_f$	kg/m³	2,500	-	-	-	-	-	-
Water mass density	$ ho_w$	kg/m³	1,000	-	-	-	-	-	-
Wave velocity in water	C_w	m/s	1,440	-	-	-	-	-	-
Wave reflection coefficient at the bottom	$lpha_w$	-	0.80	-	-	-	-	-	-
Sediment/silt mass density	$ ho_s$	kg/m³	1,360	-	-	-	-	-	-

DOE: Design of Experiment; UQ: Uncertainty Quantification; COV: Coefficient of Variation.

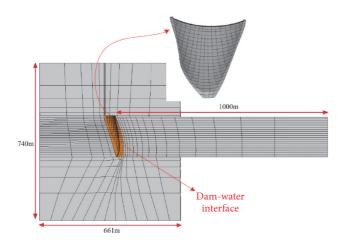


FIGURE 4: Finite element model of dam, reservoir, and foundation system.

All the nodes on the far-end boundary of the foundation are restricted in three transitional directions. Nonlinearity stems only from the concrete cracking and the contraction joints are modeled in this study. This is to keep the number of overall variables in a reasonable range to perform the response surface metamodeling.

Table 1 lists the most important material properties that were used to develop the finite element model. Four material

properties are assumed to be random variables (RVs). Three of them belong to concrete, i.e., elasticity, mass density, and compressive strength, and the remaining one belongs to the foundation, i.e., modulus of elasticity. These parameters are among those most sensitive RVs identified for concrete dams in [37]. Furthermore, it is noteworthy to say that a full correlation is assumed among the concrete tensile and compressive strength through a deterministic relationship $f_t' = 0.1 \, f_c'$.

Having four RVs, many of the DOE techniques in Section 2 can be adopted. For example, two-level and three-level FFD require 16 and 81 simulations, respectively. A SED needs 9 and a CCD requires 25 simulations. However, in the present study, the BBED technique is used. The main reason can be attributed to the fact that it is an incomplete three-level FFD. Thus, it can capture the potential curvature of the response surface, while it requires less simulations compared to FFD. Box and Behnken [17] determine the required number of simulations as

(i)
$$k = 3$$
, $N_{DOE} = 12 + 1 = 13$

(ii)
$$k = 4$$
, $N_{DOF} = 24 + 1 = 25$

(iii)
$$k = 5$$
, $N_{DOE} = 40 + 1 = 41$

(iv)
$$k = 6$$
, $N_{DOE} = 48 + 1 = 49$

In two-level designs (e.g., FFD and SED), lower and upper bounds are assumed for experimental design. However, in three-level designs, another level is assumed in between

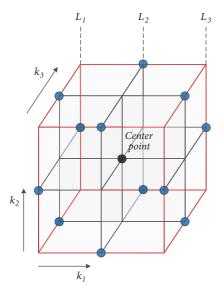


FIGURE 5: Graphical representation of Box-Behnken experimental design for k=3.

Table 2: Tabulated simulations in a Box-Behnken experimental design with k=4.

Simulations		Codeo	d values	
Simulations	x_1	x_2	x_3	x_4
1-4	±1	±1	0	0
5-8	±1	0	±1	0
9-12	±1	0	0	±1
13-16	0	±1	±1	0
17-20	0	±1	0	±1
21-24	0	0	±1	±1
25	0	0	0	0

which is referred to mean. It is convenient to use the "coded" (standardized) factors, x_i^{coded} , instead of the actual values, x_i^{actual} . In the case of two-level designs, they are referred to "±1", and in the case of three-level designs, they are "-1", "0" and "+1". Any desired value in the range of (min, max) of the actual values can be converted to the coded one:

$$x_i^{coded} = \frac{x_i^{actual} - \left(x_i^{actual} + x_i^{actual}\right)/2}{\left(x_i^{actual} - x_i^{actual}\right)/2}$$
(19)

where the superscripts *U* and *L* present the upper and lower bounds of the actual values, respectively.

It is possible to graphically show the BBED with three factors (as a 3D cube), Figure 5, where the samples are at the center and middle of the edges. Such a plot is not possible for k=4 in the Cartesian coordinate system; however, the simulations can be presented in the form of Table 2. In this table, x_1 to x_4 correspond to E_c , ρ_c , f_c' , and E_f , respectively. The lower bound, mean, and the upper bound for each RV can be found in Table 1.

6. Results

The coupled system is excited using the ground motion shown in Figure 6(a). This ground motion is scaled to maximum design level (MDL) for the dam site Hariri-Ardebili and Kianoush [6]. Displacement response of the pilot dam subjected to this signal is also shown in Figure 6(b). Pilot dam is referred to the one with all the material properties at their mean value, Table 1. The pilot model is also called Sim-25 in Table 2. Note that there is an initial displacement towards downstream due to hydrostatic pressure. Figure 7 illustrates the cracking and crushing of pilot dams. As discussed already, cracking is allowed in three orthogonal directions and they are presented as first, second, and third cracks. Obviously, the damage distribution is higher in Figure 7(a) than Figures 7(b) and 7(c). Furthermore, there is no concrete crushing for this pilot model, Figure 7(d). Note that color variation presents the degree of element damage.

Next, the BBED analyses are performed as illustrated in Table 3. Note that f_t' always is assumed to be 10% of the compressive strength. The displacement response is considered in two levels: (1) preseismic and (2) maximum seismic. The major observations based on static displacement are as follows:

- (i) In general, the ratio of maximum dynamic displacement to the static one is 5-7 for all the 25 simulations.
- (ii) There is no cracking in the dam under the static loads.
- (iii) Based on the results, f'_c (and f'_t) has no effect on the static displacement.
- (iv) Per this table, increasing E_c , ρ_c , and E_f reduces the displacement. However, sensitivity of E_c is higher than the others, and ρ_c has the minimum impact.

On the other hand, 5 quantities are reported for the seismic simulations, i.e., maximum displacement, cracking in three directions, and crushing. Except the displacement, the others are presented in terms of the volumetric damage index, DI:

$$DI_{vol} = \frac{\text{Damaged volume}}{\text{Total volume}}$$
 (20)

Note that all the solid elements in the present formulation have eight Gaussian points in which the damage may occur in these points. Subsequently, status of each element can be presented with a number as 0, 1/8, ..., 7/8, 1, in which zero means no damage in the element and one shows the full damage. It is worth mentioning that $DI_{vol}^{cr3} \subset DI_{vol}^{cr2} \subset DI_{vol}^{cr1}$. Furthermore, Figures 8, 9, 10, and 11 show the damage distribution results from first and third cracks on upstream (US) and downstream (DS) faces of dam, respectively. The major observations are the following:

- (i) Dynamic displacement varies from 95 to about 177 mm in different models.
- (ii) DI_{vol}^{cr1} varies from 0.8 to 24.4%, DI_{vol}^{cr2} varies from 0 to 9.5%, DI_{vol}^{cr3} varies from 0 to 7.0%, and DI_{vol}^{crush} is limited to 2.4%.

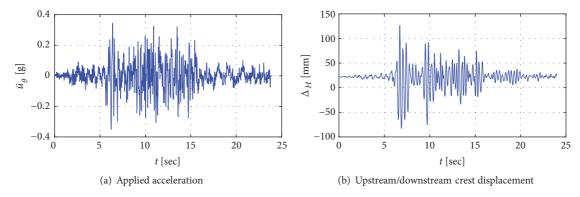


FIGURE 6: Structural analysis of pilot model.

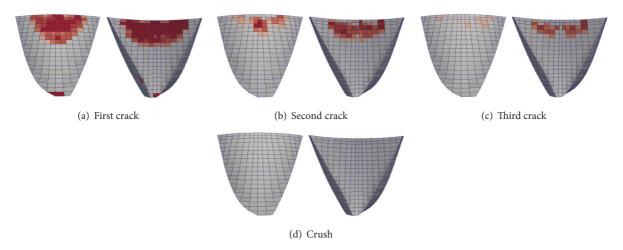


Figure 7: Damage distribution in upstream and downstream faces of pilot model.

- (iii) As seen, the main cracking is distributed in central upper parts of the dam in vicinity of crest. In some cases, there are limited cracking at the lower parts, near the dam-foundation interface.
- (iv) Cracking in the third direction is more concentrated on the downstream face, which shows its vulnerability.

In order to quantify the sensitivity of all material trampers, and also derive a response surface metamodel, a second-order polynomial including the interaction terms is used:

$$\widehat{EDP} = \beta_1 + \beta_2 E_c + \beta_3 \rho_c + \beta_4 f_c' + \beta_5 E_f + \beta_6 E_c^2$$

$$+ \beta_7 \rho_c^2 + \beta_8 f_c'^2 + \beta_9 E_f^2 + \beta_{10} E_c \rho_c + \beta_{11} E_c f_c'$$

$$+ \beta_{12} E_c E_f + \beta_{13} \rho_c f_c' + \beta_{14} \rho_c E_f + \beta_{15} f_c' E_f$$
(21)

where the hat sign represents the estimated EDP.

Five EDPs are used in (21), i.e., two displacements, and three cracking-based DIs. The predicted β_i values are shown in Figure 12. To make the comparison easy, the absolute logarithmic values are shown. Large negative values for $\log |\beta_i|$ present the lower contribution of that parameter in overall response surface metamodel. For example, based on

Figure 12(a), contribution of f'_c (i.e., β_4) is negligible in static analyses; however, it plays an important role in dynamic part (Figure 12(b)).

In addition, the probability of exceedance of response parameters is shown in the last column of Figure 12. In each plot, the empirical cumulative distribution function (CDF) of the FEM and BBED is plotted, as well as the fitted curves using the log-normal (LN) distributional model. LN is the best model to fit the data points among others (e.g., normal, beta). In all cases, these are a good match between the empirical and fitted curves. For all five responses, the BBED model fluctuates around the FEM, and two fitted curves cross at the probability of 0.50-0.65.

The estimated response surfaces should be validated using an independent data set. For this purpose, 250 samples for each of four RVs are computed using the LHS technique [38]. No correlation is assumed among the RVs. Mean, COV, and the upper and lower bounds are already provided in Table 1. The resulting samples are shown in Figure 13. Subsequently, 250 extra nonlinear transient analyses are performed and the EDPs are computed. Real versus estimated values are also shown in Figure 12. As seen the individual data points are close to equity line. The estimated coefficient of determination, R^2 , is 0.96, 0.92, 0.91, 0.90, and 0.88 for

Sim	E_c	ρ_c	f_c'	E_f	Δ_{max}^{sta} [mm]	Δ_{max}^{dyn} [mm]	$DI_{vol}^{cr1}[\%]$	$DI_{vol}^{cr2}[\%]$	$DI_{vol}^{cr3}[\%]$	$DI_{vol}^{crush}[\%]$
1	46	2640	35	20	19.7	117.6	17.6	6.3	3.2	0.1
1	46	2160	35	20	19.8	95.1	11.5	2.1	0.7	0.0
3	34	2640	35	20	25.4	168.7	14.2	5.8	3.7	0.3
4	34	2160	35	20	25.4	137.6	11.6	3.0	1.2	0.0
5	46	2400	42	20	19.8	99.5	8.4	1.0	0.3	0.0
6	46	2400	28	20	19.8	99.5	8.4	1.0	0.3	0.0
7	34	2400	42	20	25.4	141.6	8.9	1.3	0.3	0.0
8	34	2400	28	20	25.4	177.0	16.8	7.8	5.6	1.0
9	46	2400	35	25	19.0	98.2	13.5	3.3	1.3	0.0
10	46	2400	35	15	21.1	113.7	19.8	4.3	1.7	0.1
11	34	2400	35	25	24.7	146.8	12.3	4.4	1.9	0.0
12	34	2400	35	15	26.7	159.5	15.0	5.2	2.1	0.1
13	40	2640	42	20	22.1	130.2	0.8	0.0	0.0	0.0
14	40	2640	28	20	22.1	149.0	22.4	9.5	6.5	1.9
15	40	2160	42	20	22.2	108.8	5.5	0.3	0.1	0.0
16	40	2160	28	20	22.2	151.0	18.7	9.2	7.0	2.4
17	40	2640	35	25	21.4	133.0	14.4	5.8	2.7	0.0
18	40	2640	35	15	23.3	151.0	19.1	6.3	3.2	0.2
19	40	2160	35	25	21.4	109.1	10.2	1.9	0.8	0.0
20	40	2160	35	15	23.5	122.4	14.1	3.1	1.0	0.1
21	40	2400	42	25	21.4	114.8	7.8	1.3	0.4	0.0
22	40	2400	42	15	23.4	127.0	10.9	1.4	0.2	0.0
23	40	2400	28	25	21.4	145.0	17.4	8.4	5.9	1.3
24	40	2400	28	15	23.4	168.0	24.4	8.8	6.1	1.7
25	40	2400	35	20	22.2	126.3	14.7	4.5	1.9	0.0

TABLE 3: Summary of the BBED simulations.

 Δ_{max}^{sta} , Δ_{max}^{dyn} , $DI_{vol}^{cr1}[\%]$, $DI_{vol}^{cr2}[\%]$, and $DI_{vol}^{cr3}[\%]$, respectively. Smaller R^2 for the third crack can be attributed to this fact that there is a smaller variation among the percent cracking of the models. Moreover, the root mean square error, $RMSE = \sqrt{(1/N)\sum_{i=1}^{N}(EDP_i - \widehat{EDP}_i)^2}$, for the five EDPs is 0.24, 3.89, 0.65, 0.43, and 40.

7. Summary

This paper presented the results of probabilistic analysis of an arch dam with uncertainty in the material properties. A detailed finite element model of the dam-foundation-reservoir coupled system is developed. The fluid-structure interaction is modeled by Eulerian approach. The nonlinearity in the system is originated from the smeared crack modeling in the mass concrete. The coupled system is excited using an earthquake record in the maximum design level of the dam site.

Over ten different designs of experiment techniques are critically reviewed and the Box-Behnken experimental design (BBED) is chosen to be used in this paper. Advantage of BBED over the other techniques is that it is an incomplete three-level full factorial design and thus it can capture the nonlinearity of the design space, while it requires small number of simulations.

For an engineering problem with four random variables, BBED requires only 25 simulations. The outputs of these analyses are reported in terms of the preseismic and seismic displacements, as well as the volumetric damage index in three orthogonal cracking directions. Then, a response surface metamodel is developed for each of the engineering demand parameters. The metamodels are provided in the explicit form based on the quadratic polynomial including the interaction terms.

Next, it is important to validate the applicability of the developed analytical models through another set of independent simulations. Since nonlinear dynamic analysis of 3D arch dams with foundation and reservoir is computationally expensive, Latin Hypercube Sampling is used with 250 simulations. No correlation is assumed among the generated random numbers.

Results show a good consistency between the finite element based outputs and those estimated by response surface metamodel. Coefficient of determination is about 0.9 in all cases. Furthermore, a discussion is provided about the cracking pattern of arch dams under the material uncertainty.

Results of this study are important since they provide a framework for uncertainty quantification of the material properties in the structural and infrastructural system subjected to varying environmental conditions. There are a large number of dams, bridges, and nuclear power plants which

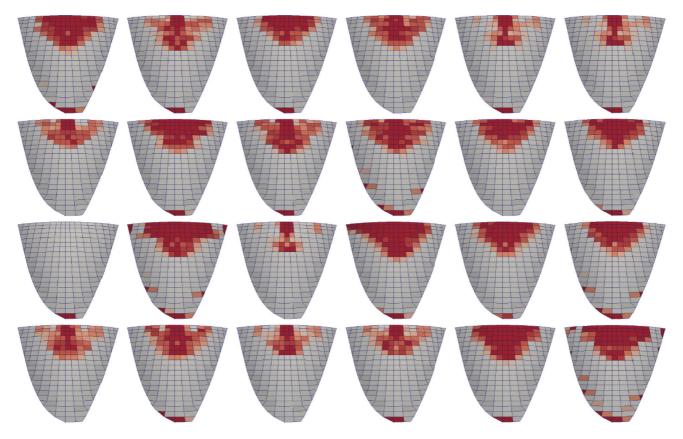


Figure 8: Distribution of first crack on upstream face; top left: Sim-1; first row: 1 to 6; bottom right: Sim-24.

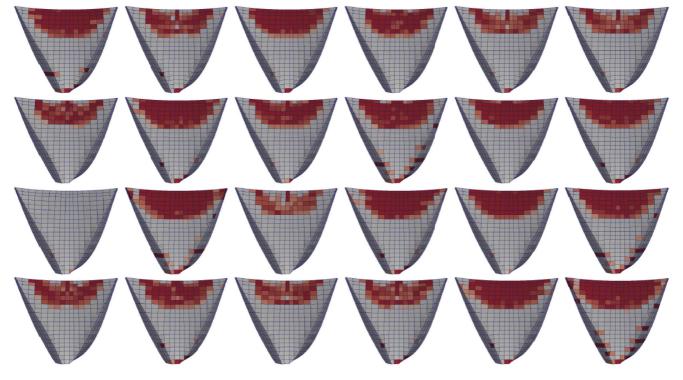


Figure 9: Distribution of first crack on downstream face; top left: Sim-1; first row: 1 to 6; bottom right: Sim-24.

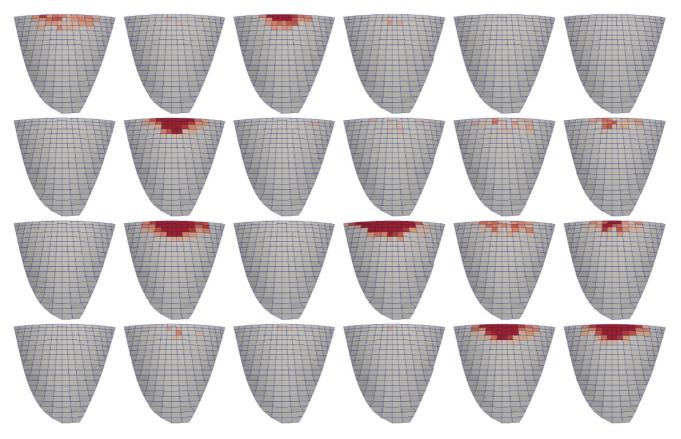


Figure 10: Distribution of third crack on upstream face; top left: Sim-1; first row: 1 to 6; bottom right: Sim-24.

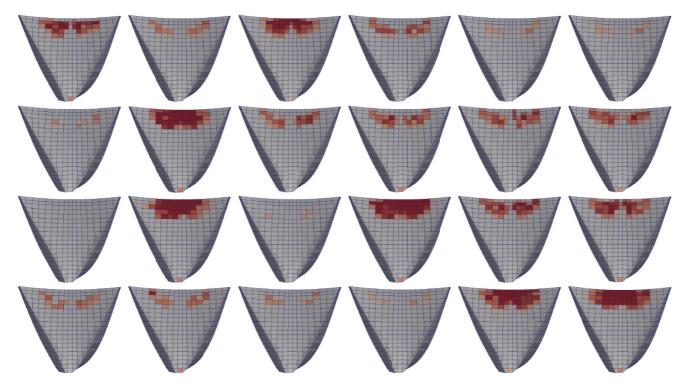


Figure 11: Distribution of third crack on downstream face; top left: Sim-1; first row: 1 to 6; bottom right: Sim-24.

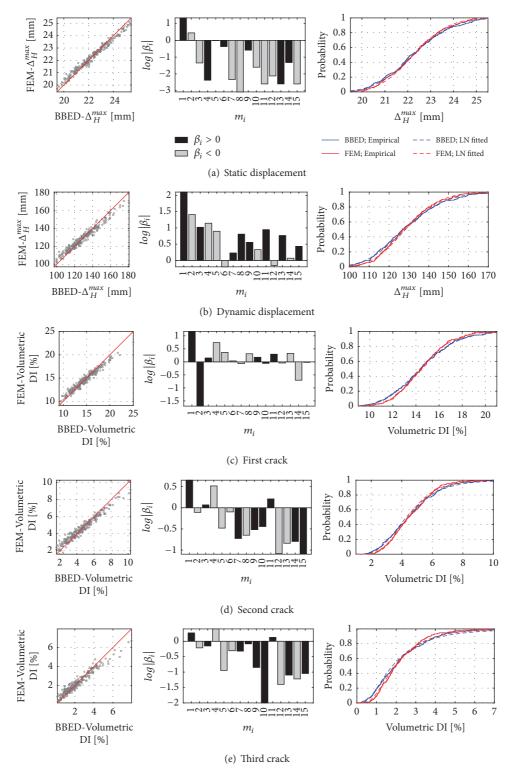
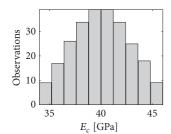
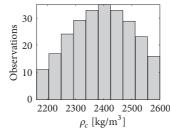
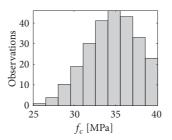


FIGURE 12: Validation of the predicted response surface using LHS method.







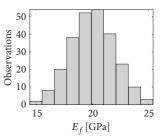


FIGURE 13: LHS-based sampling for validation of metamodels.

are aging and they need to be reevaluated regularly based on the updated (or degraded) material properties. Once such metamodels are developed, they can be used without any extra cost to evaluate the reliability of the system under the new condition. This saves a considerable amount of money and time and facilitates the risk-based decision-making.

Data Availability

All the raw data used to support the findings of this study (resulting from numerical simulations) are included within the article. However, the finite element models are available from the corresponding author upon request.

Conflicts of Interest

The authors declare that there are no conflicts of interest regarding the publication of this paper.

Acknowledgments

The first author would like to express his sincere appreciation to his former advisor (and the current PI), Professor Victor E. Saouma, at the University of Colorado Boulder for his enthusiastic guidance and advice throughout this research.

References

- [1] A. Der Kiureghian and O. Ditlevsen, "Aleatory or epistemic? Does it matter?" *Structural Safety*, vol. 31, no. 2, pp. 105–112, 2009.
- [2] M. A. Hariri-Ardebili and V. E. Saouma, "Seismic fragility analysis of concrete dams: A state-of-the-art review," *Engineering Structures*, vol. 128, pp. 374–399, 2016.
- [3] P. B. Tekie and B. R. Ellingwood, "Seismic fragility assessment of concrete gravity dams," *Earthquake Engineering & Structural Dynamics*, vol. 32, no. 14, pp. 2221–2240, 2003.
- [4] A. Lupoi and C. Callari, "A probabilistic method for the seismic assessment of existing concrete gravity dams," Structure and Infrastructure Engineering, vol. 8, no. 10, pp. 985–998, 2012.
- [5] Y. Ghanaat, R. Patev, and A. Chudgar, "Seismic fragility for risk assessment of concrete gravity dams," in *Proceedings of the 2015* USSD Annual Conference, pp. 645–660, 2015.
- [6] M. A. Hariri-Ardebili and M. R. Kianoush, "Integrative seismic safety evaluation of a high concrete arch dam," *Soil Dynamics and Earthquake Engineering*, vol. 67, pp. 85–101, 2014.

- [7] A. Azarbakht and M. Dolšek, "Prediction of the median IDA curve by employing a limited number of ground motion records," *Earthquake Engineering & Structural Dynamics*, vol. 36, no. 15, pp. 2401–2421, 2007.
- [8] M. R. Rajashekhar and B. R. Ellingwood, "A new look at the response surface approach for reliability analysis," *Structural Safety*, vol. 12, no. 3, pp. 205–220, 1993.
- [9] Q. Guo, L. Pei, Z. Zhou, J. Chen, and F. Yao, "Response surface and genetic method of deformation back analysis for high core rockfill dams," *Computers & Geosciences*, vol. 74, pp. 132–140, 2016.
- [10] M. E. Kartal, H. B. Başaĝa, and A. Bayraktar, "Probabilistic nonlinear analysis of CFR dams by MCS using response surface method," *Applied Mathematical Modelling*, vol. 35, no. 6, pp. 2752–2770, 2011.
- [11] F. S. Wong, "Slope reliability and response surface method," Journal of Geotechnical Engineering, vol. 111, no. 1, pp. 32–53, 1985.
- [12] X.-H. Tan, M.-F. Shen, X.-L. Hou, D. Li, and N. Hu, "Response surface method of reliability analysis and its application in slope stability analysis," *Geotechnical and Geological Engineering*, vol. 31, no. 4, pp. 1011–1025, 2013.
- [13] D.-Q. Li, D. Zheng, Z.-J. Cao, X.-S. Tang, and K.-K. Phoon, "Response surface methods for slope reliability analysis: Review and comparison," *Engineering Geology*, vol. 203, pp. 3–14, 2016.
- [14] J.-Y. Chen, Q. Xu, J. Li, and S.-L. Fan, "Improved response surface method for anti-slide reliability analysis of gravity dam based on weighted regression," *Journal of Zhejiang University SCIENCE A*, vol. 11, no. 6, pp. 432–439, 2010.
- [15] M. Klun, A. Kryžanowski, and S. Schnabl, "Application of response surface method in the analysis of hydraulic structures," in Proceedings of the International Symposium on Appropriate technology to ensure proper Development, Operation and Maintenance of Dams in Developing Countries. SANCOLD, 2016.
- [16] M. Cavazzuti, Optimization Methods: from Theory to Design Scientific And Technological Aspects in Mechanics, Springer Science & Business Media, 2012.
- [17] G. E. Box and D. W. Behnken, "Some new three level designs for the study of quantitative variables," *Technometrics. A Journal of Statistics for the Physical, Chemical and Engineering Sciences*, vol. 2, pp. 455–475, 1960.
- [18] M. Amin Hariri-Ardebili and V. E. Saouma, "Random Response Spectrum Analysis of Gravity Dam Classes: Simplified, Practical and Fast Approach," *Earthquake Spectra*, 2018.
- [19] M. D. McKay, R. J. Beckman, and W. J. Conover, "A comparison of three methods for selecting values of input variables in the analysis of output from a computer code," *Technometrics. A Journal of Statistics for the Physical, Chemical and Engineering Sciences*, vol. 21, no. 2, pp. 239–245, 1979.

[20] L. Faravelli, "Response-surface approach for reliability analysis," Journal of Engineering Mechanics, vol. 115, no. 12, pp. 2763–2781, 1989.

- [21] B. D. Youn and K. K. Choi, "A new response surface methodology for reliability-based design optimization," *Computers & Structures*, vol. 82, no. 2-3, pp. 241–256, 2004.
- [22] S. M. Wong, R. E. Hobbs, and C. Onof, "An adaptive response surface method for reliability analysis of structures with multiple loading sequences," *Structural Safety*, vol. 27, no. 4, pp. 287– 308, 2005.
- [23] A. I. Khuri and S. Mukhopadhyay, "Response surface methodology," *Wiley Interdisciplinary Reviews: Computational Statistics*, vol. 2, no. 2, pp. 128–149, 2010.
- [24] D. L. Allaix and V. I. Carbone, "An improvement of the response surface method," *Structural Safety*, vol. 33, no. 2, pp. 165–172, 2011
- [25] W. Zhao and Z. Qiu, "An efficient response surface method and its application to structural reliability and reliability-based optimization," *Finite Elements in Analysis and Design*, vol. 67, pp. 34–42, 2013.
- [26] N. Roussouly, F. Petitjean, and M. Salaun, "A new adaptive response surface method for reliability analysis," *Probabilistic Engineering Mechanics*, vol. 32, pp. 103–115, 2013.
- [27] D. Zhang, X. Han, C. Jiang, J. Liu, and Q. Li, "Time-Dependent Reliability Analysis Through Response Surface Method," *Journal of Mechanical Design*, vol. 139, no. 4, p. 041404, 2017.
- [28] J. Gauss, Combinationis Observationum Erroribus Minimis Obnoxiae, University of Gottingen, Gottingen, Germany, 1825.
- [29] S. Valliappan, M. Yazdchi, and N. Khalili, "Earthquake analysis of gravity dams based on damage mechanics concept," International Journal for Numerical and Analytical Methods in Geomechanics, vol. 20, no. 10, pp. 725–751, 1996.
- [30] J. Lee and G. L. Fenves, "A plastic-damage concrete model for earthquake analysis of dams," *Earthquake Engineering & Structural Dynamics*, vol. 27, no. 9, pp. 937–956, 1998.
- [31] O. Omidi, S. Valliappan, and V. Lotfi, "Seismic cracking of concrete gravity dams by plastic-damage model using different damping mechanisms," *Finite Elements in Analysis and Design*, vol. 63, pp. 80–97, 2013.
- [32] M. Ghaemian and A. Ghobarah, "Nonlinear seismic response of concrete gravity dams with dam-reservoir interaction," *Engi*neering Structures, vol. 21, no. 4, pp. 306–315, 1999.
- [33] R. Espandar and V. Lotfi, "Comparison of non-orthogonal smeared crack and plasticity models for dynamic analysis of concrete arch dams," *Computers & Structures*, vol. 81, pp. 1461–1474, 2003.
- [34] H. Mirzabozorg and M. Ghaemian, "Non-linear behavior of mass concrete in three-dimensional problems using a smeared crack approach," *Earthquake Engineering & Structural Dynamics*, vol. 34, no. 3, pp. 247–269, 2005.
- [35] K. Willam and E. Warnke, Constitutive model for triaxial behavior of concrete, International Association for Bridges and Structural Engineering, Italy, 1974.
- [36] ANSYS, Ansys software reference manuals, release notes, mechanical apdl, elements reference, commands reference and theory reference, version release 11, 2007.
- [37] M. A. Hariri-Ardebili, S. M. Seyed-Kolbadi, and M. R. Kianoush, "FEM-based parametric analysis of a typical gravity dam considering input excitation mechanism," *Soil Dynamics* and Earthquake Engineering, vol. 84, pp. 22–43, 2016.

[38] R. L. Iman, "A Distribution-Free Approach to Inducing Rank Correlation Among Input Variables," *Communications in Statistics - Simulation and Computation*, vol. 11, no. 3, pp. 311–334, 1982

Hindawi Shock and Vibration Volume 2018, Article ID 8031735, 12 pages https://doi.org/10.1155/2018/8031735

Research Article

Blast Parameter Optimization Study Based on a Blast Crater Experiment

Xi-liang Zhang,^{1,2} Hai-bao Yi , Hong-hao Ma, And Zhao-wu Shen¹

¹CAS Key Laboratory of Mechanical Behavior and Design of Materials, University of Science and Technology of China, Anhui, Hefei 230026, China

Correspondence should be addressed to Hai-bao Yi; hang_tianfeiji@126.com

Received 16 January 2018; Revised 2 April 2018; Accepted 8 May 2018; Published 5 July 2018

Academic Editor: Elena Dragomirescu

Copyright © 2018 Xi-liang Zhang et al. This is an open access article distributed under the Creative Commons Attribution License, which permits unrestricted use, distribution, and reproduction in any medium, provided the original work is properly cited.

The blasting quality and the rock volume blasted directly affect the cost of mines. A small charge-forward blast crater experiment was conducted to study the relationships between the rock volume blasted, the explosive unit consumption, the bulk yield, and the depth ratio. The results showed that the rational resistant line or explosive charge depth should be 0.86 times the optimal resistant line. Based on theoretical analysis of the large spacing of the holes and the small resistance line, the uniform design method was used to conduct the lateral blasting crater tests. The relationship equations among the blasting parameters, the blasting volume, and the bulk yield were obtained by regression analysis. The results illustrated that the rock volume blasted was negatively correlated with the bulk yield. The contribution rates of the resistance lines and the spacing of the holes to the blasting volume regression were 32.4% and 13.9%, respectively, and to the bulk yield regression were 65.0% and 0.256%. The impact of the resistance line on the blasting volume and the bulk yield was more significant than that of the spacing of the holes. The blasting effect of the rectangular blast hole arrangement was better than that of the square pattern. The blasting technology of large hole spacing and a small resistance line could achieve a better blasting effect while ensuring a higher rock volume blasted. The economical and reasonable blasting parameters were determined as the hole spacing of a=8.5 m and the resistance line width of W=5.5 m, with the rock volume blasted of 413.1 m³ and the bulk rate of 0.218%. This method provides an effective method for optimization of the blasting parameters and has important guiding significance for efficient and economical mining.

1. Introduction

In the mining process, open pits are often faced with the problem of balancing the blasting quality and the volume of rock blasted. If the blasting quality is poor, the large block rate is high, and the block size is not uniform, it will bring difficulty to the loading and crushing work, resulting in an increase in production costs. If the blasting quality is good but the blasting volume is often low, then the overall cost is still relatively high.

Therefore, obtaining a better blasting quality, reducing the bulk rate, reducing the unit consumption of explosives, and controlling the overall cost are the actual technical problems that must be resolved under the condition of ensuring a high blasting volume. The scientific determination of reasonable blasting parameters is the key to obtaining a good blasting effect. In the blasting design, the blasting parameters are generally selected with reference to the similar conditions for the mine; this approach has certain limitations and often has a certain deviation from the actual site. Usually, the blast parameters are not the same, even if the same type of explosive is used, because of the different rock characteristics. It is well-known that Livingstone's blasting crater theory plays an important role in finalizing the blast parameters [1].

Many experts and scholars have conducted many research studies to reduce the blasting cost in the mines; such studies can be categorized into three types. The first type is blasting crater theoretical analysis. Mr. W. L. Fourney conducted

²Sinosteel Maanshan Institute of Mining Research, Co., Ltd., Anhui, Maanshan 243000, China

³State Key Laboratory of Safety and Health for Metal Mines, Anhui, Maanshan 243000, China

⁴State Key Laboratory of Fire Science, University of Science and Technology of China, Anhui, Hefei 230026, China

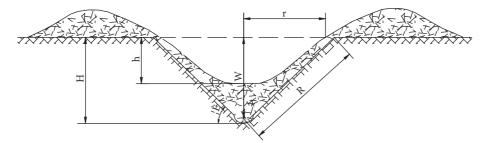


FIGURE 1: **Blasting crater schematic**. r-Radius of the blasting crater; W-minimum resistant line; R-blasting crater crashed radius; h-visible depth of the blasting crater; H-depth of the blasting crater; θ -crater angle.

a study of the crushing mechanism of the blasting crater. The mechanism of fragmentation was one in which the material between the borehole and the free surface is greatly weakened by the stress waves over the first 50 μ sec or so after detonation. It was proposed that this greatly weakened area is subsequently acted upon by the residual pressure in the hole to create the final crater [2, 3]. Mr. Ze Liu's optimization study was conducted using blast parameters of the reduced section tunnel in hard rock based on the blasting mechanism. The optimization of the blasting construction parameters is a dynamic process. The timely adjustments should be made based on the rock conditions to improve the blasting efficiency and reduce the blasting cost [4]. Yixian Wang and his colleagues generated shape-changing energy indices of the rock in coal mines by setting up the formula of the blasting crater parameters based on the theoretical analysis according to the energy balance rule of the Livingstone Blasting Crater. The deformation energy coefficient of hard coal, mid-hard coal, and soft coal was found to be $2/62 \text{ m/kg}^{1/3}$, $3.05 \text{ m/kg}^{1/3}$, and 3.49 m/kg^{1/3}, respectively [5]. Jin Xu-hao illustrated the important status and function of the blasting crater in the study of the rock blasting mechanism. He noted that the use of the research methods of using fracture mechanics and damage mechanics to establish a blasting failure model and the use of numerical models to calculate and analyze the formation of blasting craters will further deepen the analysis of the mechanism of blasting craters [6]. The second type is the numerical simulation of the blasting crater formation process. Zheming Zhu established the blasting crater value model and analyzed the crushing impact of the stress on both the blasting crater and bench blasting; the study mainly focused on the stress wave loading on rock blasting that had a very important effect on the control and predictions of fragmentation of rock in actual blasting [7]. Mr. P. Yan imitated the dynamic crushing process using a 3DEC model. An equivalent blasting load considering the detonation gas pressure was adopted. The results of the study showed that the muck-pile profile of bench blasting is more sensitive to the burden distance [8]. The third type is the analysis of the rock dynamic fracture process. Y. Zhang studied the dynamic characteristics of thin-layered sandy frozen soil in blasting and discovered that, regardless of the stage of the explosive, there appears a critical point of the changes from tension to compression along the direction from the explosive center to the surroundings within a radius of approximately 0.9

m [9]. SH Cho and K. Kanekoanalied studied the influence of the applied pressure waveform on the dynamic fracture processes in rock. The study results showed that the fracture processes are affected more by the rise time increases than by the decay time. A higher stress-loading rate increases the number of radial cracks and leads to intense stress release around running cracks. These fracture processes reveal that crack extension increases with the rise time increase [10].

It could achieve a better blasting effect with the method of parameter optimization [11]. The relationships between the rational crushing resistant line and the optimal blasting resistant line were analyzed by the blasting crater experiments. The tests were conducted with the uniform design method. The formulas for the parameters, rock volume blasted, and the blasting quality were obtained by regression analysis. Taking the comprehensive cost into consideration, the rational blasting parameters were decided to provide guidance to achieve efficient mining.

2. Small Charge-forward Blasting Crater Experiment

2.1. Experimental Methods. The tests aim to explore the blasting crater parameters and seek the reasonable blasting resistant line to improve the blasting quality, reduce the explosive consumption, and increase the explosive usage efficiency. The experiments were conducted on a +24 m bench in an open pit, where the rock was rich in cracks with the hardness of f=12 to 16 and unit weight of 3.4 t/m³. The diameter of the blasting holes was 250 mm, with the explosive charge of 12 kg per blast hole. The depth of the explosive was 1.5 to 3.9 m. To eliminate the interaction between the adjacent holes, the distance between two holes that were in the same row was more than 15 m.

The parameters of crater sizes to be measured are the crater radius, the crater volume, and the crater depth; it is commonly accepted that the first two can well reflect the characteristics of a blasting crater. The crater parameters are shown in Figure 1. The explosive locations distribution is shown in Figure 2. Every direction of the radius was measured, as shown in Figure 3; the crater radius (R) is the average of the crater radius in eight different directions with an interval angle of 45°, the center of which is the blast hole. The bulk yield was determined based on the image analysis method. The crater shape can be obtained by averaging the

No.	Explosive depth L/m	Depth ratio∆ (L/Le)	Crater depth H/m	Crater radius R/m	Crater angle	Crater volume V/m ³	Explosive consumption (kg/m³)	Remarks
1	1.5	0.38	1.7	2.0	99.3°	7.12	1.69	
2	1.8	0.46	2.0	2.2	95.4°	10.14	1.19	
3	2.1	0.54	2.4	2.4	90.1°	14.46	0.83	Optimal explosive depth Lj
4	2.5	0.64	2.2	2.0	84.5°	9.22	1.32	
5	2.9	0.75	1.9	1.6	80.2°	5.09	2.38	
6	3.3	0.84	1.3	1.1	75.1°	1.36	9.09	
7	3.9	1.00						Max. explosive depth Le

TABLE 1: Field experiment results.

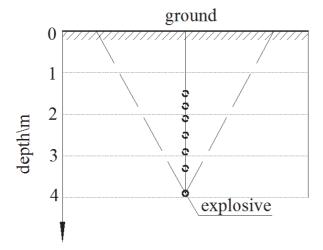


FIGURE 2: Distribution of the locations of the explosives.

heights. The volume of the rock blasted was measured by the Parabolic Method (i.e., the Simpson Method).

2.2. Experiment Results. The explosive depths were chosen from 1.5 m to 3.9 m. Table 1 shows the results of the experiment.

The relationship between the characteristics of the crater V/Q (the crater volume blasted by unit explosive charge) and the depth ratio \triangle is shown in Figure 4. The relationship curve between the unit explosive consumption Q/V and the depth ratio is presented in Figure 5.

The maximum explosive charge depth was 3.9 m. With increasing depth ratio, the crater volume blasted by unit explosive V/Q demonstrated a trend of first increasing and then decreasing. When the explosive depth was at the optimal value of 2.1 m, the value of V/Q reached the maximum of $1.21 \, \mathrm{m}^3/\mathrm{kg}$, with the crater volume blasted of $14.46 \, \mathrm{m}^3$. With increasing depth ratio \triangle , the unit explosive consumption showed a trend of first decreasing and then increasing. V/Q reached the minimum of $0.83 \, \mathrm{kg/m}^3$ when the optimal explosive charge depth was $2.1 \, \mathrm{m}$. The bulk yield reached the maximum of 0.82% at the explosive depth of $2.1 \, \mathrm{m}$ (or

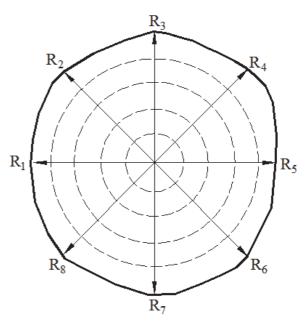


FIGURE 3: Measurement of the crater radius.

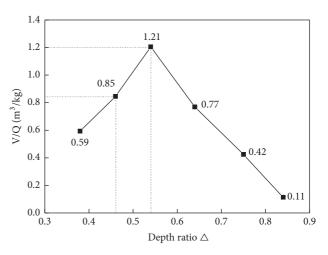


FIGURE 4: Curve of V/Q versus the depth ratio.

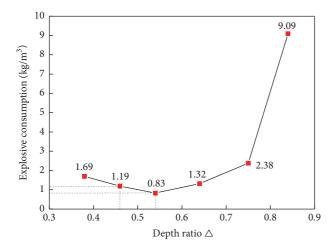


FIGURE 5: Curve of the consumption of explosives versus the depth ratio.

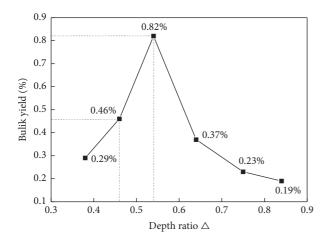


FIGURE 6: Curve of the bulk yield versus the depth of the explosives.

at the optimal resistant line), as shown in Figure 6. When the explosive depth was 1.8 m, with the depth ratio 0.46, the unit consumption of explosives reached 1.19 kg/m³, but the crater volume blasted was high at 10.14 m³. Compared with the depth of 2.1 m, the bulk yield at a depth of 1.8 m reduced to 0.46%, with the reduction rate of 43.9%. This result illustrated that reducing the explosive depth or decreasing the resistance line properly to 1.8 m could still achieve a better blast quality. Here, the ratio of 1.8-m/2.1-m is 0.86.

Obviously, the volume of rock blasted and the blast quality are interassociated and mutually conflicting; thus, it is necessary to balance the relationship between them, as mentioned above. From the perspective of the explosive usage efficiency, the explosive energy implied on the rock crushing is a maximum when the crater volume blasted is the maximum with the minimum unit explosive consumption. From the perspective of the mining operation, the blasting quality directly affects the efficiency of the loading, transportation, and crushing, which requires that the bulk yield should be controlled and the rational resistant line must be found.

In summary, the depth ratio must be modestly reduced; i.e., the resistant line should be decreased to guarantee the reasonable resistant line and thus modify the blasting quality in the mining operation. In other words, the optimal blasting quality should be obtained with the premise of achieving a relatively high volume of rock blasted. Based on the analysis above, the reasonable resistant line or the explosive charge depth should be 0.86 times the optimal resistant line, from which the advantage of the reduced resistant line can be enjoyed.

3. Theoretical Analysis

3.1. Wave Interference Theory. Research studies have shown that when a few waves propagate in a medium at the same time, whether they meet each other or not, they maintain the original characteristics, including frequency, wavelength, amplitude, and vibration direction. Moreover, they are not affected by other waves. The vibration of any particle in the meeting area is the synthesis of the vibration caused by each wave at this point. This rule is called the wave superposition principle or the independent propagation principle of the wave, as shown in Figure 7.

When two waves of the same frequency are superimposed, the vibrations in some areas are strengthened, the vibrations in some areas are weakened, and the vibrationenhanced area and the vibration-reduced area are separated from each other. This phenomenon is called wave interference [12–14]. When both wave peaks and (or) both wave troughs of the two waves meet, the vibration is strengthened and the vibrations at the peaks and troughs are reduced. If the distance between a certain point to the two wave sources is an integral multiple of the wavelength, then the vibration of the point is strengthened; if the difference is an odd multiple of the half wavelength, then the vibration is weakened (see Figure 8).

Assuming the two wave sources are both simple harmonic vibration, they can be described as follows:

$$y_1 = A_1 \cos(\omega t + \varphi_1) \tag{1}$$

$$y_2 = A_2 \cos(\omega t + \varphi_2) \tag{2}$$

where A1, A2 are amplitude, ω is angular frequency, and φ_1 , φ_2 are initial phase.

If the one wave travels along r_1 and the other travels along r_2 , meeting at a point P in the same medium (see Figure 9), then the partial vibrations caused by these two waves at point P are

$$y_1 = A_1 \cos\left(\omega t + \varphi_1 - \frac{2\pi r_1}{\lambda}\right) \tag{3}$$

$$y_2 = A_2 \cos\left(\omega t + \varphi_2 - \frac{2\pi r_2}{\lambda}\right) \tag{4}$$

According to the principle of wave superposition, the combined vibration at point P is the synthesis of these

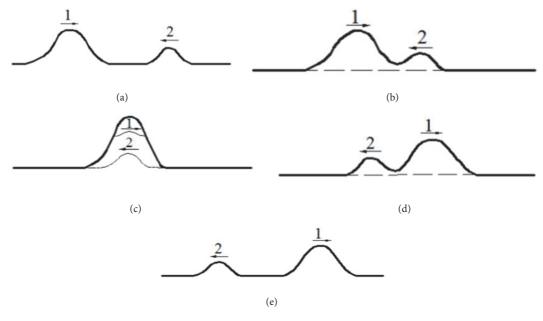


FIGURE 7: Wave superposition principle.

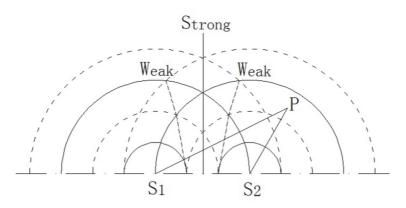


FIGURE 8: Wave interference.

two partial vibrations. The combined vibration equation is expressed as

$$y = y_1 + y_2$$

$$= A_1 \cos \left(\omega t + \phi_1 - \frac{2\pi r_1}{\lambda}\right)$$

$$+ A_2 \cos \left(\omega t + \phi_2 - \frac{2\pi r_2}{\lambda}\right)$$
(5)

where λ is wavelength.

The combined vibration is still simple harmonic vibration given by

$$y = A\cos(\omega t + \phi) \tag{6}$$

where A is amplitude of the combined vibration and ϕ is initial phase of the combined vibration.

Thus, we have

$$A = \sqrt{A_1^2 + A_2^2 + 2A_1A_2\cos\left(\phi_2 - \phi_1 - 2\pi\frac{r_2 - r_1}{\lambda}\right)}$$
 (7)

φ

$$=\arctan\frac{A_{1}\sin(\phi_{1}-2\pi r_{1}/\lambda)+A_{2}\sin(\phi_{2}-2\pi r_{2}/\lambda)}{A_{1}\cos(\phi_{1}-2\pi r_{1}/\lambda)+A_{2}\cos(\phi_{2}-2\pi r_{2}/\lambda)}$$
(8)

If $\phi_1 = \phi_2$, then set $\Delta s = r_2 - r_1$ to express the wavelength difference arriving at point *P* from the two wave sources.

When $\Delta s = r_2 - r_1 = k\lambda$, $k = 0, \pm 1, \pm 2...$, A reaches the maximum value, $A = A_1 + A_2$.

When $\Delta s = r_2 - r_1 = (2k + 1)(\lambda/2), k = 0, \pm 1, \pm 2..., A$ reaches the minimum value, $A = |A_1 - A_2|$.

3.2. Mechanism of the Large Spacing of Holes and Small Resistant Line. The blasting technology of large hole spacing *a* and small resistant line width *W* is to enhance the distance

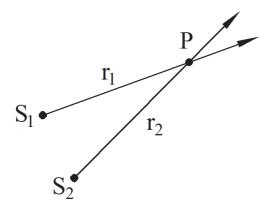


FIGURE 9: Two waves meet at point P.

between two blasting holes that are within the same row and to reduce the distance between two rows under the premise of keeping the square blasted by each hole constant or slightly increased to increase the coefficient of a/W. As shown in Figure 10, with the decrease of resistant line W and increase of hole spacing a, the two separated blasting craters will be connected.

It has been proved that this technology is effective in improving the blasting effect, reducing the unit consumption of explosives, increasing the amount of detonation, and reducing the blasting cost, as has been well recognized by experts both at home and abroad.

The blasting mechanism is as follows.

- (1) The reduction of the resistant line and widening of the blasting crater angle with the blasting impact index of n>1 lead to the generation of an arc surface, which creates a favorable crushing condition.
- (2) The enhanced hole spacing eliminates the stress wave interaction between adjacent holes and avoids the early emission of the blasting gas, thereby prolonging the blasting impact duration and improving the usage of the blasting energy.
- (3) The increase of hole spacing makes the stress reduction area caused by the interaction between the peak and trough of the blasting holes' radiant wave move out of the blasting impact area. This approach accomplishes the following: makes full use of the role of explosion stress, increases the uniformity of the block, reduces the bulk rate, and improves the blasting crushing quality.

4. On-Site Lateral Blasting Crater Experiment

4.1. Uniform Design Method. Uniform design is also called Uniform Design Experimentation. Uniform design was jointly proposed by Professors Fang Kaitai and Wang Yuan of the Applied Mathematics Institute of the Chinese Academy of Sciences in 1978. Uniform design is an application of the "pseudo-Monte Carlo method" in number theory.

Uniform design is implemented through a set of well-designed tables and only considers the test points evenly distributed within the test range. The experimental points

Table 2: Evenly designed $U_5(5^2)$ experiment schedule.

No.	Holes spacing/m	Resistant line/m
1	6	5.5
2	7	6.5
3	8	5
4	9	6
5	10	7

are well balanced and dispersed within the scope of the test, but they still reflect the main characteristics of the system. Uniform design can greatly reduce the number of experiments and can achieve the test results by performing at least one test of orthogonal design.

Because the test results do not have the orderly comparability of the orthogonal test results, the regression analysis method is used for the processing of the test results. Using the model derived from regression analysis, the importance of influencing factors can be analyzed. Moreover, the new conditional tests can be estimated, predicted, and optimized. At present, this method has gained international recognition and has been widely used in fields such as aerospace, chemical engineering, pharmaceuticals, materials, automobiles, and the environment at home and abroad [15–20].

4.2. Experiment Method. To ensure the high volume of rock blasted with favorable blasting quality, the density of blasting holes must be considered to obtain the optimal combination of hole spacing and the resistant line. The experiments were conducted in the Heshangqiao open pit of Nanshan Mining Company, where the rock hardness is f=8 to 12 and the rock has good integrity. The diameter of the holes was 200 mm, with the depth of 12.5 m and explosive charge of 180 kg per hole. The rock emulsion explosives used were produced by Maanshan Jiangnan Chemical Co., Ltd. The explosive diameter was 170 mm, with a density of 1.10 g/cm³ ~ 1.35 g/cm³. The detonation speed was ≥3200 m/s.

To reduce the number of experiments performed and reduce the effect on mine production, the uniform design method was implemented. Two holes were initiated simultaneously in each experiment. The program of two factors and five levels was chosen. The two factors were the hole spacing and the resistant line width. The hole spacing was from 6 m to 10 m, and the resistant line width was from 5 m to 7 m. A total of five tests were conducted. Based on the application table of uniform design, the $\rm U_5(5^2)$ test schedule was produced, as shown in Table 2. The blast hole layout is presented in Figure 11.

A picture of the field experiment is shown in Figure 12, and the blasting crushing effect is shown in Figure 13.

4.3. Analysis of the Experimental Results. The experimental results are presented in Table 3. The measurement method of the crater parameters was the same as that of the small chargeforward blasting crater experiments.

The choice of regression equation has an important influence on the research results. Through comparative analysis

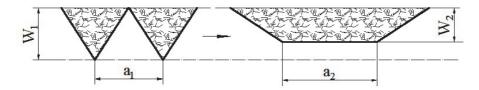


Figure 10: Mechanism of the large hole spacing with a small resistant line $(a_2 > a_1; W_2 < W_1)$.

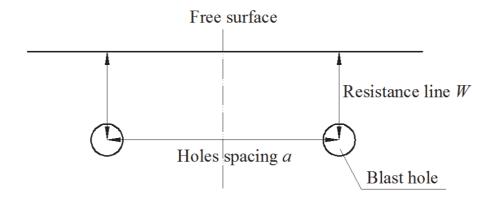


FIGURE 11: Blast hole layout.



Figure 12: Picture of the field experiment.



FIGURE 13: Blasting effect.

of each built-in equation, the equation with the highest coefficient of determination, R^2 , is chosen as the objective equation of this paper under the condition that the regression equation is significant.

(1) The regression equation to be established was

$$y = b(0) + b(1) * x(1) \wedge 2 + b(2) * x(2) \wedge 2$$
 (9)

Through the multiple factors regression analysis of the experiment results, regression coefficients b(i) were

$$b(0) = -43.6;$$

 $b(1) = 2.34;$ (10)
 $b(2) = 9.51.$

Thus, the regression equation for the rock volume blasted was obtained.

$$y = -43.6 + 2.34x_1^2 + 9.51x_2^2$$
 (11)

where *y* is rock volume blasted, m^3 ; x_1 is hole spacing, m; and x_2 is resistant line, m.

The regression analysis coefficients are shown in Table 4 and Figure 14.

The regression formula produced the following significant results: sample N=5, significance level α =0.05; test value F_t=82.87; critical value F(0.05,2,2)=19.00; and F_t >F(0.05,2,2). The regression equation was significant.

Sorted by the partial regression quadratic sum, the contributions of the resistant line and the hole spacing were 32.4%

No.	Holes spacing <i>a</i> /m	Resistant line <i>W</i> /m	Rock volume blasted Q/m ³	Crater angle	Explosive consumption (kg/m³)	Bulk Yield/%
1	6	5.5	338.3	98°	0.532	0.21
2	7	6.5	463.6	106°	0.390	0.33
3	8	5	350.4	104°	0.519	0.18
4	9	6	467.1	113°	0.392	0.25
5	10	7	670.0	115°	0.275	0.42

TABLE 3: Experiment results.

TABLE 4: Regression analysis coefficient.

Name	1	2
Regression coefficient b(i)	b(1)=2.34	b(2)=9.51
Standard regression coefficient B(i)	B(1)=0.444	B(2)=0.678
Partial regression square sum U(i)	$U(1)=9.79e^{+3}$	$U(2)=2.28e^{+4}$
Partial correlation coefficient $\rho(i)$	$\rho(1,2)=0.9593$	$\rho(2,1)=0.9819$
Multiple correlation coefficient	R=0.9940	$R^2 = 0.9881$
Regression square sum:	$U=7.03e^{+4}$	

TABLE 5: Regression analysis coefficient.

Name	1	2
Regression coefficient b(i)	$b(1)=2.29e^{-4}$	$b(2)=9.75e^{-3}$
Standard regression coefficient B(i)	$B(1)=5.98e^{-2}$	B(2)=0.952
Partial regression square sum U(i)	$U(1)=9.44e^{-5}$	$U(2)=2.39e^{-2}$
Partial correlation coefficient $\rho(i)$	$\rho(1,2)=0.2847$	$\rho(2,1)=0.9783$
Multiple correlation coefficient	R=0.9858	$R^2 = 0.9717$
Regression square sum:	$U=3.68e^{-2}$	

(U(2)/U) and 13.9% (U(1)/U), respectively. The resistant line's contribution was larger than that of hole spacing, demonstrating that the resistant line had a greater impact on the volume of rock blasted.

(2) Based on the regression analysis of multiple factors, the regression equation to be established was

$$y = b(0) + b(1) * x(1) \wedge 2 + b(2) * x(2) \wedge 2$$
 (12)

The regression coefficient b(i) was

b (0) =
$$-9.30e^{-2}$$
;
b (1) = $2.29e^{-4}$; (13)
b (2) = $9.75e^{-3}$.

The bulk yield formula was the following:

$$y = -9.3 \times 10^{-2} + 2.29 \times 10^{-4} x_1^2 + 9.75 \times 10^{-3} x_2^2$$
 (14)

where *y* is rock volume blasted, m^3 ; x_1 is hole spacing, m; x_2 is resistant line, m.

The regression analysis coefficients are shown in Table 5 and Figure 15.

The regression formula produced the following significant results: sample content N=5; significance level α =0.05;

test value F_t =34.39; critical value F(0.05,2,2)=19.00; and $F_t > F(0.05,2,2)$. This result showed that the regression formula is significant.

The contributions of the resistant line and the hole spacing (sorted by the partial regression quadratic sum) were 65.0% and 0.256%, respectively. The resistant line's contribution was greater than that of the hole spacing, demonstrating that the resistant line had a greater impact on the bulk yield. The reduction of the resistant line and increase of the hole spacing are beneficial to controlling the bulk yield.

Considering that the resistant line has a greater impact on the volume of rock blasted and the bulk yield than the hole spacing, reasonably reducing the resistant line and increasing the hole spacing at the same time can obtain favorable blasting quality with a high volume of rock blasted. Thus, the technology of large hole spacing and a small resistant line is reasonable and practical.

4.4. Determination of the Blasting Parameters. The objective function of total mining cost is

$$C = C_1 + C_2 + C_3 + C_4 + C_5 \tag{15}$$

where C_1 is drilling cost, C_2 is blast cost, C_3 is shovel and loading, C_4 is transport cost, and C_5 is crushing cost.

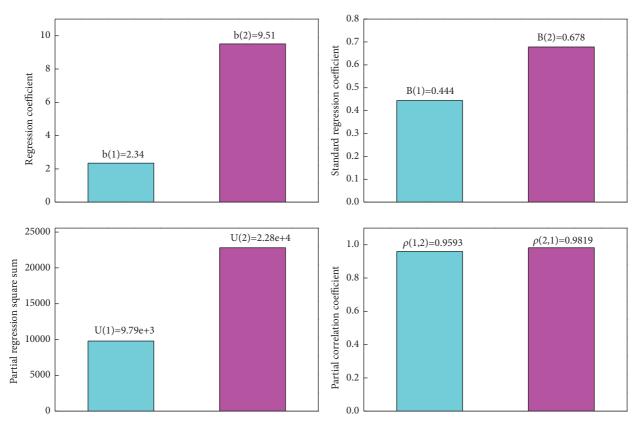


FIGURE 14: Regression analysis coefficient of equation (11).

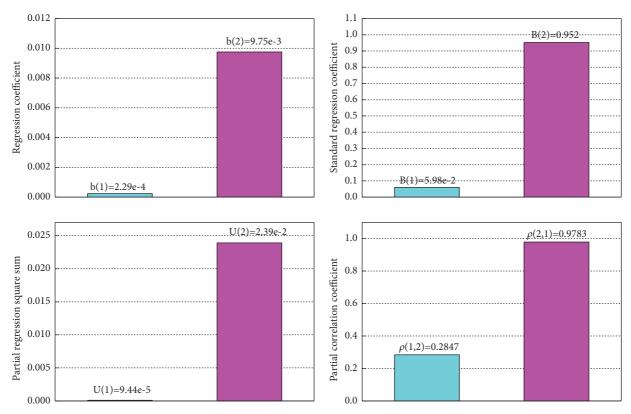


FIGURE 15: Regression analysis coefficient of equation (14).

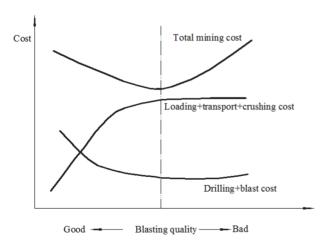


FIGURE 16: Blasting quality and mining cost.

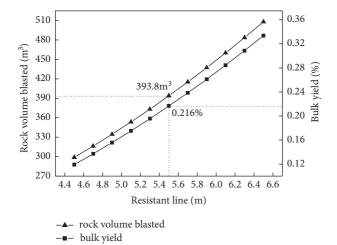


FIGURE 17: Curves of the resistance line, blasting volume, and bulk yield (hole spacing a=8 m).

The blasting effect not only reflects the accuracy and rationality of the blasting design parameters and the blasting methods but also directly affects the subsequent processes, such as shoveling and loading, transportation and crushing, and the total mining cost.

In general, the costs of drilling and blasting increase with the decrease of blasting quality, and the operating costs of subsequent processes decrease with the improvement of blasting quality. In theory, there is an "optimum blasting effect" that makes the total mining cost the lowest (see Figure 16). On the basis of blasting parameter optimization, the purpose of controlling the comprehensive mining cost can be achieved.

By comparing Figures 17 and 18, under similar hole spacing conditions and with the increase of the resistance line, the amounts of blasting volume and bulk yield both increase. To obtain a larger volume of rock blasted, it is appropriate to increase the resistance line. However, to achieve a better blasting effect and reduce the bulk yield, the resistance line should be reduced properly.

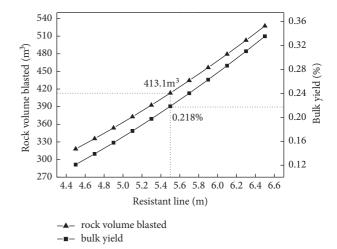


FIGURE 18: Curves of the resistance line, blasting volume, and bulk yield (hole spacing a=8.5 m).

Moreover, if the resistance line is too large, it is difficult to blast the rock, making it not conducive to the formation of a good free surface. Therefore, under the premise of ensuring a higher blasting volume, while the blasting effect is improved, the blasting method of large hole spacing and a small resistance line is suitable.

According to many years of production practice of the Heshangqiao iron mine, comprehensively taking the efficiency of loading/crushing and the total mining cost into consideration, the reasonable and economical blasting parameters are as follows: the hole spacing a=8.5 m and resistant line (distance between rows) W=5.5 m, with the ratio a/W=1.55.

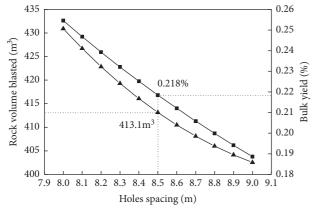
Figures 17 and 18 show that, under the condition that the bulk rate remains basically unchanged, when the resistance line is 5.5 m, the rock volume blasted of a=8.5 m can be increased from 393.8 m 3 of a=8 m to 413.1 m 3 , representing a 4.9% increase, thus better illustrating the superiority of the determined blasting parameters.

4.5. Blasting Quality under the Same Blast Area. Figure 19 further verifies the relationships among hole spacing, the volume of rock blasted and bulk yield, in the case of equal blasting area $a \times W = 46.75 \text{ m}^2$ (8.5 m \times 5.5 m). In the same blasting area of 46.75 m^2 , with the increase of hole spacing, the resistance line decreases correspondingly. Moreover, the rock volume blasted and bulk yield simultaneously shows a decreasing trend. The negative correlation between blasting volume and bulk yield can be obtained. Thus, it is necessary to comprehensively balance the two relationships above to make the best economic benefits for mining production.

4.6. Blasting Quality Comparison with Perfectly Square Patterns. The blasting quality and volume of six perfectly square patterns were compared, as shown in Table 6 and Figure 20. Here, the hole spacing was equal to the resistance line, a=W. As the hole spacing and the resistance line increase, the blasting volume and the bulk yield increase synchronously.

Number	Holes spacing/m	Resistance line/m	Blasting area/m ²	Rock volume blasted/m ³	Bulk yield/%
1	4	4	16	146.0	0.067
2	5	5	25	252.7	0.156
3	6	6	36	383.0	0.266
4	6.837	6.837	46.75	510.3	0.373
5	7	7	49	537.1	0.396
6	8	8	64	714.8	0.546

TABLE 6: The blasting quality of six perfectly square patterns.



- _▲ rock volume blasted
- −∎− bulk yield

FIGURE 19: Curve of the same blasting area of 46.75 m².

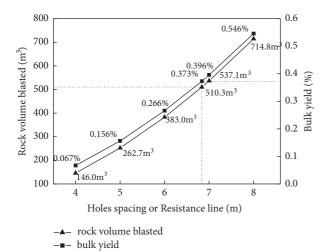


FIGURE 20: The blasting quality of square patterns.

For the perfect square $a \times W = 6.837 \text{ m} \times 6.837 \text{ m}$ (area of 46.75 m²), the blasting rock volume is 510.3 m³, but the bulk rate reaches 0.373%, which is 71.1% higher than 0.218% of $a \times W = 8.5 \text{ m} \times 5.5 \text{ m}$, which corresponds to a worse blasting quality.

It can be seen that blasting quality of a rectangle is better than that of the square pattern. The rectangle of $a\times W$ =8.5 m \times 5.5 m had a better blast quality with a large rock volume

blasted. The advantages of large hole spacing with a small resistance line were proved.

5. Conclusions

- (1) The volume of rock blasted and the blast quality are interassociated and mutually conflicting. To ensure good blasting quality and reduce the bulk yield, the charge depth or the resistant line should be reasonably reduced. This rational resistant line should be 0.86 times the reasonable resistant line (or the optimal charge depth).
- (2) Uniform design was found to be an effective method for designing the program of blasting crater experiments that can reduce the number of tests, decrease the workload of blasting parameters optimization, and reduce the labor intensity. R^2 of the regression equations for the volume of rock blasted and the bulk yield were 0.9881 and 0.9717, respectively. The two regression equations are reliable.
- (3) The contribution rates of the resistance lines and the spacing of the holes to the blasting volume regression were 32.4% and 13.9%, respectively, and to the bulk yield regression were 65.0% and 0.256%, respectively. The effect of the resistance line on the volume of rock blasted and bulk rate is more significant than that of hole spacing. The amount of blasting is negatively related to the bulk yield.
- (4) The blasting technology of large hole spacing and a small resistance line can reduce the bulk yield and improve blasting quality under the condition of ensuring a high blasting volume. The blasting effect of the rectangular blast hole arrangement is better than that of the square pattern. The economically reasonable blasting parameters are defined as a hole spacing of 8.5 m and a resistance line width of 5.5 m, with a blasting volume of 413.1 m³ and bulk yield of 0.218%. The bulk rate of a perfect square of $a \times W = 6.843$ m $\times 6.837$ m (46.75 m²) in the same blasting area reached up to 0.373%, which was 71.1% higher than that of an 8.5 m $\times 5.5$ m rectangle.

Data Availability

The data used to support the findings of this study are available from the corresponding author upon request.

Conflicts of Interest

The authors declare no conflicts of interest in preparing this article.

Acknowledgments

This work was supported by the National Key R&D Program of China (no. 2017YFC0602902), the National Natural Science Foundation of China (no. 51674229 and no. 51374189), and the Fundamental Research Funds for the Central Universities (no. WK2480000002). The authors acknowledge their financial support of this work.

References

- [1] W. Xu-guang, *Blasting Manual*, Metallurgical Industry Press, Beijing, China, 2010.
- [2] W. L. Fourney, R. D. Dick, X. J. Wang, and Y. Wei, "Fragmentation mechanism in crater blasting," in *Proceedings of the International Journal of Rock Mechanics and Mining Sciences Geomechanics Abstracts*, vol. 30, pp. 413–429, 1993.
- [3] W. L. Fourney, R. D. Dick, and K. R. Y. Simha, "Model study of crater blasting," *Rock Mechanics and Rock Engineering*, vol. 21, no. 3, pp. 183–205, 1988.
- [4] Z. LIU, Z. Chuan-qu, X. Dong-hai, C. Cai-xian, and H. Lei, "Optimized design and practice of blasting parameters for hard rock roadway with small cross-section," *Journal of Mining & Safety Engineering*, vol. 24, no. 1, pp. 70–73, 2007 (Chinese).
- [5] W. Yi-xian, Y. Yong-qiang, Y. Xiao-lin, and C. Huaibao, "Study on blasting parameters of coal based on blasting crater test," *Blasting*, vol. 27, no. 1, pp. 1–4, 2010 (Chinese).
- [6] Y. Zhang and F. Xie, "Theoretical and test study on dynamicu characteristics of thin-layered sandy frozen soil in blasting," *Journal of Computers*, vol. 6, no. 6, pp. 1131–1138, 2011.
- [7] Z. Zhe-ming, "Numerical prediction of crater blasting and bench blastisng," *International Journal of Rock Mechanics & Mining Sciences*, vol. 46, no. 6, pp. 1088–1096, 2009.
- [8] P. Yan, W. Zhou, W. Lu, M. Chen, and C. Zhou, "Simulation of bench blasting considering fragmentation size distribution," *International Journal of Impact Engineering*, vol. 90, pp. 132–145, 2016
- [9] S. H. Cho and K. Kaneko, "Influence of the applied pressure waveform on the dynamic fracture processes in rock," *Interna*tional Journal of Rock Mechanics and Mining Sciences, vol. 41, no. 5, pp. 771–784, 2004.
- [10] X. H. Jin, "Discussion on blasting crater theory," *Rock & Soil Mechanics*, vol. 33, pp. 205–208, 2002 (Chinese).
- [11] W. Ming-zheng, S. Xiu-zhi, Z. Jian, and Q. Xian-yang, "Multiplanar detection optimization algorithm for the interval charging structure of large-diameter longhole blasting design based on rock fragmentation aspects," *Engineering Optimization*, vol. 5, pp. 1–15, 2018.
- [12] M. Yamamoto, H. Noda, and K. Kaneko, "Experimental study on blast vibration control method, which is based upon wave interference," Smart Structures & Systems, vol. 59, no. 1, pp. 119– 137, 1998.
- [13] S. K. Mandal, "Mathematical model to locate interference of blast waves from multi-hole blasting rounds," *Engineering*, vol. 4, no. 3, pp. 146–154, 2012.
- [14] D. Baratoux and H. J. Melosh, "The formation of shatter cones by shock wave interference during impacting," *Earth and Planetary Science Letters*, vol. 216, no. 1-2, pp. 43–54, 2003.
- [15] F. Kai-Tai, K. J. L. Dennis, P. Winker, and Y. Zhang, "Uniform design: theory and application," *Technometrics*, vol. 42, no. 3, pp. 237–248, 2000.

[16] Y.-Z. Liang, F. Kai-Tai, and Q.-S. Xu, "Uniform design and its applications in chemistry and chemical engineering," *Chemo*metrics Intelligent Laboratory Systems, vol. 58, no. 1, pp. 43–57, 2001.

- [17] F. Kai-Tai, "The uniform design: Application of number-theoretic methods in experimental design," Acta Mathematicae Applicatae Sinica, vol. 3, no. 4, p. 9, 1980.
- [18] C.-M. Huang, Y.-J. Lee, D. K. J. Lin, and S-Y. Huang, "Model selection for support vector machines via uniform design," *Computational Statistics & Data Analysis*, vol. 52, no. 1, pp. 335– 346, 2007.
- [19] J.-P. Wang, Y.-Z. Chen, Y. Wang, S.-J. Yuan, and H.-Q. Yu, "Optimization of the coagulation-flocculation process for pulp mill wastewater treatment using a combination of uniform design and response surface methodology," *Water Research*, vol. 45, no. 17, pp. 5633–5640, 2011.
- [20] Y. Kuo, T. Yang, B. A. Peters, and I. Chang, "Simulation metamodel development using uniform design and neural networks for automated material handling systems in semiconductor wafer fabrication," Simulation Modelling Practice and Theory, vol. 15, no. 8, pp. 1002–1015, 2007.

Hindawi Shock and Vibration Volume 2018, Article ID 5643872, 14 pages https://doi.org/10.1155/2018/5643872

Research Article

Quasi-Static Cyclic Test on a Concrete-Encased Frame-Reinforced Concrete Tube Building Model

Lei Zeng , Yunfeng Xiao, Juan Chen, and Yiguang Chen

¹School of Urban Construction, Yangtze University, Jingzhou 434023, China ²School of Civil Engineering and Mechanics, Huazhong University of Science and Technology, Wuhan 430074, China

Correspondence should be addressed to Lei Zeng; zenglei@yangtzeu.edu.cn

Received 7 February 2018; Revised 7 May 2018; Accepted 22 May 2018; Published 13 June 2018

Academic Editor: Mohammad A. Hariri-Ardebili

Copyright © 2018 Lei Zeng et al. This is an open access article distributed under the Creative Commons Attribution License, which permits unrestricted use, distribution, and reproduction in any medium, provided the original work is properly cited.

This paper experimentally investigated the seismic behavior of a 1:5 reduced-scale model of concrete-encased steel frame-reinforced concrete core tube building. The quasi-static testing with multipoint loading was carried out, and mode-superposition response spectrum method was adopted to control the amplitude of displacement. The damage process, crack pattern, and failure mode were observed. Various parameters were obtained, including lateral deformation, hysteretic characteristics, strain distribution, ductility, and energy dissipation capacity. The test revealed the distributions of base shear between the core tube and frame. The result indicated that the core tube bears major loading and exhibited overturning failure, afterwards frame carry the surplus load and exhibited column tensile failure and joint panel shear failure. The characteristic of two seismic resistant systems are reflected by the excellent cooperation of core tube and frame.

1. Introduction

Concrete-encased steel frame-reinforced concrete core tube (CS frame-RC core tube) buildings are becoming increasingly popular around the world in high-rise buildings [1-3]. This composite structural system consists of columns located on the periphery of the building and tube located on the center of the building. This arrangement embodies the design concept of two lines to resist shear force [4, 5]. The first line of defense is RC core tube with high lateral stiffness; it will bear most of the shear force caused by the horizontal earthquake. The second is CS frame, which mainly undertakes the vertical load and partial overturning moment caused by horizontal load. Meanwhile, when the stiffness and resistance of core tube degenerate under a strong earthquake, the framework will continue to bear the surplus loading. Compared with RC frame structure, the bearing capacity of this composite structural system is obviously improved, and the lateral deformation of the building can be limited to an expected

As a distinctive component in this composite structural system, the CS member has been systematically studied. Li et al. [6] have conducted experiment for limit values of axial

compression ratio for CS column. Chen et al. [7] explores an analytical model to predict the compressive bearing capacity. The core concrete is enhanced by the steel, which results in the higher bearing capacity. Meanwhile, the steel skeleton can improve the ductility [8, 9]. Thus, CS member is suitable for the frame of composite structural system. CS frame is proved to have the advantages of reducing cross-section area and excellent global stability [10]. In particular, the exterior joints with unsymmetrical section (T- and L-shaped steel section) can satisfy the nonuniform force state and save space [11, 12]. The failure mechanism of the frame is the beam-hinged mechanism, which satisfies the seismic design principle of strong column and weak beam. The ductility and energy dissipation capacity of CS frame are much better than RC frame [13]. The reinforced concrete core tube provides high initial stiffness and bears major shear. The deformation would be strictly controlled, and lateral instability is effectively prevented [14]. The CS frame-RC core tube buildings benefit from the two components with individual characteristics [15].

There are only a limited number of researches about experiment on the composite structural system. Several shaking table tests were carried out and seismic performance was analyzed [16–18]. The results showed that the whole specimen

generally exhibited bending failure. The damage mainly occurred at the bottom of core tube and joint. The lateral displacement was still under the safety limits regulated by Chinese Code. As an alternative, numerical simulation methods were also proposed. Some macroelement based models were established for seismic analysis of composite high-rise buildings aiming at predicting their global responses under earthquakes [19–22]. Static pushover analysis, dynamic time history analysis, and incremental dynamic analysis (IDA) method were applied to evaluate the nonlinear responses of composite high-rise buildings [23, 24].

However the test models above are designed with small similarity ratio (1/20, 1/35) [16–18], which is restricted by the shaking table capacities. The disparity between the acceleration similarity ratio of earthquake actions and actual similarity ratio for gravity acceleration cannot be ignored [25]. In addition, lateral force caused by earthquake is expected to resist by both frame and core tube through composite action. Because there are remarkable differences in stiffness between frame and core tube [23, 24, 26], the frame columns may fail by shear and crush in resisting strong earthquakes and eventually leads to sudden collapse of whole structure [27, 28]. It is significant to evaluate the seismic performance of this composite structural system through specimen with a larger similarity ratio, which can represent the general behavior of the prototype. Mechanical behavior of the parts (the bottom of core tube and joint of frame) under complicated force state should be carefully analyzed.

In this paper, a 1:5 reduced-scale model of concreteencased steel frame-reinforced concrete core tube building is constructed, and quasi-static testing is conducted to assess the response under axial compression and cyclic horizontal load. The lateral load and corresponding displacement and strain of steel and concrete are measured. The crack pattern and failure mode of each component are observed. The seismic performance is evaluated by the obtained hysteretic curve, ductility, energy dissipation capacity, and stiffness degradation. The function of two seismic resistant systems of this structure is verified.

2. Experimental Program

2.1. Test Model Design. A typical multistory CS frame-RC core tube building prototype was designed in accordance with the Code for Seismic Design of Buildings of China (GB50023-2009). The effects of vertical loads (live- and dead-loads) and lateral loads were provided referring to the Technical Specification for Concrete Structures of Tall Building (JGJ3-2002). The prototype building was designed based on an 8degree seismic fortification intensity zone and a II-type of site classification. The design basic acceleration of ground motion $a_{\rm g}$ was 0.20g, which was with a reference probability of exceedance, 10% in 50 years. The site was classified according to the equivalent shear-wave velocity of soil and the site overlying depth, the design characteristic period of ground motion $T_{\rm g}$ was 0.35s for a II-type of site. It should be noted that the seismic intensity and response spectrum used during the design were those given in the Chinese seismic code.

TABLE 1: Similarity relationship of the model.

Physical quantity	Dimensions	Ratio of similitude
Length	L	$S_{\rm L} = 1/5$
Young's modulus	FL^{-2}	$S_{\rm E} = 1$
Mass	$\mathrm{FT}^2\mathrm{L}^{-1}$	$S_{\rm m} = 1/25$
Stress	FL^{-2}	$S_{\sigma} = 1$
Time	T	$S_{\rm T} =$
Poisson ratio	1	$\nu = 1$
Force	F	$S_{\rm F} = 1/25$

The frame is composed of CS columns and steel beams with I cross-section, while the core tube is made of reinforced concrete. Considering the laboratory conditions, a 1:5 reduced-scale model was constructed for the quasi-static tests. The model was 10 stories with square cross-sections, with 20 beams and 12 columns in each story. The total height of the model was 8700 mm. The depth of the foundation, the first story, and the rest of the stories were 500 mm, 1000 mm, and 800 mm, respectively. Two holes were arranged on each story for elevator doors. The details and dimensions of the specimen are shown in Figure 1. It should be mentioned that the selected span is small because of the limitation of laboratory conditions. Compared with typical building, the linear stiffness ratio of beams and floor system increases. The capacity of shear transferring between core tube and frame is enlarged. It may lead to less damage degree of beams and floor system.

Based on the requirements of Architectural Structure Load Standards (GB50009-2001) of China, the live- and deadloads for the test model are 2.0 kN/m² and 1.6 kN/m², respectively. A certain amount of sandbags is stacked on floors to simulate the uniform load. Because it is difficult and dangerous in construction, only the tenth-floor slab is not constructed. But the columns, beams, and core tube are still constructed, and the ninth-floor slab is defined as the top of specimen. The removed dead load is added by the additional sandbags in the ninth floor. The materials used for the test model were identical to those of the prototype structure, thereby indicating that the scaling factor of the elastic modulus was $S_{\rm E}=1$. Table 1 shows the similarity relationships.

 $2.2.\ Test\ Model\ Construction.$ The CS columns had a square cross-section of 100 mm \times 100 mm. Figure 2 shows the configurations and skeleton of the CS columns. The cross-shaped structural steel used in the columns consisted of several hotrolled steel plates. The steel plates were welded to create a cross-shaped steel section. Figure 3 shows the steel beams and configurations of beam-column joints. An I cross-section was adopted in the steel beams. The beams steel plates were welded to the columns steel skeleton.

The composite slab was adopted. The slab system was composed of thin steel plate, concrete, steel bar, and stud connectors. Single-layer mesh reinforcement is used, and 10 mm length stud connectors were welded to the steel plate to strengthen the bond between the steel plate and concrete. A

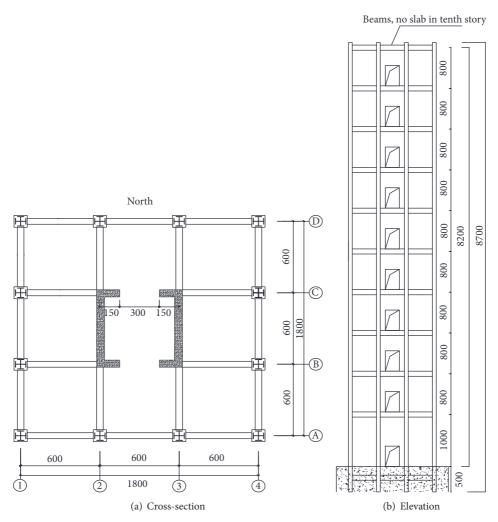


FIGURE 1: Dimensions of specimen (units: mm).

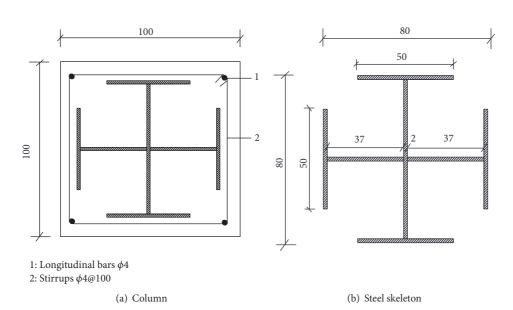


Figure 2: Configurations and skeleton of CS columns (units: mm).

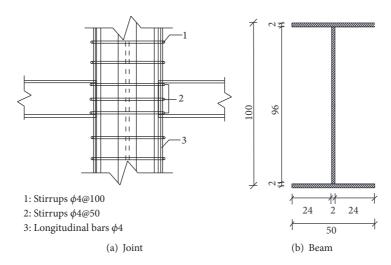


FIGURE 3: Details of joint and beam (units: mm).

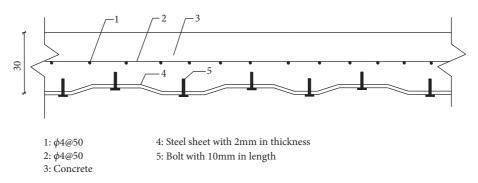


FIGURE 4: Composite slab system (units: mm).

TABLE 2: Materials properties of steel.

Material	Yield Strength	Ultimate Strength	Elastic Modulus
	$f_{\rm v} ({\rm N/mm}^2)$	$f_{\rm u}~({ m N/mm}^2)$	$E_{\rm s} ({\rm N/mm}^2)$
Φ4 bars	305	424	2.1×10^{5}
Φ12 bars	347	451	2.1×10^{5}
Steel plate	327	463	2.0×10^{5}

sectional view and details of the reinforcements are shown in Figure 4.

A square cross-section is used for the core tube, and the dimensions are shown in Figure 5. The thickness is 60 mm for the first two floors and 40 mm for the rest. Double-layer mesh reinforcing is arranged in the tube, including four 12mm diameter bars in the corners. For the actual structure, the cross-section indeed decreases along with the height. As the scale of specimen is reduced by similarity ratio, there is a small difference in dimension. For the convenience of construction, the using cross-section is identical.

2.3. Material Properties. The material properties of the steel plate and reinforcement were tested as shown in Table 2. The spot mixed concrete was used for the CS columns, composite slabs, and core tube. The measured cube compressive strength ($f_{\rm cu}$) before test was 41.5 N/mm².

- 2.4. Test Setup and Loading Histories. The structural vibration induced by earthquakes is contributed by all modal responses. The mode-superposition response spectrum method is an effective and accurate method, which can consider the influence of higher mode shapes [29]. The contribution of each mode shape is different in the total response; thus the participation coefficient η is introduced to describe this proportion. The loading program is detailed as follows.
- (1) Reference [5] has carefully described the program about measuring dynamic characteristics. Several vibration pickup sensors were installed as shown in Figure 6(a). A signal acquisition system with at most six channels was connected to record the data; however it was enough for measuring the mode shapes. The details of vibration pickup sensors and acquisition process are shown in Figure 7.

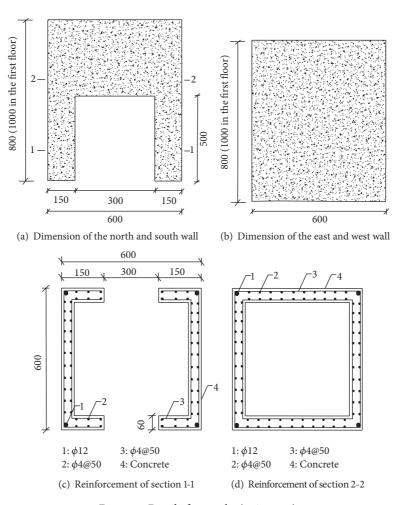
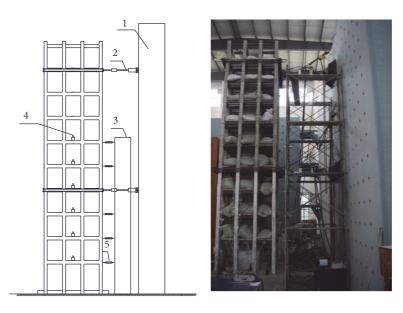


Figure 5: Detail of core tube (units: mm).



- 1: Reaction wall 4: Vibration pickup sensor
- 2: Actuator 5: Displacement meter
- 3: Scaffold
 - (a) Loading and measuring device
- (b) Picture of specimen

Figure 6: The test setup.

TABLE 3: Participation coefficients of mode shapes.

Mode shape	1st-order	2nd-order	3rd-order	4th-order	5th-order
Participation coefficient η_i /%	74.41	14.26	5.50	2.82	1.49





(a) Vibration pickup sensors and DASP system

(b) Measuring process

FIGURE 7: Measurement for dynamic characteristics.

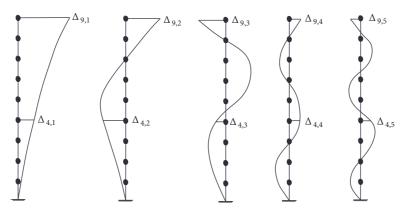


FIGURE 8: The first five mode shapes.

(2) Based on the dynamic characteristics, Data Acquisition and Signal Processing (DASP) program was adopted to carry out the modal analysis (see Figure 7(b)). The higher mode shapes and corresponding participation coefficient η were obtained. According to Code for Seismic Design of Buildings (GB 50011-2010), the number of selected mode shapes is determined by the sum of η , which should be more than 90%. Table 3 shows the η of first five modes; the sum has already satisfied the requirement. The density of used material should be enlarged to five times based on the scale effect. However the steel and concrete material with 5fold density are not available, and the mass missing is not considered. But the required live- and dead-loads are taken into account and calculated by scale factors. This part of mass (including the mass of removed 10th-floor slabs) is applied by sandbags. The missing mass due to scaled material density leads to the decrease of effective floor masses and

total mass. The mode shapes and participation coefficients are influenced.

(3) The reverse cyclic loading applied by multipoint is proved to accurately consider the influence of higher mode shapes [19]. According to existing experimental equipment, two actuators were set up at the 4th- and 9th-floor slabs (see Figure 6). The displacement-controlled method was adopted, and Figure 8 shows the first five mode shapes. The amplitude of displacement is defined by (1) [29] and finally Δ_9/Δ_4 =1.5:1. In the loading program, displacement increment at 9th floor is 8 mm per level, and three cycles are applied at each level as shown in Figure 9. Once the bearing capacity falls to 85% of the ultimate lateral load, or the specimen is unable to continue bearing axial forces, the test is regarded as finished.

$$\frac{\Delta_9}{\Delta_4} = \frac{\sum_{i=1}^N \eta_i \Delta_{9,i}}{\sum_{i=1}^N \eta_i \Delta_{4,i}} \quad i = 1, 2, 3, 4, 5 \tag{1}$$

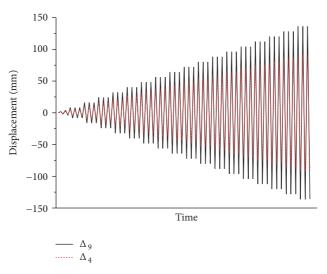


FIGURE 9: The history of loading program.

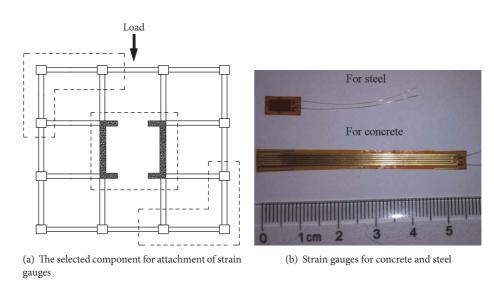


FIGURE 10: The arrangement of strain gauges.

where Δ_9 and Δ_4 are the actual displacement applied on 9th and 4th floor; $\Delta_{9,i}$ and $\Delta_{4,i}$ are lateral displacement of *i*-th mode shape as shown in Figure 8; η_i is participation coefficients of *i*-th mode shapes.

2.5. Instrumentation. The measuring points were defined to capture the overall response of the test model during loading as well as any local effects, such as CS columns and core tube yielding. Displacement sensors were mounted on the slabs of each story at the loading side. Due to the symmetry of cross-section, the components at 1st and 2nd floor in Figure 10(a) were selected for attaching strain gauges as shown in Figure 10(b), and the detail is shown in Figure 11.

3. Experimental Results

3.1. Experimental Phenomena. Figures 12–15 show the development of crack pattern. In the initial stage, the specimen

exhibited elastic state after loading and unloading. As the top displacement reached 16 mm, horizontal cracks primarily occurred at the boundaries along the wall height, and microcracks developed at the bottom of column on the first floor. Then the cracks gradually extended with opening and closing. When the top displacement reached 32 mm, diagonal cracks with 45° angle were observed on the west and east of core tube on the first floor. As the top displacement reached 56 mm, shear cracks appeared in column-beam joints, and local bulge occurred on the profiled steel sheets on 4th, 7th, 8th, and 9th floors. The diagonal cracks on the core tube eventually developed to X-shaped intersecting cracks. Once top displacement reached 88 mm, concrete at wall edges seriously spalled and crushed. The longitudinal reinforcements were exposed, which were accompanied by the buckling and fracture. At present the core tube was regarded as overturning failure, and the frame continued to bear the surplus loading. Horizontal cracks were found on

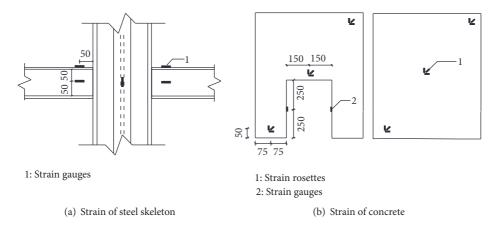


FIGURE 11: Arrangement of strain gauges and rosettes at the first and second floors (units: mm).

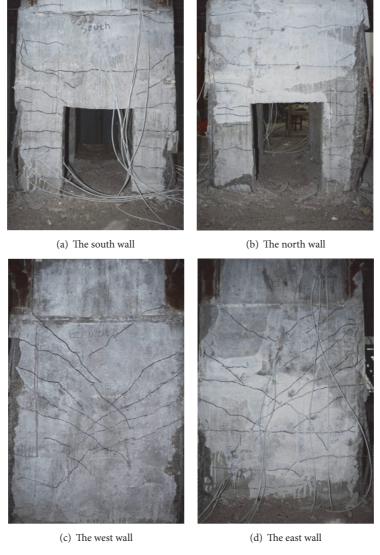


FIGURE 12: Cracks on core tube at the first floor.

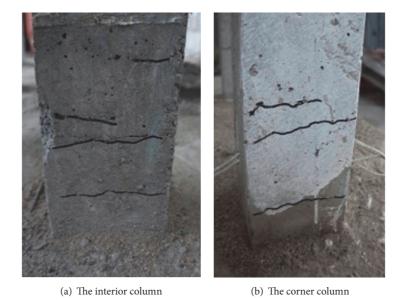


FIGURE 13: Cracks on columns at the first floor.



FIGURE 14: Cracks on joints at the second floor.



FIGURE 15: Cracks on slab at the second floor.

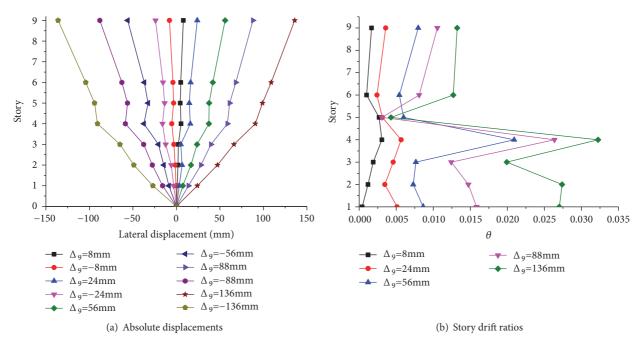


FIGURE 16: Lateral deformation.

the surfaces of the 1st- and 2nd-floor slabs, massive spalling of concrete occurred in the joint, and the steel skeleton was deformed. Once the top displacement reached 136 mm, the load reduced to 85% of the ultimate bearing capacity, the specimen was severely damaged, and experiment was concluded.

Each component of the specimen exhibited various failure modes. The core tube exhibited relatively wide cracks and severe concrete crushing localized at the bottom. There were two types of cracks as shown in Figure 12; one was horizontal tension cracks, which mainly occurred on the north and south of core tube (perpendicular to the loading direction). Under the action of tension and compression, the concrete was seriously crushed, and the width of the cracks was approximately 10 mm (see Figures 12(a) and 12(b)). The other was oblique shear cracks, which mainly occurred on the west and east of core tube (parallel to the loading direction). Cracks gradually extended at 45° angle and eventually formed X-shaped intersecting cracks (see Figures 12(c) and 12(d)).

Compared with the core tube, frame exhibited relatively few cracks as shown in Figures 13 and 14. Horizontal tension cracks occurred at the bottom of the column, with a small amount of concrete spalling. Shear cracks were observed in the joints particularly on the 1st and 2nd floors, which were accompanied by severe concrete crushing. The longitudinal reinforcements and steel skeleton were exposed and bent. As shown in Figure 15, horizontal cracks mainly occurred on the floor slabs. Concrete was crushed at the boundary between floor slabs and the core tube, and the steel plate was compressed and exhibited locally bulging.

In general the core tube characterized by large lateral stiffness had borne major loading and worked as first seismic resistant system. Once it failed by overturning, the frame supported the structure as the second seismic resistant system.

3.2. Deformation and Strains. The lateral displacement of each floor at stages of $\Delta_9 = \pm 8$ mm, ± 24 mm, ± 56 mm, ± 88 mm, and ± 136 mm is shown in Figure 16. Interstory drift ratio θ_i is defined as follows:

$$\theta_i = \frac{(\Delta_i - \Delta_{i-1})}{h_i}$$
 $i = 1, 2, 3, ..., 9$ (2)

where Δ_i is lateral displacement of the *i*-th floor and h_i is the height of *i*th floor.

The absolute displacements and story drift ratios are shown in Figure 16. According to (2) and measured data, the maximum story drift ratio is θ_4 . During the loading process, the damage patterns at 4th floor presented previously. As the lateral displacement increased, the stiffness at 4th floor obviously degenerated, and the damage degree was larger than other floors. According to Technical Specification for Concrete Structures of Tall Building (JGJ3-2002) of China, the limiting value of elastic-plastic interstory ratio for framecore tube structure is 0.01. It is clear that when Δ_9 reached 32 mm, the specimen begins to enter the plastic stage.

The strain of steel skeleton in columns is at range of 1974–3148 $\mu\epsilon$, which gets into the yielding stage. The strain of steel skeleton in beam is generally less than 500 $\mu\epsilon$, and it remains in the elastic stage. The concrete strain is 1284–3539 $\mu\epsilon$, exceeding the ultimate compressive strain of 0.003. In general, under the action of cyclic loading, both of the columns and core tube mainly bear lateral loads.

3.3. Hysteretic Curve. The hysteretic curve of the specimen indicates the relationship between base shear and top displacement. The hysteresis curve shape is between the spindle and the "S" form, as shown in Figure 17. The specimen generally exhibited three stages: yielding, ultimate, and failure stage. In the initial stage of loading, the specimen remains

Top displace	ment /mm	88	96	104	112	120	128
λ_i /%	Positive	1	0.97	0.98	0.98	0.96	0.96
	Negative	1	0.97	0.97	0.97	0.94	0.95

TABLE 4: Degradation of bearing capacity.

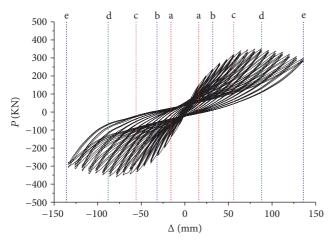


Figure 17: Hysteretic curve.

elastic, the loading and unloading curves are straight, and minor residual deformation occurs. With increasing horizontal displacement, the specimen reaches the elastic-plastic stage, and the area of the hysteresis loops increases. The peak loads of the subsequent two cycles, at one displacement level, gradually decline. When top displacement reaches 32 mm, the hysteresis loop inclines toward the horizontal axis, and obvious stiffness degradation and residual deformation indicate that the specimen attains yielding stage. The specimen reaches the ultimate stage at 88 mm, where the maximum load is 356 kN. The core tube completely fails at this point, the frames have varying levels of damage, and the bearing capacity of the specimen begins to decrease. As the top displacement reaches 136 mm the specimen moves into the failure stage.

The damage process of different components can be described as follows (zones a–e as shown in Figure 17): (a) when Δ_9 was less than 16 mm, no damage occurred and the specimen was intact. Then minor damage occurred on the columns at first floor. (b) When Δ_9 reached 32 mm, the core tube began to get damaged; however the columns did not develop further damage. (c) When Δ_9 reached 56 mm, the core tube seriously got damaged; meanwhile the joints and floor slabs slightly got damaged. (d) When Δ_9 reached 88 mm, the core tube failed and the damage degree of joints and slabs was aggravated. (e) When Δ_9 reached 136 mm, the frame got into failure stage.

According to the Specification of Testing Methods for Earthquake Resistant Building (JGJ101-96) of China, the degradation of bearing capacity can be described by coefficient λ_i in (3), shown in Table 4.

$$\lambda_i = \frac{P_i}{P_{i-1}} \tag{3}$$

where P_i is the peak load at *i*-th displacement level.

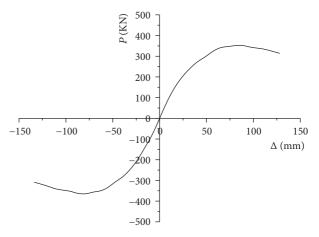


FIGURE 18: Skeleton curve.

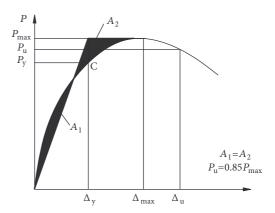


FIGURE 19: Equivalent energy method.

The peak loads of the specimen during the second and third cycles of each displacement level are both lower than the previous ones, and, finally, the bearing capacity degenerates by about 5%.

3.4. Envelope Curve. The skeleton curve of the specimen is symmetrical in both positive and negative directions as shown in Figure 18. In order to confirm the yield and damage points, the equivalent energy method is adopted, as shown in Figure 19. A_1 and A_2 are the shaded areas. The loads and displacements at the yield point, limit point, and failure point are presented in Table 5, where P_y , Δ_y , $P_{\rm max}$, $\Delta_{\rm max}$, $P_{\rm u}$, and $\Delta_{\rm u}$ are the loads and displacements at yielding, ultimate, and failure points, respectively.

The skeleton curve shows the elastic-, plastic-, and degradation-stages. In the initial stage, the curve is a straight line, bearing capacity increases rapidly, and stiffness remains stable. With increasing loads, concrete cracks and steel

Stage	Yielding		Ultimate		Failure	
	$P_{\rm y}/{\rm kN}$	Δ_y /mm	$P_{\rm max}/{\rm kN}$	$\Delta_{\rm max}/{ m mm}$	$P_{\rm u}/{\rm kN}$	$\Delta_{\rm u}/{\rm mm}$
Positive	238.49	32.15	351.72	87.93	298.46	136.27
Negative	-243.52	-31.39	-356.12	-86.55	-304.95	-133.92

TABLE 5: Yielding, ultimate and failure point of specimen.

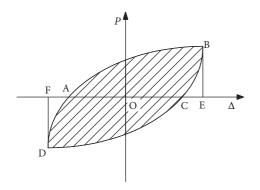


FIGURE 20: Hysteretic loop and energy dissipation capacity.

yields, and the skeleton curve gradually inclines toward the horizontal axis. The maximum base shear is 356 kN at the ultimate stage. The bearing capacity then decreases to 298 kN at failure owing to the serious damage of the core tube and frame.

3.5. Ductility and Energy Dissipation. The displacement ductility coefficient, μ , is calculated by (4), and an equivalent viscous coefficient, $h_{\rm e}$, to evaluate the energy dissipation of specimen, is calculated by (5).

$$\mu = \frac{\Delta_{\mathrm{u}}}{\Delta_{\mathrm{v}}} \tag{4}$$

$$h_{\rm e} = \frac{1}{2\pi} \cdot \frac{S_{\rm (\Delta ABC + \Delta CDA)}}{S_{\rm (\Delta OBE + \Delta ODF)}} \tag{5}$$

where $\Delta_{\rm u}$ and $\Delta_{\rm y}$ are parameters as described in Table 5, $S_{(\Delta {\rm ABC}+\Delta {\rm CDA})}$ is the area of one hysteretic loop as shown in Figure 20, and $S_{(\Delta {\rm OBE}+\Delta {\rm ODF})}$ is the total area of $\Delta {\rm OBE}$ and $\Delta {\rm ODF}$.

The displacement ductility coefficient μ is 4.27. The equivalent viscous coefficient $h_{\rm e}$ is shown in Figure 21, and the maximum value is 0.374 when Δ_9 reaches 88 mm. It meets the requirement of $\mu{\ge}3$ in Code for Seismic Design of Buildings (GB50011-2010). Compared with the results of other frames (L-shaped column composed of concrete-filled steel tubes frame [30]), the mentioned parameters are $\mu{=}3.31$ and $h_{\rm e}{=}0.336$. It is proved that specimen for CS frame-RC core tube building allows larger inelastic deformation.

3.6. Stiffness Degradation. The stiffness of specimen can be described by secant stiffness K_i , as calculated by

$$K_i = \frac{\left| +P_i \right| + \left| -P_i \right|}{\left| +\Delta_i \right| + \left| -\Delta_i \right|} \tag{6}$$

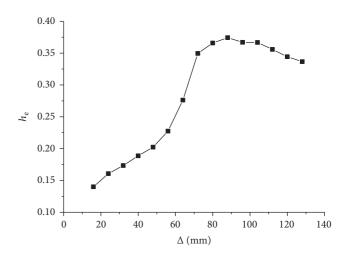


FIGURE 21: Energy dissipation capacity.

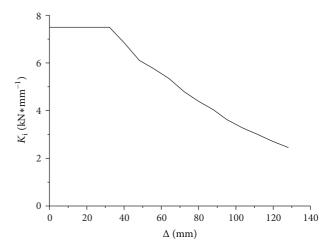


FIGURE 22: Degradation of stiffness.

where P_i and Δ_i are the peak load and corresponding displacement at *i*-th displacement level of 9th floor, respectively.

The stiffness degradation is shown in Figure 22. It can be seen that the stiffness of the specimen remains constant in the initial stage, but it degenerates rapidly once the core tube damage. Platform segment shows the elastic stage of specimen, and the degradation reveals the cumulative damage of structure. Finally the stiffness degenerates for about 67.49%. Compared with the result of [30], in which stiffness degradation is 79.07%, CS frame-RC core tube buildings maintain larger stiffness even at failure stage.

4. Conclusions

The seismic behavior of CS frame-RC core tube building was investigated, the damage process, crack pattern, and failure mode were observed, and the following was concluded.

- (1) In the quasi-static test, the specimen failed mainly by the overturning mode. As the first seismic resistant system, the core tube carried the major load and suffered extensive damage. Major horizontal tension cracks and X-shaped oblique shear cracks occurred at the bottom of core tube. Once the core tube got damaged, the frame played the role of second seismic resistant system and continued to carry the surplus load. The joint experienced shear failure and the column experienced tensile failure, and the floor slabs failed in compression. The structure design satisfied the concept of "two seismic resistant systems."
- (2) The hysteresis curve shape was between the spindle and the S form, and the skeleton curve of the specimen was symmetrical in both positive and negative directions. The specimen generally exhibited yielding, ultimate, and failure stages. The specimen began to enter the plastic stage at top displacement 32 mm. The structural maximum lateral bearing capacity was 356 kN at 88 mm and failed at 132 mm
- (3) The strain of steel skeleton in columns and concrete at the bottom of core tube exceeded 3000 $\mu\epsilon$. However strain of beams was generally less than 500 $\mu\epsilon$ and did not yield in the experiment. The frame design conformed to the seismic principles of "strong columns and weak beams" and "strong joints and weak members."
- (4) The displacement ductility coefficient μ was 4.27, which had met the requirement of $\mu \ge 3$ in Code for Seismic Design of Buildings. The equivalent viscous coefficient $h_{\rm e}$ was 0.374, and the stiffness decreased by approximately 67.49% at failure stage. Compared with the result of similar structure, CS frame-RC core tube building allowed larger inelastic deformation, indicating the excellent seismic performance.

Data Availability

The data used to support the findings of this study are available from the corresponding author upon request.

Conflicts of Interest

The authors declare that there are no conflicts of interest regarding the publication of this paper.

Acknowledgments

This research was funded by Natural Science Foundation of Hubei Province of China (Grant no. 2016CFB604), Natural Science Foundation of China (Grant nos. 51108041 and 51378077), and Science Foundation of the Education Department of Hubei Province of China (Grant no. D20161305), and their support is gratefully acknowledged.

References

- [1] J. Nie, M. Tao, Y. Huang, S. Tian, and G. Chen, "Research advances of steel-concrete composite structural systems," *Journal of Building Materials and Structures*, vol. 31, pp. 71–80, 2010.
- [2] J.-W. Hu, Y.-S. Kang, D.-H. Choi, and T. Park, "Seismic design, performance, and behavior of composite-moment frames with steel beam-to-concrete filledtube column connections," *International Journal of Steel Structures*, vol. 10, no. 2, pp. 177–191, 2010
- [3] S. C. Goel, "United States-Japan cooperative earthquake engineering research program on composite and hybrid structures," *Journal of Structural Engineering*, vol. 130, no. 2, pp. 157-158, 2004.
- [4] Y. Xiao, L. Zeng, Z. Cui, S. Jin, and Y. Chen, "Experimental and analytical performance evaluation of steel beam to concreteencased composite column with unsymmetrical steel section joints," Steel and Composite Structures, vol. 23, no. 1, pp. 17–29, 2017
- [5] L. Zeng, Y. Xiao, Y. Chen, S. Jin, W. Xie, and X. Li, "Seismic damage evaluation of concrete-encased steel frame-reinforced concrete core tube buildings based on dynamic characteristics," *Applied Sciences (Switzerland)*, vol. 7, no. 4, 2017.
- [6] S. Chen and P. Wu, "Analytical model for predicting axial compressive behavior of steel reinforced concrete column," *Journal of Constructional Steel Research*, vol. 128, pp. 649–660, 2017.
- [7] Y. Y. Li and B. S. Yang, "Discussion on limit values of axial compression ratio of steel reinforced concrete columns," *Applied Mechanics and Materials*, vol. 578-579, pp. 37–40, 2014.
- [8] M. Lin and K. Wang, "Seismic slope behavior in a large-scale shaking table model test," *Engineering Geology*, vol. 86, no. 2-3, pp. 118–133, 2006.
- [9] X. Lu, Y. Zou, W. Lu, and B. Zhao, "Shaking table model test on Shanghai World Financial Center Tower," *Earthquake Engineering & Structural Dynamics*, vol. 36, no. 4, pp. 439–457, 2007.
- [10] J. B. M. Sousa Jr. and C. F. D. G. Muniz, "Analytical integration of cross section properties for numerical analysis of reinforced concrete, steel and composite frames," *Engineering Structures*, vol. 29, no. 4, pp. 618–625, 2007.
- [11] X. Wang, "Study on ductility performance of T-shaped section steel reinforced concrete columns," *Applied Mechanics and Materials*, vol. 351-352, pp. 359–362, 2013.
- [12] Z. Li, H. Qin, H. Dang, H. Li, and J.-S. Zhang, "Experimental study on mechanical property of steel reinforced concrete L-shaped short columns," *International Journal of Modern Physics B*, vol. 22, no. 31-32, pp. 5755–5761, 2009.
- [13] J. Xue, L. Qi, L. Gao, and Z. Liu, "Mechanical behavior of lattice steel reinforced concrete inner frame with irregular section columns under cyclic reversed loading," *Engineering Structures*, vol. 128, pp. 225–236, 2016.
- [14] B. Yuan, M. Zeng, and K. Ma, "Crack resistance capacity analysis of SRC column-RC beam node," *Applied Mechanics and Materials*, vol. 204-208, pp. 2994–3001, 2012.
- [15] B. Wang, H. Jiang, and X. Lu, "Experimental and numerical investigations on seismic behavior of steel truss reinforced concrete core walls," *Engineering Structures*, vol. 140, pp. 164– 176, 2017.
- [16] L. Guoqiang, X. Zhou, and D. Xiang, "Shaking Table Study on a Model of Steel-Concrete Hybrid Structure Tall Buildings," *Journal of Building Structures*, vol. 22, no. 02, pp. 2–7, 2001.

[17] M. Wu and X. Lü, "Shaking table model test and theoretical analysis for seismic resistance of hybrid structures," *Earthquake Engineering and Engineering Vibration*, vol. 24, no. 6, pp. 103– 108, 2004.

- [18] G. Zhiguo, L. Xilin, L. Wensheng, L. Peizhen, Y. Song, and Z. Bin, "Shaking table model test of a hybrid high-rise building structure," *Earthquake Engineering and Engineering Vibration*, vol. 24, no. 4, pp. 99–105, 2004.
- [19] X. Yantao, Design and experimental study on steel reinforced concrete frame-core wall structure with transfer floor, China Academy of Building Research, 2007.
- [20] G. S. Kamaris, K. A. Skalomenos, G. D. Hatzigeorgiou, and D. E. Beskos, "Seismic damage estimation of in-plane regular steel/concrete composite moment resisting frames," *Engineering Structures*, vol. 115, pp. 67–77, 2016.
- [21] E. Ellobody, B. Young, and D. Lam, "Eccentrically loaded concrete encased steel composite columns," *Thin-Walled Structures*, vol. 49, no. 1, pp. 53–65, 2011.
- [22] Y. Yang, P. Wang, J. Wang, and X. Jin, "Seismic analysis of the hung curtain wall structure in Shanghai Center Tower," *The* Structural Design of Tall and Special Buildings, vol. 22, no. 11, pp. 847–861, 2013.
- [23] N. Fanaie and S. Ezzatshoar, "Studying the seismic behavior of gate braced frames by incremental dynamic analysis (IDA)," *Journal of Constructional Steel Research*, vol. 99, pp. 111–120, 2014.
- [24] E. Fereshtehnejad, M. Banazadeh, and A. Shafieezadeh, "System reliability-based seismic collapse assessment of steel moment frames using incremental dynamic analysis and Bayesian probability network," *Engineering Structures*, vol. 118, pp. 274–286, 2016
- [25] Z. Xu, P. Xu, and C. Xiao, "A study on the seismic performance of steel-reinforced concrete frame-concrete core wall high-rise mixed structure by large-scale shaking table tests and numerical simulations," *Earthquake Engineering & Structural Dynamics*, vol. 42, no. 13, pp. 1951–1969, 2014.
- [26] S.-S. Zheng, W. Yang, Q.-L. Tao, and Y. Hu, "Analysis of storey damage effect factors of SRC frame-RC core tube hybrid structure under cyclic loading," *Applied Mechanics and Materials*, vol. 166-169, pp. 52–55, 2012.
- [27] P. Xu, Y. Xue, and C. Xiao, "Experimental Study on Seismic Performance of High-rise SRC Hybrid Structures," *Building Structure*, vol. 35, no. 5, pp. 3–8, 2005.
- [28] Z. Lu, X. Chen, X. Lu, and Z. Yang, "Shaking table test and numerical simulation of an RC frame-core tube structure for earthquake-induced collapse," *Earthquake Engineering & Structural Dynamics*, vol. 45, no. 9, pp. 1537–1556, 2016.
- [29] S. Li, W. Zhao, and J. Jin, "The application of modesuperposition response spectrum method in seismic calculation of the boiler steel structure," *Advanced Materials Research*, vol. 594-597, pp. 1645–1651, 2012.
- [30] T. Zhou, Y. Jia, M. Xu, X. Wang, and Z. Chen, "Experimental study on the seismic performance of L-shaped column composed of concrete-filled steel tubes frame structures," *Journal of Constructional Steel Research*, vol. 114, pp. 77–88, 2015.

Hindawi Shock and Vibration Volume 2018, Article ID 3762685, 11 pages https://doi.org/10.1155/2018/3762685

Research Article

Research on the Fatigue Properties of High Strength Concrete after Exposure to High Temperature under Low Cyclic Compressive Loading

Linhao Wang, Haijing Gao (1), Haibiao Gao, and Zhili Luo 1

¹College of Architecture and Civil Engineering, Taiyuan University of Technology, Taiyuan, China

Correspondence should be addressed to Haijing Gao; baboon007@126.com

Received 28 February 2018; Accepted 15 April 2018; Published 23 May 2018

Academic Editor: Aly M. Aly

Copyright © 2018 Linhao Wang et al. This is an open access article distributed under the Creative Commons Attribution License, which permits unrestricted use, distribution, and reproduction in any medium, provided the original work is properly cited.

By using an electrohydraulic servo fatigue testing machine, fatigue tests were performed on C60 high strength concrete (HSC) under low cyclic compressive loading after undergoing normal temperature, 200°C, 400°C, 600°C, and 800°C. Failure patterns of high strength concrete under low cyclic compressive loading were observed. The influence of the high temperature process on the static elastic modulus of high strength concrete was analyzed. By studying the development law of fatigue strain, regression equations of fatigue strain after different high temperatures were established. Furthermore, the fatigue deformation modulus ratio was defined as the damage variable and the relationship models between the high temperature process and the fatigue damage were established. It provides the experimental foundation for fatigue damage analysis of high strength concrete in objective working conditions, which includes repeated loading and different high temperature processes.

1. Introduction

High strength concrete (HSC) has been widely used with the increasing complex structures of modern architecture. For instance, the Petronas Twin Towers in Kuala Lumpur City Centre, Malaysia, used C80 HSC. 311 South Wacker Drive in Chicago, USA, used C95 HSC. Two Union Square Building in Seattle, USA, used C135 HSC, Television Culture Center of China (TVCC), Shanghai World Financial Center (SWFC), adopted C60 HSC. In practice, concrete structures not only undertake static loading and the cyclic loading (vehicle loads, wind loads, wave loads, etc.), but also may suffer high temperature processes caused by fire or other reasons, which further results in serious damage of its structural properties.

At present, researches on mechanical properties of HSC after exposure to high temperature have been deeply carried out worldwide. Most studies [1–10] focused on the basic properties of HSC, such as appearance, mass, tensile strength, failure pattern, multiaxle strength, and stress-strain curve; those studies established the formula for failure criterion of HSC in

multiaxial stress state. However, the study on fatigue behavior of HSC after exposure to high temperature has not been carried out yet, especially after exposure to different high temperature processes. Several researches were concentrated on uniaxial fatigue behavior of ordinary concrete after exposure to high temperature [11–13]. In those studies, the tensile fatigue behavior of concrete under constant amplitude cyclic load after 100°C and 200°C has been investigated, the static performance of concrete has been analyzed, and the relationship between total strain growth rates at the second stage and fatigue life has been given. Nevertheless, the relationship model between the high temperature process and the fatigue damage of HSC failed to be established, and huge gap in the fatigue damage evaluation of fire-damaged HSC structure remains.

This paper presents the variation discipline of appearance, static elastic modulus, fatigue strain, residual strain, and fatigue deformation modulus of C60 HSC structure which was tested at various stress ratios after suffering room temperature, 200, 400, 600, and 800°C. The static load test and

²Wangzuo Township People's Government of Fengtai District of Beijing Municipality, Beijing 10007, China

³Jiangling Motors Co., Ltd., Taiyuan, China

fatigue test were performed with electrohydraulic servo pressure machine and electrohydraulic servo fatigue machine, respectively. And the relationship models between the high temperature process and the fatigue damage are established, those provide reference to fatigue damage assessment of high strength concrete subjected to different high temperature processes.

2. Materials and Experimental Procedures

2.1. Materials and Mix Proportions. The materials used in this investigation are standard cube specimens, as shown in Figure 1(b), which are made of C60 concrete (the matching ratio is shown in Table 1). Heating temperature was room temperature (20°C), 200°C, 400°C, 600°C, and 800°C respectively. Each set of specimens are constantly heated for 0.5 h, 1 h, 2 h, and 3 h after reaching the specified temperature.

2.2. Apparatus and Testing Methods. The high temperature test was carried out in a box-type resistance furnace, as shown in Figure 1(a), whose size is $300 \text{ mm} \times 500 \text{ mm} \times 200 \text{ mm}$. The maximal permitted temperature of resistance for furnace is 1000° C, and the temperature control precision is $\pm 1^{\circ}$ C. After specimens were put into the resistance furnace, the temperature gradually rose from the room temperature to the preset temperature in a rate of 10° C/min [14], and the temperature was maintained constantly for a certain time. In order to prevent the specimens from bursting during heating process, the specimens were wrapped around with high temperature barbed wire.

The static load test was carried out with the electrohydraulic servo pressure machine, as shown in Figure 1(c). The axis of specimen should be coincident with the axis of the machine panel before test, then repeatedly preloading and unloading the specimen three times with 20% of the upper limit load with 20% of the upper limit load; then pressure was applied at a rate of 0.3 MPa/s-0.8 MPa/s on the specimen until failure, and the ultimate bearing capacity of the specimen was obtained.

The fatigue test was carried out with an electrohydraulic servo fatigue machine, as shown in Figure 1(d). The fatigue load was applied by a 500 kN actuator in the vertical direction; the pressure is monitored by the voltmeter. The GTC 450 full digital electrohydraulic servo controller was used to control and collect data in real time. Cyclic loading waveform was sine wave, the minimum stress level S_{\min} (the ratio of minimum lateral compressive stress σ_{\min} and tensile strength f_t) was 0.1, and the maximum stress levels S_{\max} were 0.80, 0.85, and 0.90, respectively. Each principal stress direction must be perpendicular to the surface of the specimen. The deformation was measured with a 50 mm foil resistive strain gauge, which was applied to the two free surfaces of the specimen.

All tests were carried out by using three layers of plastic films spread with butter as the friction-reducing pad to ensure the test was conducted with few friction.

3. Test Results and Discussion

- 3.1. Experimental Results and Analysis
- 3.1.1. Apparent Appearance. HSC specimens have a series of apparent characteristics changes during the heating process

from the room temperature (20°C) to the specified temperature, including the color variation, crack propagation, scaling, broken corners, and looseness, as shown in Figure 2 and Table 2. When the temperature exceeded 200°C, irritating odor was generated. When the temperature exceeded 400°C, water mist emitted from the furnish door and irritating odor increased; when temperature reached 600°C, the water mist mostly disappeared and remarkable sound of bursting came out occasionally of box-type resistance furnace. When the heating process finished and the furnace door was opened, there were water droplets on the upper and lower sides of the furnace door.

As shown in Figure 2, the color of cooled specimens had no significant difference between before and after suffering 200°C [14]. The whole or part of specimens appeared rust red after suffering 400°C for one hour, which had a significant contrast with the color of the corresponding specimen at the room temperature. After heating up for 3 hours, the red disappeared and the light gray appeared on the specimen surface. Crack increased, but it did not spread across the entire surface. A small number of specimens had peeled pieces and broken corners, but most of the specimens kept a unbroken appearance. A small number of specimens had burst during the heating process, which caused rough section area, many holes, and cracks. After suffering 800°C, the specimens' appearance turned into offwhite, and some coarse cracks came out, and the overall structure was relatively loose.

It was analyzed that, at 400° C, hydration of calcium ferrite (CaO·Fe₂O₃·H₂O) in the concrete has a chemical reaction with Ca(OH)₂, which results in reddish-brown Fe(OH)₃ [12]. With 600° C, Fe(OH)₃ was decomposed into iron oxide and the red disappears.

3.1.2. Failure Mode. The failure modes of HSC under low cyclic compressive loading after different high temperature processes are shown in Figure 3. Due to suffering the high temperature, there were already some visible cracks on the specimens surface before loading. During 600°C procedure, some specimens sustained brittle failure and burst with splitting sound. This is because the strength of cement gel is close to the strength of coarse aggregate, which makes the development of cracks unable to be blocked and buffered by coarse aggregate like ordinary concrete. When reaching the peak stress, the energy accumulated inside is released in a rapid and violent manner and it made the specimen burst. It was obvious to see that, under uniaxial compressive stress, the HSC specimen split into multiple small cylinders. The failure surface of HSC was parallel to the compressive stress direction and perpendicular to the free surface, causing formation of one or more failure surfaces, and this phenomenon is called columnar damage. The failure mode of HSC was columnshaped conquassation, and the specific form is related to the applied stress level. Some specimens even show the failure mode of bulk fragments. This conclusion is consistent with the experimental results of Lv [12] and Xu [15].

3.1.3. Relative Compressive Strength. Through the static test, the compressive strength of the specimen after the antifriction at room temperature was 49.6 MPa, and the compressive



FIGURE 1: Apparatus and specimens: (a) box-type resistance furnace; (b) specimens; (c) electrohydraulic servo pressure machine; (d) electrohydraulic servo fatigue machine.

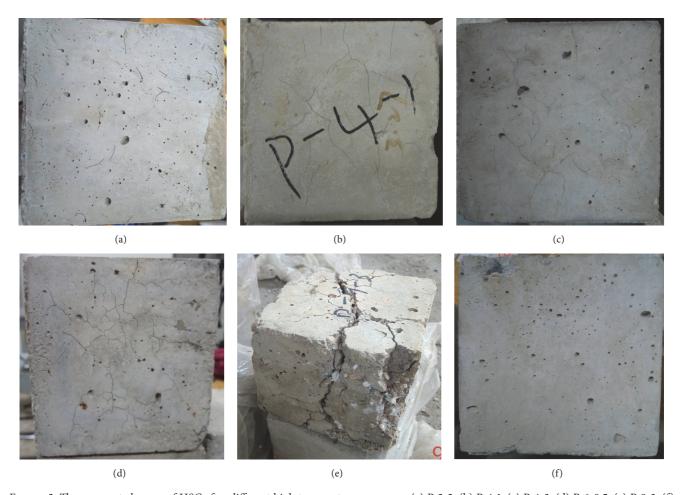


Figure 2: The apparent changes of HSC after different high temperature processes: (a) P-2-2; (b) P-4-1; (c) P-4-3; (d) P-6-0.5; (e) P-8-3; (f) normal temperature (P-X-X indicates fatigue test, heating temperature ($\times100^{\circ}$ C), holding time (h), such as P-2-2 indicates holding 2 h after heating up to 200°C).

TABLE 1: Mix proportions of HSC.

Cement: kg/m ³	Sand: kg/m ³	Gravel: kg/m ³	Water: kg/m ³	Water-reducing agent: kg/m ³	Water-to-binder ratio
510	720	1040	163	11	0.32



FIGURE 3: Failure mode of HSC specimens under uniaxial compression loads after different high temperature processes: (a) P-2-0.5, $S_{\max} = 0.80, 0.5N_f$; (b) P-2-3, $S_{\max} = 0.85, 0.5N_f$; (c) P-5-0.5, $S_{\max} = 0.90, 0.25N_f$; (d) P-6-3, $S_{\max} = 0.85, 0.75N_f$; (e) P-8-2, $S_{\max} = 0.90, N_f$; (f) critical failure state of fatigue.

Table 2: Appearance characteristics of HSC after exposure to high temperatures and then room temperature cooling.

Temperature: °C	Color	Crack propagation	scaling	Broken edges and corners	Looseness
20	Cinereous	None	None	None	None
200	Cinereous	None	None	None	None
400 (0.5 h, 1 h)	Reddish	Little	Little	Little	Mild
600	Grey	Some	Some	Some	A little heavy
800	Offwhite	Throughout the surface	Mostly	All the cornerS	Heavy

strength of the HSC specimen after different high temperature processes is shown in Table 3.

3.1.4. Fatigue Life. The fatigue life of the HSC specimens under uniaxial compression cyclic loading is shown in Table 4. Since it is generally believed that the fatigue life of concrete material obeys the lognormal distribution [16, 17], the logarithm of the mean value of fatigue life obtained under the same stress level is used as the average fatigue life of specimens under this condition.

3.1.5. Fatigue Deformation. In this experiment, the maximum strain $\varepsilon_{T,\max}$ at the fatigue direction of the HSC was measured, and its relationship with the relative fatigue cycles was shown in Figure 4. It can be seen that when specimens are under fatigue load, the longitudinal fatigue total strain increases with the maximum stress level and fatigue load cycle number and its development can be divided into three stages, which is the same as the fatigue strain behavior of ordinary concrete (Zhao DF, 2002); [18, 19]. The first stage was the crack initiation stage, the fatigue strain increased rapidly from zero to the

Table 3: Basic mechanical values of HSC after different high temperature processes.

Specimen number	f_c^T : Mpa	E^{T} : (10 ⁴ N/mm ²)	ε_p : 10^{-6}
P-2-0.5	42.6	3.21	1920
P-2-1	40.1	3.33	1999
P-2-2	41.2	3.59	1948
P-2-3	46.5	3.54	2076
P-4-0.5	45.2	3.44	2515
P-4-1	44.3	3.43	2505
P-4-2	42.4	3.43	2631
P-4-3	39.9	3.37	3056
P-6-0.5	32.5	3.37	3784
P-6-1	30.2	3.11	3101
P-6-2	28.5	3.04	3985
P-6-3	25.9	2.96	3624
P-8-0.5	19.2	2.87	4203
P-8-1	18.0	2.80	4574
P-8-2	15.3	2.72	4799
P-8-3	11.8	2.66	4816

Note. P-X-X indicates fatigue test-heating temperature-holding time, and P-0 indicates HSC at room temperature.

TABLE 4: Test data of fatigue for HSC.

Specimen number		Average fatigue lij	fe
specimen number	$0.9f_c^T$	$0.85 f_c^T$	$0.8f_c^T$
P-0	4.19	4.83	5.29
P-2-0.5	2.25	3.37	5.08
P-2-1	3.16	4.53	5.01
P-2-2	2.07	4.34	4.91
P-2-3	2.74	3.60	4.74
P-4-0.5	1.83	4.62	5.15
P-4-1	2.80	4.83	4.97
P-4-2	2.09	2.82	3.08
P-4-3	2.37	4.65	5.04
P-6-0.5	3.47	4.87	5.06
P-6-1	3.52	4.74	4.96
P-6-2	3.50	4.80	5.08
P-6-3	1.49	2.32	4.49
P-8-0.5	3.36	4.20	4.83
P-8-1	3.22	4.02	4.820
P-8-2	3.17	3.87	4.73
P-8-3	3.10	3.74	4.60

Note. P-X-X indicates fatigue test-heating temperature-holding time, and P-0 indicates HSC at room temperature.

steady state, the strain growth rate was large, and this stage accounted for about 10% of the whole fatigue life; that is, $N/N_f \leq 0.10$; the second stage was the stable crack expansion stage, the fatigue strain was linearly increasing and the growth rate was relatively stable, and it accounted for about 75% of the whole fatigue life; that is, $0.10 < N/N_f \leq 0.85$; the third stage was the crack instability damage stage, as the fatigue strain suddenly increased, the test block quickly entered the failure

stage, and the ultimate strain during failure was smaller than the ordinary concrete under uniaxle. This law is consistent with the development law given by Holmen [19].

Further analysis of Figure 4 shows that the fatigue strain of HSC was not only related to the heating temperature and holding time duration but also related to the magnitude of the stress level. When the holding time was the same and the heating temperature was different, the fatigue strain growth was small before 400°C but increased rapidly after 400°C, and the fatigue strain at 800°C was quintuple larger that at 200°C. It can be seen from Figures 4(a)–4(g) showed that the heating temperature had a greater effect on the fatigue strain of HSC than the holding time and stress level. When the heating temperature was the same and the holding time was different, the fatigue strain of HSC increased with the stress level, but the growth trend was not obvious.

The regression equation of the fatigue strain of HSC after different high temperature processes was obtained by nonlinear multivariate regression of the measured strain, the cycle times, and stress levels:

$$\varepsilon_{T,\text{max}} = a \left(\frac{N}{N_f}\right)^3 + b \left(\frac{N}{N_f}\right)^2 + c \left(\frac{N}{N_f}\right) + dT + et$$

$$+ f.$$
(1)

In order to facilitate the engineering application and analysis, this paper analyzed the relationship between the strain and the cycle times of the HSC after the high temperature history under various stress levels and put forward a unified formula.

When
$$S_{\text{max}} = 0.80$$
, $S_{\text{min}} = 0.10$,
$$\varepsilon_{T,m} = \left\{ 768.45 \left(\frac{N}{N_f} \right)^3 - 1007.02 \left(\frac{N}{N_f} \right)^2 + 1057 \left(\frac{N}{N_f} \right) + 6.91T + 201.55t + 2295.23 \right\}$$
(2a)
$$(20^{\circ}\text{C} < T \le 800^{\circ}\text{C}) \ R^2 = 0.9017.$$
When $S_{\text{max}} = 0.85$, $S_{\text{min}} = 0.10$,
$$\varepsilon_{T,m} = \left\{ 829.58 \left(\frac{N}{N_f} \right)^3 - 847.15 \left(\frac{N}{N_f} \right)^2 + 866.41 \left(\frac{N}{N_f} \right) + 6.02T + 481.21t + 2366.90 \right\}$$
(2b)
$$(20^{\circ}\text{C} < T \le 800^{\circ}\text{C}) \ R^2 = 0.8992.$$
When $S_{\text{max}} = 0.90$, $S_{\text{min}} = 0.10$,
$$\varepsilon_{T,m} = \left\{ 1321.76 \left(\frac{N}{N_f} \right)^3 - 2178.95 \left(\frac{N}{N_f} \right)^2 \right\}$$

 $+1695.13\left(\frac{N}{N_c}\right)+9.44T+199.37t+1698.39$

 $(20^{\circ}C < T \le 800^{\circ}C) R^2 = 0.8346.$

(2c)

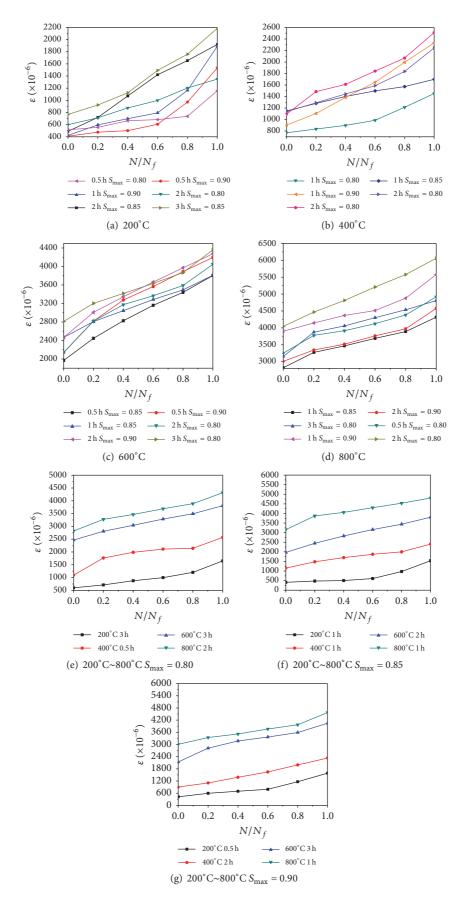


FIGURE 4: Relationship between fatigue strain and relative fatigue cycles: (a) 200° C; (b) 400° C; (c) 600° C; (d) 800° C; (e) 200° C~ 800° C, $S_{max} = 0.80$; (f) 200° C~ 800° C, $S_{max} = 0.85$; (g) 200° C~ 800° C, $S_{max} = 0.90$.

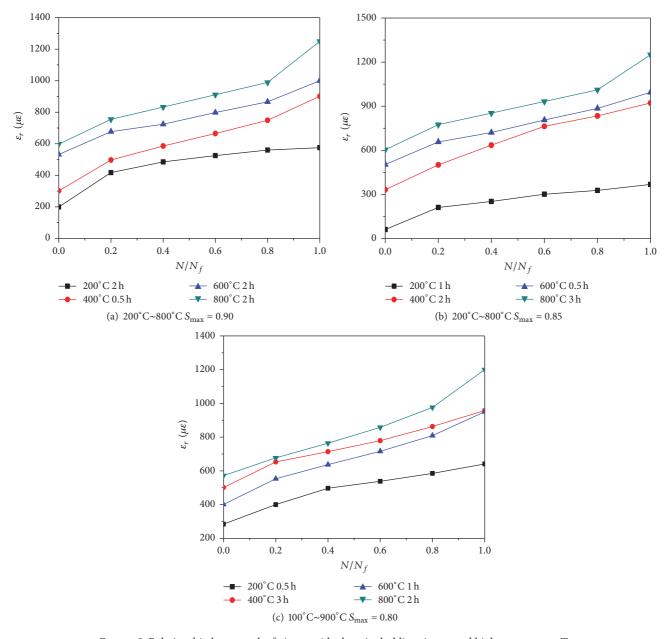


Figure 5: Relationship between the fatigue residual strain, holding time t, and high temperature T.

3.2. Fatigue Damage

3.2.1. Fatigue Residual Strain. It is pointed out that, with the increase of fatigue cycle times, the residual strain of concrete in uniaxial stress state was the same with total fatigue strain, which showed a three-stage development law. And the residual strain value under fatigue failure was not affected by the stress level but also had nothing to do with the loading process; it was constant [12, 15, 20]. In this paper, the uniaxial compression fatigue test of HSC after different high temperature process was carried out and the residual strain was measured. The development history is shown in Figure 5, which verifies the above conclusion.

The regression equation of the fatigue residual strain $\varepsilon_{r,T}$ of HSC and relative fatigue number N/N_f was obtained by nonlinear regression under the number of cycles and stress levels:

$$\varepsilon_{r,T} = a \left(\frac{N}{N_f}\right)^3 + b \left(\frac{N}{N_f}\right)^2 + c \left(\frac{N}{N_f}\right) + dt + e.$$
 (3)

In order to facilitate engineering application and analysis, this paper analyzed the relationship between the fatigue modulus and the number of cycles of HSC after the different high temperature process under various stress levels and put forward unified formulas.

From Figure 5 and formulas (4a), (4b), and (4c) it can be seen that the residual strain of HSC under fatigue failure is related to the heating temperature and the holding time duration but not related to the magnitude of the stress level and the fatigue cycle times. And it is almost the same with the uniaxial fatigue residual strain development of ordinary concrete. The residual strains of HSC at high temperature from 200°C to 800°C are 471 μ , 927 μ , 997 μ , and 1233 μ , which are larger than the uniaxial fatigue residual strain of ordinary concrete. All above can be used as fatigue damage guidelines of HSC after high temperature process.

 $20^{\circ}C < T \le 800^{\circ}C \ (R^2 = 0.8346)$.

3.2.2. Fatigue Damage Based on Fatigue Residual Strain. Fatigue damage of concrete is due to its internal microcracks expansion which will lead to an unstable state, so taking the fatigue residual strain as a measure criterion of fatigue damage is scientific and reasonable. According to the basic concepts of damage mechanics, the relative residual strain is defined; that is, the residual strain $\varepsilon_{r,T}$ and fatigue failure ultimate residual strain $\varepsilon_{r,T}^0$ are damage variables; the damage equation is

$$D_{m} = \frac{\varepsilon_{r,T}}{\varepsilon_{r,m}^{0}}$$

$$= a \left(\frac{N}{N_{f}}\right)^{3} + b \left(\frac{N}{N_{f}}\right)^{2} + c \left(\frac{N}{N_{f}}\right) + dT + et$$

$$+ f, \quad D_{m} \in (0,1).$$
(5)

TABLE 5: Fatigue life.

Specimen number	D_m	$N_{e0.9}$	$N_{e0.85}$	$N_{e0.8}$
P-2-0.5	0.835	2.19	4.46	5.20
P-2-1	0.961	2.97	4.87	5.27
P-2-2	0.735	1.88	4.27	5.03
P-2-3	0.686	1.76	4.11	4.96
P-4-0.5	0.770	2.01	4.30	5.11
P-4-1	0.735	1.88	4.27	5.04
P-4-2	0.746	1.92	4.30	5.09
P-4-3	0.739	1.89	4.28	5.06
P-6-0.5	0.415	1.53	3.77	4.62
P-6-1	0.399	1.51	3.74	4.45
P-6-2	0.418	1.53	3.78	4.64
P-6-3	0.402	1.51	3.70	4.60
P-8-0.5	0.394	1.50	3.66	4.39
P-8-1	0.389	1.49	3.62	4.28
P-8-2	0.393	1.50	3.66	4.34
P-8-3	0.395	1.50	3.67	4.33

Note. P-X-X indicates fatigue test-heating temperature- holding time, and P-0 indicates HSC at room temperature.

TABLE 6: Distribution table of relative errors (%).

Specimen number	$E_{0.9}$	$E_{0.85}$	$E_{0.8}$
P-2-0.5	2.667	32.34	2.36
P-2-1	6.01	7.51	5.19
P-2-2	9.18	1.61	2.44
P-2-3	35.77	14.17	4.64
P-4-0.5	9.84	6.93	0.78
P-4-1	32.86	11.59	1.41
P-4-2	8.13	52.48	65.26
P-4-3	20.25	7.96	0.405
P-6-0.5	55.91	22.59	8.70
P-6-1	57.10	21.10	10.28
P-6-2	56.29	21.25	8.66
P-6-3	1.34	59.48	2.45
P-8-0.5	55.36	12.86	9.11
P-8-1	53.73	9.95	11.20
P-8-2	52.68	5.43	8.25
P-8-3	51.61	1.87	5.87

Note. Exx in this table is the absolute value of the relative error.

Figure 6 shows the relationship between the damage variables of HSC and the relative fatigue cycle times after different high temperature process. The fatigue damage model can be used to analyze the accumulated fatigue damage of HSC under low temperature uniaxial compression after different high temperature processes.

The remaining fatigue life of the HSC under low cyclic uniaxial compression after suffering different high temperature process was predicted, which was shown in Table 5. Compared to the test results in Table 4, the relative error distribution of the fatigue life of HSC under uniaxial compression after suffering different high temperature processes can be obtained as shown in Table 6.

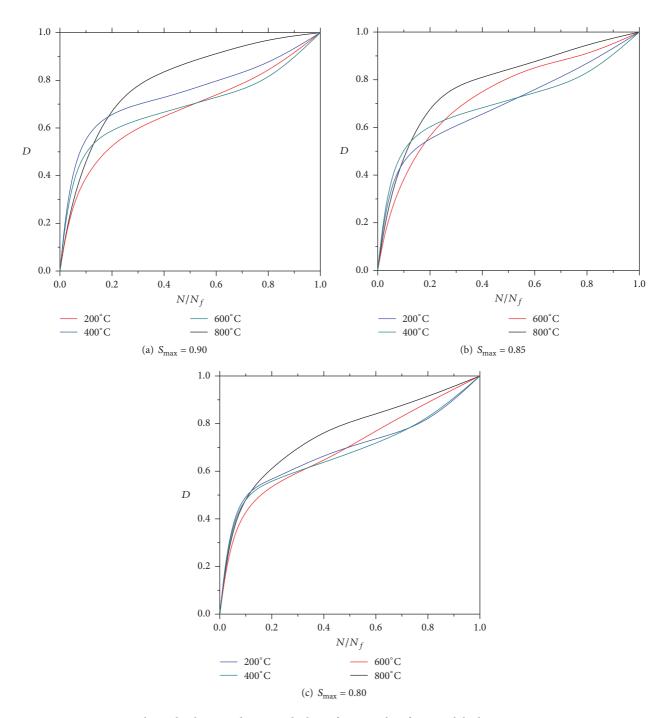


FIGURE 6: Relationship between damage and relative fatigue cycles of HSC with high temperature process.

It can be seen from the calculated results that, among the absolute values of the relative error between predicted and measured values, the values which are less than 30% account for more than 85% of the total. With the huge difficulties in testing, the numerous influential factors, and the big discrepancy of experimental data taken into consideration, the predicted value was satisfactory for the low cyclic uniaxial

compressive fatigue test of HSC after suffering different high temperature processes. Thus, an effective method was developed to predict the fatigue residual life of HSC after different high temperature processes.

The damage equation at different stress levels from formulas (4a), (4b), and (4c) to (5) and Figure 6 was obtained by nonlinear regression under the number of cycles and stress levels.

$$\begin{aligned} & \text{When } S_{\text{max}} = 0.80, S_{\text{min}} = 0.10, \\ & D_m = \left\{ 3.3141 \left(\frac{N}{N_f} \right)^3 - 5.6933 \left(\frac{N}{N_f} \right)^2 \right. \\ & + 3.2574 \left(\frac{N}{N_f} \right) - 0.001 \left(\frac{T}{100} \right) + 0.0029t \\ & + 0.1423 \right\} \quad 20^{\circ}\text{C} < T \leq 800^{\circ}\text{C} \, \left(R^2 = 0.9027 \right). \end{aligned} \tag{6a}$$

When
$$S_{\text{max}} = 0.85$$
, $S_{\text{min}} = 0.10$,

$$D_{m} = \left\{ 3.3604 \left(\frac{N}{N_{f}} \right)^{3} - 6.0469 \left(\frac{N}{N_{f}} \right)^{2} + 3.6014 \left(\frac{N}{N_{f}} \right) - 0.004 \left(\frac{T}{100} \right) + 0.0038t \right.$$

$$\left. + 0.1036 \right\} \quad 20^{\circ} \text{C} < T \le 800^{\circ} \text{C} \left(R^{2} = 0.8844 \right).$$

$$(6b)$$

When
$$S_{\text{max}} = 0.90$$
, $S_{\text{min}} = 0.10$,

$$D_{m} = \left\{ 3.6074 \left(\frac{N}{N_{f}} \right)^{3} - 6.3556 \left(\frac{N}{N_{f}} \right)^{2} + 3.6530 \left(\frac{N}{N_{f}} \right) - 0.003 \left(\frac{T}{100} \right) + 0.0133t \right.$$

$$\left. + 0.1152 \right\} \quad 20^{\circ} \text{C} < T \le 800^{\circ} \text{C} \left(R^{2} = 0.8171 \right).$$

$$(6c)$$

4. Conclusions

The color of HSC turns lighter after the high temperature processes. At about 500°C, the specimens are light gray and parts of them have a serious burst; the cross-section is relatively rough and some holes and cracks exist in the broken specimens. After 800°C, the specimens' appearance are offwhite, some coarse cracks appear, and some even run throughout the specimen. The structure of the specimen is relatively loose.

The maximum longitudinal total strain of the HSC after exposure to high temperature processes under low cyclic uniaxial compressive loading is in accordance with the three-stage development law. The second stage is the stable crack propagation stage, which accounts for about 75% of the whole fatigue life. The formulas to figure out the longitudinal total strains at each stage were given. Compared with the stress level, the effect of high temperature process on the fatigue strain of HSC is more significant, especially the influence of heating temperature.

The relative residual strain was defined as the damage variable, and the fatigue damage model of HSC after different high temperature processes, under low cyclic uniaxial compressive loading, was established. According to the damage model established by the relative residual strain, the fatigue life of high strength concrete was predicted. More than 85% of the absolute values of the relative error between predicted and measured values are less than 30%, and the result is satisfactory.

Data Availability

The data used to support the findings of this study are available from the corresponding author upon request.

Conflicts of Interest

The authors declare that they have no conflicts of interest.

Acknowledgments

The present work was supported by the National Natural Science Foundation of China (no. 51378045). The authors gratefully acknowledge the support.

References

- [1] A. H. Al-Gadhib, M. H. Baluch, A. Shaalan, and A. R. Khan, "Damage model for monotonic and fatigue response of high strength concrete," *International Journal of Damage Mechanics*, vol. 9, no. 1, pp. 57–78, 2000.
- [2] M. Ayman and A. E. Mohamed, "Mechanical properties of high strength concrete with scrap tire rubber," *Construction and Building Materials*, vol. 93, pp. 249–256, 2015.
- [3] F.-P. Cheng, V. K. R. Kodur, and T.-C. Wang, "Stress-strain curves for high strength concrete at elevated temperatures," *Journal of Materials in Civil Engineering*, vol. 16, no. 1, pp. 84–90, 2004.
- [4] Z. J. He and Y. P. Song, "Multiaxial tensile-compressive mechanical behaviour of plain high-strength high-performance concrete," *Engineering Mechanics*, vol. 67, pp. 190–195, 2010.
- [5] J. L. Liu, J. Y. Xu, and W. B. Ren, "Mechanical properties of high strength concrete under impact loading," *Bulletin Chinese Ceramic Society*, vol. 35, pp. 261–266, 2016.
- [6] M. Ghandehari, A. Behnood, and M. Khanzadi, "Residual mechanical properties of high-strength concretes after exposure to elevated temperatures," *Journal of Materials in Civil Engineering*, vol. 22, no. 1, Article ID 004001QMT, pp. 59–64, 2010.
- [7] M. Amin and K. Abu El-Hassan, "Effect of using different types of nano materials on mechanical properties of high strength concrete," *Construction and Building Materials*, vol. 80, pp. 116– 124, 2015.
- [8] F. Saber and N. Mahdi, "Mechanical properties and durability of high-strength concrete containing macro-polymeric and polypropylene fibers with nano-silica and silica fume," Construction and Building Materials, vol. 132, pp. 170–187, 2017.
- [9] V. Afroughsabet and T. Ozbakkaloglu, "Mechanical and durability properties of high-strength concrete containing steel and polypropylene fibers," *Construction and Building Materials*, vol. 94, pp. 73–82, 2015.
- [10] J. Xiao, Z. Li, Q. Xie, and L. Shen, "Effect of strain rate on compressive behaviour of high-strength concrete after exposure to elevated temperatures," *Fire Safety Journal*, vol. 83, pp. 25–37, 2016.

[11] P. Y. Lv and Y. P. Song, "Tensile mechanical behaviour of concrete under different temperatures," *Engineering Mechanics*, vol. 20, pp. 80–85, 2003.

- [12] P. Y. Lv, Experimental Study on Dynamic Strength and Deformation of Concrete Under Uniaxial and Blaxial Action [Ph.D. thesis], Dalian University of Technology, Dalian, China, 2002.
- [13] X. G. Zhou and J. L. Wu, "Preliminary research on fatigue behavior of concrete after exposed to high temperature," *Industrial Constructions*, vol. 26, pp. 33–36, 1996.
- [14] D. Zhao and M. Liu, "Experimental study on residual strength and nondestructive testing of high strength concrete after high temperature," *Jianzhu Jiegou Xuebao/Journal of Building Structures*, vol. 36, pp. 365–372, 2015.
- [15] J. F. Xu, Experimental Investigation of the Complete Stressstrain Curve of High Strength Concrete, [Ph.D. thesis], Tsinghua University, Beijing, China, 1986.
- [16] H. K. Cheong and H. Zeng, "Stress-strain relationship for concrete confined by lateral steel reinforcement," ACI Materials Journal, vol. 99, no. 3, pp. 250–255, 2002.
- [17] J. T. McCall, "Probability of fatigue failure of plain concrete," *ACI Journal Proceedings*, vol. 55, no. 8, pp. 233–244, 1958.
- [18] R. M. Wang, Y. P. Song, and G. P. Zhao, "Study on fatigue properties of concrete under compression," *Engineering Mechanics*, vol. 24, pp. 38–47, 1991.
- [19] J. O. Holmen, "Fatigue of concrete by constant and variable amplitude tests," ACI Journal, vol. 75, no. 4, pp. 71–110, 1982.
- [20] D. Zhao, H. Gao, H. Liu, P. Jia, and J. Yang, "Fatigue Properties of Plain Concrete under Triaxial Tension-Compression-Compression Cyclic Loading," Shock and Vibration, vol. 2017, Article ID 9351820, 10 pages, 2017.

Hindawi Shock and Vibration Volume 2018, Article ID 4923898, 13 pages https://doi.org/10.1155/2018/4923898

Research Article

Study on the Nonlinear Characteristics of a Rotating Flexible Blade with Dovetail Interface Feature

Chaofeng Li , ^{1,2} Zengchuang Shen, ¹ Bingfu Zhong, ¹ and Bangchun Wen ^{1,2}

¹School of Mechanical Engineering and Automation, Northeastern University, Shenyang 110819, China

Correspondence should be addressed to Chaofeng Li; chfli@mail.neu.edu.cn

Received 6 December 2017; Revised 28 February 2018; Accepted 27 March 2018; Published 9 May 2018

Academic Editor: Mohammad A. Hariri-Ardebili

Copyright © 2018 Chaofeng Li et al. This is an open access article distributed under the Creative Commons Attribution License, which permits unrestricted use, distribution, and reproduction in any medium, provided the original work is properly cited.

A dynamic model is proposed in this paper for analyzing the nonlinear characteristics of a flexible blade. The dynamical equation of motion for a rotational flexible blade in a centrifugal force field is established based on the finite element method. A macro-stick-slip mechanical model of dry friction is established to simulate the constraint condition of the flexible blade. The combined motion of the external excitation and friction produces a piecewise linear vibration which is actually nonlinear. The numerical integration method is employed to calculate the vibration reduction characteristics of the nonlinear constrained rotating blade. The results show that the nonlinear dry friction force produced by the dovetail interface plays an important role in vibration reduction. And the effect of dry friction vibration reduction is significant when the rotating speed is slow or the friction coefficient is small. Besides, the magnitude of external excitation also has a great impact on the state of the friction. Therefore, some relevant experimental researches should be done in the future.

1. Introduction

In the aeroengine components, the blade has the largest number and is the most prone to accident. The blade is inevitably affected by the aerodynamic force and the centrifugal force during the process of starting, running, and stopping of the engine. This is one of the main reasons for the blade damage. The dovetail attachment structure is often used in the installation of modern aeroengine blades. This structure has the advantage of simple manufacture. And it can also use the dry friction to reduce the vibration level of blade. Thus, the high cycle fatigue damage of the blade is reduced. And the service life of the blade is longer. Therefore, the design of the blade connection structure and the construction of the dry friction mechanics model are the important contents of the research and design of aeroengine blade. In recent decades, many scholars at home and abroad have carried out in-depth theoretical analysis and experimental research on the dynamic characteristics of the blade. They have achieved fruitful results and laid a solid foundation for the further study of the later generations.

The natural characteristics of the blade have been studied in the early studies of blade. Turhan and Bulut [1] investigated

the nonlinear bending vibrations of a rotating beam. The perturbation analysis was used to obtain the natural frequencies and the frequency responses. Chung and Yoo [2] used the finite element method and the discretized equations to investigate the behaviors of the natural frequencies with the variation of the rotating speed. Tsai [3] used the FEM to explore the dynamic characteristics of a single blade, 6-blade groups, and 12-blade groups and found that the vibration frequency and mode shape of single blade are in good agreement with that of the whole blade. Yan et al. [4] used the experimental mode analysis and mode correction methods to investigate the coupling vibration of the mistuned bladedisk in aeroengine and found the right working frequency range of aeroengine. Park et al. [5] investigated the vibration characteristics of the rotating blades of the wind-turbine and obtained the accurate natural frequencies of blades through the numerical method.

In order to find out the reason for blade damage and prevent it, many experts have done a lot of researches on the dynamic characteristics of the blade. Choi and Lee [6] used the modal analysis for one blade and the assembly of the blades to check the dynamic characteristics of the blades. The results showed that it is close to the resonance condition

²Key Laboratory of Vibration and Control of Aero-Propulsion Systems, Northeastern University, Shenyang 110819, China

of the assembled blades when the blade is broken. Al-Bedoor and Al-Qaisia [7] used a reduced order nonlinear dynamic model to investigate the forced vibrations of a flexible rotating blade under the excitation of shaft torsional vibration. Yao et al. [8] investigated the nonlinear dynamic characteristics of the rotating blade and used the bifurcation diagram, phase portrait, and power spectrum to demonstrate that periodic motions and chaotic motions occur in nonlinear vibrations of the rotating blade under certain conditions. Lee et al. [9] developed a computational model for the dynamic characteristics of a rotor-blade system. The dynamic characteristics of the system for various system parameters were obtained. Li et al. [10, 11] established a dynamic model of rotor-blade coupling system with elastic restraints to investigate the influence of shaft bending on the coupling vibration of rotorblades system and analyze the nonlinear dynamic behavior of a continuum model. Allara [12] established different contact models to investigate the dynamic response characteristics of turbine blades and obtained the hysteresis curves of the oscillating tangential contact force versus relation tangential displacements and the dissipated energy at the contact for different contact geometries.

It is known that the damage caused by the resonance vibration of the blade is through analyzing the vibration characteristics of the blade. Proper method must be found to restrain the vibration of blade and increase the service life of blades. There are many works that have been done on the vibration reduction, but the primary method is to reduce the vibration by friction. Hartog [13] developed an ideal dry friction model which can qualitatively analyze the effect of the dry friction vibration reduction. Iwan [14] proposed the famous piecewise nonlinear hysteresis model and studied the dynamic responses of the system of a single degree of freedom and two degrees of freedom. Yang and Meng [15] used the Coulomb friction law and the macroslip model to investigate the coupling contact kinematics and developed the mathematical expression of the dry friction force. Ciğeroğlu and Özgüven [16] indicated that the microslip model can provide more accurate results by applying a quasilinearization technique. They proposed a new model about all blades around the disk, which developed the microslip method and validated feasibility of the model. Xu et al. [17, 18] presented a macroslip model to determine the dry friction force on the contact interface between the blade dovetail attachment and the disk dovetail groove. And a lumped-mass-spring model was used to explore the effect of some control parameters of a damped structure on its forced

Several suitable friction models are obtained through the studies of the above. And there are some suitable methods which can be used to study the possibility of friction vibration reduction. Wang and Chen [19] used the HBM to explore the vibration characteristics of blade and computed the accurate steady-state response of blade with damper. Ding et al. [20, 21] presented an analytical method for determining the steady-state response of a system with dry friction damper. Sinha [22] discussed the transient response of the rotor with the blades deforming. And the Numerical results were presented for the highly nonlinear impact dynamics problem of hard

rub with Coulomb friction. Cao et al. [23] analyzed the 2D friction contact problem of a flexible blade and found that the gap between the tips and the rotating speed of the blade significantly influence the dynamics of the system. Wang and Long [24] established the mechanical model of bladed disks with random mistuning of hysteretic dry friction damping, and used an incremental harmonic balance method to analyze the effects of parameters of bladed disks on its forced response. Zhang et al. [25] developed the constitutive relation of dry friction force for blade-root damper based on a microslip friction model and used the harmonic balance method to analyze the effect of dry friction on vibration performances of mistuned bladed disk system. Pust et al. [26] used a harmonic excitation near the natural frequency of blade to act on a blade system with damping element and investigated the vibration response characteristics of blade with dry friction dampers. Zhang et al. [27] described an efficient method to predict the nonlinear steady-state response of a complex structure with multiscattered friction contacts and analyzed the nonlinear response of the blade with underplatform dampers. Ozaydin and Ciğeroğlu [28] used onedimensional macroslip friction model with constant normal load to model the dry friction damper and investigated the effect of dry friction damping on vibration attenuation of helicopter tail shaft.

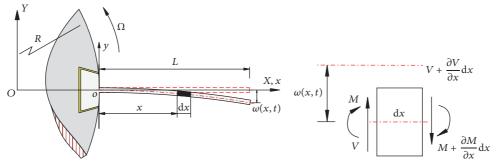
As can be seen from the previous references, the damage of blade mostly occurs in the resonance region. And most present studies simplify blade as the lumped-mass model. The deviation of this model from the actual shape of the blade is large. In order to simulate the actual shape of flexible blade more accurately and reduce the resonance peak, the discrete model of the blade based on the finite element method is established. And the ideal dry friction mechanical model is used to simulate the boundary conditions of the blade. This conforms to the dynamic environment of the rotating flexible blade. The effects of the parameters of blade system like the rotating speed, the friction coefficient, and the amplitude of external excitation on the vibration reduction characteristics of the blade are studied and the transient response of the blade is analyzed in this paper.

2. The Establishment of Dynamic Model

The structural diagram of the rotating blade with dovetail interface is shown in the Figure 1(a). In the model, R, Ω , and L stand for the radius of the disk, the rotating speed of blade, and the length of blade, respectively. $\omega(x,t)$ is the transverse displacement of the blade. The force analysis of the infinitesimal body dx is shown in Figure 1(b). M and V stand for the bending moment and the shearing force, respectively.

According to the knowledge of mechanics of elasticity, the influence of shearing deformation is considered. When the blade is deformed by the external excitation in the rotating state, the total energy equation Π can be written as follows:

$$\Pi = \frac{1}{2} \int_{R}^{R+L} EI \left(\frac{\partial^{2} \omega_{b}(x,t)}{\partial x^{2}} \right)^{2} dx + \frac{1}{2} \int_{R}^{R+L} \frac{GA}{k} \left(\frac{\partial \omega_{s}(x,t)}{\partial x} \right)^{2} dx$$



(a) The structural representation of the rotating blade

(b) The force analysis of the infinitesimal body

FIGURE 1: The continuous model of the blade with dovetail interface.

$$+ \frac{1}{2} \int_{R}^{R+L} N_{\Omega} \left(\frac{\partial \omega (x,t)}{\partial x} \right)^{2} dx$$

$$+ \frac{1}{2} \int_{R}^{R+L} \rho A \left(\frac{\partial \omega (x,t)}{\partial t} \right)^{2} dx,$$
(1)

where the first item on the right of equal sign is the bending strain energy. The second is the shearing strain energy. The third is the centrifugal strain energy. And the fourth is the kinetic energy of blade. $\omega(x,t)$ is the transverse displacement resulting from the deformation of blade; $\omega_{\rm b}(x,t)$ is the transverse displacement caused by the bending deformation; $\omega_{\rm s}(x,t)$ is the transverse displacement due to the shearing displacement; what is more $\omega(x,t)=\omega_{\rm b}(x,t)+\omega_{\rm s}(x,t)$; E, G, and I denote Young's Modulus, the modulus of shearing, and the moment of inertia, respectively; N_{Ω} is the centrifugal force of the blade, A is the cross-sectional area, and ρ is density and k is the correction factor for considering the fact that the actual shearing strain and shearing stress are not uniformly distributed.

There are generally two methods for the numerical discretization of the total energy which is shown in (1). The first is the numerical discretization by using its modal functions. The second is the discretization of the finite element method by using the shape functions. The plane beam element is used to discretize the blade in this paper. And the whole blade is divided into 30 elements. The stiffness matrix and the mass matrix of the element are derived from the local coordinate system *oxy*. The transverse displacement of an element is $\omega^e = \omega^e_b + \omega^e_s$ in the discrete modal considering the effect of the shearing deformation.

In the local coordinate system *oxy*, the strain energy caused by bending and shearing deformation of any element can be written as follows:

$$U_{b}^{e} = \frac{1}{2} \int_{(i-1)l}^{il} EI\left(\frac{\partial^{2} \omega_{b}^{e}}{\partial x^{2}}\right)^{2} dx,$$

$$U_{s}^{e} = \frac{1}{2} \int_{(i-1)l}^{il} \frac{GA}{k} \left(\frac{\partial \omega_{s}^{e}}{\partial x}\right)^{2} dx,$$
(2)

where l is the length of an element, i is the ordinal number of the elements, and i = 1, 2, 3, ..., n. In this paper n = 30.

The blade is affected by the centrifugal force under the working condition. And the centrifugal strain energy which is produced by any elements can be shown as

$$U_{c}^{e} = \frac{1}{2} \int_{(i-1)l}^{il} N_{i}^{e} (x_{e}) \dot{\omega}^{e2} (x_{e}, t) dx_{e},$$
 (3)

where x_e is the distance from a point in an element to the front end of the element; $\omega^e(x_e,t)$ is the transverse displacement of this point; $N_i^e(x_e)$ is the centrifugal force of this point and can be written as follows:

$$N_i^e(x_e) = \int_{(i-1)l+x_e}^{L} \rho A\Omega^2 \left[R + (i-1)l + x_e \right] dx.$$
 (4)

 $N_{\rm b}(x),~N_{\rm s}(x)$ are the element shape functions. And $\delta_{\rm b}^{\rm e},~\delta_{\rm s}^{\rm e}$ are the element nodal displacement arrays. They are substituted into the element strain energy equations after the bending strain energy $U_{\rm b}^{\rm e},$ the shearing strain energy $U_{\rm s}^{\rm e},$ and the centrifugal strain energy $U_{\rm c}^{\rm e}$ of the element are obtained. The bending stiffness matrix $\mathbf{k}_{\rm b}^{\rm e},$ the shearing stiffness matrix, and the centrifugal stiffness matrix $\mathbf{k}_{\rm c}^{\rm e}$ are obtained. Therefore, the element stiffness matrix $\mathbf{k}^{\rm e}$ is obtained by integrating the above three matrices.

The kinetic energy of any element consists of two parties. It can be expressed as given below:

$$T^{e} = T_{b}^{e} + T_{s}^{e}$$

$$= \frac{1}{2} \int_{(i-1)l}^{il} \rho A \left(\frac{\partial \omega_{b}}{\partial t}\right)^{2} dx$$

$$+ \frac{1}{2} \int_{(i-1)l}^{il} \rho A \left(\frac{\partial \omega_{s}}{\partial t}\right)^{2} dx,$$
(5)

where $T_{\rm b}^e$ and $T_{\rm s}^e$ are the kinetic energy caused by the bending deformation and the shearing deformation, respectively. Similarly, the mass matrices $m_{\rm b}^e$ and $m_{\rm s}^e$ can be obtained based on the kinetic energy of the element. Then, the two mass matrices are integrated to obtain the element mass matrix \mathbf{m}^e .

After obtaining the strain energy and the kinetic energy of the element, the total energy Π of the discretized model can be written as follows:

$$\Pi = \sum_{i=1}^{n} U_{b}^{i} + \sum_{i=1}^{n} U_{s}^{i} + \sum_{i=1}^{n} U_{c}^{i} + \sum_{i=1}^{n} T^{i}.$$
 (6)

The element stiffness matrix \mathbf{k}^e and the element mass matrix \mathbf{m}^e are transformed from the local coordinate system to the whole coordinate system. Then, the whole stiffness matrix \mathbf{K} and the whole mass matrix \mathbf{M} are obtained by means of the set of element matrices. The damping of the whole blade system is expressed by Rayleigh damping; its expression is

$$\mathbf{C} = \alpha \mathbf{M} + \beta \mathbf{K}.\tag{7}$$

 α and β are the coefficients of Rayleigh damping. They can be expressed as follows:

$$\alpha = \frac{2(\xi_2/\omega_2 - \xi_1/\omega_1)}{(1/\omega_2^2 - 1/\omega_1^2)},\tag{7.1}$$

$$\beta = \frac{2(\xi_2 \omega_2 - \xi_1 \omega_1)}{(\omega_2^2 - \omega_1^2)},\tag{7.2}$$

where ω_1 and ω_2 are the first-order and the second-order natural angular frequency of the blade, respectively; ξ_1 and ξ_2 are the damping coefficients corresponding to the two natural frequencies, respectively.

3. The Establishment of Mechanical Model

The tenons are closely connected together to form the contact interfaces due to the centrifugal force of the blade. There are complicated nonlinear forces at the contact interfaces. In order to research the effect of the nonlinear force on the natural characteristics of the blade, an ideal dry friction model is established to simulate the nonlinear force of the tenon joint. The mechanical model of the dry friction is illustrated in Figure 2, where γ is tenon angle and ϕ and η are the angle between the contact interface and the vertical direction. A₁ and A₂ are the contact interfaces of the tenon; x(t) is the horizontal displacement of the blade-root; d_{u} and d_{v} are the displacement of the contact interfaces A_{1} and A_{2} , respectively; N_{Ω} is the centrifugal force of blade; N_1 and N_2 are the normal pressure on the two contact interfaces; k_1 , f_1 , and μ_1 are the shearing stiffness, the friction force, and the friction coefficient of the contact interface A₁, respectively. k_2 , f_2 , and μ_2 stand for the shearing stiffness, the friction force, and the friction coefficient of the contact interface A_2 , respectively. w_1 and w_2 are the displacement of the dry friction damper.

In order to facilitate analysis and calculation, the following simplifications are made in this paper.

- (1) The influence of the change of the friction force on the normal pressure acting on the contact interface is ignored.
- (2) The effects of the twisting, the spanwise displacement, and the installation angle of the blade are neglected. Only the transverse displacement of the blade is considered.
- (3) It is assumed that the contact interfaces are always in contact with each other. No separation occurs under the action of the centrifugal force.

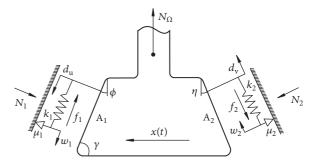


Figure 2: The mechanical model of the dry friction.

The displacements of the two contact interfaces are obtained from the geometric relation in Figure 2:

$$d_{\rm u} = \frac{x(t)}{\cos \gamma},$$

$$d_{\rm v} = \frac{x(t)}{\cos \gamma}.$$
(8)

As shown in Figure 2, when the elasticity of the shearing spring is smaller than the slipping friction force, the contact interfaces are in sticking state. On the contrary, the contact interfaces are in slipping state. Therefore, the mathematical expression of the dry friction force can be written as follows:

$$f_{1} = \begin{cases} k_{1} (d_{u} - w_{1}) & k_{1} |d_{u} - w_{1}| < \mu_{1} N_{1} \\ \mu_{1} N_{1} \operatorname{sgn} (\dot{w}_{1}) & k_{1} |d_{u} - w_{1}| \ge \mu_{1} N_{1}, \end{cases}$$

$$f_{2} = \begin{cases} k_{2} (d_{v} - w_{2}) & k_{2} |d_{v} - w_{2}| < \mu_{2} N_{2} \\ \mu_{2} N_{2} \operatorname{sgn} (\dot{w}_{2}) & k_{2} |d_{v} - w_{2}| \ge \mu_{2} N_{2}. \end{cases}$$

$$(9)$$

According to the mechanical balance and neglecting the influence of the friction force, the positive pressure acting on the contact interface can be expressed as follows:

$$N_1 = N_2 = \frac{N_{\Omega}}{2\cos\gamma}. (10)$$

Assuming that the rotating speed is Ω , the centrifugal force of the blade is

$$N_{\Omega} = \int_{R}^{R+L} \rho A \Omega^2 x \, \mathrm{d}x. \tag{11}$$

It can be seen that the dry friction force is segmented in the period of blade vibration from its mathematical expression. Taking the contact interface A_1 as an example, the contact interfaces of the tenon-mortise will be in sticking state when the elasticity $k_1|d_u-w_1|$ is smaller than the slipping friction force μ_1N_1 . Then the speed of the damper is $\dot{w}_1=0$. The contact interfaces of the tenon-mortise will be in slipping state when the elasticity $k_1|d_u-w_1|$ is bigger than or equal to the slipping friction force μ_1N_1 . Then the speed of the damper is $\dot{w}_1=\dot{d}_u$. Therefore, the speed of the damper can be used to judge the state of the contact interfaces.

$$\dot{w}_1 = \begin{cases} 0 & \text{sticking state} \\ \dot{d}_{\text{u}} & \text{slipping state.} \end{cases}$$
 (12)

Paramete	Disk radius (R)	Blade length (<i>L</i>)	Blade width (b)	Blade thickness (h)	Density (ρ)	Element number (n)	Young's modulus (E)	Poisson's ratio (ν)	Correction factor (k)	Shear stiffness (k_1, k_2)
Value	350 mm	150 mm	60 mm	7 mm	7850 kg/m ³	30	200 GPa	0.3	6/5	$8 \times 10^6 \text{ N/m}$
10 - 4.5										

TABLE 1: The default parameters of the blade system.

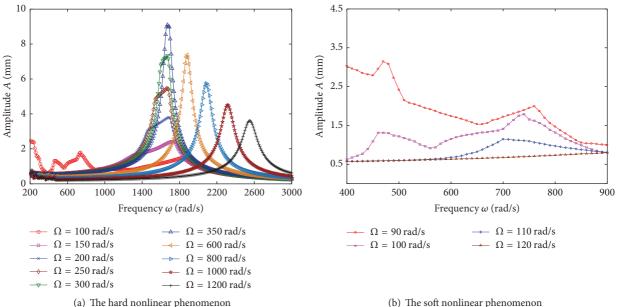


FIGURE 3: The amplitude-frequency response curves of blade at different rotating speeds.

The integral of the above equation is obtained:

$$w_1 = \begin{cases} c_1 & \text{sticking state} \\ d_u + c_2 & \text{slipping state,} \end{cases}$$
 (13)

where c_1, c_2 are constant number. But the values of c_1, c_2 are unknown. Therefore, the influence of c_1 and c_2 can be eliminated by using the displacement difference between the former and later moments of the damper in the process of iterative calculation. Then the expression from formula (13) can be obtained:

$$\Delta w_{1s} = w_{1s} - w_{1(s-1)} = \begin{cases} 0 & \text{sticking state} \\ \Delta d_{\text{us}} & \text{slipping state,} \end{cases}$$
 (14)

where s represents the order of iterations. From (14), it can be seen that the displacement difference $\Delta w_{1s}=0$ when the contact interfaces of the tenon-mortise are in sticking state and $\Delta w_{1s}=\Delta d_{\rm us}$ when the contact interfaces of the tenon-mortise are in slipping state.

The friction forces of the two contact interfaces are all along the contact interface, but in the opposite direction. The components of the friction force in vertical and horizontal direction are

$$f_{v} = f_{1} \sin \gamma - f_{2} \sin \gamma,$$

$$f_{h} = f_{1} \cos \gamma + f_{2} \cos \gamma.$$
(15)

The geometric relationship of the tenon shows that $f_{\rm v}=0$. The stiffness matrix **K**, the mass matrix **M**, and the damping matrix **C** of the system are known. The dynamic equation of the system can be written as follows:

$$\mathbf{M}\ddot{\mathbf{X}} + \mathbf{C}\dot{\mathbf{X}} + \mathbf{K}\mathbf{X} = \mathbf{Q}(t) - \mathbf{F}_{h}(x, t). \tag{16}$$

where $\mathbf{Q}(t)$ is the external excitation and $\mathbf{F}_{h}(x,t)$ is the friction vector.

4. The Natural Characteristics

In this paper, the default parameters of rotating blades are shown in Table 1.

The rotating speed of blade is $\Omega=200$ rad/s. The friction coefficients of the contact interfaces are equal: $\mu_1=\mu_2=0.2$. The harmonic excitation $\mathbf{Q}(t)=P_{\rm a}\sin(\omega t)$ is used to simulate the aerodynamic excitation, where the excitation amplitude $p_{\rm a}=500$ N and the angular frequency of excitation $\omega=1600$ rad/s. This section will analyze the effect of the rotating speed of blade, the friction coefficient, and the excitation amplitude on the nonlinear characteristics of blade, respectively.

4.1. The Effect of Rotating Speeds. Figure 3 shows the amplitude-frequency response curve of the blade-tip at different rotating speeds. And each curve corresponds to different rotating speeds. In Figure 3(a), the amplitude-frequency

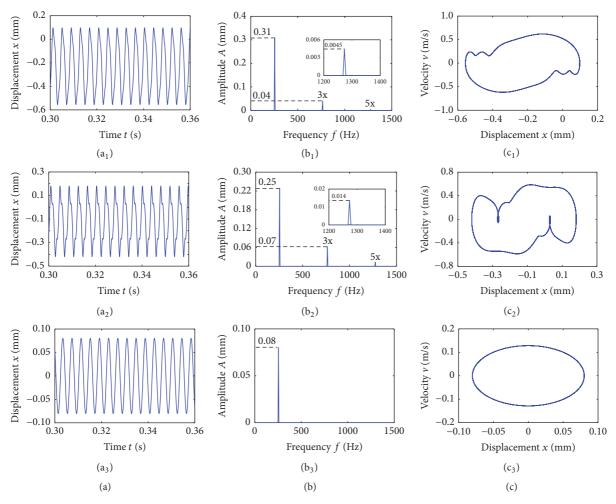


FIGURE 4: The responses of blade-root at different rotating speeds ((a) is the time-domain response, (b) is the frequency spectrum, and (c) is the phase diagram).

response curve of the blade shows a certain hard nonlinear phenomenon when the rotating speed of blade is less than 350 rad/s. The resonance peak of the blade has a tendency of shift to the right. And the value is obviously lower than that of the linear phenomenon. At the same time, the resonance peak of blade increases with the rotating speed. When the rotating speed is higher than 350 rad/s, the amplitude-frequency response curve is no longer nonlinear. However, the resonant frequency of the blade increases gradually. And the resonance peak decreases gradually with the rotating speed. It can also be seen from the diagram that when the rotating speed is lower, the blade also has a large response amplitude in the low-frequency area. Figure 3(b) shows the amplitudefrequency response curve of blade at slow speed. In addition to the higher response amplitude at low frequencies, the amplitude-frequency response curve exhibits a soft nonlinear phenomenon when the excitation angular frequency ranges from 600 rad/s to 900 rad/s. There is the same trend as the result which is obtained in [15]. In the current excitation frequency range, which is far less than the first natural frequency, the blade should behave as a rigid body. But the

soft nonlinear phenomenon disappeared immediately with the increase of the rotating speed of blade.

This paper takes the response of the blade-root as an example. The transient response characteristics of the blade are observed because of the friction force acting on the tenon of blade. In order to make the response more obvious, the excitation angle frequency is 1600 rad/s which is close to the first natural frequency of the blade. When the rotating speeds are 100 rad/s, 200 rad/s, and 600 rad/s, the time-domain response diagram, the frequency spectrum, and the phase diagram of blade-root are shown as (a_1) , (b_1) , (c_1) ; (a_2) , (b_2) , (c_2) ; and (a_3) , (b_3) , (c_3) of Figure 4, respectively. When the rotating speeds are slow, such as 100 rad/s and 200 rad/s, the time-domain waveform shows a harmonic phenomenon and the response amplitude decreases because of the nonlinear dry friction force. There are not only dominant frequency, but also obvious 3x and 5x components in the frequency spectrum. And the phase diagram of the blade-root is no longer smooth, indicating that the motion of the blade is complicated. When the rotating speed is higher, such as 600 rad/s, the time-domain waveform of blade-root shows that a simple

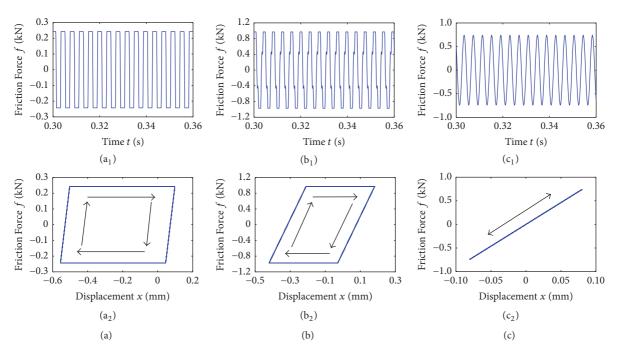


FIGURE 5: The variation curves of dry friction force at different rotating speeds (subscript 1 represents the variation curve of dry friction force and subscript 2 represents the hysteresis loop).

harmonic variation and the response amplitude are small. There is only dominant frequency in the frequency spectrum. It proves that there is not nonlinear phenomenon at this moment. The phase diagram changes smoothly and regularly.

In Figure 5, (a_1) and (a_2) , (b_1) and (b_2) , and (c_1) and (c₂) show the variation curves of dry friction force and the hysteresis loops when the rotating speeds are 100 rad/s, 200 rad/s, and 600 rad/s, respectively. They can reveal the variation of dry friction force at different rotating speeds. When the rotating speeds are 100 rad/s and 200 rad/s, the dry friction force shows a wave clipping phenomenon with time and will keep constant for a period after it reaches the maximum value. The maximum value of dry friction force will increase with the rotating speed. But the time of the dry friction force at its peak will gradually decrease. The dry friction force varies piecewise linearly with the displacement of blade-root under these speeds. The hysteresis loop of dry friction force is a closed parallelogram. And the area of it represents the energy consumed by dry friction. The area of the hysteresis loop (2 \times the peak of dry friction force \times slipping distance = 0.76) in Figure $5(b_2)$ is larger than that $(2 \times \text{the peak of dry friction force} \times \text{slipping distance} =$ 0.29) in Figure $5(a_2)$. The result illustrates that the energy consumption of dry friction is larger when the rotating speed is 200 rad/s. That makes the response amplitude of blade-root smaller. When the rotating speed of the blade is 600 rad/s, the dry friction force presents a simple harmonic variation with time and the hysteresis loop is a reciprocating straight line. There is no energy consumption at this moment.

4.2. The Effect of Friction Coefficient. The dry friction force and the vibration reduction characteristics of the blade are

directly affected by the change of friction coefficient. In order to research the effect of friction coefficient on the vibration reduction characteristics, the amplitude-frequency curves of blade-tip at different friction coefficients are obtained when the rotating speeds are 200 rad/s and 400 rad/s, respectively. It can be seen form Figure 6(a) that when the friction coefficient of the contact interfaces is small, the amplitudefrequency curves of the blade-tip exhibit a certain hard nonlinear phenomenon. And the response amplitude of the blade increases and the nonlinear phenomenon decreases gradually with the friction coefficient in resonance region. There is no longer nonlinearity in the amplitude-frequency curve of blade-tip when the friction coefficient is bigger than before. It can be obtained by comparing Figure 6(a) with Figure 6(b) that the response amplitude of the blade in resonance region is larger and the nonlinear phenomenon is relatively weak when the friction coefficients are the same and the rotating speed is higher. Therefore, the effect of dry friction vibration reduction is more obvious when the friction coefficient is small and the rotating speed is slow.

In order to further research the effect of the friction coefficient on the vibration reduction characteristics of blade. The transient response of the blade-root at different friction coefficients is observed. When the friction coefficients are 0.2, 0.4, and 0.8, the time-domain response diagram, the frequency spectrum, and the phase diagram of blade-root are shown as (a_1) , (b_1) , (c_1) ; (a_2) , (b_2) , (c_2) ; and (a_3) , (b_3) , (c_3) of Figure 7, respectively. When the friction coefficients are small, such as 0.2 and 0.4, the time-domain waveform shows a harmonic phenomenon and the response amplitude decreases because of the nonlinear dry friction force. There is not only dominant frequency, but also obvious 3x and

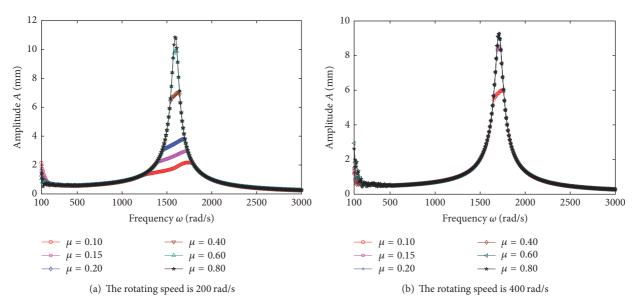


FIGURE 6: The amplitude-frequency response curves of blade at different friction coefficients.

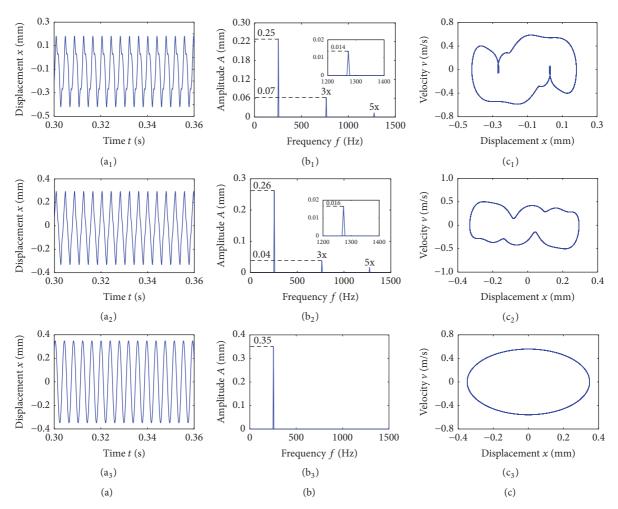


FIGURE 7: The responses of blade-root at different friction coefficients ((a) is the time-domain response, (b) is the frequency spectrum, and (c) is the phase diagram).

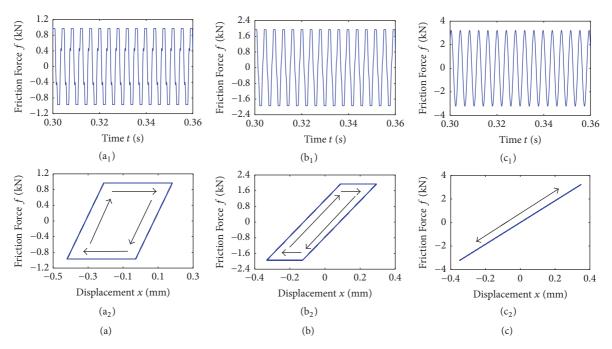


FIGURE 8: The variation curves of dry friction force at different friction coefficients (subscript 1 represents the variation curve of dry friction force and subscript 2 represents the hysteresis loop).

5x components in the frequency spectrum. And the phase diagram of the blade-root is also shown as a complicated curve. When the friction coefficient is bigger, such as 0.8, the time-domain waveform of blade-root shows a simple harmonic variation and the response amplitude is bigger than that of before. There is only dominant frequency in the frequency spectrum. And the phase diagram changes smoothly and regularly.

In Figure 8, (a_1) and (a_2) , (b_1) and (b_2) , and (c_1) and (c_2) show the variation curves of dry friction force and the hysteresis loops when the friction coefficients are 0.2, 0.4, and 0.8, respectively. They can reveal the variation of dry friction force at different friction coefficients of contact interfaces. When the friction coefficients are 0.2 and 0.4, the dry friction force shows a wave clipping phenomenon with time and will keep constant for a period after it reaches the maximum value. The maximum value of dry friction force will increase with the friction coefficient. But the time of the dry friction force at its peak will gradually decrease. The dry friction force varies piecewise linearly with the displacement of bladeroot. Meanwhile, the hysteresis loop of dry friction force is a closed parallelogram. And the area of the parallelogram ($2 \times$ the peak of dry friction force × slipping distance) decreases gradually with the increase of the friction coefficient. The vibration dissipation by dry friction is low when the area of the parallelogram is small. The dry friction force presents a simple harmonic variation with the time and the hysteresis loop is a reciprocating straight line when the friction coefficient is 0.8. And there is no energy consumption.

4.3. The Effect of Excitation Amplitude. Considering the soft and hard nonlinear phenomena of the amplitude-frequency

curves at low and high rotating speed, the effect of different excitation amplitudes on the vibration reduction characteristics of the blade at a high or low speed is studied. Figure 9 shows the amplitude-frequency response curves of blade-tip at different excitation amplitudes when the rotating speeds are 200 rad/s and 400 rad/s, respectively. Each curve corresponds to different excitation amplitudes. It can be seen from Figure 9(a) that the nonlinear phenomenon of the amplitude-frequency curves is more obvious with the increase of excitation amplitude. But the resonance peak value of blade increases and the resonance zone also expands. There is also a large response amplitude at the low frequency when the excitation amplitude is too large. That is extremely dangerous. In Figure 9(b), the amplitude-frequency curve of the blade-tip does not show a nonlinear phenomenon when the excitation amplitude is small. With the increase of excitation amplitude, the nonlinear phenomenon is more and more obvious. And the value of resonance peak also increases gradually. It can be known by comparing Figure 9(a) with Figure 9(b) that the effect of dry friction vibration reduction is obvious in the resonant region when the rotating speed is slow. And the effect of vibration reduction is related to the value of excitation amplitude.

In order to further research the effect of excitation amplitude on the vibration reduction characteristics of blade, the transient response characteristics of the blade-root at different excitation amplitudes are observed. When the excitation amplitudes are $100 \, \text{N}$, $500 \, \text{N}$, and $1000 \, \text{N}$, the timedomain response diagram, the frequency spectrum, and the phase diagram of blade-root are shown as (a_1) , (b_1) , (c_1) ; (a_2) , (b_2) , (c_2) ; and (a_3) , (b_3) , (c_3) of Figure 10, respectively. When the excitation amplitude is small, such as $100 \, \text{N}$,

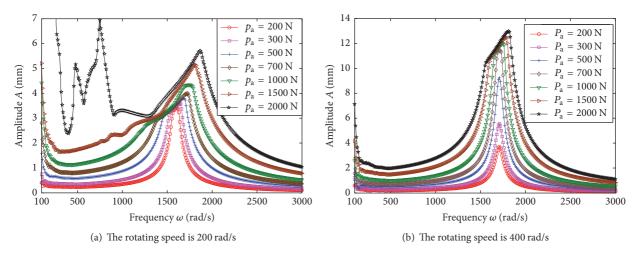


FIGURE 9: The amplitude-frequency response curves at different excitation amplitudes.

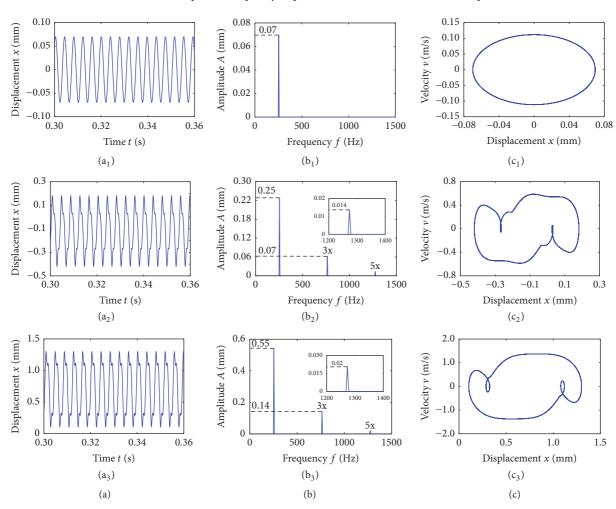


FIGURE 10: The responses of blade-root at different excitation amplitudes ((a) is the time-domain response, (b) is the frequency spectrum, and (c) is the phase diagram).

the time-domain waveform of blade-root shows a simple harmonic variation. There is only dominant frequency in the frequency spectrum. And the phase diagram is smooth and varies regularly. When the excitation amplitudes are bigger than former, such as 500 N and 1000 N, the time-domain

waveform shows a harmonic phenomenon because of the nonlinear dry friction force. There is not only dominant frequency but also obvious 3x and 5x components in the frequency spectrum. And the phase diagram of the bladeroot is also shown as a complicated curve. Compared with

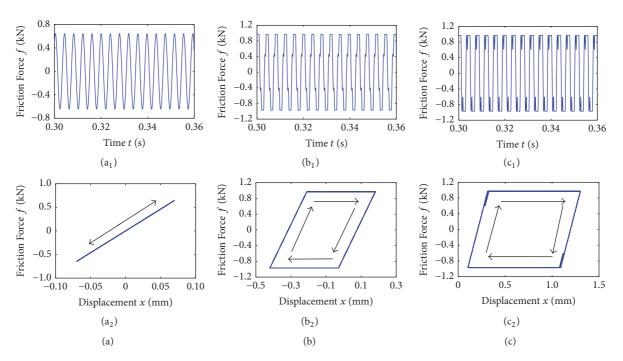


FIGURE 11: The variation curves of dry friction force at different excitation amplitudes (subscript 1 represents the variation curve of dry friction force and subscript 2 represents the hysteresis loop).

 (b_1) , (b_2) , and (b_3) , it is found that the response amplitude of the blade-root increases with the excitation amplitude.

In Figure 11, (a_1) and (a_2) , (b_1) and (b_2) , and (c_1) and (c_2) show the variation curves of dry friction force and the hysteresis loops when the excitation amplitudes are 100 N, 500 N, and 1000 N, respectively. They can reveal the variation of dry friction force at different excitation amplitudes. The dry friction force represents a simple harmonic variation and the hysteresis loop is a reciprocating straight line when the excitation amplitude is 100 N. The dry friction does not consume energy at this moment. The dry friction force shows a wave clipping phenomenon with time and will keep constant for a period after it reaches the maximum value when the excitation amplitudes are 500 N and 1000 N. The maximum value of dry friction force will not change with the increase of the excitation amplitude. But the time of the dry friction force at its peak will gradually increase. The dry friction force varies piecewise linearly with the displacement of blade-root. Meanwhile, the hysteresis loop of dry friction force is a closed parallelogram. And the area of the parallelogram ($2 \times$ the peak of dry friction force \times slipping distance) increases gradually with the excitation amplitude. The vibration dissipation by dry friction is large when the area of the parallelogram is large.

5. Discussion

The constraining force of the blade changes with the rotating speed. The constraining force is small so that the tenonmortise is in completely loosing state when the rotating speed of the blade is slow. The blade will show the whole rigid body vibration under the action of external excitation.

And the amplitude-frequency curve of the blade has a soft nonlinear phenomenon in the low-frequency range. The constraining force increases rapidly with the square of the speed ($N_{\Omega} \propto \Omega^2$). The dry friction force shows piecewise linearly change with the displacement of blade-root when the rotating speed is less than 350 rad/s. That makes the amplitude-frequency curve of blade represent a certain hard nonlinear phenomenon. When the rotating speed continues to increase, the constraining force is too large so that the tenon and mortise are tightly attached together. Therefore, the dry friction force shows linearly change with the displacement of blade-root. And there is no nonlinear phenomenon in the amplitude-frequency curve of the blade.

The dry friction can consume the energy generated by the vibration of the blade when the blade is excited by the external excitation, that reduces the response amplitude of the blade. It is known that the sliding friction force of the contact interface is proportional to the friction coefficient ($f \propto \mu$). When the friction coefficient is small, the tenon and the mortise are easy in a relatively slipping state. This will result in obvious effect of the dry friction vibration reduction. On the contrary, the tenon and the mortise will be in a sticking state for a longer time if the friction coefficient is bigger. And the effect of the dry friction vibration reduction is weakened.

Although the effect of the dry friction vibration reduction is different when the blade is at a lower speed and higher speed, respectively, the energy dissipation of dry friction is also affected by the friction coefficient. But the rotating speed of blade, the friction coefficient, and the amplitude of the external excitation are affected by each other. Therefore, the dry friction vibration reduction has different results in different situations.

6. Conclusion

In this paper, the effect of the rotating speed of the blade, the friction coefficient of contact interface, and the amplitude of the external excitation on the natural characteristics of the blade is studied, respectively, based on the ideal dry friction model and finite element method. The conclusions are as follows.

- (1) The amplitude-frequency curve of the blade has a soft nonlinear phenomenon at the low-frequency range when the rotating speed is small. The soft nonlinear phenomenon disappears gradually with the increase of the rotating speed. And the amplitude-frequency curve begins to show a certain hard nonlinear phenomenon in the resonance region of the blade. There is an obvious effect of dry friction vibration reduction. But when the rotating speed is too high, there is no nonlinear phenomenon in the amplitude-frequency curve of blade and the effect of dry friction vibration reduction disappears. Therefore, it is important to pay more attention to the structure design of tenon-mortise. There are different vibration reduction effects with different structural parameters.
- (2) The change of the friction coefficient has a great effect on the vibration reduction characteristics of the blade. When the friction coefficient is small, the amplitude-frequency curve of blade is easy to show nonlinear phenomenon. And the effect of the dry friction vibration reduction is obvious. But with the increase of the friction coefficient, both the nonlinear phenomenon and the effect of dry friction vibration reduction begin to decrease.
- (3) The change of the excitation amplitude also has a certain effect on the vibration reduction characteristics of the blade. The nonlinear phenomenon of the amplitude-frequency curves is more obvious with the increase of the excitation amplitude. Although the effect of dry friction vibration reduction is increased, the blade response amplitude also increases. Therefore, it is very important to prevent the blade from being excited by the external excitation with too large fluctuation.

Conflicts of Interest

The authors declare that there are no conflicts of interest regarding the publication of this paper.

Acknowledgments

The project is supported by the China Natural Science Funds (no. 51575093) and the Fundamental Research Funds for the Central Universities (nos. N160313001 and N140301001).

References

- [1] Ö. Turhan and G. Bulut, "On nonlinear vibrations of a rotating beam," *Journal of Sound and Vibration*, vol. 322, no. 1-2, pp. 314–335, 2009.
- [2] J. Chung and H. H. Yoo, "Dynamic analysis of a rotating cantilever beam by using the finite element metho," *Journal of Sound & Vibration*, vol. 249, no. 1, pp. 147–164, 2002.

[3] G.-C. Tsai, "Rotating vibration behavior of the turbine blades with different groups of blades," *Journal of Sound and Vibration*, vol. 271, no. 3-5, pp. 547–575, 2004.

- [4] Y. J. Yan, P. L. Cui, and H. N. Hao, "Vibration mechanism of a mistuned bladed-disk," *Journal of Sound and Vibration*, vol. 317, no. 1-2, pp. 294–307, 2008.
- [5] J.-H. Park, H.-Y. Park, S.-Y. Jeong, S.-I. Lee, Y.-H. Shin, and J.-P. Park, "Linear vibration analysis of rotating wind-turbine blade," *Current Applied Physics*, vol. 10, no. 2, pp. S332–S334, 2010.
- [6] Y. S. Choi and K. H. Lee, "Investigation of blade failure in a gas turbine," *Journal of Mechanical Science & Technology*, vol. 24, no. 10, pp. 1969–1974, 2010.
- [7] B. O. Al-Bedoor and A. A. Al-Qaisia, "Stability analysis of rotating blade bending vibration due to torsional excitation," *Journal of Sound and Vibration*, vol. 282, no. 3–5, pp. 1065–1083, 2005.
- [8] M. H. Yao, Y. P. Chen, and W. Zhang, "Nonlinear vibrations of blade with varying rotating speed," *Nonlinear Dynamics*, vol. 68, no. 4, pp. 487–504, 2012.
- [9] H. Lee, J. S. Song, S. J. Cha, and S. Na, "Dynamic response of coupled shaft torsion and blade benging in rotor blade system," *Journal of Mechanical Science & Technology*, vol. 27, no. 9, pp. 2585–2597, 2013.
- [10] C.-f. Li, H.-x. She, W. Liu, and B.-c. Wen, "The influence of shaft's bending on the coupling vibration of a flexible bladerotor system," *Mathematical Problems in Engineering*, vol. 1, Article ID 7313956, 19 pages, 2017.
- [11] C. Li, H. She, Q. Tang, and B. Wen, "The effect of blade vibration on the nonlinear characteristics of rotor-bearing system supported by nonlinear suspension," *Nonlinear Dynamics*, vol. 89, no. 2, pp. 987–1010, 2017.
- [12] M. Allara, "A model for the characterization of friction contacts in turbine blades," *Journal of Sound and Vibration*, vol. 320, no. 3, pp. 527–544, 2009.
- [13] J. Hartog, "LXXIII. Forced vibrations with combined viscous and coulomb damping," *The London, Edinburgh, and Dublin Philosophical Magazine and Journal of Science*, vol. 9, no. 59, pp. 801–817, 2009.
- [14] W. D. Iwan, *The Dynamic response of bilinear hysteretic systems*, California Institute of Technology, 1961.
- [15] B. D. Yang and C. H. Menq, "Characterization of contact kinematics and application to the design of wedge dampers in turbomachinery blading: Part 1-stick-slip contact kinematics," *Journal of Engineering for Gas Turbines and Power*, vol. 120, no. 2, pp. 410–417, 1998.
- [16] E. Ciğeroğlu and H. N. Özgüven, "Nonlinear vibration analysis of bladed disks with dry friction dampers," *Journal of Sound and Vibration*, vol. 295, no. 3–5, pp. 1028–1043, 2006.
- [17] Z. L. Xu, G. B. Shang, and Q. L. Wu, "Dry friction force model and dynamic response analysis of blades with loosely assembled dovetail attachment," *Journal of XiAn JiaoTong University*, vol. 43, no. 7, pp. 1–5, 2009 (Chinese).
- [18] G. B. Shang, Y. L. Liu, and Z. L. Xu, "Effects of parameters of a blade system with loosely assembled dovetail attachment on dry friction damping," *Journal of Vibration and Shock*, vol. 31, no. 19, pp. 180–182, 2012 (Chinese).
- [19] J. H. Wang and W. K. Chen, "Investigation of the vibration of a blade with friction damper by HBM," *Journal of Engineering for Gas Turbines & Power*, vol. 115, no. 2, pp. 660–664, 1993.
- [20] Q. Ding and X. Zhou, "Analytical method determining resonant response of blade with dry friction damper," *Transactions of Tianjin University*, vol. 13, no. 4, pp. 291–296, 2007.

[21] Q. Ding and Y. Chen, "Analyzing resonant response of a system with dry friction damper using an analytical method," *Journal of Vibration and Control*, vol. 14, no. 8, pp. 1111–1123, 2008.

- [22] S. K. Sinha, "Dynamic characteristics of a flexible bladed-rotor with Coulomb damping due to tip-rub," *Journal of Sound and Vibration*, vol. 273, no. 4-5, pp. 875–919, 2004.
- [23] D. Cao, X. Gong, D. Wei, S. Chu, and L. Wang, "Nonlinear vibration characteristics of a flexible blade with friction damping due to tip-rub," *Shock and Vibration*, vol. 18, no. 1-2, pp. 105–114, 2011.
- [24] A.-L. Wang and Q. Long, "Forced response characteristics of bladed disks with mistuning non-linear friction," *Journal of Central South University of Technology (English Edition)*, vol. 18, no. 3, pp. 679–684, 2011.
- [25] L. Zhang, H.-Q. Yuan, Q.-K. Han, S.-M. Yang, L. Song, and Y. Li, "Vibration analysis of mistuned bladed disk system based on microslip friction model," *Zhendong Gongcheng Xuebao*, vol. 25, no. 3, pp. 289–293, 2012.
- [26] L. Pust, L. Pesek, and A. Radolfová, "Blade couple with dry friction connection," *Applied & Computational Mechanics*, vol. 9, no. 1, pp. 31–40, 2015.
- [27] D. Zhang, J. Fu, Q. Zhang, and J. Hong, "An effective numerical method for calculating nonlinear dynamics of structures with dry friction: application to predict the vibration response of blades with underplatform dampers," *Nonlinear Dynamics*, vol. 88, no. 1, pp. 223–237, 2017.
- [28] O. Ozaydin and E. Ciğeroğlu, "Effect of dry friction damping on the dynamic response of helicopter tail shaft," *Rotating Machinery, Hybid Test Methods, Vibro-Acoustics Laser Vibrometry*, vol. 8, no. 1, pp. 23–30, 2017.

Hindawi Shock and Vibration Volume 2018, Article ID 9632523, 22 pages https://doi.org/10.1155/2018/9632523

Research Article

Seismic Performance of Base-Isolated Precast Concrete Shear Wall Structure with AHW Connections

Wei Wang (1), Aiqun Li, 2,3 and Xingxing Wang 1

¹School of Architecture and Civil Engineering, Jiangsu University of Science and Technology, 2 Mengxi Road, Zhenjiang 212003, China ²Beijing Advanced Innovation Center for Future Urban Design, Beijing University of Civil Engineering and Architecture, 1 Zhanlanguan Road, Beijing 100044, China

Correspondence should be addressed to Wei Wang; wangweidimias@sina.com

Received 7 December 2017; Revised 25 February 2018; Accepted 7 March 2018; Published 22 April 2018

Academic Editor: Aly M. Aly

Copyright © 2018 Wei Wang et al. This is an open access article distributed under the Creative Commons Attribution License, which permits unrestricted use, distribution, and reproduction in any medium, provided the original work is properly cited.

To improve the seismic performance and seismic reliability of precast concrete shear wall (PCSW) structure with improved assembly horizontal wall connections (AHW connections), base isolation technology was proposed to be applied in the PCSW structure. Two 1/4-scaled structure models using the improved AHW connections were constructed: a lead-rubber bearing (LRB) base-isolated PCSW structure model and a base-fixed PCSW structure model. Shaking table tests were conducted on these two models with three strong ground motions to assess the seismic performance of the structures. It was found that the improved AHW connections in the base-isolated PCSW structure are useful and effective and that they fulfil the requirements to be met by the connections to withstand an earthquake. In addition, the maximum absolute acceleration and base shear force of the base-isolated PCSW structure model were less than those of the base-fixed PCSW structure model, and the isolation effect on the absolute acceleration responses and base shear responses increased with increase in the intensity of ground motions. In a word, the seismic performance and seismic reliability of PCSW structures can be effectively improved using base isolation technology. After this investigation, the seismic responses of the base-isolated PCSW structure model were numerically simulated using OpenSees software. There was a reasonable agreement between the numerically simulated results and test results; thus, the numerical simulation method and analysis model used for the base-isolated PCSW structure model were verified.

1. Introduction

Cast-in-place concrete shear wall structures (CCSW structures) are widely used throughout the world for their high strength and stiffness. Unlike in the case of CCSW structures, part of the field work can be transferred to the plant in the case of precast concrete shear wall (PCSW) structures; this can save a large amount of labour, reduce material consumption, and shorten the time for construction projects. Thus, PCSW structures can support the development of industrialised construction [1–6].

1.1. Horizontal Connection. Assembly wall connections are the key elements of PCSW structures, which consist of assembly vertical wall connections and assembly horizontal wall connections (AHW connections). Assembly vertical wall

connections are normally employed as energy dissipation connections or emulation connections. However, reliable AHW connections can normally guarantee the normal function of the PCSW structures.

There are three methods of assembling the AHW connections in the PCSW structures: (a) splicing longitudinal rebars using sleeves or stirrups combined with high-strength mortar [7–9]; (b) tying together the horizontal connections using unbounded posttensioned (UPT) precast concrete wall plates [2, 10, 11]; (c) connecting the longitudinal rebars using bolted connections [12, 13]. Several studies [1, 8, 11] indicate that the required mechanical properties of the AHW connections can be achieved with the assembly connection methods mentioned above by adopting effective construction measures.

³School of Civil Engineering, Southeast University, 2 Sipailou, Nanjing 210096, China

There are some studies on the seismic performance of PCSW structures with UPT connections and sleeve connections combined with high-strength mortar. One such study [5, 6] presents shaking table tests and numerical analysis of the UPT wall structures. The results show that the UPT wall structures exhibit no residual deformation and show minimal damage during an earthquake. Some studies [1, 14] indicate that the seismic performance of the PCSW structure with AHW connection (i.e., longitudinal rebars spliced using sleeves combined with high-strength mortar) and the CCSW structure are similar. However, there has been little investigation on the seismic behaviour of PCSW structures with AHW connection using bolted connections.

1.2. Base Isolation Technology. Seismic isolation is a useful technology to reduce the seismic forces acting on structures. Base-isolated systems are effective because of their excellent energy dissipation characteristics and flexibility. Over the years, many studies have dealt with reliability analysis and reliability-based optimization of base-isolated systems including uncertainties such as isolation device properties and ground motion characteristics [15-17]. The results indicate that base isolation technology can improve the seismic reliability of structures subjected to earthquakes [18–20]. Lead-rubber bearing (LRB) is one of the most useful isolation devices in practice. During an earthquake, the LRBs dissipate most of the input earthquake energy. After the earthquake, because of the recentering capacity of the LRBs, the original position (corresponding to zero deformation) can be restored [21-23]. In recent years, LRBs have been extensively employed in structures to reduce the seismic effects because of their energy dissipation and recentering capacity [24, 25]. In addition, one such study [26] presents sensitivity analysis on mechanical characteristics of LRBs. The results show that the lead core radius is the dominant parameter in affecting LRBs' performance.

1.3. Scope of Present Study. As base isolation can reduce the seismic forces acting on the structures, the forces acting on the base-isolated structures are less than those on the base-fixed structures; accordingly, the forces acting on the AHW connections in the base-isolated PCSW structures are lower. In other words, the performance of the AHW connections can be improved in the base-isolated PCSW structures. However, there has been little study on the seismic properties of base-isolated PCSW structures with AHW connections.

An improved AHW connection for PCSW structures has been presented in literature [1], and shaking table tests, and numerical simulation have been performed to evaluate the seismic performance of a base-fixed PCSW structure with the improved AHW connections [1]. The tested results indicate that there will be some cracks in the AHW connection area of the PCSW structure with improved AHW connections during server earthquakes. In order to reduce the cracks in the AHW connection area of the PCSW structure, base isolation technology is proposed to be applied in the PCSW structure.

This paper presents the seismic properties of a base-isolated PCSW structure model with the improved AHW connections. To study the seismic performance and energy dissipation capacity of the base-isolated PCSW structures, two 1/4-scaled models of the PCSW structure were built: a base-isolated PCSW structure model and a base-fixed PCSW structure model. Shaking table tests of the two models were conducted, and the absolute acceleration responses and the displacement responses of the base-isolated PCSW structure model were measured to reveal the dynamic properties of the structure. In addition, the seismic behaviour of the improved AHW connections was studied. Finally, the acceleration responses in the fourth storey and shear force-displacement responses in the isolation storey of the base-isolated PCSW structure were numerically simulated using OpenSees software.

2. Improved AHW Connection

The improved AHW connection technology used to realize the horizontal connection of the precast shear wall is shown in Figure 1 [1]. Connection steel plates and bolts are used to make the AHW connection between the lower and upper wall plates. The assembly sequence of the improved AHW connection is as follows.

- (1) Weld the longitudinal rebars to their corresponding connection steel plates (see Figure 1(a)).
- (2) Before hoisting the precast wall plates, cast a layer of high-strength mortar on the top of the lower wall plate; during the hoisting of the precast wall plates, insert the connection steel plates of the lower wall plate into the reserved channels of the upper wall plate at bottom (see Figure 1(b)).
- (3) Adjust the positions of the upper and lower wall plates to align the reserved bolt holes in the connection steel plates and wall plates, insert the bolts in the aligned holes, and tighten the nuts to complete the improved AHW connection (see Figure 1(c)).

3. Description of the Experiment

3.1. Test Specimens. A four-storey base-isolated PCSW structure prototype was designed according to the "code for design of concrete structures" (GB50010-2010) of China [27]. Then, two four-storey 1/4-scaled superstructure models of the base-isolated PCSW structure were constructed. The similitude coefficients of the model are presented in Table 1. One is mounted on four LRBs to form the base isolation model (denoted as Specimen A); the other is bolted to the shaking table to form the base-fixed structure model (denoted as Specimen B). The drawings and images of Specimens A and B are shown in Figure 2 [1]. The scaled model of the superstructure has a dimension of 1400×1400 mm in the plan view; the thickness of the shear walls is 35 mm; the height of the storey is 750 mm; and the cross section of the coupling beams is 100×100 mm.

Ready-mixed concrete was used for casting the structure. The design compressive strength of the concrete was 22 MPa.

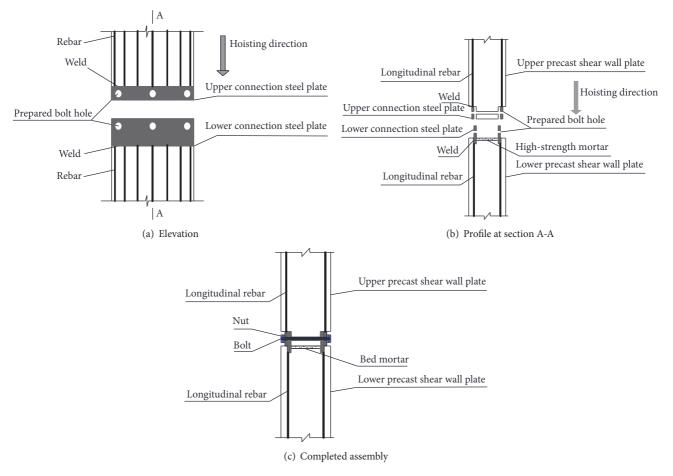


FIGURE 1: Improved AHW connection [1].

TABLE 1: Similitude coefficients.

Physical quantity	Ratio of similitude
Mass	$S_m = 1/16$
Length	$S_L = 1/4$
Elastic modulus	$S_E = 1$
Acceleration	$S_a = 1$
Velocity	$S_V = 1/2$
Displacement	$S_U = 1/4$
Volume	$S_V = 1/64$
Time	$S_t = 1/2$
Frequency	$S_f = 2$
Force	$S_F = 1/16$

Table 2 presents the measured mechanical properties of the concrete.

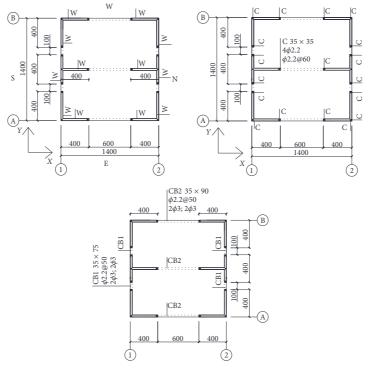
Galvanized iron wires of ϕ 2.2 were used for the longitudinal rebars and the transverse rebars in the shear walls and for the stirrups of the coupling beams and columns. Galvanized iron wires of ϕ 3 were used for the longitudinal rebars of the beams in the *X*-direction. The measured mechanical properties of the galvanized iron wires are presented in Table 3.

Table 2: Measured mechanical properties of concrete.

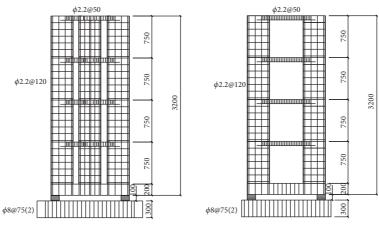
Specimen	Cubic compressive strength fcu (MPa)	
1st storey	21.63	
2nd storey	22.26	
3rd storey	22.33	
4th storey	21.10	
Isolation storey	25.76	

Three types of connection steel plates were used; their dimensions are shown in Figure 3. The thickness of the steel plates is 3 mm; the diameter of the bolt holes is 8.5 mm; the 3 mm diameter holes are used for connecting the rebars. Figure 4 shows the improved AHW connections, transverse rebars, and longitudinal rebars used in the model.

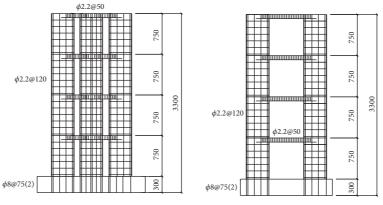
The weights of the base beam, and the wall and floor of each storey are 2.48 t, 0.35 t, and 0.25 t, respectively. Based on the scaling relation, the added mass of each storey is 0.6 t, and accordingly the total weight of the model is 7.06 t. Highstrength mortar was used to fix the gravity load trough to the structure.



(a) Plan layout of a standard storey (unit: mm)



(b) Distribution of rebars in Specimen A (unit: mm)



(c) Distribution of rebars in Specimen B (unit: mm)

FIGURE 2: Continued.



(d) Images of the installations of Specimens A and B

FIGURE 2: Test models and drawings.

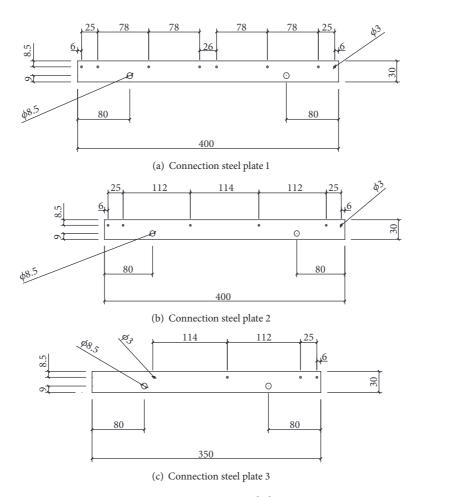


FIGURE 3: Connection steel plates.

3.2. LRB. The LRBs were formed by bonding 14 rubber layers and 13 shim layers alternatively (Figure 5). Table 4 summarizes the related parameters of the LRB. The mechanical properties of the LRBs were tested in the previous cyclic

loading experiments. Figure 6 depicts the load-deformation curves of the LRB with 100% shear strain and 250% shear strain. It is observed that the lateral stiffness of the LRB shows approximately a bilinear mode.

m 2.16 1 1 1 1 1		1 . 1	
TABLE 3: Measured mechanical	properties of o	galvanized	iron wires
THEE S. MICUSUICA INCCHAINCAI	properties or ,	gair airidea	ii oii mii co.

Mechanical properties	Diameter (mm)	Yield strength (MPa)	Tensile strength (MPa)	Elongation (%)	Elastic modulus (MPa)
φ2.2	2.2	241.6	330.6	19.7	1.8×10^{5}
φ3	3	235.7	319.6	20.2	1.8×10^{5}

TABLE 4: Parameters of LRB.

Scale parameter	Value	Force property parameter	Value
Diameter d_0 (mm)	100	Rubber shear modulus G (N/mm2)	0.4
Rubber height t_r (mm)	1.5	Equivalent lateral stiffness (kN/mm)	0.24
Total rubber height T_r (mm)	21	Equivalent damping ratio	0.11
Shim height t_s (mm)	4	Post-yielding stiffness (kN/mm)	0.13
Total shim height (mm)	52	Yield displacement (mm)	0.81
Total height (mm)	89	Initial lateral stiffness (kN/mm)	1.21
Diameter of lead (mm)	10		

Note. Mechanical parameters of the LRB with 100% shear strain.

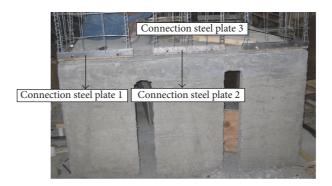


FIGURE 4: Construction of precast shear wall plates.



FIGURE 5: Image of LRB.

3.3. Test Procedure and Measurements. The dimension of the shaking table is 4×6 m; the maximum acceleration is 1.5 g. During testing, the shaking table was driven in the *Y*-direction of the structure model.

Three ground motions were selected: the 1968 Castaic (CA) ground motion, the 1952 Taft (TA) ground motion, and a 2015 artificial (AR) ground motion; these motions are compatible with the response spectrum for soil type II in the "code for seismic design of buildings," GB 50011-2010 [27]. Figure 7 shows the acceleration time histories corresponding to the three ground motions with 100% PGA

scale, and Figure 8 shows the response spectrum curves of the acceleration time histories with a damping ratio of 5% ((peak ground acceleration (PGA) = 400 gal)).

To excite the specimens, ground motions with PGAs of 70 gal, 200 gal, and 400 gal were inputted in the shaking table, corresponding to the intensities of minor earthquakes, moderate earthquakes, and rare earthquakes, respectively, with a seismic fortification intensity of 8 degrees, as mentioned in the "code for seismic design of buildings" (GB50011-2010) [28]. Further, a white-noise ground motion (PGA = 25 gal) in the *Y*-direction was inputted in the shaking table to identify

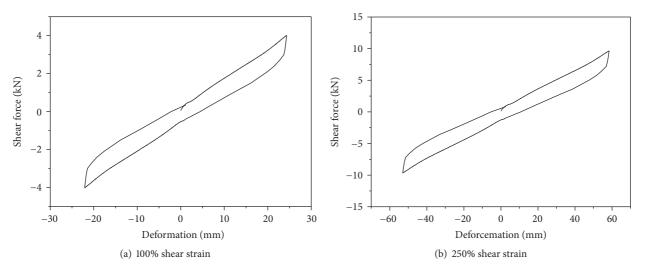


FIGURE 6: Hysteresis curve of LRB.

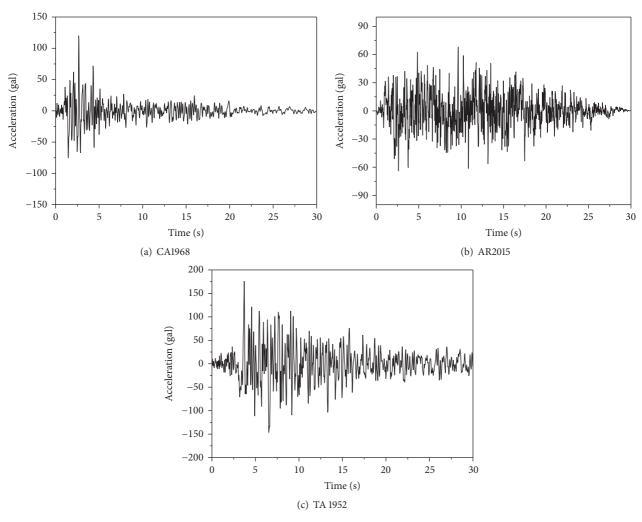


FIGURE 7: Acceleration time histories of input ground motions.

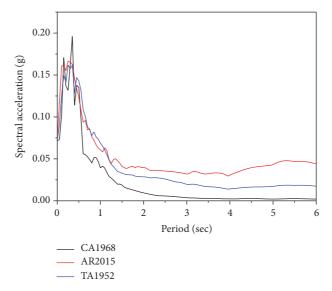


FIGURE 8: Response spectrum curves (damping ratio: 5%) for input ground motions with PGA = 400 gal.





(a) Cracks in coupling beams

(b) Cracks in shear walls

FIGURE 9: Typical crack distribution in specimens.

TABLE 5: Test cases.

Test case	Input excitation	PGA (gal)
Rnd 1	White noise	25
Test 1	CA (1968), TA (1952), AR (2015)	70
Rnd 2	White noise	25
Test 2	CA (1968), TA (1952), AR (2015)	200
Rnd 3	White noise	25
Test 3	CA (1968), TA (1952), AR (2015)	400
Rnd 4	White noise	25

the dynamic properties of the specimens. The test sequence is presented in Table 5.

The absolute acceleration and absolute displacements of the storeys of the test models were measured using piezoelectric accelerometers and displacement transducers, respectively.

4. Experimental Results

4.1. Test Phenomenon and Failure Modes. Typical cracks in the specimens are shown in Figure 9. It should be noted that the cracks in the structure model are relatively smaller than the whole structure, and it is difficult to see the crack marks in the whole structure photograph. Hence, the crack distribution in specimens is provided using pictures drawn by software CAD, as depicted in Figures 10 and 11. They reflect the failure modes and seismic properties of the specimens. It can be seen that compared with Specimen B, Specimen A had less cracks in the coupling beams and shear walls, indicating that the isolation system had reduced the crack formation effectively. In addition, there was no crack in the AHW connection area in Specimen A, indicating that the reliability of the improved AHW connection and the safety of the PCSW structure can be ensured during earthquakes.

4.2. Modes. Figure 12 illustrates the first modes of Specimens A and B obtained from the experiment. It is observed that, in the first mode of Specimen A, the isolation storey undergoes deformation but the superstructure behaves as essentially rigid, while the first mode of Specimen B corresponds to a typical flexure type deformation. It can be seen that the modes of Specimens A and B before and after the tests are almost the same.

4.3. Dynamic Characteristics. The frequencies and damping ratios of the structure models were obtained from the transfer

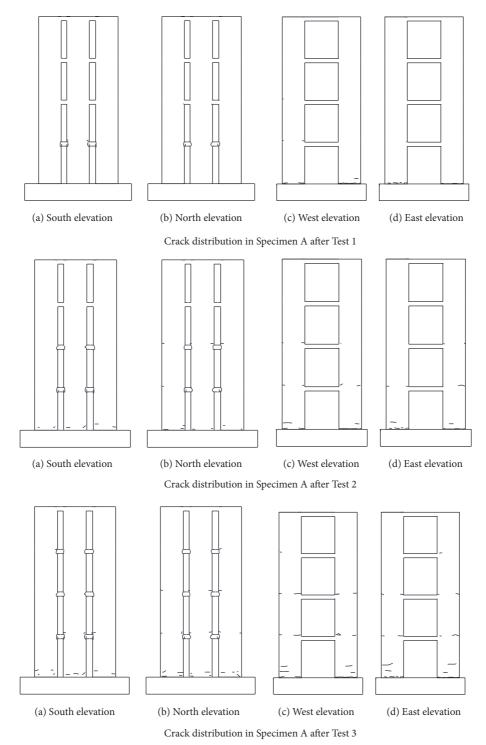
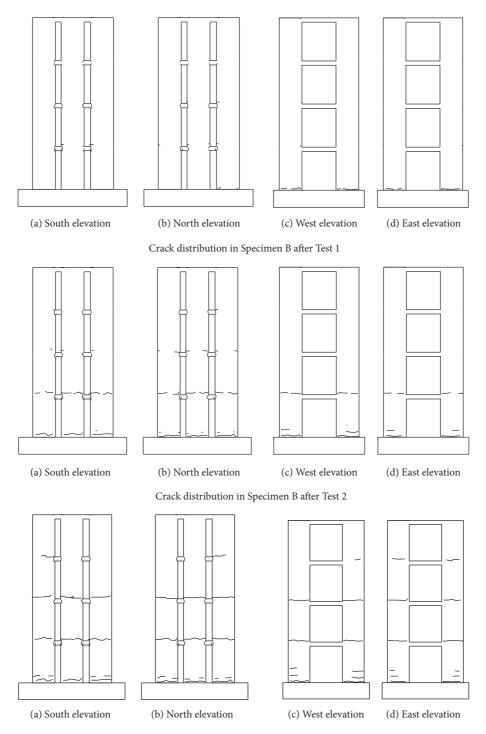


FIGURE 10: Crack distribution in Specimen A.

functions, which were derived from the recorded acceleration responses. Figures 13 and 14 show the frequencies and damping ratios of the first modes, respectively, of Specimens A and B. Based on the results, conclusions are made as follows.

With increase in the input PGA, the frequency in the case of Specimen A remains almost constant at approximately

2.2 Hz, whereas in the case of Specimen B, the frequency decreases. When the input PGA is less than 70 gal, the frequency in the case of Specimen B is approximately 16.5 Hz, and when the input PGA is 400 gal, the frequency reduced to 3.12 Hz. It can be inferred that the stiffness of Specimen A is less than that of Specimen B.



Crack distribution in Specimen B after Test 3

FIGURE 11: Crack distribution in Specimen B.

With increase in the input PGA, the damping ratio of Specimen A remains almost constant at approximately 16%. When the input PGA is less than 70 gal, the damping ratio of Specimen B is approximately 3.6%, and when the input PGA is 400 gal, the damping ratio increases to 7.54%. Thus, the

damping ratio of Specimen A is larger than that of Specimen B.

The frequency and the damping ratio of Specimen A are mainly decided by the LRBs. Because there are no significant changes in the mechanical properties of the LRBs during

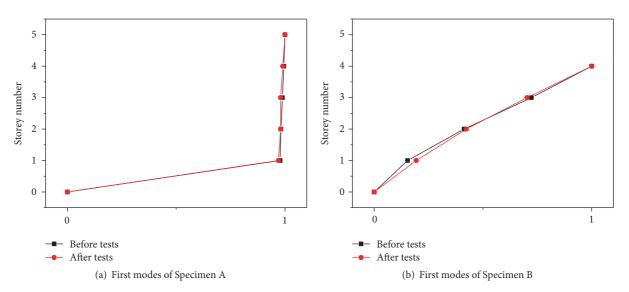


FIGURE 12: Modes obtained from the experiment. Note. Storey number "0" corresponds to the isolation storey.

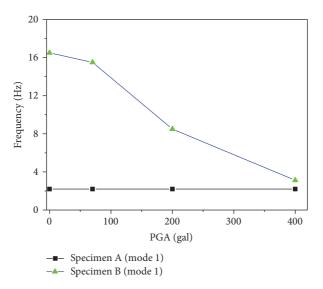


FIGURE 13: Frequency versus PGA.

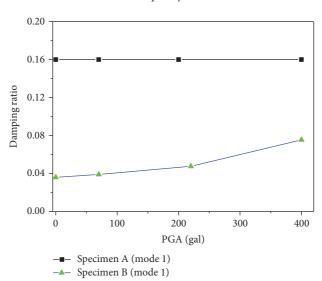


FIGURE 14: Damping ratio versus PGA.

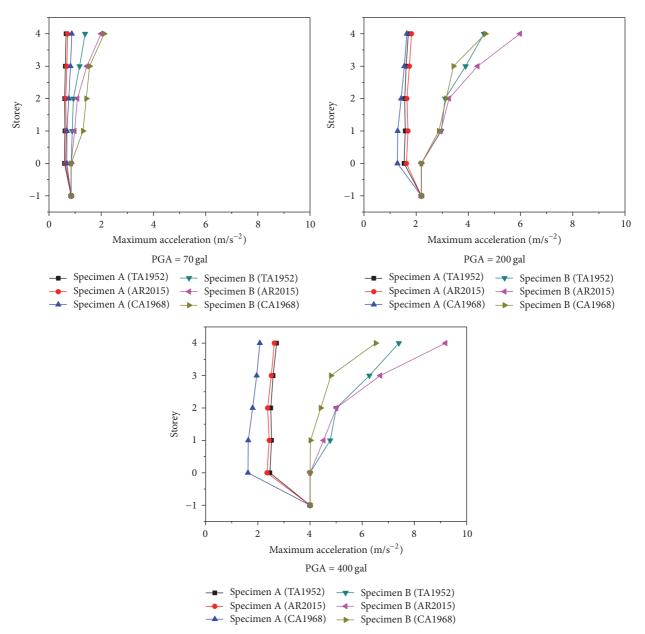


FIGURE 15: Acceleration.

the tests, there are no remarkable changes in the frequency and damping ratio of Specimen A. However, in the case of Specimen B, the frequency decreases and the damping ratio increases during the tests because of the cumulative damage in this specimen.

4.4. Acceleration Responses. The maximum storey acceleration of Specimens A and B is shown in Figure 15, and the maximum fourth-storey acceleration in all the test stages is displayed in Figure 16. It is clear that the maximum storey acceleration of both Specimens A and B increases when the input PGA increases. In addition, with increase in the input PGA, there is insignificant increase in the maximum storey acceleration of the superstructure of Specimen A;

however, there is a significant increase in the maximum storey acceleration of Specimen B.

The equation for the acceleration reduction ratio ψ_A of the base-isolated structure is as follows:

$$\psi_A = \frac{\left(A_F - A_I\right)}{A_F},\tag{1}$$

where A_F is the maximum acceleration of the base-fixed structure and A_I is the maximum acceleration of the base-isolated structure.

Figure 17 depicts the acceleration reduction ratios in the fourth storey of Specimen A. It can be seen that, with the increase in the input PGA from 70 gal to 400 gal, there

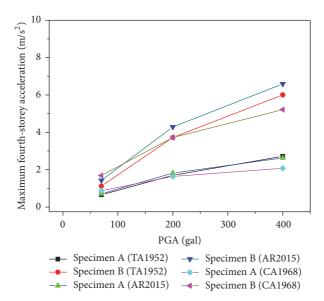


FIGURE 16: Maximum fourth-storey acceleration. Note. Storey number -1 represents the shaking table facility, and 0 represents the base beam.

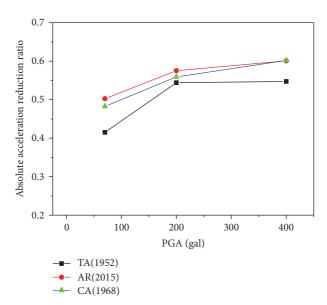


FIGURE 17: Fourth-storey acceleration reduction ratios. *Note*. Storey number –1 represents the shaking table facility, and 0 represents the base beam.

is an improvement in the reduction effect of acceleration responses. When the input PGA is 70 gal, the acceleration reduction ratio in the fourth storey is approximately 45%, and when input PGA is 400 gal, the ratio increases to approximately 55%. Compared to Specimen B, Specimen A with LRB base isolation system experienced significantly smaller acceleration. This auspicious response of Specimen A in terms of storey acceleration responses as compared to Specimen B is the result of the combined effect of a smaller equivalent lateral stiffness and a higher equivalent damping ratio of the LRBs.

4.5. Interstorey Drift (ISD) Responses. The ISD is closely related to structural damage. Figure 18 describes the maximum ISDs of Specimens A and B; Figures 19 and 20 depict

the maximum ISDs in the fourth storey and the isolation storey in all the test stages, respectively. It is clear that the maximum ISDs of both specimens increase with the increase in the intensity of ground motion. Further, the maximum ISDs of Specimen A are less than those of Specimen B. For Specimen A, the ISDs in the base-isolated storey are much larger than those in the superstructure.

The equation for the ISD reduction ratio ψ_D of the base-isolated structure is as follows:

$$\psi_D = \frac{\left(D_F - D_I\right)}{D_F},\tag{2}$$

where D_F is the maximum ISD of the base-fixed structure and D_I is the maximum ISD of the base-isolated structure.

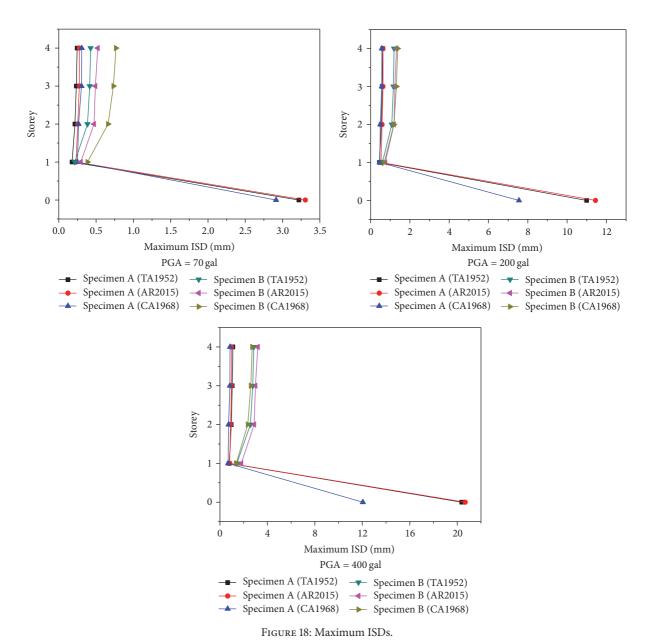


Figure 21 depicts the ISD reduction ratios in the fourth storey. It can be seen that the ISD reduction ratios increase with increase in the input PGA. When the input PGA is 70 gal, the ISD isolation ratio in the fourth storey is approximately 35%, and when the input PGA is 400 gal, the ISD isolation ratio increases to approximately 60%. The present LRB base isolation system reduces the ISDs to a great extent when subjected to ground motions with various PGA levels. This demonstrates the capability of the LRB base isolation system in protecting the PCSW structure against earthquakes.

4.6. Interstorey Shear Force (ISSF) Responses. Figure 22 shows the maximum ISSFs in Specimens A and B when subjected to ground motions with PGAs of 70 gal, 220 gal, and 400 gal. Figure 23 displays the maximum ISSFs of the first storey in

the specimens in all the test stages. It can be seen that the maximum ISSFs in both specimens increase with the increase in the intensity of ground motions. The maximum ISSFs of Specimen A are less than those of Specimen B.

The equation for the ISSF reduction ratio ψ_V of the base-isolated structure is as follows:

$$\psi_V = \frac{(V_F - V_I)}{V_F},\tag{3}$$

where V_F is the ISSF of the base-fixed structure and V_I is the ISSF of the base-isolated structure.

The ISSF reduction ratios of the first storey in Specimen A are shown in Figure 24. It can be observed that, with increase in the input PGA, the ISSF reduction ratios in the first storey increase. When the input PGA is 70 gal, the ISSF

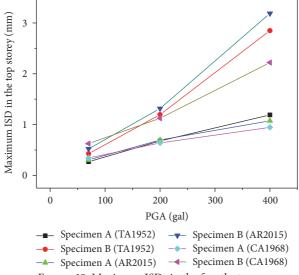


FIGURE 19: Maximum ISDs in the fourth storey.

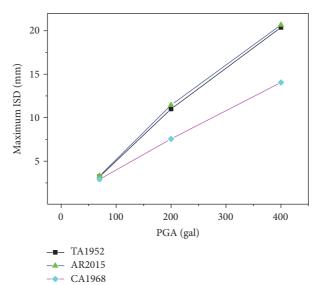


FIGURE 20: Maximum ISDs in the isolation storey.

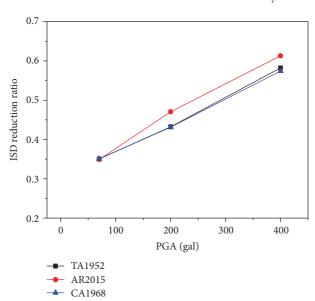


FIGURE 21: ISD reduction ratios in the fourth storey.

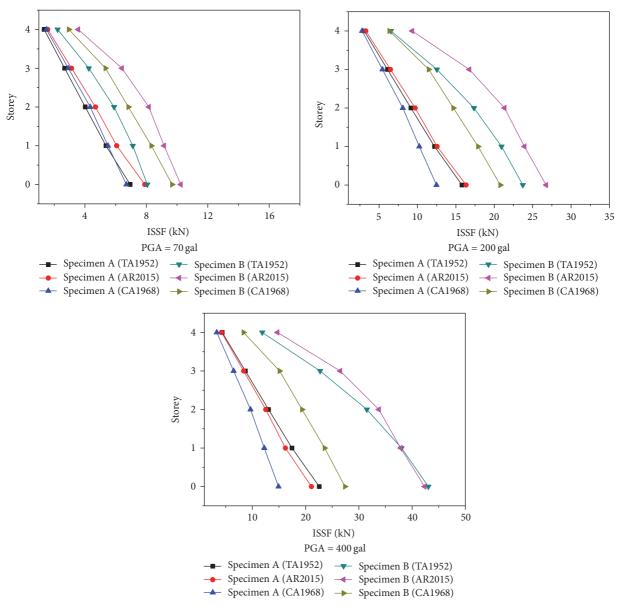


FIGURE 22: Maximum ISSFs.

reduction ratio in the first storey is approximately 25%, and when the input PGAs are low, the ISSF reduction effect of the LRB is not significant. With increase in the input PGA, Specimen A exhibited better ISSF reduction capacity. When the input PGA is 400 gal, the ISSF reduction ratio of the first storey increases to approximately 50%. In the case of a minor earthquake, the lateral stiffness of the LRB is relatively high, and the ISSF reduction effect is not significant. In the case of severe earthquakes, the equivalent lateral stiffness of the LRB decreases, and the ISSF reduction effect improves.

4.7. Energy Dissipation Property of Isolation Storey. Figure 25 shows the shear force-displacement hysteresis curves of the isolation storey in Specimen A, when subjected to input excitations with PGAs of 70 gal, 220 gal, and 400 gal. The dissipation energies of the isolation storey in all the test

stages are shown in Figure 26. It can be seen that the shear force-displacement hysteresis curves of the isolation storey are spindle-shaped; this demonstrates the satisfactory energy dissipation property of the LRBs.

5. Numerical Simulation

The responses of the LRB base-isolated PCSW structure with improved AHW connections obtained during the tests were simulated using OpenSees software. As the improved AHW connection was in elastic state during the shaking table tests and there was no crack in the AHW connection area, it is assumed that mechanical performance of the improved AHW connection is akin to the equivalent cast-in-place connection and that the longitudinal rebars in the AHW connection region are continuous.

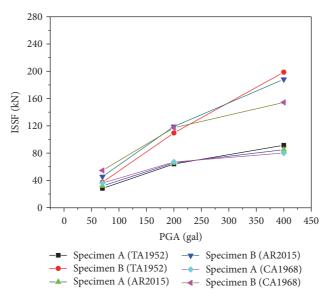


FIGURE 23: ISSFs of first storey.

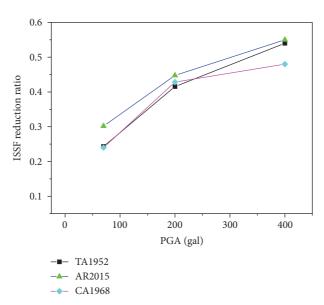


FIGURE 24: ISSF reduction ratios of first storey.

In the OpenSees modelling, the LRB was defined using the LeadRubberX element. The multilayer shell element was used to simulate the shear wall (refer http://www.luxinzheng.net). The concrete was divided into six layers, and the rebars were smeared into four layers. Point-mass model was used to simulate the added mass on each floor of the structures. The Rayleigh damping coefficient was taken as 0.05 to simulate the energy dissipation in the models.

The numerically simulated structural responses were compared with the test results, and the acceleration time history responses for the fourth storey of Specimen A, obtained from simulation and tests, are shown in Figure 27. It can be observed that the numerically simulated storey acceleration is close to the values obtained during the tests. The shear

force-displacement hysteresis curves for the isolation storey of Specimen A, obtained from simulation and tests, are shown in Figure 28; the figure shows that the two curves match well. The results shown in Figures 27 and 28 indicate that the multilayer shell element and LeadRubberX element can be used to simulate the precast reinforced concrete shear wall and the LRB, respectively, and that the assumption of the longitudinal rebars in the AHW connection region being continuous is reasonable.

6. Conclusions

Shaking table tests and numerical simulation were performed to evaluate the seismic behaviour of a base-isolated PCSW structure model using improved AHW connections. During

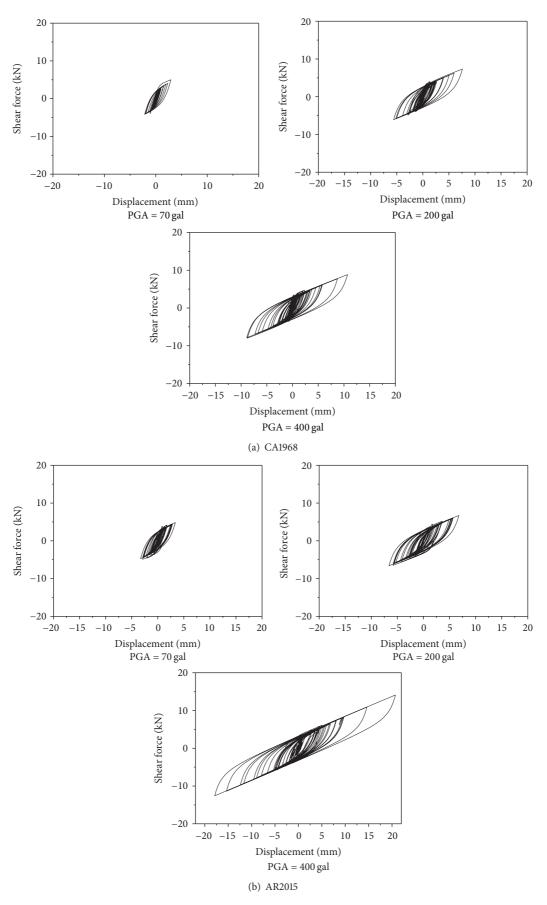


FIGURE 25: Continued.

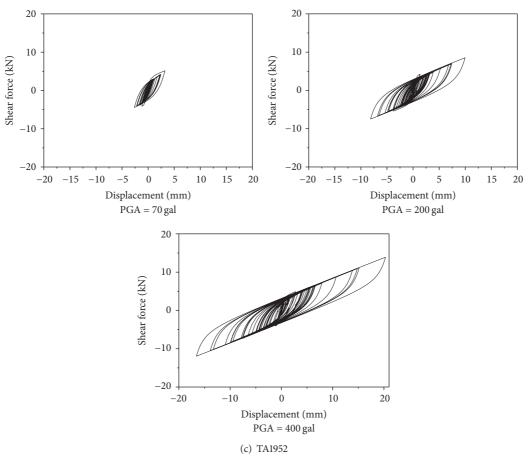


FIGURE 25: Shear force-displacement hysteresis curves of the isolation system.

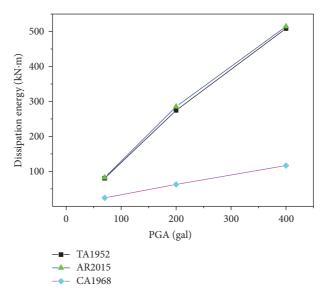


FIGURE 26: Dissipation energy of the isolation storey.

the tests, performance of the improved AHW connections was especially studied. The absolute acceleration responses and deformation responses of the base-isolated PCSW structure model were measured to reveal the dynamic properties

and failure modes of the structure. Furthermore, OpenSees software was used to simulate the seismic response of the base-isolated PCSW structure model. Based on the results, conclusions are draw as follows.

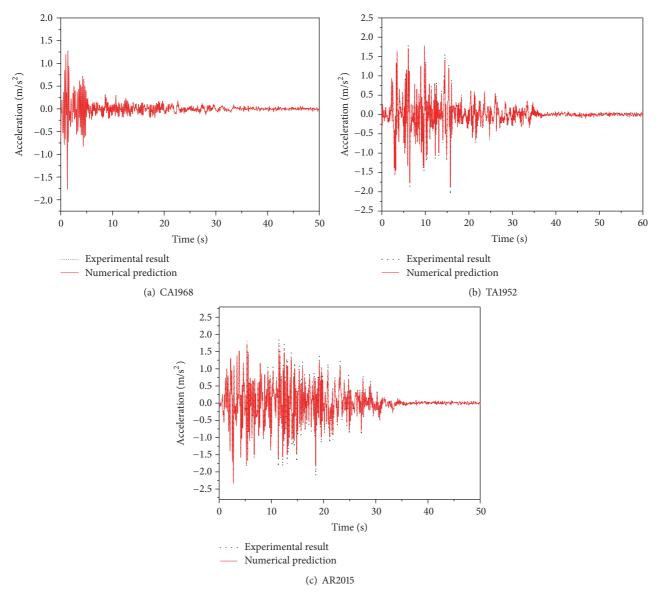


FIGURE 27: Comparison of acceleration history responses of the fourth storey for PGA = 400 gal.

- (1) There was no crack in the AHW connection area in the base-isolated PCSW structure model, indicating that the reliability of the improved AHW connection and the safety of the PCSW structure can be ensured during earthquakes.
- (2) Compared with the base-fixed PCSW structure model, the base-isolated PCSW structure model had less cracks in the AHW connection area, coupling beams and shear walls, indicating that the LRB isolation system can reduce cracks effectively.
- (3) The structural damping ratio can be increased to 16% by installation of LRBs, and the frequency of the structure can be reduced to 2.2 Hz.
- (4) The absolute acceleration response, ISD response, and maximum ISSF response of the PCSW structure model can be reduced significantly by the installation of LRBs. When

- the input PGA is 400 gal, the acceleration reduction ratio was approximately 55%; the ISD isolation ratio was approximately 60%; and the ISSF reduction ratio of the first storey was approximately 50%.
- (5) The seismic responses of the base-isolated PCSW structures with the improved AHW connections can be numerically simulated using OpenSees software, based on the assumptions that mechanical performance of the improved AHW connection is akin to the equivalent cast-in-place connection and that the longitudinal rebars in the AHW connection region are continuous.

Conflicts of Interest

The authors declare that they have no conflicts of interest.

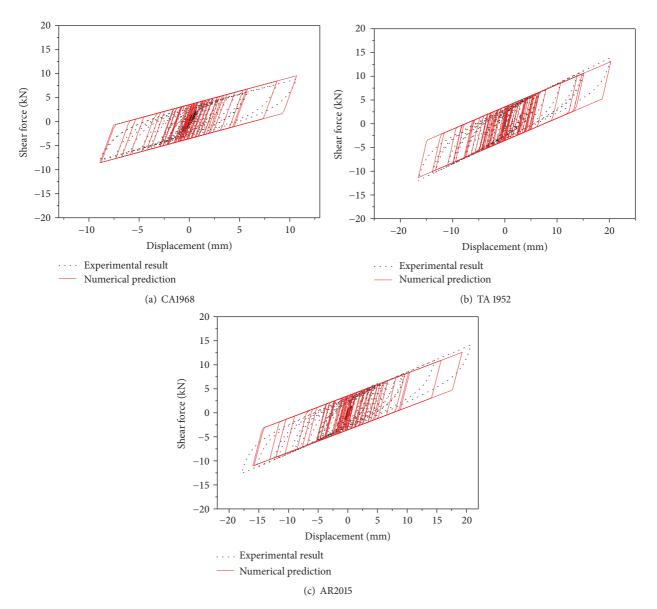


FIGURE 28: Comparison of shear force-displacement hysteresis loops of the isolation system for PGA = 400 gal.

Acknowledgments

The authors are grateful for the funding provided by National Key Research and Development Program of China (Grant No. 2017YFC0703602), the National Natural Science Foundation of China (Grants nos. 51708257 and 51708258), Natural Science Foundation for Colleges and Universities in Jiangsu Province (17KJB560002), and the Science Foundation of Jiangsu University of Science and Technology (Grant no. 1122931605).

References

[1] W. Wang, A. Li, and X. X. Wang, "Seismic performance of precast concrete shear wall structure with novel assembly horizontal wall connections," *Bulletin of Earthquake Engineering*, pp. 1–26, 2018.

- [2] Y. Kurama, S. Pessiki, R. Sause, and L.-W. Lu, "Seismic behavior and design of unbonded post-tensioned precast concrete walls," *PCI journal*, vol. 44, no. 3, pp. 72–89, 1999.
- [3] A. Belleri, M. J. Schoettler, J. I. Restrepo, and R. B. Fleischman, "Dynamic behavior of rocking and hybrid cantilever walls in a precast concrete building," *ACI Structural Journal*, vol. 111, no. 3, pp. 661–671, 2014.
- [4] K. S. Elliott, Precast Concrete Structures, CRC Press, 2016.
- [5] S. Gavridou, J. W. Wallace, T. Nagae, T. Matsumori, K. Tahara, and K. Fukuyama, "Shake-Table test of a full-scale 4-story precast concrete building. I: overview and experimental results," *Journal of Structural Engineering (United States)*, vol. 143, no. 6, Article ID 04017034, 2017.
- [6] S. Gavridou, J. W. Wallace, T. Nagae, T. Matsumori, K. Tahara, and K. Fukuyama, "Shake-table test of a full-scale 4-story precast concrete building. II: analytical studies," *Journal of*

Structural Engineering (United States), vol. 143, no. 6, Article ID 04017035, 2017.

- [7] J. Qian, X. Yang, H. Qin, Y. Peng, J. Zhang, and J. Li, "Tests on seismic behavior of pre-cast shear walls with various methods of vertical reinforcement splicing," *Journal of Building Structures*, vol. 32, no. 6, pp. 51–59, 2011 (Chinese).
- [8] M. J. Ameli, J. E. Parks, D. N. Brown, and C. P. Pantelides, "Seismic evaluation of grouted splice sleeve connections for reinforced precast concrete column-to-cap beam joints in accelerated bridge construction," *PCI journal*, vol. 60, no. 2, pp. 80–103, 2015.
- [9] A. Solak, Y. S. Tama, S. Yılmaz, and H. Kaplan, "Experimental study on behavior of anchored external shear wall panel connections," *Bulletin of Earthquake Engineering*, vol. 13, no. 10, pp. 3065–3081, 2015.
- [10] F. J. Perez, R. Sause, and S. Pessiki, "Analytical and experimental lateral load behavior of unbonded posttensioned precast concrete walls," *Journal of Structural Engineering*, vol. 133, no. 11, pp. 1531–1540, 2007.
- [11] F. J. Perez, S. Pessiki, and R. Sause, "Experimental lateral load response of unbonded post-tensioned precast concrete walls," *ACI Structural Journal*, vol. 110, no. 6, pp. 1045–1055, 2013.
- [12] A. S. Pall, C. Marsh, and P. Fazio, "Friction joints for seismic control of large panel structures," *PCI Journal*, vol. 25, no. 6, pp. 38–61, 1980.
- [13] O. A. Pekau and D. Hum, "Seismic response of friction jointed precast panel shear walls," *PCI Journal*, vol. 36, no. 2, pp. 56–71, 1991
- [14] E. Villalobos, D. Escolano-Margarit, A. L. Ramírez-Márquez, and S. Pujol, "Seismic response of reinforced concrete walls with lap splices," *Bulletin of Earthquake Engineering*, vol. 15, no. 5, pp. 1–22, 2016.
- [15] C. Alhan and H. P. Gavin, "Reliability of base isolation for the protection of critical equipment from earthquake hazards," *Engineering Structures*, vol. 27, no. 9, pp. 1435–1449, 2005.
- [16] X. K. Zou, Q. Wang, G. Li, and C. M. Chan, "Integrated reliability-based seismic drift design optimization of baseisolated concrete buildings," *Journal of Structural Engineering*, vol. 136, no. 10, pp. 1282–1295, 2010.
- [17] C. Zhao and J. Chen, "Numerical simulation and investigation of the base isolated NPPC building under three-directional seismic loading," *Nuclear Engineering and Design*, vol. 265, pp. 484–496, 2013.
- [18] Y.-M. Fang and J.-P. Pu, "Field tests and simulation of lion-head river bridge," *Shock and Vibration*, vol. 14, no. 3, pp. 181–228, 2005.
- [19] P. Zhou, W. L. Li, W. Li, and Z. Shuai, "Reconstruction of input excitation acting on vibration isolation system," *Shock and Vibration*, vol. 2016, Article ID 2784380, 12 pages, 2016.
- [20] H. Moeindarbari and T. Taghikhany, "Novel procedure for reliability-based cost optimization of seismically isolated structures for the protection of critical equipment: a case study using single curved surface sliders," *Structural Control and Health Monitoring*, no. 1, 2017.
- [21] A. R. Bhuiyan and M. S. Alam, "Seismic performance assessment of highway bridges equipped with superelastic shape memory alloy-based laminated rubber isolation bearing," *Engi*neering Structures, vol. 49, no. 4, pp. 396–407, 2013.
- [22] A. B. M. S. Islam, S. I. Ahmad, M. Z. Jumaat, R. R. Hussain, M. A. Rahman, and K. M. U. Darain, "Efficient design in building construction with rubber bearing in medium risk seismicity:

- Case study and assessment," *Journal of Civil Engineering and Management*, vol. 20, no. 5, pp. 621–631, 2014.
- [23] M. Ohsaki, T. Miyamura, M. Kohiyama, T. Yamashita, M. Yamamoto, and N. Nakamura, "Finite-element analysis of laminated rubber bearing of building frame under seismic excitation," *Earthquake Engineering & Structural Dynamics*, vol. 44, no. 11, pp. 1881–1898, 2015.
- [24] G. Özdemir, "Formulations of equivalent linearization of lead-rubber bearings for incorporating the effect of lead core heating," *Earthquake Spectra*, vol. 31, no. 1, pp. 317–337, 2015.
- [25] D. Lee and M. C. Constantinou, "Further results on the heating of single and multi-core lead-rubber bearings and dampers," *Bulletin of Earthquake Engineering*, vol. 14, no. 4, pp. 999–1016, 2016.
- [26] M. Ahmadipour and M. S. Alam, "Sensitivity analysis on mechanical characteristics of lead-core steel-reinforced elastomeric bearings under cyclic loading," *Engineering Structures*, vol. 140, no. 1, pp. 39–50, 2017.
- [27] MHUCPRC, Code for Design of Concrete Structures (GB 50010-2010), Ministry of Housing and Urban-Rural Construction of the People's Republic of China, Beijing, China, 2010.
- [28] MHUCPRC, Code for Seismic Design of Buildings (GB 50011-2010), Ministry of Housing and Urban-Rural Construction of the People's Republic of China, Beijing, China, 2010.

Hindawi Shock and Vibration Volume 2018, Article ID 3529479, 7 pages https://doi.org/10.1155/2018/3529479

Research Article

Hybrid Structural Reliability Analysis under Multisource Uncertainties Based on Universal Grey Numbers

Xingfa Yang,^{1,2} Jie Liu,^{1,3} Xiaoyue Chen,² Qixiang Qing,² and Guilin Wen ^{1,2,3}

¹State Key Laboratory of Advanced Design and Manufacturing for Vehicle Body, Hunan University, Changsha, Hunan 410082, China ²Key Laboratory of Advanced Design and Simulation Techniques for Special Equipment, Ministry of Education, Hunan University, Changsha, Hunan 410082, China

Correspondence should be addressed to Guilin Wen; glwen@hnu.edu.cn

Received 26 December 2017; Accepted 8 March 2018; Published 17 April 2018

Academic Editor: Mohammad A. Hariri-Ardebili

Copyright © 2018 Xingfa Yang et al. This is an open access article distributed under the Creative Commons Attribution License, which permits unrestricted use, distribution, and reproduction in any medium, provided the original work is properly cited.

Nondeterministic parameters of certain distribution are employed to model structural uncertainties, which are usually assumed as stochastic factors. However, model parameters may not be precisely represented due to some factors in engineering practices, such as lack of sufficient data, data with fuzziness, and unknown-but-bounded conditions. To this end, interval and fuzzy parameters are implemented and an efficient approach to structural reliability analysis with random-interval-fuzzy hybrid parameters is proposed in this study. Fuzzy parameters are first converted to equivalent random ones based on the equal entropy principle. 3σ criterion is then employed to transform the equivalent random and the original random parameters to interval variables. In doing this, the hybrid reliability problem is transformed into the one only with interval variables, in other words, nonprobabilistic reliability analysis problem. Nevertheless, the problem of interval extension existed in interval arithmetic, especially for the nonlinear systems. Therefore, universal grey mathematics, which can tackle the issue of interval extension, is employed to solve the nonprobabilistic reliability analysis problem. The results show that the proposed method can obtain more conservative results of the hybrid structural reliability.

1. Introduction

In most cases, uncertain structural parameters could have undesired effects on the reliability of structures and systems. Normally, probability model [1, 2] and fuzzy model [3] are utilized to obtain structural reliability based on probability theory and fuzzy set theory, respectively. Since probability and fuzzy models have been developed rapidly over the past decades, both of them have been applied in an ocean of engineering fields [4]. Unfortunately, when it comes to the situation that the experimental samples and data are not sufficient to construct the precise distribution or membership function, these two methods are no longer reliable.

Ben-Haim [5, 6] and Elishakoff [7] pioneered to develop the nonprobabilistic convex model to deal with the uncertainty lacking of information and introduced the concept of nonprobabilistic reliability. They suggested that uncertain parameters should be treated as convex set, such as interval and ellipsoid, so that uncertainty model can be obtained with the information of those parameters' bounds. Since then interval reliability analysis has arisen wide concern. Du [8] and Du et al. [9] systematically studied the structural reliability analysis consisting of interval parameters. Various techniques have also proposed to solve this kind of reliability and design problem [10-18]. However, there could be the circumstance that the designing parameters of a structure have different kinds of uncertainties. For example, the geometry parameters of the structure are random variable, but the subjected force is fuzzy [19], or vice verse [20]. Developing an effective method to solve this problem is vital for engineers to predict the structural reliability precisely. Haldar and Reddy [21] proposed two approaches to estimate the reliability of existing structures by considering both the randomness and the fuzzy uncertainty in some parameters. Ni and Qiu [22]

³Center for Research on Leading Technology of Special Equipment, School of Mechanical and Electric Engineering, Guangzhou University, Guangzhou 510006, China

presented an innovative method to calculate the structural reliability of linear and nonlinear structural systems when probabilistic, fuzzy, and nonprobabilistic uncertainties are involved. A multitude of researchers have worked this filed recently and fruitful achievements have been obtained [23–28], including calculating the reliability of motion mechanism, solving time-dependent problems, and designing metamaterials.

However, interval expansion is unavoidable when interval mathematics is used, which is often neglected by the researchers. Rao and Berke [29] proposed an interval-truncation approach to narrow interval expansion, but the truncation principle is hard to control. Shao and Su [30] applied interval finite element method to narrow interval expansion. In this study, we attempt to put forward alternative approach to handle the interval expansion problem in structural reliability analysis when hybrid uncertainties are involved. The main focus of this work will introduce a new approach by utilizing universal grey number to avoid interval expansion in reliability analysis. Meanwhile, techniques, like 3σ criterion and equal entropy principle, are used as well.

The rest of this paper is organized as follows. Section 2 introduces an interval reliability model; Section 3 presents reliability analysis with random, fuzzy, and interval parameters and introduces the methods and theory of transformation among random, fuzzy, and interval variables. Section 4 introduces the universal grey number. Section 5 discusses and analyzes some numerical examples; the conclusion is given in Section 6.

2. Interval Reliability Model

For interval reliability analysis, structural performance is commonly expressed by performance function which is determined by failure criteria. Assuming that $\mathbf{Z}^{\mathbf{I}}$ is a k-dimension vector of interval variable with independent elements

$$\mathbf{Z} \in \mathbf{Z}^{\mathbf{I}} = \left[\underline{\mathbf{Z}}, \overline{\mathbf{Z}}\right],$$

$$Z_{i} \in Z_{i}^{\mathbf{I}} = \left[Z_{i}, \overline{Z_{i}}\right], \quad i = 1, 2, \dots, k,$$
(1)

where Z_i and $\overline{Z_i}$ represent the lower and upper bounds of interval, respectively. Then the structural performance function can be expressed as

$$Q = g\left(\mathbf{Z}^{\mathbf{I}}\right) = g\left(Z_1^{\mathbf{I}}, Z_2^{\mathbf{I}}, \dots, Z_k^{\mathbf{I}}\right). \tag{2}$$

The reliability can be defined as

$$P_r = P\left\{g\left(\mathbf{Z}^{\mathbf{I}}\right) \ge 0\right\}. \tag{3}$$

And limit-state function of the structure writes

$$Q = g(\mathbf{Z}^{I}) = g(Z_{1}^{I}, Z_{2}^{I}, \dots, Z_{k}^{I}) = 0$$
 (4)

which defines the limit-state surface. The basic variable space will be divided into safe region and failure region by the limit-state function, and if taking the example of two-dimensional linear performance function $Q=Z_2-Z_1$, $(Z_2\in Z_2^I=[\underline{Z_2},\overline{Z_2}],Z_1\in Z_1^I=[\underline{Z_1},\overline{Z_1}])$, the safe region and failure

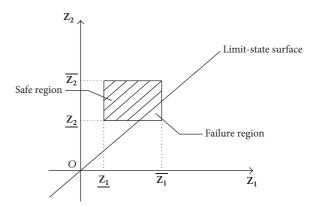


FIGURE 1: Scheme for safe region and failure region.

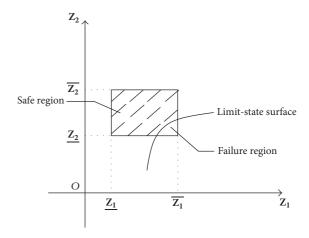


FIGURE 2: Nonlinear structural performance function.

region would be separated as shown in Figure 1. The interval safety probability can be defined as the ratio of safe region to the total area of variable space [22].

$$P_r = \frac{V_{\text{safe}}}{V_{\text{total}}}. (5)$$

When the performance function is nonlinear or multidimensional, the variable space will be divided into safe region and failure region by limit-state surface or hyper-surface as well, as shown in Figure 2. So the safe probability can still be defined by the ratio of safe region to total variable region like (5).

3. Reliability Analysis with Random, Fuzzy, and Interval Parameters

Limit-state function with random variables, fuzzy variables, and interval variables can be expressed as follows:

$$Q = g\left(\boldsymbol{x}, \widetilde{\boldsymbol{y}}, \mathbf{z}^{I}\right)$$

$$= g\left(x_{1}, x_{2}, \dots, x_{m}, \widetilde{y}_{1}, \widetilde{y}_{2}, \dots, \widetilde{y}_{n}, z_{1}^{I}, z_{2}^{I}, \dots, z_{l}^{I}\right)$$

$$= 0,$$

$$(6)$$

where $\boldsymbol{x}=(x_1,x_2,\ldots,x_m)$ denotes a random variable vector with independent elements of normal distribution. The probability density function of x_i ($i=1,2,\ldots,m$), which are the random variables, is $f_i(x_i)$ ($i=1,2,\ldots,m$). $\widetilde{\mathbf{y}}=(\widetilde{y}_1,\widetilde{y}_2,\ldots,\widetilde{y}_n)$ denotes a fuzzy variable vector with independent elements. Membership functions of \widetilde{y}_j ($j=1,2,\ldots,n$), the fuzzy variables, are represented by $\mu_j(y_j)$ ($j=1,2,\ldots,n$). $\mathbf{z}^I=(z_1^I,z_2^I,\ldots,z_l^I)$ denotes an independent nonprobabilistic interval variable vector, and $z_k^I=[\underline{z}_k,\overline{z}_k]$ ($k=1,2,\ldots,l$). So the structural hybrid reliability can be expressed as

$$P_r = P\left(Q = g\left(\boldsymbol{x}, \widetilde{\mathbf{y}}, \mathbf{z}^I\right) \ge 0\right). \tag{7}$$

3.1. Transforming Fuzzy Variable into Random Variable. Entropy [31], a basic concept in thermodynamics, is used for expressing the degree of the irregular movement of molecules. It can be regarded as a measure of uncertainty. Entropy is not only a measure of random uncertainty but also fuzzy uncertainty. The measure of random uncertainty and fuzzy uncertainty are defined as probabilistic entropy and fuzzy entropy, respectively.

The probabilistic H entropy of continuous variables X is defined as follows:

$$H_X = -\int_R f(x) \ln f(x) \, dx,\tag{8}$$

where f(x) is the probability density function of X.

The definition of fuzzy entropy can be described as:

$$G'_{Y} = -\int_{P} f'(y) \ln f'(y) dy,$$
 (9)

where $f'(y) = \mu(y) / \int_R \mu(y) dy$ and $\mu(y)$ is the membership function of Y.

According to the principle that the equivalent probabilistic entropy equals to the fuzzy entropy, fuzzy uncertainty can be transformed into random ones. So the transformation from fuzzy entropy to equivalent random entropy can be constructed on the basis of (8) and (9):

$$H = G'. (10)$$

Supposing the equivalent random variable transformed from fuzzy variable Y is X. The entropy of a normal variable can be obtained by evaluating (8) as

$$H_{\text{eq}} = -\int_{\mathbb{R}} f(x) \ln f(x) \, dy = \ln \left(\sqrt{2\pi e} \sigma \right). \tag{11}$$

The equivalent standard deviation of the transform from fuzzy variable to random variable can be obtained according to (11):

$$\widehat{\sigma} = \frac{1}{\sqrt{2\pi}} e^{G' - 0.5}.\tag{12}$$

The equivalent mean is assumed to be the fuzzy variable mean and the correspondent mean value when the membership value is 1, represented by *a*. Then the probabilistic density function of equivalent random variable with normal distribution can be obtained:

$$\widehat{f}_{I}(x) = \frac{1}{\sqrt{2\pi}\widehat{\sigma}} e^{-(1/2)((x-a)/\widehat{\sigma})^{2}}.$$
(13)

3.2. Transforming Random Variable into Interval Variable. 3σ principal reveals that most of the random variable values are in the interval of $(\mu - 3\sigma, \mu + 3\sigma)$ and the excess accounts for less than 0.3%. So the equivalent probabilistic variable and probabilistic variable can be transformed into uncertain but limited interval variable.

x is transformed into x^I , an interval variable located in $[\mu - 3\sigma, \mu + 3\sigma]$, where μ is the mean value of the normally distributed random variable and σ is the deviation. The equivalent probabilistic uncertain variable of \widetilde{y} , the fuzzy variable, is transformed into \widetilde{y}^I , the interval variable located in the interval of $[\widehat{\mu} - 3\widehat{\sigma}, \widehat{\mu} + 3\widehat{\sigma}]$. Then the hybrid structural reliability solving problem has turned into a nonprobabilistic reliability solving problem only with interval variables.

4. Universal Grey Mathematics

4.1. Brief Introduction of Universal Grey Number

Definition 1. Suppose discussed region U = R (real number set). Then the universal grey number of R is named universal grey number set, noted g(R), and the element of g(R) is named universal grey number, noted

$$g = (x, [\mu, \overline{\mu}]), \hat{a}NLx \in R, \ \mu, \overline{\mu} \in R,$$
 (14)

where x is the observation value, $[\underline{\mu}, \overline{\mu}]$ is the grey information part, and $g^{(0)}=(0,[0,0])$ and $g^{(1)}=(1,[1,1])$ are the zero unit and unit, respectively. The universal grey number, whose observation part is naught but information part is not naught, is noted as $g'^{(0)}$ and named subzero unit. Zero unit and subzero unit are called by a joint name of universal zero unit, noted as $g'^{(0)}$.

Definition 2. $\forall g = (x, [\underline{\mu}, \overline{\mu}]) \in g(R), -g = (-x, [\underline{\mu}, \overline{\mu}])$ is called negative unit on g in g(R) and $g^{-1} = (x^{-1}, [\underline{\mu}^{-1}, \overline{\mu}^{-1}])$ is called inverse unit on g in g(R).

On the basis of Definitions 1 and 2, the four arithmetic operations of universal number are regulated. The multiplication operation of universal grey number meets closure, association law, and exchange law. The four arithmetic operations are as follows:

$$g_{1} + g_{2} = \left(x_{1} + x_{2}, \left[\frac{x_{1}\underline{\mu}_{1} + x_{2}\underline{\mu}_{2}}{x_{1} + x_{2}}, \frac{x_{1}\overline{\mu}_{1} + x_{2}\overline{\mu}_{2}}{x_{1} + x_{2}}\right]\right)$$

$$g_{1} - g_{2} = \left(x_{1} - x_{2}, \left[\frac{x_{1}\underline{\mu}_{1} - x_{2}\underline{\mu}_{2}}{x_{1} - x_{2}}, \frac{x_{1}\overline{\mu}_{1} - x_{2}\overline{\mu}_{2}}{x_{1} - x_{2}}\right]\right)$$

$$g_{1} \times g_{2} = \left(x_{1}x_{2}, \left[\underline{\mu}_{1}\underline{\mu}_{2}, \overline{\mu}_{1}\overline{\mu}_{2}\right]\right)$$

$$\frac{g_{1}}{g_{2}} = \left(\frac{x_{1}}{x_{2}}, \left[\frac{\underline{\mu}_{1}}{\underline{\mu}_{2}}, \frac{\overline{\mu}_{1}}{\overline{\mu}_{2}}\right]\right), \quad \text{(if } g \neq g'^{(0)}).$$

$$(15)$$

4.2. The Transformation of Universal Grey Number and Interval Number. According to the definition of universal grey

number, $\underline{\mu}$ and $\overline{\mu}$ of $(x, [\underline{\mu}, \overline{\mu}])$, a universal grey number, can be, respectively, looked as the lowest and highest trust degree. So, when $\underline{\mu}, \overline{\mu} \in [-1, 1]$, a universal grey number can be expressed by an interval number, namely,

$$\left(x, \left[\mu, \overline{\mu}\right]\right) = \left(\mu x, \overline{\mu} x\right). \tag{16}$$

 $\forall [a,b] \in I(R)$ (an interval number set) it can be expressed by an interval number $(x, [\mu, \overline{\mu}])$:

- (1) When there is a > 0, there is [a, b] = (b, [a/b, 1]).
- (2) When there are ab < 0 and $\max\{|a|, |b|\} = |a|$, there is [a, b] = (a, [b/a, 1]).
- (3) When there are ab < 0 and $\max\{|a|, |b|\} = |b|$, there is [a, b] = (b, [a/b, 1]).
- (4) When there is b < 0, there is [a, b] = (a, [b/a, 1]).

Universal grey number not only has the capability of interval analysis but also can avoid the disadvantage of interval computation, and effectively solve the issue of interval extension. Taking advantage of universal grey number, the interval number can be transformed into universal grey number when computing structural reliability, resulting in a more precise outcome.

Based on the discussion above, the proposed procedure for computing the hybrid reliability of the structural system and overcoming the interval expansion at the same time is briefly shown as follows:

- (a) Input hybrid parameters, including random, interval, and fuzzy ones.
- (b) Transform the fuzzy variable into equivalent random ones on the basis of the equal entropy principle.
- (c) Convert the random and equivalent random variables to equivalent interval ones based on the 3σ principal.
- (d) Transform all interval variables into universal grey numbers based on (16).
- (e) Calculate the hybrid reliability using (5) and (15).

5. Numerical Example

In this section, two classical numerical examples and one engineering problem are presented to manifest the validity of the proposed method.

5.1. A Cantilever Tube. A cantilever tube is taken as the first test example, which is presented in Figure 3. Both of the two forces on it are interval variables, and $F \in [2850, 3150]$ (N), $P \in [11700, 12300]$ (N). The thickness of the tube is denoted as t, which is fuzzy and its membership function is shown in Figure 4. Considering that, the stress at the right end of the tube should be less than R_y , which is a random variable and follows a normal distribution of N(28, 0.8). Then the limit-state function can be obtained as follows:

$$g\left(\mathbf{X}\right) = R_{v} - \sigma_{\text{max}}.\tag{17}$$

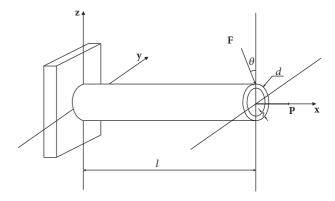


FIGURE 3: A cantilever tube.

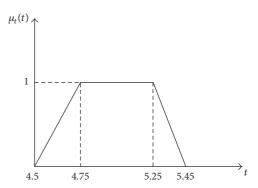


FIGURE 4: Membership function of t.

 $\sigma_{\rm max}$ is calculated by the following equations:

$$\sigma_{\text{max}} = \frac{P + F \sin \theta}{A} + \frac{M}{I}$$

$$A = \frac{\pi}{4} \left[d^2 - (d - 2t)^2 \right],$$

$$M = FL \cos \theta$$

$$I = \frac{\pi}{64} \left[d^4 - (d - 2t)^4 \right].$$
(18)

The reliability probability by using our approach is 90.47%, which is a bit lower than the interval analysis result of 91.75%. It is clearly shown that our approach can deal with the interval expansion problem such that our result is more conservative when compared with that obtained from interval analysis directly.

5.2. A Freely-Supported Beam. Figure 5 presents a freely supported beam subjecting to uniform load q, which is a random variable, and $q \sim N(210, 3^2) \, \mathrm{kN/mm^2}$. The values of section width b and height h are 120 mm and 240 mm, respectively. Length l of the beam is an interval variable, and $l \in l^I = [3880, 4120] \, \mathrm{mm}$. The beam is made of 45-steel and

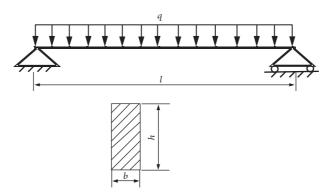


FIGURE 5: A freely supported beam.

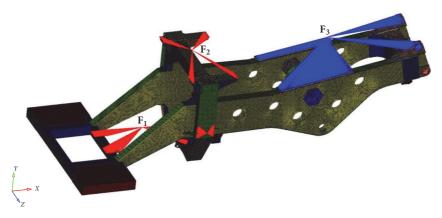


FIGURE 6: An automobile frame.

its strength \tilde{R} is a fuzzy parameter. The membership function of \tilde{R} is

$$\mu_{R}(R) \begin{cases} 0 & R < 760 \\ \frac{R - 720}{40} & 720 \le R < 760 \\ 1 & 760 \le R < 820 \\ \frac{900 - R}{80} & 820 \le R < 900 \\ 0 & R > 900. \end{cases}$$
(19)

Based on material mechanics, the maximum stress of the simple free beam is

$$S = \frac{0.75ql^2}{bh^2}. (20)$$

So the performance function can be denoted as

$$Z = \tilde{R} - \frac{0.75ql^2}{bh^2} = 0. {(21)}$$

 \widetilde{R} is converted into equivalent normal distributed random variable, so the equivalent deviation is $\widehat{\sigma}=37.28$, and the equivalent mean $\widehat{\mu}=790$. Then the random variable q and the equivalent random variable R are transforming into interval variables of q^I and R^I , respectively, and $q^I \in [201, 219]$,

 $R^I \in [679, 901]$. Finally the the hybrid reliability is obtained and its value is 0.9009, which is smaller than the outcome of interval analysis, 0.9687. Again, we can say that the proposed method can tackle the interval expansion problem and get more conservative reliability result.

5.3. An Automobile Frame. The proposed method is finally applied into calculating the reliability of a practical frame structure of a dump truck, which is shown in Figure 6. The frame is subjected to three major forces from engine assembly, carriage, and operation cabin. For the reason that these loads are alterable, they all have variation interval. The bounds of the interval parameters are presented in Table 1. Young's Modulus is a random variable because of the manufacturing error, and it follows a distribution of $E \sim N(2.1e5,50)$. The performance function is denoted as

$$g(\mathbf{X}) = d_{v} - d(E, F_{1}, F_{2}, F_{3}),$$
 (22)

where d_y is the maximum vertical displacement allowed in the static state, and it is a fuzzy variable, whose membership function is

$$\mu_{d_y} = \begin{cases} 250 \left(d_y - 0.69 \right) & 0.69 \le d_y \le 0.694 \\ 1 & 0.694 \le d_y \le 0.698 \\ 500 \left(0.7 - d_y \right) & 0.698 \le d_y \le 0.7. \end{cases}$$
 (23)

TABLE 1	· Rounds of interval	loads to automobile frame.
TABLET	: bounds of interval	Hoads to automobile trame.

	Lower bound (kN)	Upper bound (kN)
$\mathbf{F_1}$	165	170
$\mathbf{F_2}$	100	110
F_3	1560	1610

Due to the implicit relationship between the structural parameters and the structural response (displacement), the Latin Hypercube Sampling method and Design of Experiment method are employed. The displacement of the frame is obtained by finite element method (FEM) in commercial software Abaqus. After that, the equation of $d(E, F_1, F_2, F_3)$ is obtained by Moving Least Square Response Surface Method, and we reach the limit-state function. At last the hybrid reliability is obtained as 95.85%. The frame seems to be relatively reliable on its static state, but structural optimization should be performed when dynamic factors are considered.

6. Conclusion

In this paper, a hybrid reliability analysis method based on universal grey number is proposed. The method can calculate the reliability of structure under simultaneous random, interval, and fuzzy uncertainty. It can conclude a more accurate result, comparing with traditional interval analysis, because the universal grey number has the ability of reducing interval expansion. Moreover, the universal grey number calculation process is simple and has precise results. Three examples, including a engineering problem, demonstrate that our method can achieve more conservative outcomes compared with those obtained from interval analysis directly.

Conflicts of Interest

No potential conflicts of interest were reported by the authors.

Acknowledgments

This work was financially supported by the National Natural Science Foundation of China [Grant no. 11672104] and the National Science Fund for Distinguished Young Scholars in China [Grant no. 11225212].

References

- [1] A. H.-S. Ang and W. H. Tang, Probability Concepts in Engineering Planning and Design. Volume II: Decision, Risk and Reliability, John Wiley & Sons, New York, NY, USA, 1984.
- [2] J. Liu, Q. Qing, Y. Deng, G. Wen, and H. Yin, "Fatigue reliability study on T-welded component considering load shedding," *Fatigue & Fracture of Engineering Materials & Structures*, vol. 38, no. 7, pp. 780–788, 2015.
- [3] L. A. Zadeh, "Fuzzy sets," *Information and Control*, vol. 8, no. 3, pp. 338–353, 1965.
- [4] J. Liu, G. Wen, and Y. M. Xie, "Layout optimization of continuum structures considering the probabilistic and fuzzy directional uncertainty of applied loads based on the cloud model,"

- Structural and Multidisciplinary Optimization, vol. 53, no. 1, pp. 81–100, 2016.
- [5] Y. Ben-Haim, "Convex models of uncertainty in radial pulse buckling of shells," *Transactions of ASME: Journal of Applied Mechanics*, vol. 60, no. 3, pp. 683–688, 1993.
- [6] Y. Ben-Haim, "A non-probabilistic concept of reliability," Structural Safety, vol. 14, no. 4, pp. 227–245, 1994.
- [7] I. Elishakoff, "Discussion on: a non-probabilistic concept of reliability," *Structural Safety*, vol. 17, no. 3, pp. 195–199, 1995.
- [8] X. P. Du, "Interval reliability analysis," in *International Design Engineering Technical Conferences Computers and Information in Engineering conference*, The American Society of Mechanical Engineers, Cleveland, Ohio, USA, 2007.
- [9] X. P. Du, A. Sudjianto, and B. Q. Huang, "Reliability-Based Design With the Mixture of Random and Interval Variables," in ASME 2003 Design Engineering Technical Conference and Computers and Information in Engineering Conference (DETC2003), American Society of Mechanical Engineers, Chicage, IL, USA, 2005
- [10] C. Jiang, W. X. Li, X. Han, L. X. Liu, and P. H. Le, "Structural reliability analysis based on random distributions with interval parameters," *Computers & Structures*, vol. 89, no. 23, pp. 2292– 2302, 2011.
- [11] L. Wang, D. Liu, Y. Yang, X. Wang, and Z. Qiu, "A novel method of non-probabilistic reliability-based topology optimization corresponding to continuum structures with unknown but bounded uncertainties," *Computer Methods Applied Mechanics and Engineering*, vol. 326, pp. 573–595, 2017.
- [12] Z. Qiu, D. Yang, and I. Elishakoff, "Probabilistic interval reliability of structural systems," *International Journal of Solids* and Structures, vol. 45, no. 10, pp. 2850–2860, 2008.
- [13] J. Liu, G. Wen, Q. Qing, and Y. M. Xie, "An efficient method for topology optimization of continuum structures in the presence of uncertainty in loading direction," vol. 14, 2017.
- [14] F. Li, G. Sun, X. Huang, J. Rong, and Q. Li, "Multiobjective robust optimization for crashworthiness design of foam filled thin-walled structures with random and interval uncertainties," *Engineering Structures*, vol. 88, pp. 111–124, 2015.
- [15] L. Wang, X. Wang, Y. Li, G. Lin, and Z. Qiu, "Structural time-dependent reliability assessment of the vibration active control system with unknown-but-bounded uncertainties," *Structural Control and Health Monitoring*, vol. 24, no. 10, 2017.
- [16] W. Gao, D. Wu, K. Gao, X. Chen, and F. Tin-Loi, "Structural reliability analysis with imprecise random and interval fields," *Applied Mathematical Modelling*, vol. 55, pp. 49–67, 2018.
- [17] Z. Meng, G. Li, D. Yang, and L. Zhan, "A new directional stability transformation method of chaos control for first order reliability analysis," *Structural and Multidisciplinary Optimization*, vol. 55, no. 2, pp. 601–612, 2017.
- [18] L. Wang, X. Wang, H. Su, and G. Lin, "Reliability estimation of fatigue crack growth prediction via limited measured data," *International Journal of Mechanical Sciences*, vol. 121, pp. 44–57, 2017.
- [19] J. Liu and G. Wen, "Continuum topology optimization considering uncertainties in load locations based on the cloud model," *Engineering Optimization*, vol. 50, no. 6, pp. 1041–1060, 2018.
- [20] J. Liu, G. Wen, X. Chen, and Q. Qing, "Topology optimization of continuum structures with uncertainty in loading direction," in *Proceedings of the 6th International Conference on Mechanics* and Materials in Design, Ponta Delgada, Portugal, 2015.

[21] A. Haldar and R. K. Reddy, "A random-fuzzy analysis of existing structures," *Fuzzy sets and systems*, vol. 48, no. 2, pp. 201–210, 1992.

- [22] Z. Ni and Z. P. Qiu, "Hybrid probabilistic fuzzy and non-probabilistic model of structural reliability," *Computers & Industrial Engineering*, vol. 58, no. 3, pp. 463–467, 2010.
- [23] L. Wang, X. Wang, D. Wu, M. Xu, and Z. Qiu, "Structural optimization oriented time-dependent reliability methodology under static and dynamic uncertainties," Structural and Multi-disciplinary Optimization, pp. 1–19.
- [24] Z. Qin, "Random fuzzy mean-absolute deviation models for portfolio optimization problem with hybrid uncertainty," *Applied Soft Computing*, vol. 56, pp. 597–603, 2017.
- [25] J. Wu, Z. Luo, H. Li, and N. Zhang, "Level-set topology optimization for mechanical metamaterials under hybrid uncertainties," *Computer Methods Applied Mechanics and Engineering*, vol. 319, pp. 414–441, 2017.
- [26] D. Wu and W. Gao, "Hybrid uncertain static analysis with random and interval fields," *Computer Methods Applied Mechanics* and Engineering, vol. 315, pp. 222–246, 2017.
- [27] W. Wang, H. Gao, C. Zhou, and Z. Zhang, "Reliability analysis of motion mechanism under three types of hybrid uncertainties," *Mechanism and Machine Theory*, vol. 121, pp. 769–784, 2018.
- [28] L. Wang, X. J. Wang, and Y. Xia, "Hybrid reliability analysis of structures with multi-source uncertainties," *Acta Mechanica*, vol. 225, no. 2, pp. 413–430, 2014.
- [29] S. S. Rao and L. Berke, "Analysis of uncertain structural systems using interval analysis," *AIAA Journal*, vol. 35, no. 4, pp. 727–735, 1997.
- [30] G. J. Shao and J. B. Su, "Interval finite element method and its application on anti-slide stability analysis," *Applied Mathematics* and Mechanics, vol. 28, no. 4, pp. 521–529, 2007.
- [31] D. B. Miracle and O. N. Senkov, "A critical review of high entropy alloys and related concepts," *Acta Materialia*, vol. 122, pp. 448–511, 2017.